LOCAL WATERFLOODING ASSESSMENT USING 4D SEISMIC DATA & RESERVOIR SIMULATION

Nkechi Nneka Obiwulu

Thesis Submitted for the Degree of Doctor of Philosophy

Institute of Petroleum Engineering
School of Energy, Geoscience, Infrastructure and Society,
Heriot-Watt University, Edinburgh, UK

July 2018

Abstract

The substitution of oil with water that occurs during waterflooding triggers main 4D seismic effects of increased water saturation and increased pressure. In reservoir management and surveillance, increased waterflooding effects are typically interpreted for waterflood performance assessment using multiple data (geology, well logs, seismic data, production daya), reservoir simulation and seismic forward modelling technologies. This thesis focuses on the finer details of local or well-centric 4D seismic interpretation of waterflooding using integrated reservoir management. The main objective is to apply detailed interpretation of the local waterflooding 4D seismic signal to reservoir surveillance and management, through a reservoir engineering perspective. This facilitates evaluation of waterflooding performance, reservoir characterisation and reservoir model update. In this study, the influences of reservoir model scale on the synthetic seismic modelling, as well as significance of incorporating the individual waterflooding effects like salinity or temperature changes are estimated for a waterflooding scenario in a North Sea reservoir. The feasibility of resolving these influences given practical modelling conditions and approximations in reservoir engineering along with real seismic data are investigated to measure the resultant errors on the 4D seismic interpretation. Individual waterflooding effects are confirmed to impact the interpreted seismic signal. The magnitude of the added value of including this impact in 4D seismic signal interpretation is however seen to be data dependent.

The relationship between 4D seismic signal and increased water saturation from waterflooding is established and used to calibrate net injected water volumes estimated from three-dimensional geobodies of the 4D seismic water saturation signal to real production volumes. An extension of this relationship is the basis on which quantitative waterflooding seismic performance metrics are defined. The performance metrics are applicable to well-centric flood patterns for fast evaluation of oil displacement efficiencies and flood directionality. Combined resultant waterflood characterisation from the performance metrics gave good indications of field-scale sweep efficiencies, inter-well connectivity and possible waterflooding induced fractures. These interpretations of the 4D seismic flood patterns were then applied in reservoir model update via a local seismic automatic history matching using binary images and an evolutionary algorithm. Realisations from the geostatistical simulation of reservoir net-to-gross ratios constrained by seismic and well logs were used in a local automatic seismic history

matching workflow. Binary image interpretations of the 4D seismic data were utilised in the optimisation of misfit reduction between observed 4D seismic and the simulated flood patterns. A new method of handling the mapped waterflood responses of saturation and pressure in spite of known uncertainties (of the contrasting seismic signal) led to improvements in the flood pattern match and the history matching result. Limitations of reduced heterogeneity in utilising binary images and obscuration of the water saturation signal by contrasting 4D seismic pressure response were evident in the history matching. The management of these highlighted the dependence of a successful seismic history matching exercise on a suitable dataset with clear depictions of waterflooding signals of saturation and pressure. The overall study emphasises the importance of early waterflood evaluation in waterflood surveillance for reservoir characterisation, prompt mitigation of waterflooding challenges and timely reservoir management decision making.

Dedication

To my husband, Emeka
And my sons, Nnanyelugo and Makuachukwu,
All who went through the full PhD cycle,
Giving up as much blood, sweat and tears as I did,
With an addition of being chief cheerleaders.
Love you to the moon and back and back again.

Acknowledgements

It has been a really long journey to get here and there are so many and so much I am thankful for. It has been an amazing blessing thus far and I thank God for life, health, family and taking me on this amazing journey.

I would like to first thank my supervisor Prof. Colin MacBeth. For taking a chance on me, for your continued support and encouragement. You made it extremely easy to be your student, inspiring us to think, think well and differently, wanting us to excel, to push the science envelope, to be the best versions of ourselves. From challenging my grammar (I have now relegated the word "gotten" to the quaint English/American box like you insisted), to your ability to practically unearth "scientific low hanging fruit" by breaking down theories to the fundamentals, I would take your lessons along with me for life. I also consider myself really lucky to call myself one of your students especially in such a competitive world where a young mum attempting to make any kind of strides professionally or academically does not have the easiest of times, how much less when she goes on to have a baby on the job - I don't think there could have been a more supportive boss. It feels as if the rest of the world is just catching up on female empowerment; with how supportive and understanding ETLP is, it is already head and shoulders above the rest. Thank you. Thank you. Thank you.

My utmost gratitude goes to Dr Romain Chassagne for co-supervising my research and for your guidance throughout my PhD. Thanks, Romain for the lessons in French humour and for being very patient and gracious, letting me upset your routine time and time again while I exploited your computer for my work. It made all the difference, thank you.

Thank you to the ETLP family. You all make ETLP what it is: true family looking out for each other. Each one of you had an impact on my PhD and I would remain indebted to you all: Dennis (for all the initial handholding and being such a good friend), Miguel, Ming, Angel, Chong and Lee-Jean (you both have a special place in my heart), Ricardo, Ilya, Lu, Phung, David, Veronica, Gustavo, Alejandro, Sean, Qi, Ilona, Shaji, Olarinre and Eric. To Jesper, Badr, and Samarth who have just joined, it is lovely to have met you, thank you for these last days. I especially would like to thank Hamed and Maria-Daphne, outstanding geophysicists and two ridiculously kind-hearted people. You two are most of the glue that keeps ETLP together. Thank you for all your selfless help and technical discussions. MD, your family became my family away from home while you treated me as one of your own. Hamed, climbing

the Schiehallion and your kindness in practically carrying lame me all the way when you didn't have to, would remain with me. For all the times you both took time out of your crazy schedules to lend a guiding hand or be a friend, I can't thank you enough. You both are inspirations. Thank you for everything.

My sincere gratitude goes to the Edinburgh Time Lapse Project (ETLP) Phase V & VI sponsors for funding my research. Thank you to Ian Jack and the Society of Exploration Geophysicists (SEG) for the SEG/Ian G. Jack Scholarship I was privileged to receive. The talks and advice from various sponsors helped shape my research, and provided professional guidance, particularly discussions with John Wild and Ian Jack. Thank you very much. There would be no research without data and my thanks goes to BP for providing the field data used and to Linda Hodgson for her continued support and technical discussions. Schlumberger Petrel, Eclipse and MEPO software were mainly used during my research which would not be possible without their licenses. Thank you very much. With access to software came the need for I.T. support and I am extremely grateful to Alan Brown in particular, who with Ian Chisolm and the rest of the IPE Computer Support team went above and beyond making sure all my computer challenges were resolved near immediately, software regularly updated, sorting out seamless remote connection whenever I need it through changing versions over the years. To Rafael Castaneda, my first Python teacher who was very kind enough to share his busy PhD time with me teaching and crafting code, I cannot thank enough.

An African proverb says, "it takes a village to raise a child". In the same way, it has practically taken a community to get me here. To my mum and dad, thank you for your love and support - To my mum for reading between the lines every time, helping to support us every way you could. Daddy, I know how much this means to you, having one of us join you in research. Thank you for all your support and I hope I've made you proud. Thanks to my sisters Nma and Uche, two of the three *Ezedinachi musketeers*, for your continued love and support – I'm done now luvies, time to work towards lighting up our long-hibernated dream. Thank you, Uncle Chike for your support of me and mine. Your wise words were sometimes exactly what I needed. My aunties Ify and Uzo took my PhD journey personal, practically harassing me lovingly with phone calls and requests for updates. Though you continually moaned to each other about how overwhelmed I sounded each time you called me in a bid to brace yourselves for my series of complaints, your love and support meant a lot to me. To my sisters-in-law, Ifeyinwa, for all the impromptu childcare favours during sudden trips to Edinburgh, and

Adaeze holding down ‘our’ Lagos forte with typical love and grace; and to the rest of my Obiwulu clan: Ikemba, Ezenwanyi, Afam, Chizy, Obi, Ikenna and Olisa of blessed memory, thank you for all your love and prayers. To my friend and resident “cousin”, Chinedu Eze, thank you for all your support and for the instant magic you worked to effectively shelter us in Edinburgh on one occasion. Thank you very much to my *besties* Bukky, Sally, Odiong and Ijeoma that kept me sane all the while I was living under a rock working towards this. At a time, your phone calls with just the right amount of constructive gossip, simply checking up on me or discussions on American politics were all I needed to keep going. Thank you for your support and for knowing when to kick me (or yourselves) off the phone so I could study.

My sons, Makua and Lugo have worked as hard with me on this PhD. All the negotiated pages of bedtime stories, the skipped activities because mummy had to work, your patience while mummy's school deadline kept moving disrupting your countdown to the finish, time and time again. I really could not have asked for more. You both have been amazing, and this is for you. People ask how I balanced school and everything else and my answer is always the same: Your smiles and laughter, hair-raising antics and endearing gestures while watching you grow into yourselves make it worth it every day. For all the lapses in my concentration and absence, I'm back now and I'd make it all up to you.

To my husband, Emeka, I don’t have the words and can only say thank you so much for loving me the way you do. I thought it was a little ridiculous how excited you were for me when we started this journey, but you topped that with all your sacrifice, encouragement, prayers and support. In many ways, you’ve been the wind in my sails, your unique optimism and positivity carrying us through. As far as I am concerned, this is as much yours as it is mine – We did it, Babez! Now, on to the next.

Niki Obiwulu, July 2018

DECLARATION STATEMENT

(Research Thesis Submission Form should be placed here)

Table of Contents

List of Figures

Chapter 1

Introduction: Waterflooding Assessment and 4D Seismic

The use of 4D seismic in reservoir monitoring and surveillance has increasingly become important over the years, especially in the assessment of waterflooding campaigns. This chapter first introduces waterflooding and conventional assessments, expanding to the use of 4D seismic data in integrated reservoir management. From the reservoir engineering perspective, it highlights the significant benefits of 4D seismic integration at different scales from field-scale to well-scale and describes the approach of investigating and exploiting achievable profits of a well-centric 4D seismic interpretation.

1 Introduction: Waterflooding Assessment and 4D Seismic

1.1 Waterflooding

Water flooding is a widely used oil recovery method for most reservoirs and refers to the injection of water into the reservoir for the purpose of sweeping oil towards producing wells. The first accidental waterflood occurred in 1865 in the Pithole City of Pennsylvania (Craig, 1971) as a result of water from shallow water sands flowing into oil sands leading to oil sweep. Following 85 years of development and improvement, waterflooding was accepted as a general practice, and a century and a half after discovery, its advantages of relatively inexpensive availability, ease of implementation and effectiveness have ensured its continued popularity.

The North Sea oil and gas industry pioneered the approach to reservoir management based on a waterflooding campaign spanning the full lifecycle of a waterflood – from design and conception until the end of its economic viability (Dake, 2001). For an optimum waterflooding campaign with maximized recovery factor, monitoring, evaluation and prediction of the waterflooding performance are essential. These are achieved with an integrated waterflood surveillance system of reservoir characterization, design, development and maintenance of the injector wells and subsequent disposal or processing of the produced water. An example of a waterflood surveillance cycle is illustrated in Figure 1.1, with elements detailed in Table (1.1).

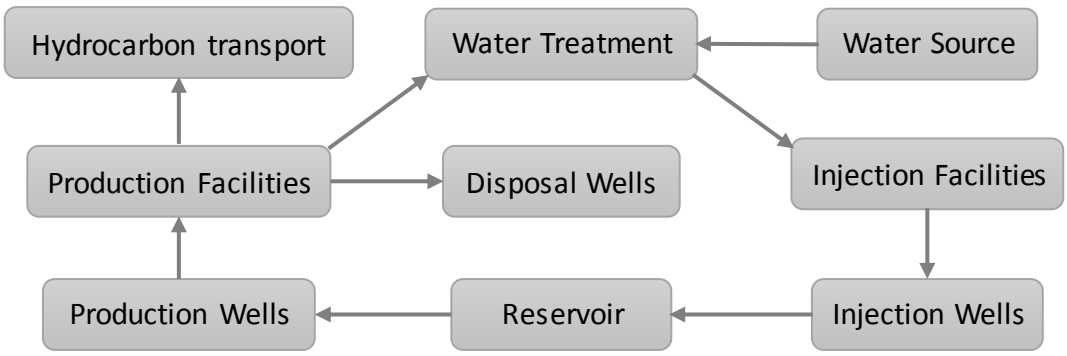

Figure 1.1: Waterflood cycle (Thakur, 1991)

1.2 Oil Recovery by Waterflooding

The percentage of oil recoverable by waterflooding is dependent on various attributes of the reservoir. Characteristics considered most influential (Smith and Cobb, 1997) are:

The end-point saturation and relative permeability values -

1. Original oil saturation - S_o,
2. Residual oil saturation to water - S_{orw},
3. Connate or irreducible water saturation - S_{wc},
4. Initial free gas saturation - S_g,
5. Relative permeability to oil and water, K_{ro} and K_{rw},
6. Effective permeability to oil at irreducible water saturation, $(K_o)_{Swirr}$,

Reservoir fluid properties -

7. Viscosities of water and oil - μ_o and μ_w,
8. Oil formation volume factor- B_o,

Geological structure dependent variables –

9. Vertical reservoir architecture (degree of stratification with noncommunicating layers or homogeneity),
10. Volume of accessible oil to waterflood given pore distribution and connectivity,

Reservoir management variables –

11. Waterflood pattern,
12. Injector-producer pressure distribution,
13. Injection rates and,
14. Waterflood economics.

1.3 Reservoir Management for Waterflooding Campaigns

Waterflood campaigns are considered successful if the waterflood campaign is economical and if the wells are functioning properly, well integrity is maintained with good balance between the injectors and producers and there is good conformance of the waterflood to the intended design. For a waterflood campaign, as illustrated in Figure 1.2 (Talash, 1988; Thakur, 1991; Terrado et al., 2007), reservoir management in the waterflood cycle is most crucial. Effective reservoir management for reservoirs undergoing waterflooding begins with a good definition of the reservoir's depositional environment and geological architecture. It continues to an evaluation of the extent and capacity of the pay zone, the design of waterflood with patterns

beneficial to the specific reservoir characteristics and ends with continued waterflooding surveillance involving analysis of waterflood conformance. There is a plethora of industry integrated tools and methods that jointly achieve these, but the preferred tool remains the reservoir simulation model. The simulation model has the ability to incorporate all the aforementioned management activities as a composite system which can be utilized in the design, evaluation and prediction of waterflood.

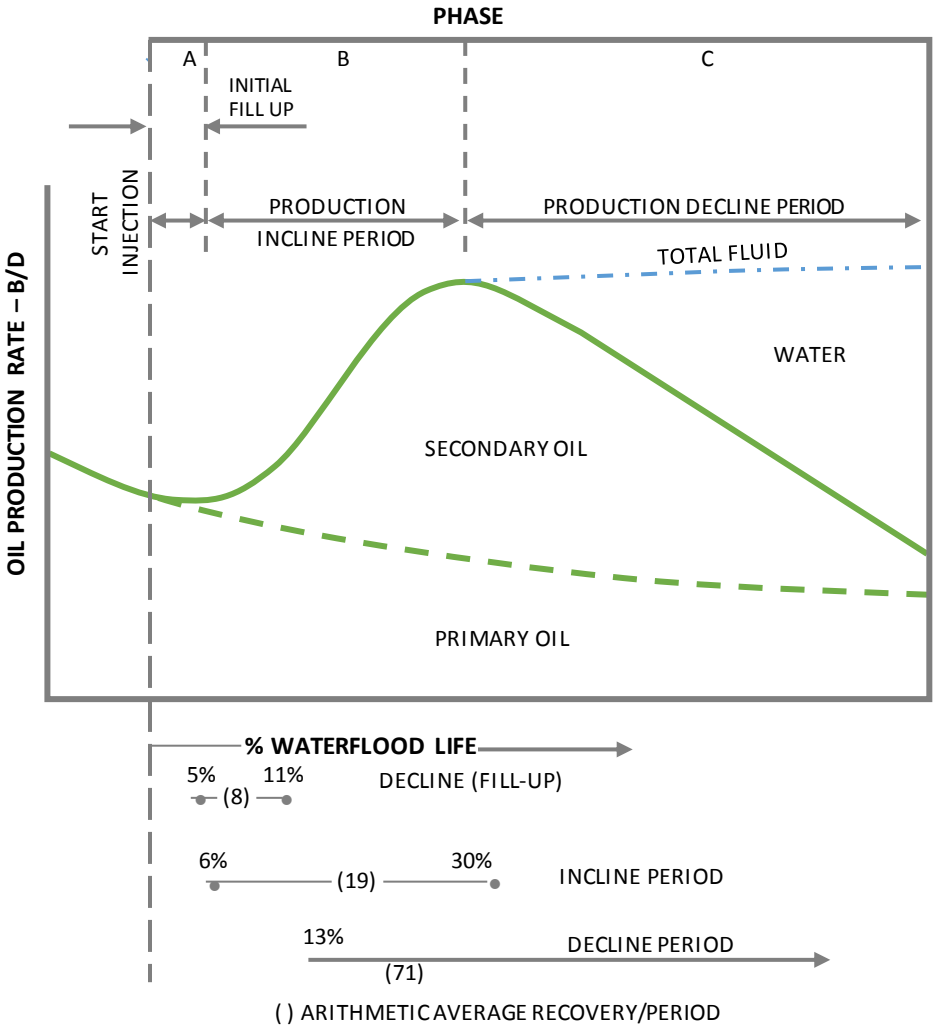

Figure 1.2: Typical successful waterflood performance (After Thakur, 1991)

WATERFLOOD SURVEILLANCE

Reservoir	**Wells**	**Facilities**	**Water System**
Pressure	Perforations	Production/injection monitoring equipment	Water quality
Rates	Production/injection logging		Presence of corrosive dissolved gases, minerals, bacterial growth, dissolved solids and suspended solids
Volumes	Injected water in target zone		
Cuts	Tracers		
Fluid samples	Tagging fill		Ion analysis
Hall plots	Cement integrity		pH analysis
Fluid drift	Downhole equipment		Corrosivity
Pattern balancing	Wellbore fractures		Oil content
Pattern realignment	Formation damage		Iron sulfide
	Perforation plugging		On-site or laboratory analysis
	Pumped-off condition		Data gathering on source and injection wells & system

Table 1.1.1: Elements of a comprehensive waterflood surveillance program (Thakur, 1991)

1.4 Waterflood Monitoring and Surveillance

During waterflooding, it is important to anticipate possible geological problems (e.g. bypassed oil, flow barriers, permeability streaks) or engineering problems (insufficient voidage replacement, ineffective perforations) and prevent or rectify them efficiently and in a timely manner. This highlights the critical importance of constant waterflood monitoring for which techniques have been frequently published (Talash, 1988; Thakur, 1991; Satter and Thakur, 1994; Gulick and McCain, 1998; De et al., 2000; Sugai and Nishikiori, 2006; Terrado et al., 2007; Das et al., 2009).

There are different levels of reservoir management for waterflooding success: 1) field level, 2) sector level 3) pattern level and 4) well level, in ascending order of dependence (the field level depends on the sector level, sector level depends on the pattern level, etc). The next sections first give an overview of the methods of performance evaluation at these levels and then contrast these with waterflood management methods using 4D seismic data.

1.4.1 Field level

A field level waterflood management involves an analysis of the field's recovery factor, the average reservoir pressure, the Voidage Replacement Ratio (VRR), percentage of total water cut, gas-oil-ratio and water-oil ratio trends, well productivity and change in fracture pressure as a result of injection (Terrado et al., 2007). The ultimate objective of waterflooding is to maximize the recovery factor. With careful management, waterflooding is known to achieve a recovery factor of 30% to 60% (Smith and Cobb, 1997; Fanchi, 2005). This effectively translates to good oil sweep and a well-maintained reservoir pressure. Good reservoir pressure support ensures the continued flow of oil towards the producers and maintains the reservoir pressure above bubble point to resist gas exsolution which decreases the mobility rate with increase in the oil viscosity.

VRR compares the volume of injected fluid to the volume of produced fluid (Terrado et al., 2007). It is a plot used to indicate when insufficient water is being injected, estimating the optimum volume of water required for waterflood conformance; When the VRR is

>1 without a noticed increase in reservoir pressure, loss of injected volumes to thief zones or out-of-zone injection should be investigated. Conversely, if VRR is a fraction with decreasing reservoir pressure, the possibility of an alternative water supply is investigated. The plot in Figure 1.3 shows the direct relationship between the VRR and the oil rate, for an oil field undergoing waterflooding (Terrado et al., 2007).

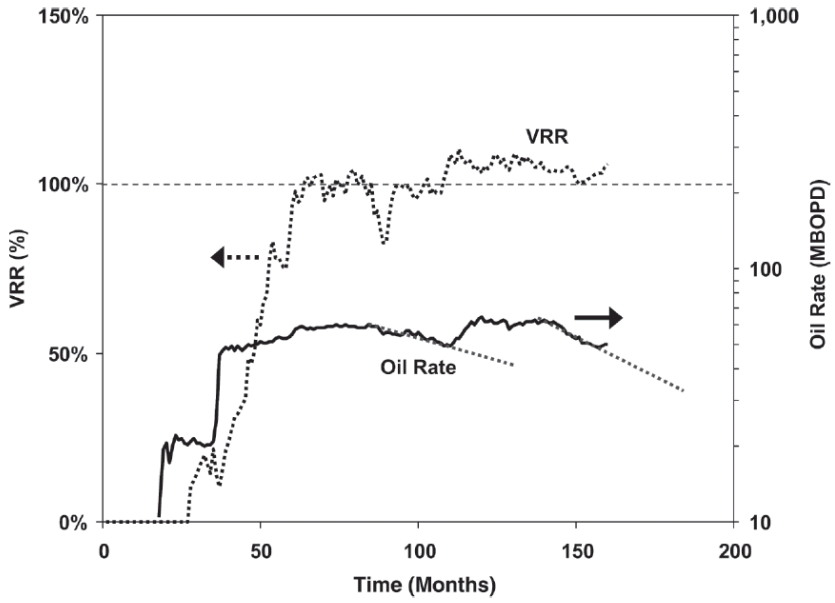

Figure 1.3: Plot showing VRR (dotted lines) with direct relationship to oil rate (Terrado et al., 2007).

Analysis of the water cut, gas-oil-ratio and water-oil-ratio all relate to the balance of cumulative water and hydrocarbons versus time in the reservoir and reveal field waterflooding performance levels. High water-cut rates without an increase in the GOR is indicative of high permeability streaks or excessive pressure support, while the reverse would point to low pressure support (Smith and Cobb, 1997).

1.4.2 Sector Level

For large fields comprising several wells, waterfloods are designed in subdivisions of sectors or blocks. These subdivisions could be defined by geological architecture like hydraulically noncommunicating barriers or production limits such as well pressure boundaries (Terrado et al., 2007).

Recovery factor, E_R, evaluated at the field level is defined by:

$$E_R = E_D \times E_{Vol} \quad (1.1)$$

where: E_R = Recovery factor, E_D = Displacement efficiency within swept volume and E_{Vol} = volumetric sweep efficiency.

Displacement efficiency, E_D, is the fraction of displaced oil within the swept rock with respect to the initial oil saturation within the rock (Collins and Simons, 1961; Satter and Thakur, 1994) and is dependent on the reservoir rock and fluid properties and the volume of flood through the rock. It can be measured using empirical equations, core flood analysis and frontal advance theory (Satter and Thakur, 1994).

Volumetric efficiency with respect to a waterflood sector is the ratio of the volume of displaced oil within the sector to the original oil in place and is defined as:

$$E_{Vol} = E_A \times E_V \quad (1.2)$$

where: E_{Vol} = volumetric sweep efficiency, E_A = areal sweep efficiency, the fraction of the oil recovered areally and E_V = vertical sweep efficiency, the fraction of the oil recovered in the reservoir cross-section.

The volumetric sweep efficiency of sectors within a field depict how different sectors contribute to the ultimate recovery factor of the field and in instances of low E_{vol}, the individual areal sweep efficiency should be investigated with available techniques, e.g. tracers, and the injection profiles analysed to determine if the low efficiency is contributed by the vertical sweep efficiency.

1.4.3 Pattern Level

At the pattern level, waterflood management is designed for each waterflood pattern configuration. Within each pattern, it could involve comparing volumes of water injected against volumes of liquid produced to determine pattern VRR or evaluating injector-producer communication and areal sweep efficiencies using tracer data. A measure of the connectivity between injectors and producers has been extensively explored in the literature with popular methods of using the Spearman's rank correlation (Heffer et al., 1997) and the Capacitance Resistance Model (Yousef et al., 2005b; Sayarpour et al.,

2009). Injector-producer connectivity, areal sweep efficiency, and water breakthrough can be geologically linked, and appropriate analysis would ultimately lead to improved understanding of reservoir heterogeneity and good control of waterflood performance at the pattern level. Waterflooding monitoring within patterns helps identify opportunities for improvement of injection rates, infill drilling or injection-producer conversions towards increased waterflood performance (Terrado et al., 2007).

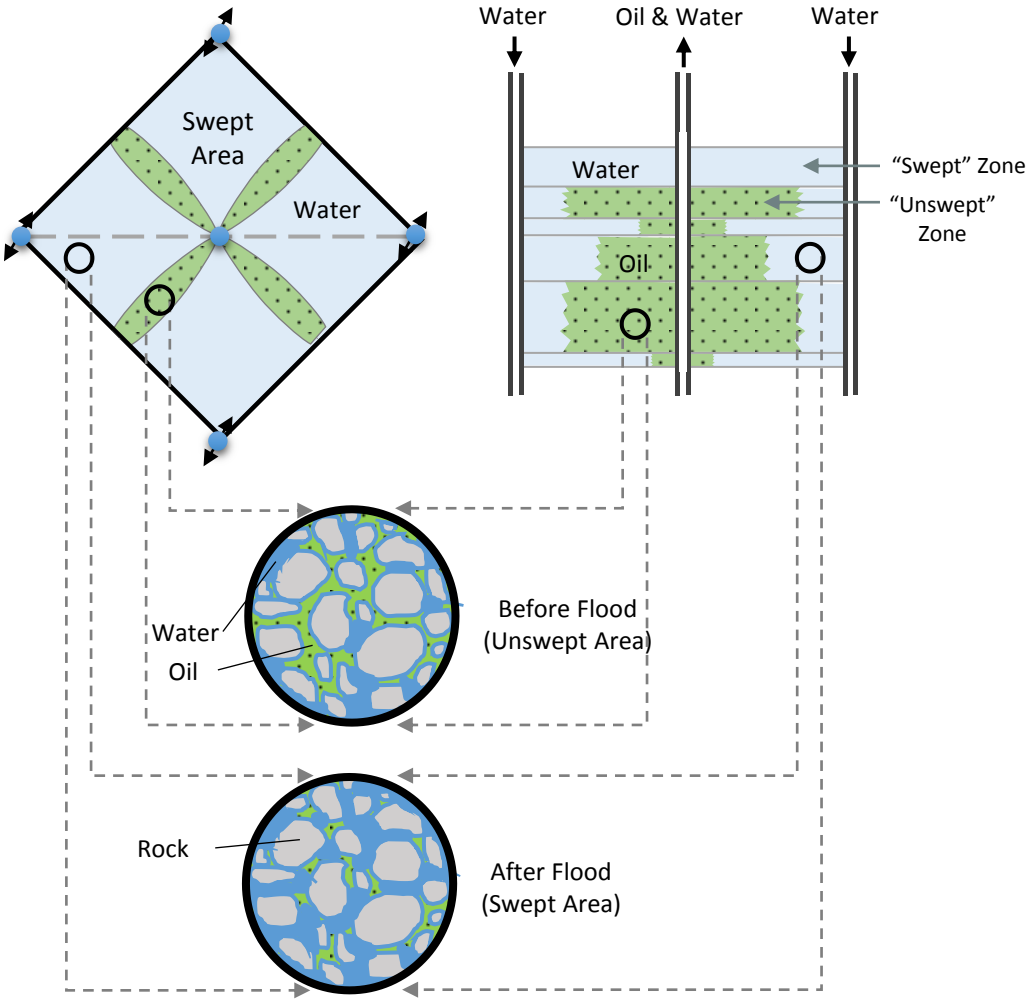

Figure 1.4: Areal sweep efficiency and cross-section showing vertical sweep (After Satter and Thakur, 1994)

Areal sweep efficiency as illustrated in Figure 1.4, is the percentage of the swept section of the pattern area (or area designated for waterflooding) (Satter and Thakur, 1994). It is also dependent on the heterogeneity of the reservoir, the waterflood pattern type, volume of flood and mobility ratio.

In waterflooding studies decades ago, areal sweep efficiency was initially evaluated using basic mathematical or physical analysis of the steady-state pressure distribution (Craig, 1971; Satter and Thakur, 1994). It then advanced to duplicating the steady-state flow with the flow of electric current in the electrolytic model (Craig, 1971). In more recent times, evaluation and prediction of areal sweep efficiency are achieved using time-lapse mapping logs, sensors, tracer analysis and numerical methods.

1.4.4 Well level

The well level waterflood management involves analysing the health of the wells to improve waterflood performance by maximizing injectivity, evaluating vertical sweep, preventing and mitigating instances of plugging, fracturing or lost volumes (Terrado et al., 2007). Wells are frequently subjected to specialised tests to estimate the formation fracture pressure, the reservoir flow capacity, reservoir pressure and possible formation damage during waterflood surveillance (Smith and Cobb, 1997). Maximizing injectivity while avoiding formation fracture requires a knowledge of the reservoir fracture pressure. Though an approximate formation fracture pressure is typically estimated as the wells are drilled, the formation fracture pressure evolves over time as pore pressure changes and in proportion to the level of injectivity the well experiences. For this, knowledge of individual well fracture pressures is important and can typically be determined using the fracture step rate test (Smith and Cobb, 1997). This test involves controlled injection at incrementally increasing rates until the formation 'parts' under what is regarded as the Formation Parting Pressure, FPP.

Injecting above formation parting pressure for long periods induces vertical fractures in the formation. Orientation of these fractures could affect flood direction and drastically reduce the sweep efficiency. The fractures could also create avenues for lost volumes or high permeability streaks, compromising the well integrity or jeopardising the reservoir seal or overburden (Crawford and Collins, 1954; Dyes et al., 1958). The Hall Plot (Hall, 1963) is a widely used diagnostic plot which evaluates the 'health' of an injection well with respect to fractures, positive or negative skin effects and injector well plugging. It uses the relationship between average bottom-hole injection pressures and cumulative injected volumes over time and is based on the principles of Darcy's law. With the assumption of steady-state flow (constant pressure, velocity and temperature) at the injection well, a change in the slope of the plot is analysed to determine possible changes

in the well condition. Deviation of the plot in an increasing or decreasing direction could be indicative of well-plugging possibly as a result of gradual skin development, or fractures and loss of injected volumes, depending on the direction of deviation (see Figure 1.5).

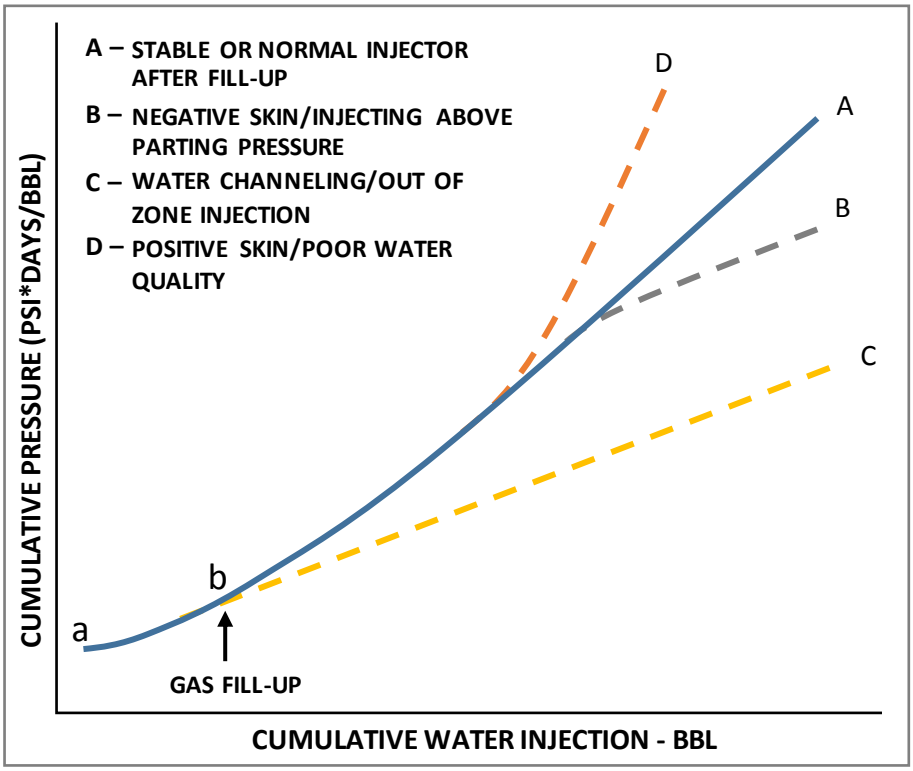

Figure 1.5: Hall's plot. (Thakur, 1991)

1.5 4D Seismic Data and Waterflood Monitoring

4D seismic with its reservoir imaging abilities and its improving quantitative interpretation delivers an invaluable contribution to waterflood surveillance and performance improvement. There have been several publications (Kolstoe et al., 2008; Mikkelsen et al., 2008; Mandal et al., 2011) highlighting the value of 4D seismic in waterflood surveillance across the different surveillance levels from field level to well level.

Field level: Field-scale reservoir heterogeneity is one of the most important factors that affect the waterflood performance, but one of the most difficult to quantitatively determine. An example of field level 4D seismic waterflooding surveillance is detailed in Staples et al. (2006). In Figure 1.6, the warm colours depict the increased water saturation (hardening) signal which prominently show the change in oil-water-contact in the Gannet

C reservoir. The 4D seismic interpretation for this field revealed previously undetermined extent of the reservoir thereby improving the reservoir characterization and reduced the uncertainties in the shape of the produced oil-water contact. By highlighting new reservoir heterogeneity and fault boundaries, it proved that the produced oil-water contact was not as flat as the original oil-water contact and explained the levels and timings of water-cuts towards an improved history match.

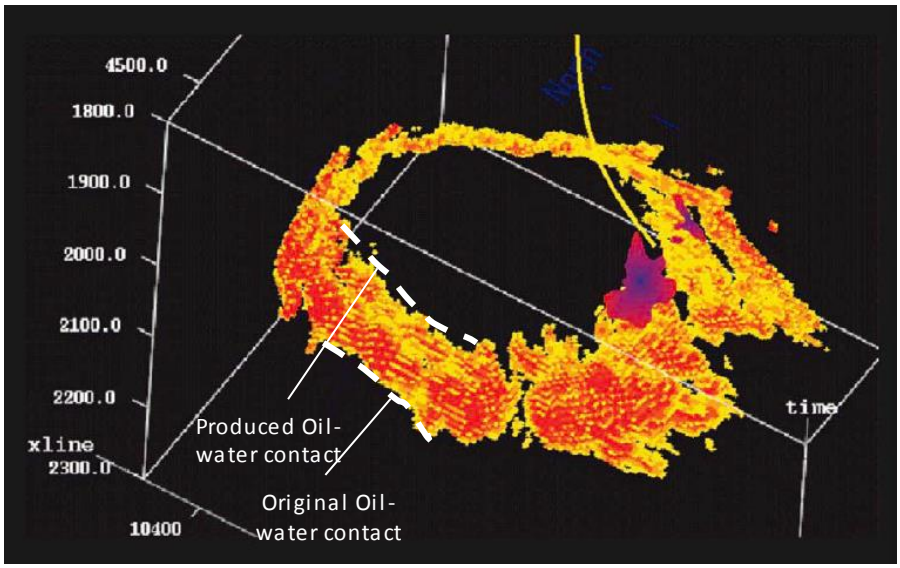

Figure 1.6: Field level waterflood surveillance - Perspective view of hardening 4D signal (yellow-red) around the field. (Staples et al., 2006)

In another example in the Draugen field, changes in the acoustic impedance as a result of increased water saturation from waterflooding show the spatial extent of the flood fronts. From these, areal sweep efficiencies can be evaluated. Figure 1.7 shows the areal sweep efficiencies, at three different monitor times: 1998, 2001 & 2004, all relative to 1990 (Mikkelsen et al., 2008). Waterflooding maintained the reservoir pressure, preventing gas from coming out of solution and keeping the reservoir in undersaturated conditions. Given the good pressure support from the water injectors, pressure changes were seen to have no significant effect on the 4D seismic signal relative to the water saturation signal. This allowed for direct calibration of the amplitude changes to the increased water saturation. Figure 1.8 has a clear hardening signal representing the flood front through a cross-section. The increasing red signal corresponds to increasing water saturation and the degree of vertical sweep efficiency of the field is inferred from the magnitude of amplitude change.

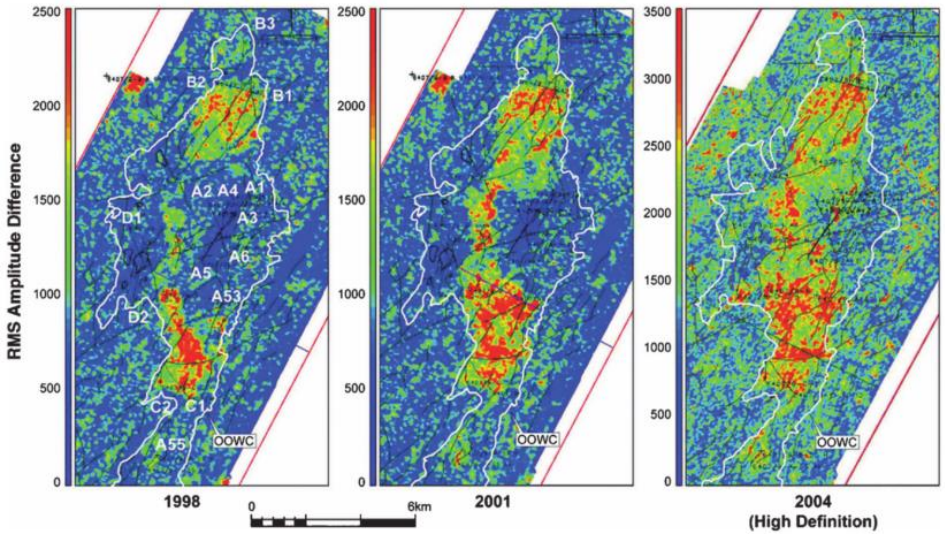

Figure 1.7: Seismic root mean square (RMS) amplitude difference showing water encroachment. OOWC - original oil-water contact. (Mikkelsen, et. al., 2008).

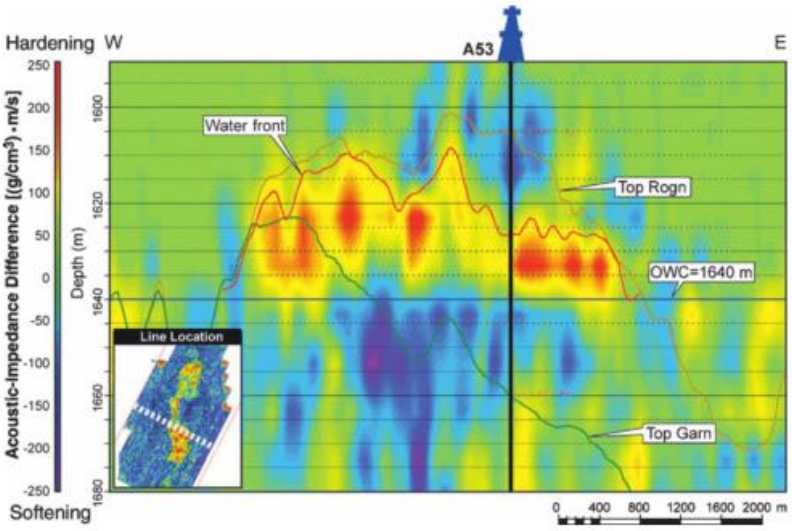

Figure 1.8: 4D seismic interpretation of the Draugen field through a cross-section. Acoustic impedance difference showing vertical water sweep (Mikkelsen et al., 2008).

On a pattern level, Mandal et al., (2011) discusses the improvement interpretation of the available 4D seismic data made on the evaluation of the peripheral radial pattern water injection in the Angsi field. Following the failure of other evaluation tools (depositional environment, tracers, and the reservoir simulation model), the challenge of explaining disorderly high water production rates, complex flood fronts and the unexpected comingled injection was not resolved until the integration of 4D seismic interpretation as part of the waterflood management system. Peripheral water injection from the west and north-west of the field began with the commencement of production in the Angsi field (Figure 1.9). Following three years of production in the field, the up-dip producers (C1

and C3) showed high water production rates, in contrat to the down dip producers' (B3 and B5) water breakthrough after six years. Without 4D seismic interpretation, it was challenging to understand the complex waterflood propagation paths explaining water breakthrough at the up-dip wells before the down-dip wells. Data integration of 4D seismic and PLT data revealed a high permeability streak connecting an injector to the up-dip producers and reduced injectivity in a lower reservoir leading to lost injected volumes helped better understand the waterflooding performance.

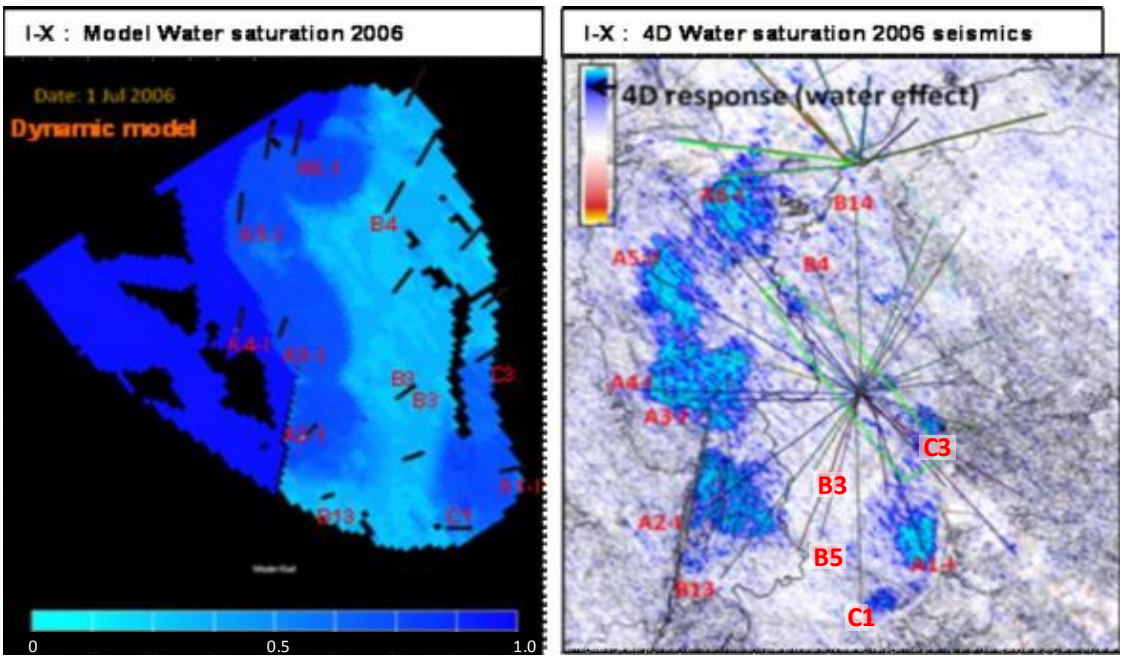

Figure 1.9: 4D hardening response around wells injecting in a peripheral radial pattern, (Mandal et al., 2011).

Well level waterflood surveillance using 4D seismic involves the added use of other tools like tracers and production logging tests (PLTs) in enhancing the 4D seismic benefit. This is true in the case detailed by Kolstoe et al. (2008). Figure 1.10 shows the cross-section through an injecting well. The hardening response as water replaces oil is seen to advance in a layer supposedly unconnected to the layer perforated for injection. Down well temperature logs confirmed that there was a cool down in the layers above the perforated layer, corresponding to the location of the hardening signal. This confirmed that the injected water was flowing to other layers via injection induced fractures.

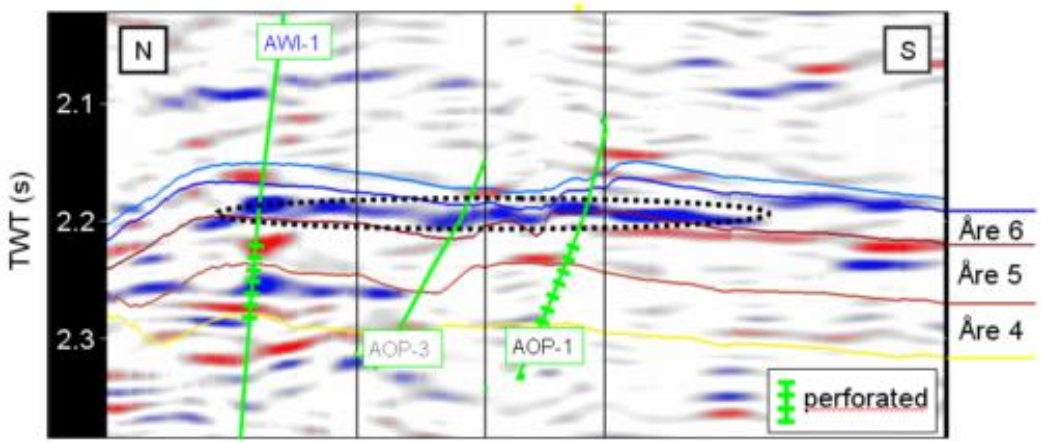

Figure 1.10: Cross-section through targeting area of AOP-3 showing the relative 4D effects between layers. Blue colour indicating hardening signal, water replacing oil in Are 6. (Kolsto et. al, 2008).

Another well level waterflooding surveillance example shows an integration of 4D seismic data and numerical well testing data. Numerical well testing is a combination of numerical simulation and pressure transient analysis and is used to monitor the advance of waterfronts. As an improvement from the conventional well-testing, the numerical well testing takes into account complex boundaries, reservoir heterogeneity and injector proximity to other wells. With a reservoir management plan incorporating frequent pressure transient analysis and available 4D seismic data, Suleen et al., (2017) were able to reduce the uncertainty in flood front size and shape as well as determine saturation in swept zones for an injecting well (Figure 1.11). Analytical and numerical transient analysis was conducted to first estimate the symmetrical flood radius. The flood front was then optimised within boundaries to corroborate the 4D seismic interpretation. A selection of numerical models was used to optimise the flood radius from pressure transient analysis and validate the 4D seismic data interpreted flood fronts (dashed lines in Figure 1.11).

(a)

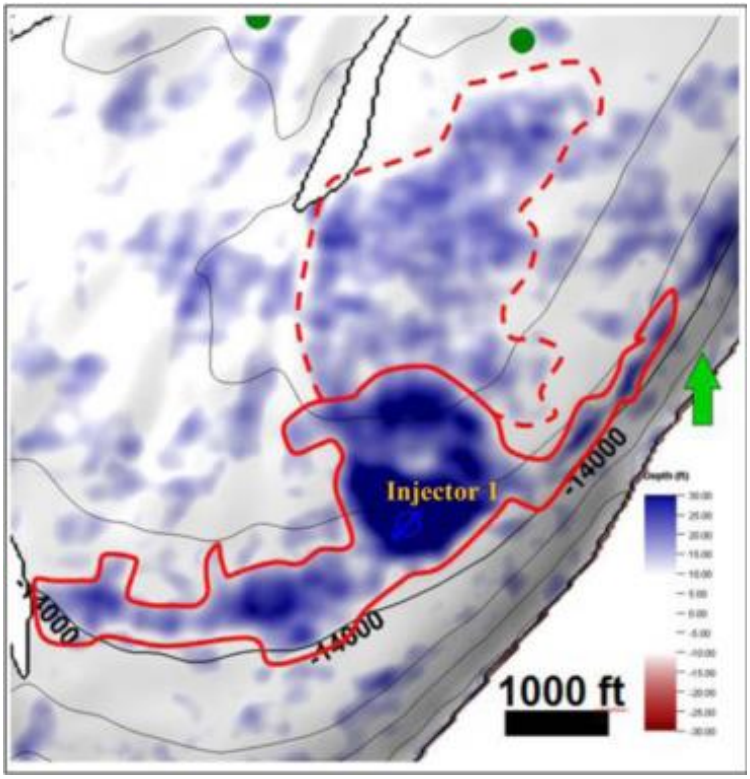

(b)

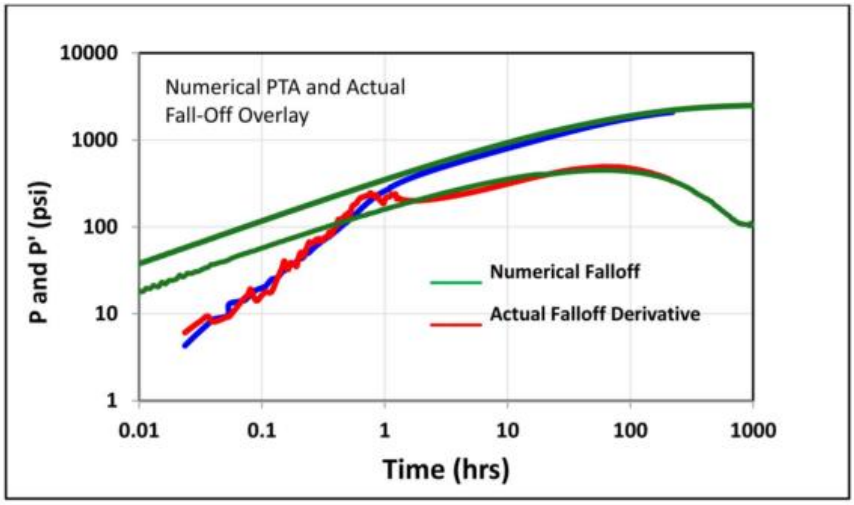

Figure 1.11: (a) 4D difference map of seismic amplitudes. Region inside solid red boundary showing significant seismic hardening; region inside dashed red boundary showing subtle/distant hardening from injector. (b) plot of numerical model that matched actual falloff test (Suleen et al., 2017).

1.6 Reservoir Simulation Model, Waterflooding and 4D Seismic Data

Reservoir modelling and simulation allows the collective input of multi-disciplinary data to model fluid flow in porous media, for maximized hydrocarbon recovery at minimal cost. Figure 1.12 shows the disciplinary contributions to reservoir simulation. With efficient integration of the different sources and formats of data at different scales (e.g. small scale well logs and large-scale seismic data), the concept of the reservoir is quantified into a grid of smaller volume elements (grid cells). The size of the gridcells determines the resolution of the reservoir model. A finer detailed description of the reservoir is achieved with small grid cells and provides more accurate predictions. This however leads to increased computational complexities and computing time. In contrast, a coarse description of the reservoir is achieved with larger cells, often leading to reservoir property approximations, loss of temporal and spatial detail and invariably reduction of the truthfulness of the reservoir model. Consequently, the quality of the reservoir model directly affects the accuracy of the waterflooding performance. There is, therefore, a trade-off between computational cost and loss of accuracy/precision with the omission of detail, with the use of reservoir simulation models. This is an inherent characteristic of the reservoir model which must be acknowledged and managed.

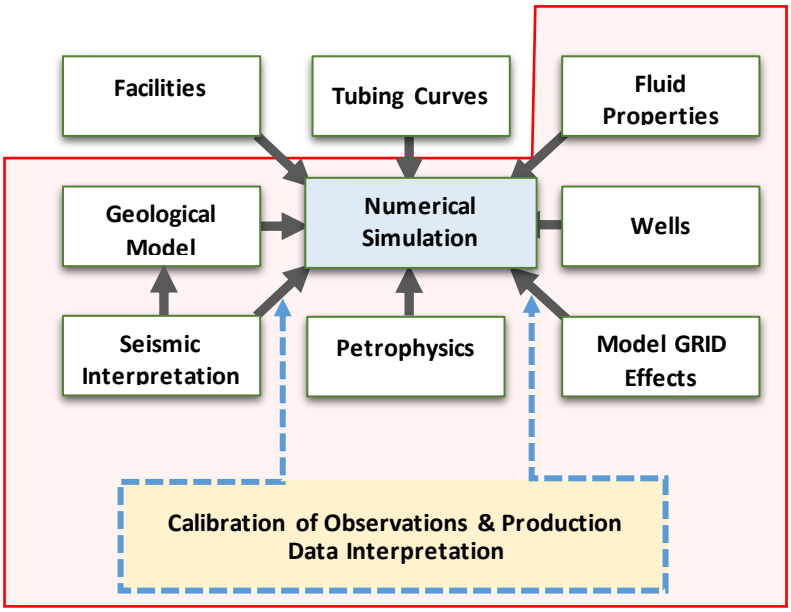

Figure 1.12: Disciplinary contributions to reservoir modelling. After Fanchi (2005)Fanchi (2005). Pink shaded area – area of focus for this thesis.

Evaluation of waterflooding performance in porous and permeable reservoirs using a reservoir simulation model considers the fluid-flow multi-dimensional, multiphase partial differential equations for fluid and rock property variations. The simulation model characterises areal and vertical heterogeneities, accounts for varying pressure and saturation as the reservoir undergoes dynamic changes as a result of water injection and waterflooding performance evaluation is not reliant on water breakthrough information (Smith and Cobb, 1997).

Despite challenges of repeatability and noise, the main attributes of 4D seismic include extensive spatial coverage with good lateral resolution but with a relatively compromised vertical resolution. With regards to reservoir management, 4D seismic is mostly used to monitor reservoir changes with ongoing production activities, imaging field wide dynamic characteristics of the reservoir. Incorporating these qualitative dynamic changes in the reservoir simulation model along with true dynamic information from the wells vastly improves the reservoir model's authenticity and prediction capabilities. Including 4D seismic data interpretations in the simulation model increases spatio-temporal benefits of waterflooding performance evaluation using the simulation model. In addition, tending towards more quantitative inclusions of 4D seismic data ensures that the full components of these benefits are captured. This is achieved with an integration of reservoir simulation, 4D seismic interpretation, simulator-to-seismic modelling and seismic history matching and model update.

1.6.1 Simulator to Seismic Modelling

Simulator-to-seismic modelling (*Sim2Seis*) links the 3D static properties of a reservoir and its dynamic changes as a result of reservoir production, to its seismic properties. This is achieved via a combination of the reservoir petroelastic model with a product of a synthetic seismic 3D volume. There are several methods of achieving this, but in this thesis, the Edinburgh Time-lapse Project, ETLP, *Sim2Seis* software is used. *Sim2Seis* calculates the elastic properties from the fluid flow simulation model and utilising a calibrated petroelastic model, applies 1D-convolution with an appropriately extracted wavelet to generate synthetic seismic data (Amini, 2014). A typical *Sim2seis* workflow is illustrated in Figure 1.13.

For waterflooding performance evaluation, synthetic seismic volumes can be generated for desired production times and used for the extended interpretation and prediction of the observed 4D seismic. This occurs, while accounting for the characteristic errors and uncertainties in the reservoir description carried through from the geologic and simulation models. For time-lapsed seismic interpretation, the corresponding baseline and monitor synthetic seismic volumes are modelled and the 4D differences of these compared to the observed differences. This helps verify the simulation model's ability to replicate the reservoir and its dynamic changes.

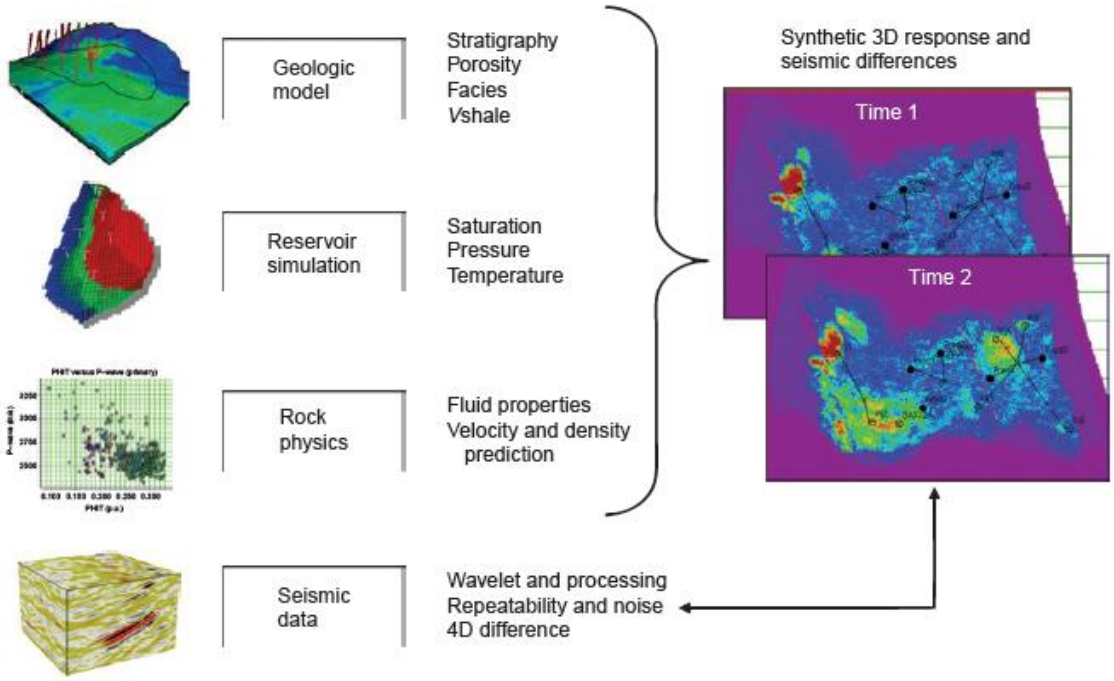

Figure 1.13: Simulation-to-Seismic modelling workflow (Johnston, 2013)

1.6.2 Seismic History Matching

The primary objective of reservoir surveillance is effective management of the reservoir and hydrocarbon production. The characteristics of the reservoir undergo continuous change with hydrocarbon production. Calibration of the reservoir model with historical production observations by tuning the parameters of the reservoir model such that the computer simulations reproduce the dynamic behaviour of the reservoir observations is referred to as *History Matching*.

The reservoir simulation model receives dynamic 4D seismic data first as a qualitative input to reservoir heterogeneity description (structure, net-to-gross, anisotropy, facies classification, faults and barriers) assisted by well logs interpretation. Production history captured by time-lapsed seismic data and input to the simulation model also includes reservoir dynamic properties of fluid flow and pressure propagation. The ultimate integration of 4D seismic in reservoir simulation is by a version of history matching, where the synergy of 4D seismic data, the well production data and the reservoir simulation model at a scale that optimizes the benefits of the different kinds of input data is achieved. This process known as *Seismic History Matching* essentially aims to minimize the discrepancies between the reservoir simulation model and the observed data 4D seismic data, and effectively closes the loop between the two. There are several publications on the integration of 4D seismic data and history matching (Waggoner and Huang; Kretz et al., 2004; Stephen and MacBeth, 2006; Roggero et al., 2008; Kazemi and Stephen, 2011; Le Ravalec et al., 2012; Roggero et al., 2012; Trani et al., 2012; Davolio et al., 2013; Obidegwu et al., 2015, 2017; Trani et al., 2017; Davolio and Schiozer, 2018), with a common challenge being the issues of difference of scale of data and calibration of the reservoir attributes.

In history matching for waterflooding using 4D seismic data, the seismic interpretations of waterflooding effects (e.g. increased pressure and increased water saturation), and the subsequent balance of other reservoir properties to accommodate these effects, are conditioned and used to update the reservoir model. Special attention is paid to the character, direction and magnitude of the waterflooding 4D seismic signal, targeting accurate replication of these with an updated reservoir simulation model.

1.7 Motivations and Objectives of the Thesis

As outlined in this introduction, in waterflooding performance surveillance and evaluation, 4D seismic contributes invaluable benefits of illuminating the inter-well reservoir characteristics, revealing waterflood paths and fluid flow barriers. Johnston (2013) refers to 4D seismic *detectability* and *interpretability* as some of the key issues of applying 4D seismic in reservoir management. We ask the questions: How much of the ongoing dynamic reservoir changes effected by waterflooding are actually detected by

4D seismic data? Are all waterflood reservoir changes detected by the 4D seismic data interpretable? Are the detectable and interpretable changes of the reservoir with waterflooding efficiently captured in the reservoir model?

The benefits of 4D seismic and waterflooding on a large/field scale have been extensively explored and established in the industry qualitatively and are developing quantitatively, but how much information is understood or overlooked from the smaller scale 4D seismic interpretations of waterflooding? In particular, the well-centric 4D seismic signal? How are local reservoir heterogeneities incorporated in reservoir models and do these need to be incorporated into the wider picture of waterflooding surveillance and evaluation?

This thesis aims to thoroughly investigate the benefits of integrated local 4D seismic data analysis to improved model accuracy and reservoir management. This is to be achieved by interpreting and understanding the seismic signal in the immediate well vicinity, applying findings to the waterflood performance surveillance and evaluation. As demonstrated by the published examples, 4D seismic is already utilized at the well level waterflood surveillance particularly in the investigation of lost volumes as a result of fractures and in the identification of waterflooded zones and evaluating vertical sweep efficiencies (Kolstoe et al., 2008; Mikkelsen et al., 2008). The focus in this thesis, however, is on a quantitative application of well-centric 4D seismic interpretation in monitoring and evaluating waterflooding performance.

We explore and quantify the individual effects of waterflooding as detected by 4D seismic data around the injectors and evaluate the value of the expected influence of these effects on interpretation results. Finer scale well-centric reservoir description carrying geological information of heterogeneity and/or connectivity is appraised and included for an improvement to the general reservoir description. The effects of including this level of detail are then applied in a seismic history matching workflow using binary images.

1.8 Outline of thesis

This thesis is divided into different sections charting a well-centric waterflood performance assessment cycle with:

Chapter 2 defines the different natures of the 4D seismic water saturation signal across various scales and configurations of reservoir models. 4D seismic signal is influenced by a combination of reservoir changes as waterflooding occurs. The combination of these changes is dependent on the individual relationships between the different reservoir rock and reservoir fluid properties and the waterflooding conditions. Contributions of these individual waterflooding effects to the saturation region defined by 4D seismic data are analysed within the limits of practical modelling constraints typical in reservoir management.

Chapter 3 establishes the relationship between the 4D seismic increased water saturation signal and real reservoir volumes. Using extracted three-dimensional 4D seismic signal geobodies, the net water volumes as estimated by the geobodies are calibrated to the actual net water volumes in the reservoir. An understanding of water volume calibration across domains is achieved leading to an estimation of the accompanying errors of calibration encountered in equating varied data forms in waterflood performance evaluation.

Chapter 4 quantitatively evaluates well-centric displacement sweep efficiencies for a North Sea turbidite field using formulated 4D seismic performance metrics. These metrics are applied in evaluating waterflood propagation and inferring the directionality of waterflooding induced fractures. The validation of the seismic performance metrics is established with the inter-well connectivity tool, the Capacitance Model (CM) and general horizontal stress orientation analysis.

Chapter 5 introduces closing the history matching loop with the inclusion of well-centric 4D seismic information, highlighting the benefits and challenges for a synthetic field study. The choice of algorithm and methods of seismic objective function formulation using binary images for the seismic objective function formulation are explored.

Chapter 6 applies the method established in the previous chapter to a real field dataset, addressing the field-specific challenges and proffering remedies to possible challenges. Well-centric properties are simultaneously updated by using geostatistical simulation

constrained by well logs and a seismic product to generate net-to-gross realisations for each iteration of the history matching loop.

Chapter 7 summaries the study with conclusions and recommendations for future work.

1.9 Publications from this Thesis

Obiwulu, N., MacBeth, C. and Chassagne, R., 2015, June. *Monitoring of Water Injector Performance Using 4D Seismic Data*. In 77th EAGE Conference and Exhibition 2015.

Chapter 2

Seismic Modelling and Waterflooding

This chapter deals with quantifying the individual waterflooding effects of salinity and temperature as well as the influence of different reservoir model scales on the 4D seismic waterflooding interpretation. The study is based on the Schiehallion field, whose reservoir properties are introduced in detail. The effects of numerical grid scale and reservoir resolution on the 4D seismic interpretation of waterflooding is examined using different progressions of simulation model grid scale. Results show that the magnitude of the effects of scaling on the seismic interpretation is largely dependent on the dataset, with clear trade-offs between interpretation detail and computational cost. The seismic response to salinity and temperature changes typical of the waterflooding scenario in the Schiehallion are simulated, evaluating signal differences as a result of tracking salinity and temperature.

2 Seismic Modelling and Waterflooding

2.1 4D Seismic and the Water Saturation Signal

Introduction of water into an oil reservoir via the water injector well leads to the fluid substitution of oil for water, propagating from the well. In reservoir engineering terms, planned water injection results in sweeping of oil along favourable reservoir flow paths towards the producer to be supported, as well as an increase in the reservoir pressure. Properties of the reservoir (lithology, reservoir pressure, reservoir temperature, etc) and injected water (sea or freshwater salinities, produced water impurities, water temperature) could trigger changes in the reservoir like induced fractures, fines migration, water-weakening, etc. This is in addition to the main effects of waterflooding - increase in water saturation and increase in pore pressure. Considering the geophysics of waterflooding in an oil reservoir, the oil to water fluid substitution results in an increase in the impedance due to the increased density and velocity of formation saturated with water over oil. Simultaneously, this increase is accompanied by a decrease in impedance with increased pore pressure.

In 4D seismic terms, the increase in impedance is referred to as "hardening" and the decrease in impedance, an opposite effect, is referred to as "softening". Separating the two contrasting effects instigated by reservoir operation activities and waterflooding in particular is a long time challenge in the interpretation of 4D seismic waterflooding signal. There are several pieces of literature detailing methods of separating pressure and saturation effects either taking advantage of the seismic P-wave and S-waves different responses to saturation and pressure (Tura and Lumley, 2000; Cole et al., 2002; Davolio et al., 2012) or using seismic amplitude-versus-offset (AVO) analysis (Landrø, 2001).

2.1.1 Waterflooding Coupled Effects of Pressure and Saturation Changes

The seismic response to a waterflood given the seismically contrasting main effects of waterflooding - increased water saturation and increased pore pressure, is dependent on the characteristics of the reservoir. The stress sensitivity of the reservoir would dictate the limits of the reservoir's response to increase in pore pressure contrasted with its response to increased water saturation. Equally, the degree of increase in water saturation would define the intensity of the reservoir's response to increased impedance. The

interplay between the magnitude of injection pressure, the volume of water injected and reservoir rock characteristics, combine to form a complicated seismic response to waterflooding. Examples of these differences can be seen Allan et al. (2011) for instance. In the case of injector WW09 in Figure 2.1, the 4D seismic amplitude map shows no hardening signal reflecting increased water saturation around the injector, but rather, shows a clear softening signal indicating increased pore pressure within a pressure compartment. Around injectors WW08 and CW12, however, there are faint hardening signals indicating increased water saturation. In the Gullfaks field example shown in Helland et al., (2008), Figure 2.2, the growing softening signal (red-yellow colours) around the injector B-33, is a response to water injection and significant pore pressure increase over three years of injection 1996 to 1999. Figure 2.3 conversely, shows a 4D seismic attribute map with predominantly hardening signals depicting distinct flood areas around four injectors in the Bonga field, West Africa (Olatunbosun, 2014).

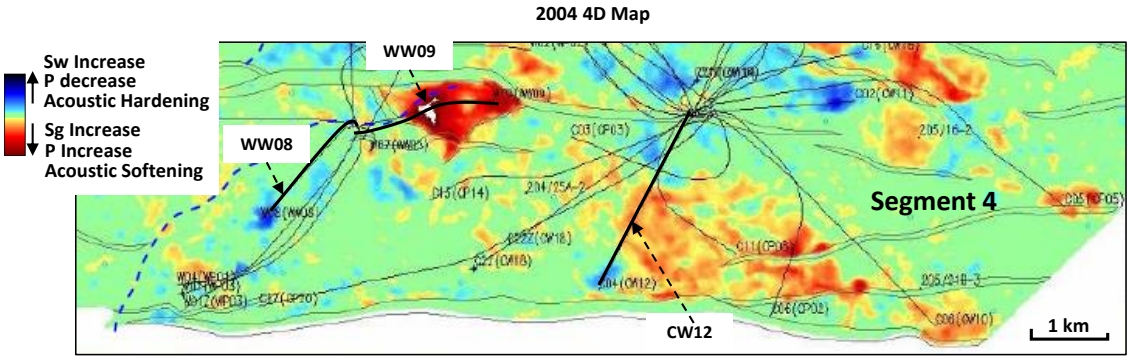

Figure 2.1: Time-lapse attributes showing increase in pressure (softening) around injector WW09. (After Allan et al., 2011)

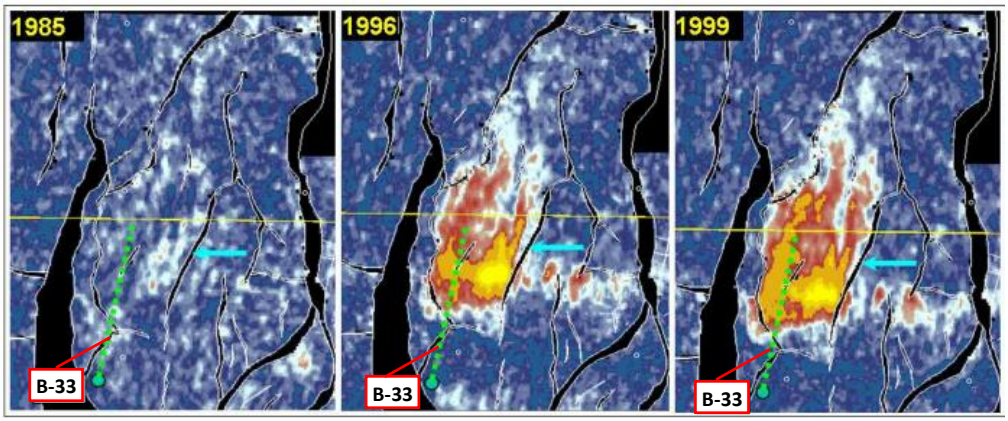

Figure 2.2: Amplitude maps at top Cook reservoir level from four seismic data vintages. The large changes that can be observed are related to varying pore pressure due to water injection in well B-33. (Modified from Helland et al., 2008)

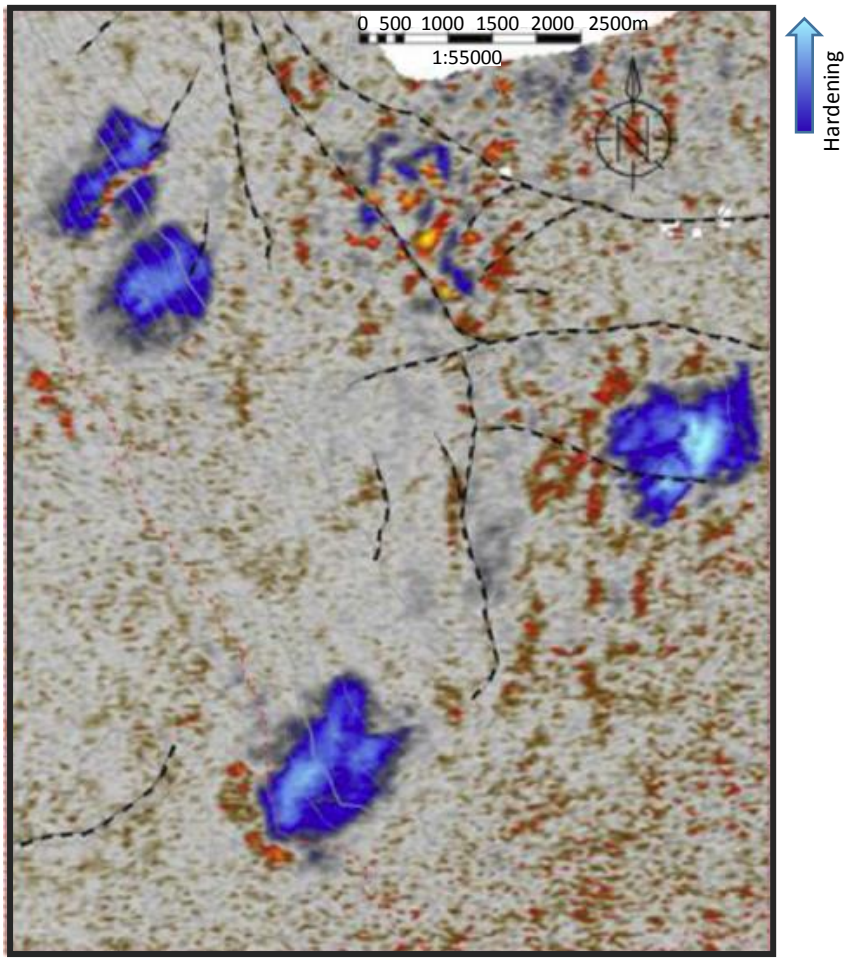

Figure 2.3: 4D seismic attribute map showing distinct increased water saturation hardening signals water around four injectors in Reservoir B of the Bonga Field (Olatunbosun, 2014).

2.2 Analysing the Saturation Signal using Seismic Modelling

The fraction of oil swept from the formation per volume of water injected is indicative of the degree of success of a waterflooding campaign. It is dependent on varying factors from the injector and reservoir pressures to microscale reservoir properties like capillary pressures and fluid viscosities. The preferred methodology for monitoring, prediction and surveillance of waterflood performance is the use of reservoir flow simulation model for optimisation and prediction of reservoir operations for a successful waterflood. However, the significant ability of 4D seismic to image the reservoir inter-well distance makes an inclusion of 4D seismic data interpretation in waterflood surveillance using reservoir simulation–a typically well data-based tool- invaluable.

Integration of 4D seismic data and reservoir simulation is facilitated with simulator-to-seismic modelling *(Sim2Seis)*. Following the *Sim2Seis* workflow shown in Figure 2.4,

synthetic seismograms are generated from the simulation model properties by modelling corresponding elastic properties predicted by the reservoir model, using appropriate wavelets and petroelastic models. Differences between the synthetic seismic data and the observed seismic data are reconciled, ensuring that the reservoir simulation model predicts the reservoir behaviour over the production period to a reasonable degree. The degree of accuracy of the simulation model is evidenced by a high correlation of the effects of the changing dynamic properties to the seismic signal. The generated synthetic seismograms can then be used for history matching and forecasting.

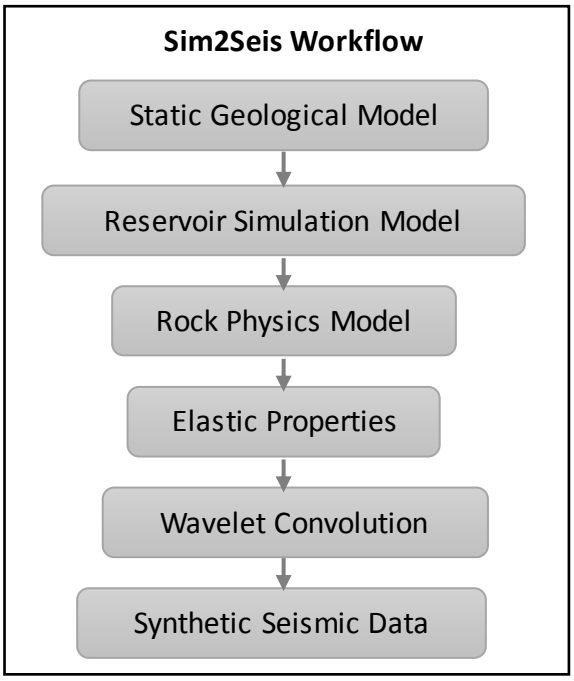

Figure 2.4: Sim2Seis Workflow

Waterflooding performance evaluation via reservoir surveillance and incorporating 4D seismic data is therefore reliant on seismic modelling. However, for a quantitative evaluation, as the reservoir simulation model undergoes different levels of conditioning to arrive at a relatively efficient model, it is important to understand the influence resulting approximations have on the seismic forward modelling results. For a North Sea turbidite reservoir undergoing waterflooding, a study of how these approximations affect the resolved waterflooding signal is carried out. Effects of static property and numerical grid averaging, the choice of petroelastic model and changes in salinity and temperature were investigated. The dataset for this study is the Schiehallion field, with characteristics as described in the next section.

2.3 The Schiehallion Field

The Schiehallion field is located in water depths of 300-500m in the North Sea on the United Kingdom Continental Shelf (UKCS), 200km West of Shetlands. It is a faulted Paleocene turbidite reservoir with channels ranging from 10 – 50m thick at approximately 2000m depth (Leach et al., 1999). Volcanic activity generated by a thermal plume under the Scottish Highlands and West Shetland platform caused a coarse clastic supply to the Faroe-Shetland deep water basin, of which the Schiehallion oilfield is a part. The Schiehallion is made up of 5 main oil-bearing sand sequences, T22, T25, T28, T31 and T34. These sand sequences comprise siliciclastic turbidite sands transported to the basin floor via North-south channels. The sand sequences are offset against mudstone basinal lithologies as a result of the East-West trending normal faults resulting in mud slump baffles and barriers at the edges and ends of main sand channels (Gainski et al., 2010b). Throughout this thesis, the T31 sequence is the study focus. The faults which intersect the north-south trending channels divide the field into four segments, Segments 1, 2, 3, and 4 with reduced hydraulic connectivity at faults between segments (Figure 2.5).

Schiehallion Reservoir Properties	
Porosity	25 – 29 %
Permeability	500 – 1500 mD
Reservoir pressure	2907 psia
Bubble point pressure	2800 psia
Reservoir temperature	57.7 °C
Reservoir salinity	18,000 ppm
Gas-oil-ratio	342 scf/bbl
Oil Gravity	22 – 28 °API
Reservoir viscosity	1.4 – 4.5 cP

Table 2.1: Schiehallion reservoir properties (Richardson et al., 1997; Leach et al., 1999)

The Schiehallion field was discovered in 1993 and commenced production in 1998 with its reservoir pressure of 200 bar close to bubble point pressure. Its properties listed in Table 2.1, include good porosity of 25 – 29% with a relatively low initial reservoir pressure of about 2907 psia at 1940m TVDSS depth. The Schiehallion has a single-phase oil with a gravity of 22 to 28° API (Richardson et al., 1997; Leach et al., 1999) trapped within the Paleocene T31 and T34 sequences (Figure 2.5). The field is developed under

waterflooding with downdip injectors and up-dip producers for oil sweep and effective reservoir pressure maintenance to prevent excessive gas exsolution.

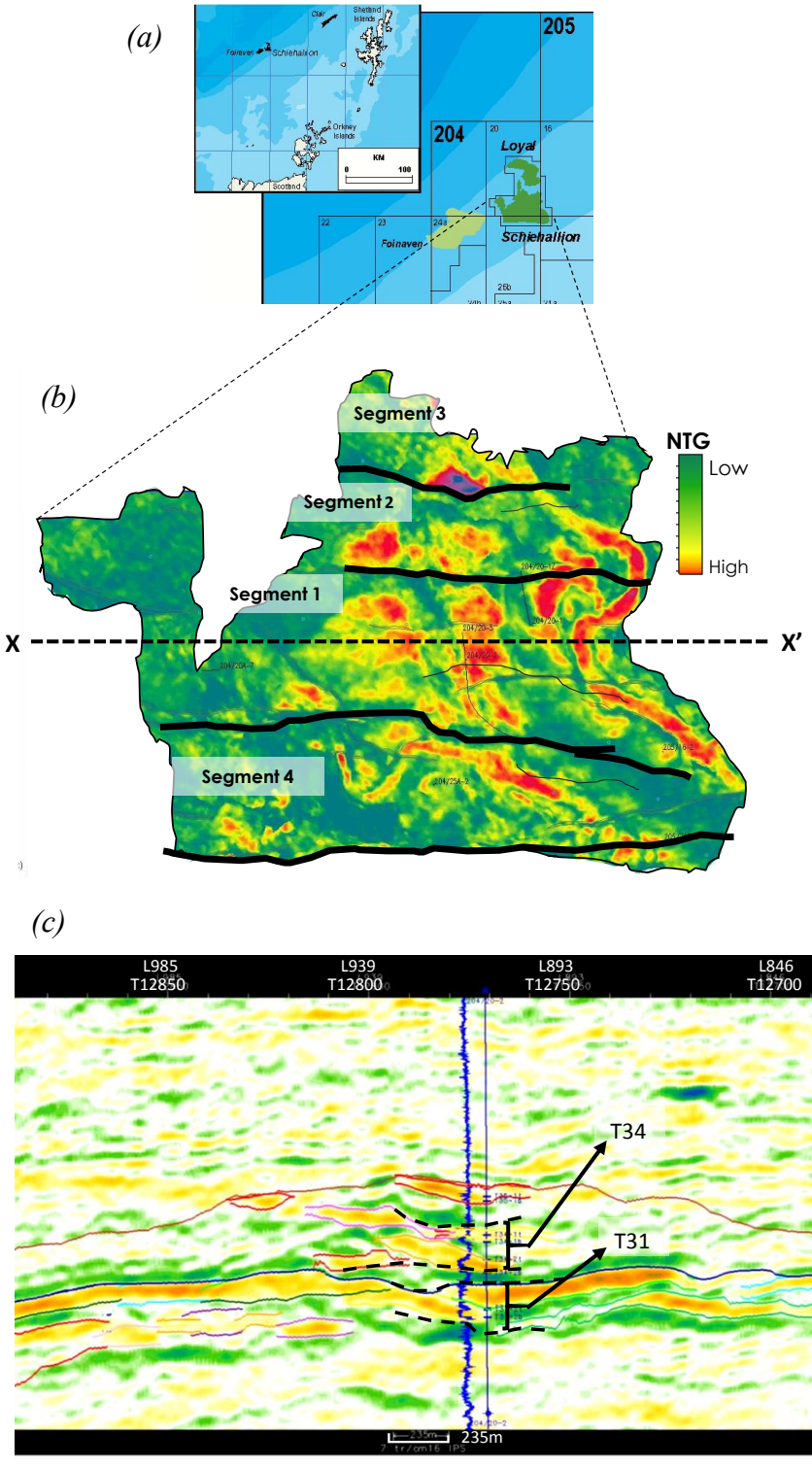

Figure 2.5: (a) Schiehallion field location. (b) Seismic map of depositional environment of Schiehallion with high net-to-gross sands (low impedance) illuminated in warm colours. Segments 1 – 4 demarcated by east-west trending faults (black lines). (c) Seismic section through plane X-X' in b, shows 3D seismic section with outlined T31 and T34 sequences. (After Gainski et al., 2010b; Martin and MacDonald, 2010).

The baseline seismic survey was shot in 1996 with six monitors shot in the ten years of production from 1998 to 2008. On a 3D seismic survey, the lack of cementation, high permeability and high porosity characteristics of the Schiehallion field attributes to the turbidite channel sands having relatively bright amplitudes as seen in Figure 2.5.

2.4 Waterflooding in the Schiehallion

Connectivity in the Schiehallion was identified as a challenge following evaluations of the Extended Well Test (EWT) results. The results indicated that the reservoir was receiving much less pressure support than previously thought, evidenced by the rapidly declining reservoir pressure and following gas exsolution. This led to a revision of the production strategy and the drilling of several infill wells for water injection and improved pressure support (Govan et al., 2006). 4D seismic data was extensively utilised in the understanding of the reservoir connectivity and planning of the infill drilling campaign. Determination of sweep efficiency of the injectors was achieved using chemical and radioactive tracers in the injectors, assessing tracer volume production after water breakthrough as an index of sweep efficiency.

Waterflooding in the Schiehallion field involves the injection of seawater into the reservoir for pressure support and oil sweep. The characteristics of seawater in the North Sea introduce salinity and temperature gradients in the waterflooded reservoir. Given the characteristics of the Schiehallion, other possible effects attributable to waterflooding like water weakening, fines migration, changes in permeability and skin generation are not applicable or are considered rare (Govan et al., 2006) and would not be analysed as part of this study.

2.5 Modelling Effects on 4D Seismic Interpretation

It is typical to combine geological, geophysical, petrophysical and seismic data into a deterministic static model. The model is then optimized for simulation incorporating dynamic properties of the reservoir. This integration of different kinds of data is transmitted in the forward modelling of seismic data.

To study the modelling effects on 4D seismic data interpretation in waterflooding surveillance, synthetic seismic data based on history matched reservoir flow simulation results were generated using *Sim2Seis* (Amini, 2014). For this, petroelastic properties calibrated from well logs for the Schiehallion field (Amini et al., 2011) are applied to the flow simulation model to predict the seismic parameters resultant from reservoir production changes. The seismic parameters which change with reservoir changes like fluid substitution are based on the formation rock's susceptibility to two seismic waves: compressional and shear waves, defined by the equations:

$$V_P = \sqrt{\frac{K + {}^{4}/_{3}\,\mu}{\rho}} \quad and \;\; I_P = \rho V_P \tag{2.1}$$

$$V_S = \sqrt{\frac{\mu}{\rho}} \; and \; I_s = \rho V_s \tag{2.2}$$

where V_P, V_S, I_P, I_S are the P-wave and S-wave velocities and impedances respectively. K, μ and ρ are, the bulk modulus, shear modulus and density respectively. Collectively, equations (2.1) and (2.2) define the basic seismic properties.

With a pre-injection description of the reservoir with respect to its elastic properties available (via the baseline survey), *Sim2Seis* utilizes Gassmann's fluid substitution model (Gassmann, 1951) to predict post-production pore fluid related changes in the reservoir elastic properties. Gassmann's equations are based on the assumptions : 1) the rock properties are homogenous and isotropic, 2) all pore spaces are interconnected, 3) fluid in pore space is frictionless (negligible viscosities), 4) pore pressure changes have equilibrated ensuring homogenous fluid saturations and 5) there is no chemical reaction between the rock and fluid (Batzle and Wang, 1992; Wang, 2000). The model is described with the equations (2.3) and (2.4).

$$K_{sat} = K_{dry} + \frac{\left(1 - {K_{dry}}/{K_m}\right)^2}{\frac{\varphi}{K_{fl}} + \frac{(1-\varphi)}{K_m} - \frac{K_{dry}}{{K_m}^2}} \tag{2.3}$$

$$\mu_{sat} = \mu_{dry} \qquad (2.4)$$

where φ is porosity and K_{dry}, K_{sat}, K_{fl} and K_m are the bulk moduli for the dry rock, saturated rock, fluid and rock mineral respectively.

The reservoir, however, is composed of combinations of rock and fluid, for which the bulk densities are represented using the equations of rock matrix density as $\rho_{matrix} = (\rho_{sand}(1 - \varphi - V_{shale}) + \rho_{shale}V_{shale})/(1\text{-}\varphi)$, for fluid bulk density as: $\rho_{fl} = S_o\rho_o + S_g\rho_g + S_w\rho_w$ and saturated rock bulk density: $\rho_{sat} = \rho_{fl}\varphi + (1 - \varphi)\rho_{matrix}$.

The reservoir fluids property changes to pore pressure and temperature were modelled with the Batzle and Wang (1992) equations, using the harmonic averaging method to calculate the moduli of the combined pore fluids and the Voigt-Reuss-Hill method of mineral mixing to estimate the rock mineral moduli. Thus, with *Sim2Seis*, the bulk density and seismic wave velocities for a reservoir under waterflooding are estimated using saturation and pressure, temperature, salinity, effective porosity and dry frame stress sensitivity of the reservoir.

2.5.1 The Reservoir Simulation Model

The base reservoir simulation model used in this study is a black oil model simulated using the industry software, ECLIPSE 100. The model has 1.6 million cells comprising 266,000 active. Each cell has approximate dimensions of 50m × 50m × 2m. Characteristic to a turbiditic deposition, the Schiehallion geology comprises of graded sandstone beds alternating with shales. Following this, the geological characterisation in the Schiehallion geological model was based on reservoir compartments mapped to interpreted 3D & 4D seismic impedance signals tied to well logs analysis and with confirmed agreement with production data (Martin and MacDonald, 2010). These seismic interpreted reservoir compartments are referred to as geobodies. The geobodies exist in the simulation model as a group of contiguous cells with similar transmissibilities. Figure 2.6 shows a 3D seismic section with interpreted reservoir compartments outlined, with the resultant geobody model representation of the compartments shown in Figure 2.7. The geological model net-to-gross property was subsequently modelled from the combination of

geobodies, well logs and 3D seismic interpretation. Figure 2.8 b, c and d show the sand-shale correlation between the model net-to-gross property and the 3D seismic section via the cross-section A-A'. For the T31 sequence of Segment 1, a selection of reservoir properties of porosity, horizontal permeability, net-to-gross and geobodies are shown in Figure 2.9.

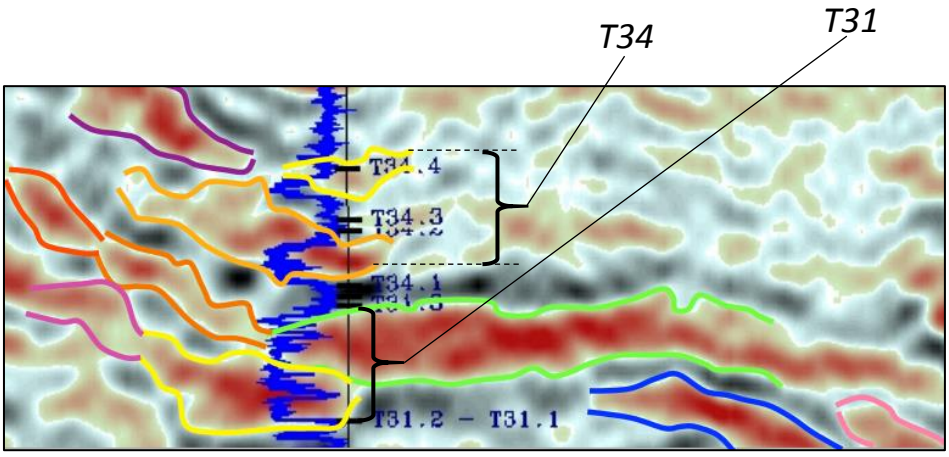

Figure 2.6: 3D coloured inversion zero phase seismic data cross-section showing geobodies mapped to seismic interpreted negative impedances (sand bodies). (Martin and MacDonald, 2010).

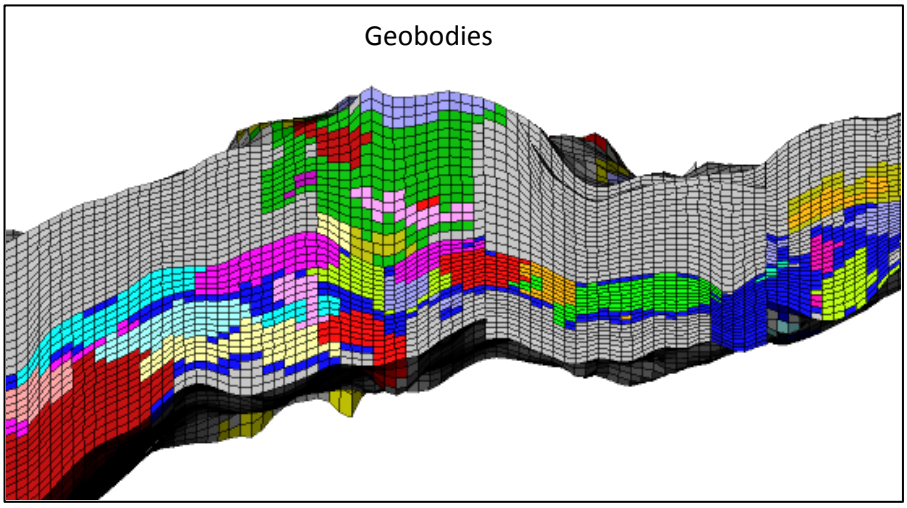

Figure 2.7: Geobody distribution cross-section in simulation model as mapped from seismic interpretation.

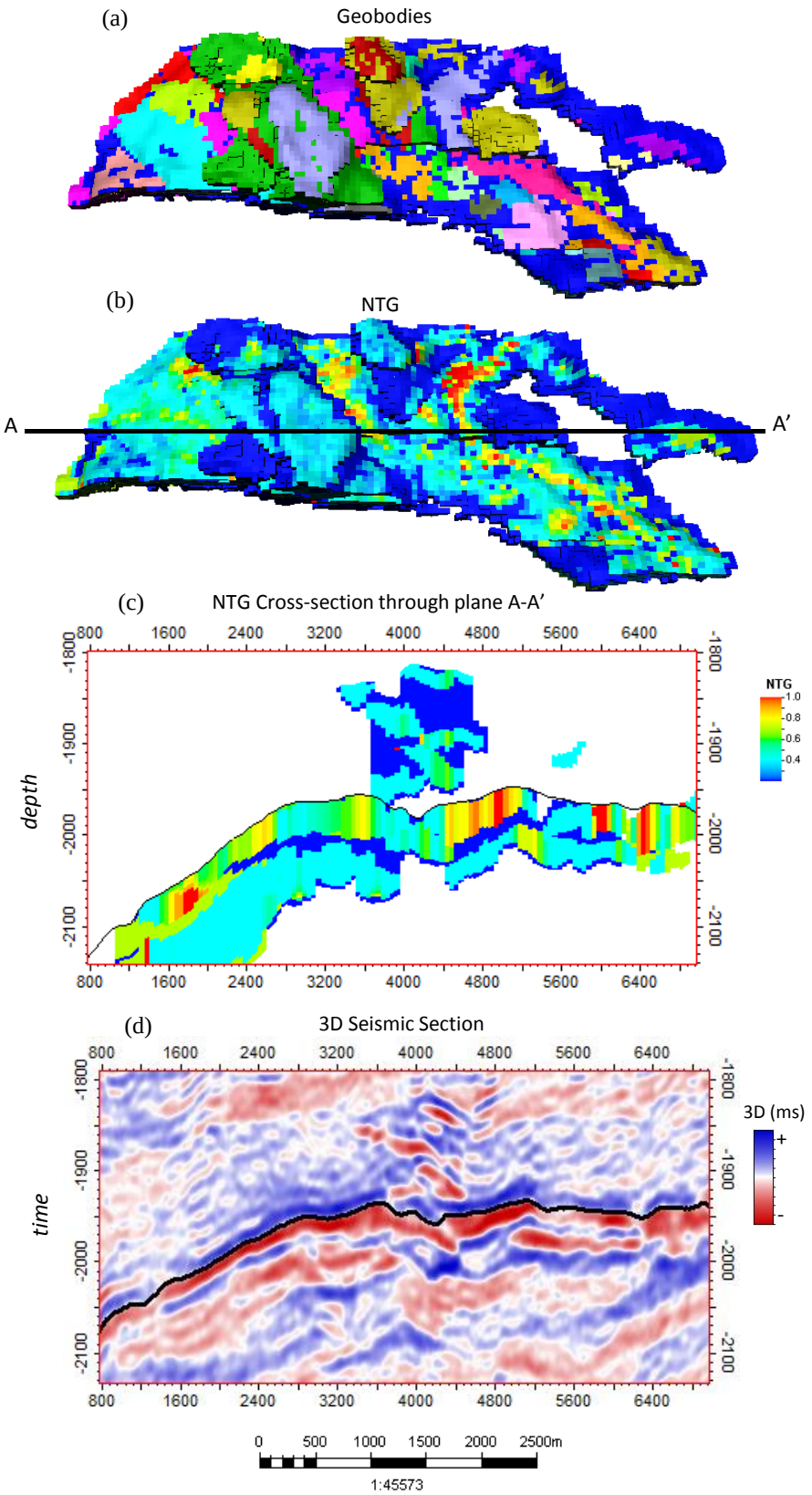

Figure 2.8: (a) Geobody distribution in simulation model as mapped from seismic interpretation, (b) Net-to-gross modelled from geobody with well log constraints and (c) cross-section through plane A-A' of the net-to-gross property showing correlation to the 3D seismic data in (d).

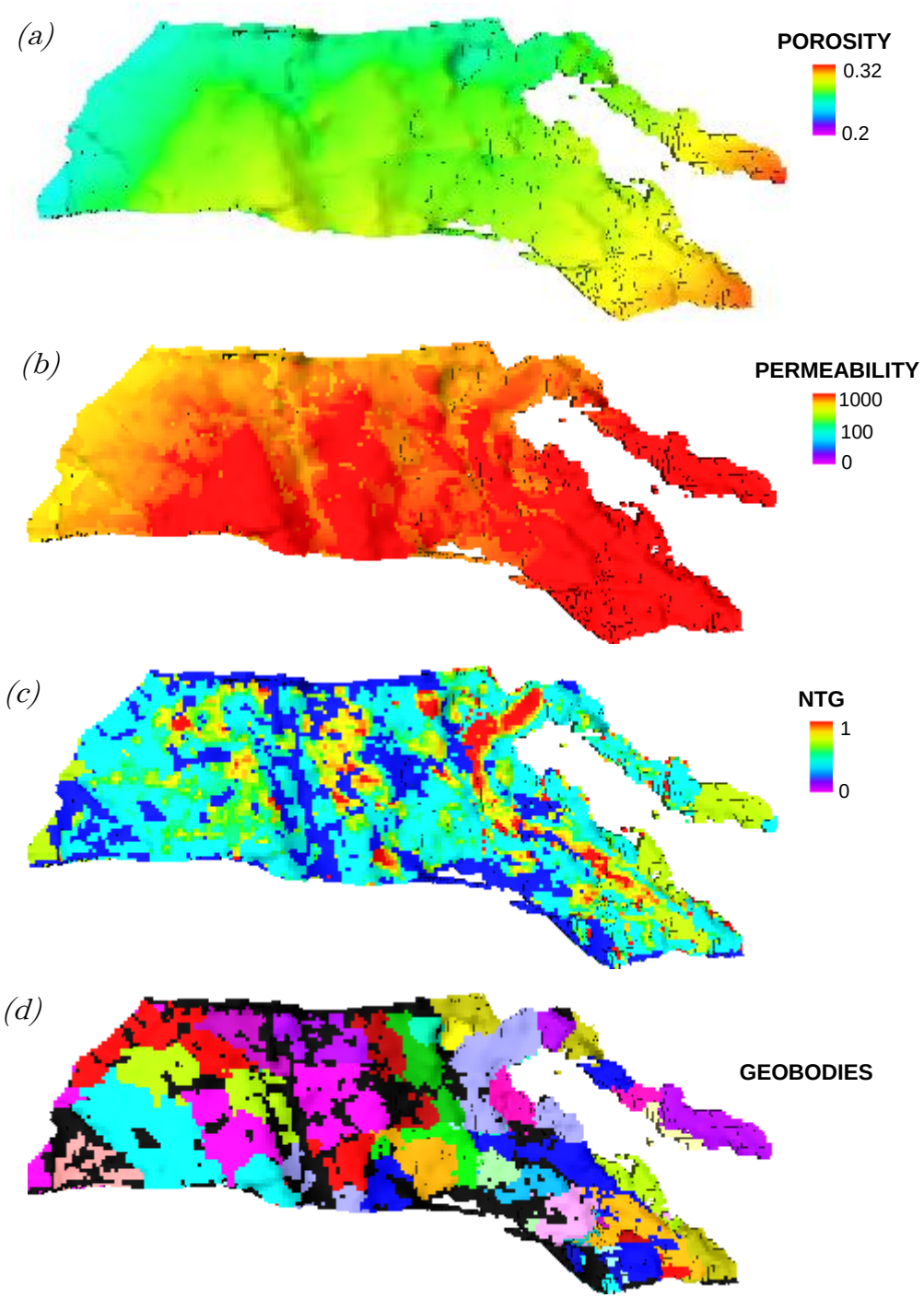

Figure 2.9: Top view of Schiehallion T31 sequence reservoirsimulation model properties – porosity, permeability, net-to-gross and geobodies.

2.5.2 Effect of Scale (Geological and Numerical)

Waterflooding into an oil filled zone is characterized by drainage patterns terminated in saturation fronts. For precise interpretation of graduated flood fronts and effects within the flooded zone, a detailed description of a reservoir's heterogeneity would have to be captured in a very fine scale geological model. Static models are of a finer scale than

simulation models and as simulation models take up to two orders of magnitude more time than creating geological models (Kelkar and Sharifi, 2012), a fine scale simulation model with a large number of grid cells is time consuming to create and computationally expensive. For the fine scale reservoir description to be practically incorporated in the relatively coarser scale numerical simulation model, the geological information is generally upscaled from the fine grid to coarse grid cells using defined upscaling functions. These functions average static properties and derive dynamic curves describing coarse flow characteristics equivalent to the fine scale characteristics. The consequent approximations per grid cell are susceptible to numerical dispersion which in conjunction with reservoir heterogeneity and upscaled rock properties could result in discrepancies in the seismogram generated from an upscaled simulation model. For a truly *quantitative* seismic study, these discrepancies should be understood, and their interpretations accounted.

Numerical Grid Scaling

Upscaling reduces the number of cells by a quadratic degree when coarsened in the lateral direction and linearly when coarsened in the vertical direction. The condition for a successful coarsening process is that the reservoir heterogeneity is generally preserved. To test this, synthetic seismic is modelled across four different numerical scales (simulation model grid size) - three variations of the base simulation model, Table 2.2. There are several specialized upgridding processes (Wen and Gómez-Hernández, 1996; Fincham et al., 2004; Durlofsky, 2005; Wen et al., 2006), however as our interest is mainly on the differences in 4D seismic interpretation for a waterflooding scenario, the upscaling technique was optimised for waterflooding (Shehata et al., 2012). Using the software, Petrel™, the geometry for the simulation model grid was refined or coarsened, and the static properties of porosity and net-to-gross as well as the saturations, were arithmetically averaged and pore-volume weighted. Permeabilities were upscaled with a flow-based algorithm.

Model	Variation/Scale	Grid Characteristics
1) Base-case		Grid: 193× 99 × 84 cells = 1,604,988 cells (266,065 active) Cell Size: 50m × 50m × 2m
2) Coarse	Coarsened grid ÷ ~2	Grid: 128 × 53 × 35 cells = 237,440 cells (68,892 active) Cell Size: 75m × 77m × 8m
3) Laterally Fine	Refined grid laterally × 3	Grid: 579 × 297 × 84 cells = 14,444,892 cells (2,469,453 active) Cell Size: 16m × 16m × 2m
4) Vertically Fine	Refined grid vertically × 3	Grid: 193× 99 × 252 cells = 4,814,964 cells (372,952 active) Cell Size: 50m × 50m × 0.7m

Table 2.2: Model variations detailing grid dimensions.

For a well injecting into the oil leg, the well-centric seismic response to waterflooding for each of the three scale modifications is compared to the previously described simulation model, the 'base-case'. For the *Laterally Fine* and *Vertically Fine* scales, the base-case simulation i-j-k grid is geometrically refined laterally (in the i-direction) and vertically (in the k-direction), respectively by a factor of 3 (within computational limits) to give two new numerical scales.

Conversely, for comparison, the base model is numerically upgridded to a larger grid by a factor of 2, to give the *Coarse* scale scenario. For these four cases of varying degrees of lateral and vertical scale described in Table (2.2), effects of scale variation on the synthetic 4D seismic signal are investigated. For the single well, Figure 2.10, shows the plan views and cross-sections through the plane A-A', illustrating the differences in grid size and the well-centric waterflood character of the flood front across the four scales studied.

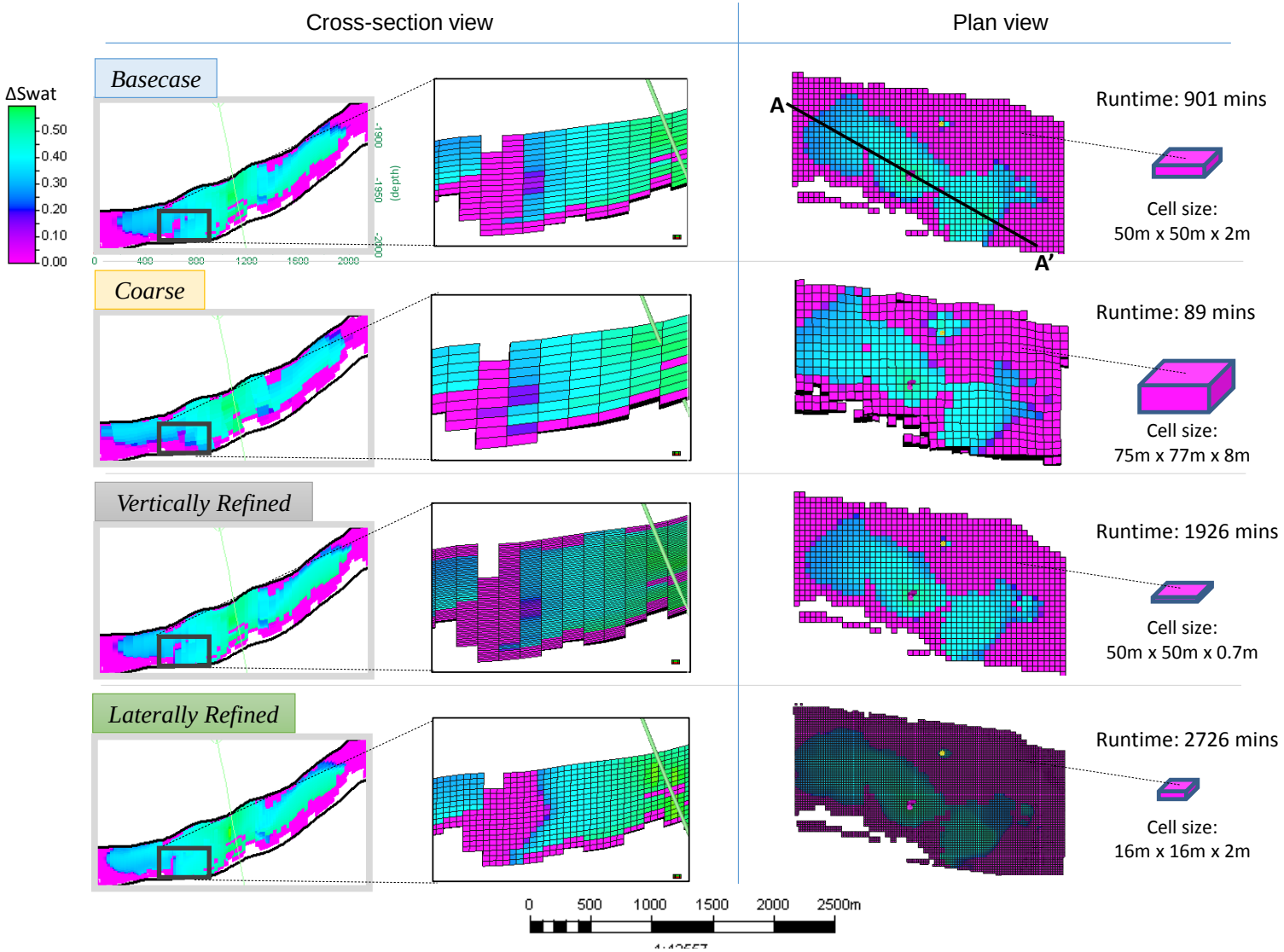

Figure 2.10: Water saturation plan views and cross-section through A-A' for model grid variations for four scale scenarios: (a) Basecase, (b) Coarse scale (c) Vertically and (d) Laterally Fine

The predicted 4D seismic signals (Figure 2.11 a) of the three scale variations show the similar architecture of the hardening anomaly propagating from the water injector. The *Coarse* scale scenario (Figure 2.11, column a, second row) compared to the *Base-case* (Figure 2.11, column a, first row) unsurprisingly lacks fine detail especially in the vertical direction. Although the simulation computation time is a tenth (89 mins) of the base-case runtime (901 mins), as a result of averaging the grid cells and thus averaging of the static properties and saturation distributions, fine detail is obscured as a trade-off. The grid cell size of the *Coarse* scale, 75m × 77m × 8m compared to the cell size of the *Base-case (*50m × 50m × 2m) translates to a larger physical spread of saturation distributions (within larger cells) for each averaged water saturation fraction (comparing Figure 2.11 a, first and second rows). This gives the visual illusion of a more advanced flood front which could be qualitatively misleading in waterflooding performance studies.

Qualitative analysis of the *Vertically Fine* 4D seismic sections (third row) reveals that this scale most accurately replicates the base-case seismic signal as the vertically refined signal detail is unresolved. This is a testament to seismic tuning limitations, where the thickness of the vertically refined model falls below the low seismic resolution threshold. Omitting the refinement in the k-direction, the *Base-case* and *Vertically Fine* scenarios are visually equal. The *Laterally Fine* scale scenario (fourth row) has a finer, more defined flood front as can be seen from Figure 2.10. With respect to flood front advancement, the reduction in the lateral size of grid cells to 16m × 16m increases the resolution of the flood front and gives the illusion of a smaller volume of injected water compared to the *Base-case*. The cross-plots between the *Base-case* and the three scale variations (Figure 2.11 d) show the least correlation with the *Coarse* scale and the most correlation with the *Vertically Fine* scale, with a Correlation Coefficient, R = 0.93.

Quantitatively, the percentage error of magnitude of seismic signal calculated by a difference of the 4D seismic volumes (difference between the 4D seismic volumes of the Base-case and each scale variation) ranged from -36% to+12% for the Coarse case, +22% for the Laterally Fine scale and +9% for the Vertically Fine scale. (Solano et al., 2001) recommends simulation models with grid cells of vertical depth of 0.6m for reasonable accuracy of oil recovery. This aligns with the results Vertically Fine scale, indicating that simulation models with grid cell size of 16m x 16m to accurately resolve the lateral flood

front (as in the Laterally Fine scale) and with grid cell depth of 0.7m (as in the Vertically Fine scale) would have higher seismic response prediction accuracy. This confirms that the finer the scale of the model, the higher the achieved interpretation accuracy, but a trade-off between a simulation model with a reasonable computational time and a model with dimensions fine enough to accurately represent smaller interpretations is necessary.

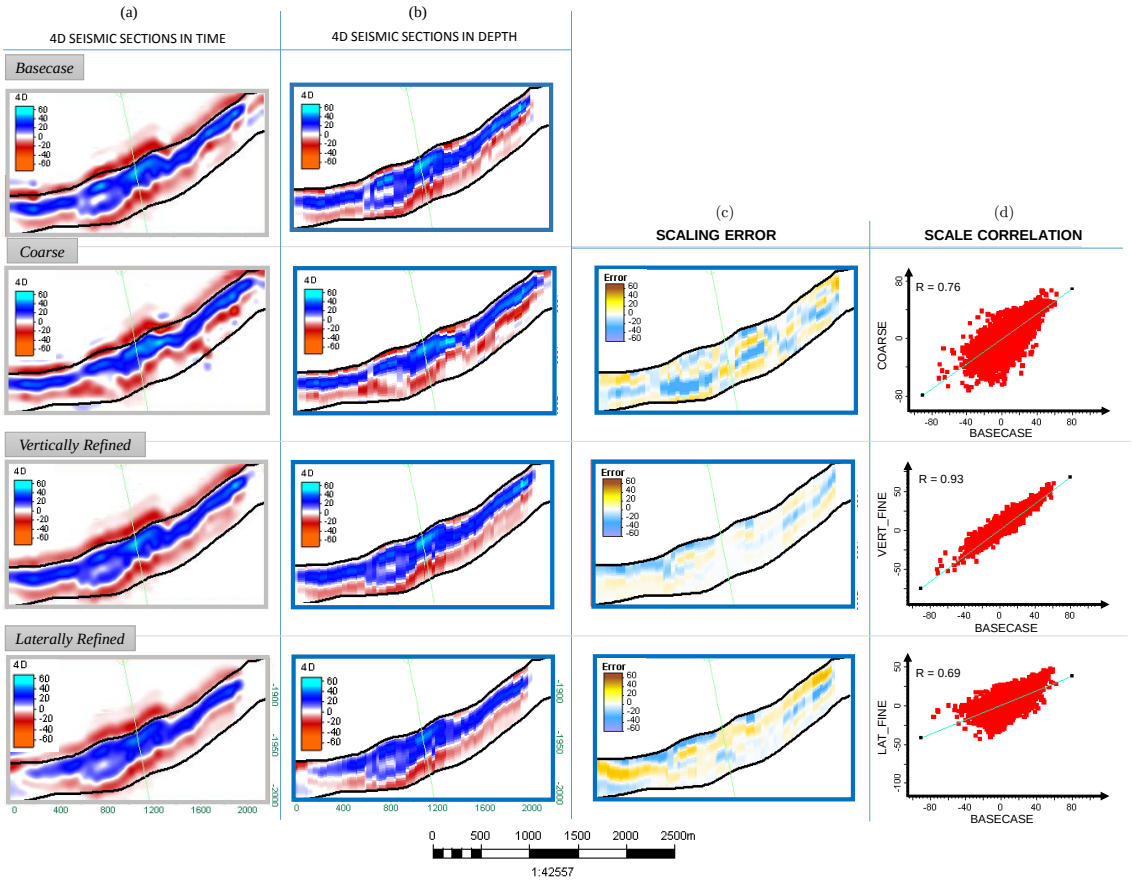

Figure 2.11: Predicted 4D seismic sections in (a) time and (b) depth for different scale scenarios. Comparing each scale scenario to the Basecase, (c) is defined as the difference between each (e.g. Basecase – Coarse) and (d) shows the correlation between the Basecase scale and the Coarse, Vertically Fine and Laterally Fine scales.

Geological Upscaling

To examine the dilution of small-scale reservoir heterogeneity with geological model upscaling, two synthetic models modelled after the Schiehallion reservoir but of different stratigraphic resolution were generated. The models were compared to qualitatively and quantitatively assess the decrease in represented global heterogeneity and the magnitude of lost information in 4D seismic interpretation with the upscaling of geological information. Given the characteristics of the reservoir under study (Gainski et al., 2010a; Martin and MacDonald, 2010):

- Palaeocene turbidite with 10 – 50m thick sands
- Channels deposited in approximately the north-east direction
- Well logs depict interbedded nature of reservoir via sand-shale distribution
- 3D seismic illuminates the low impedance sand channels

A fine grid heterogeneous simulation model with grid matrix dimension: 193 × 99 × 84 and cell size 50m × 50m × 2m was generated as the Static Base-case. Well logs and available geological information were the input to create the static properties with Sequential Gaussian simulation. The net-to-gross property was generated using the shale volume (Vshale) log within the bounds of 0.2 - 1 (20% sand to 100% sand) and the porosity was calculated as a function of net-to-gross and set with a small lateral variation as documented in the Schiehallion field description. Permeability in the x and y directions were generated using a porosity-permeability relationship from the original Schiehallion model.

Optimal coarsening is a trade-off between loss in resolution and decrease in computation time which is case-dependent. Given this, an analysis of upscaling the properties to a grid cell size by 1.5 in the x and y-direction and by 4 in the z-direction to $75m \times 75m \times 8m$ is carried out. The *Static Base-case* (the 'fine grid') static properties (NTG and porosity) were upscaled to a $128 \times 53 \times 35$ grid matrix, using the volume weighted arithmetic mean. Cross-sections of variations in reservoir properties are shown, through the same plane, A-A' as in the previous section, for the Base-case and Upscaled scenarios in Figure 2.12.

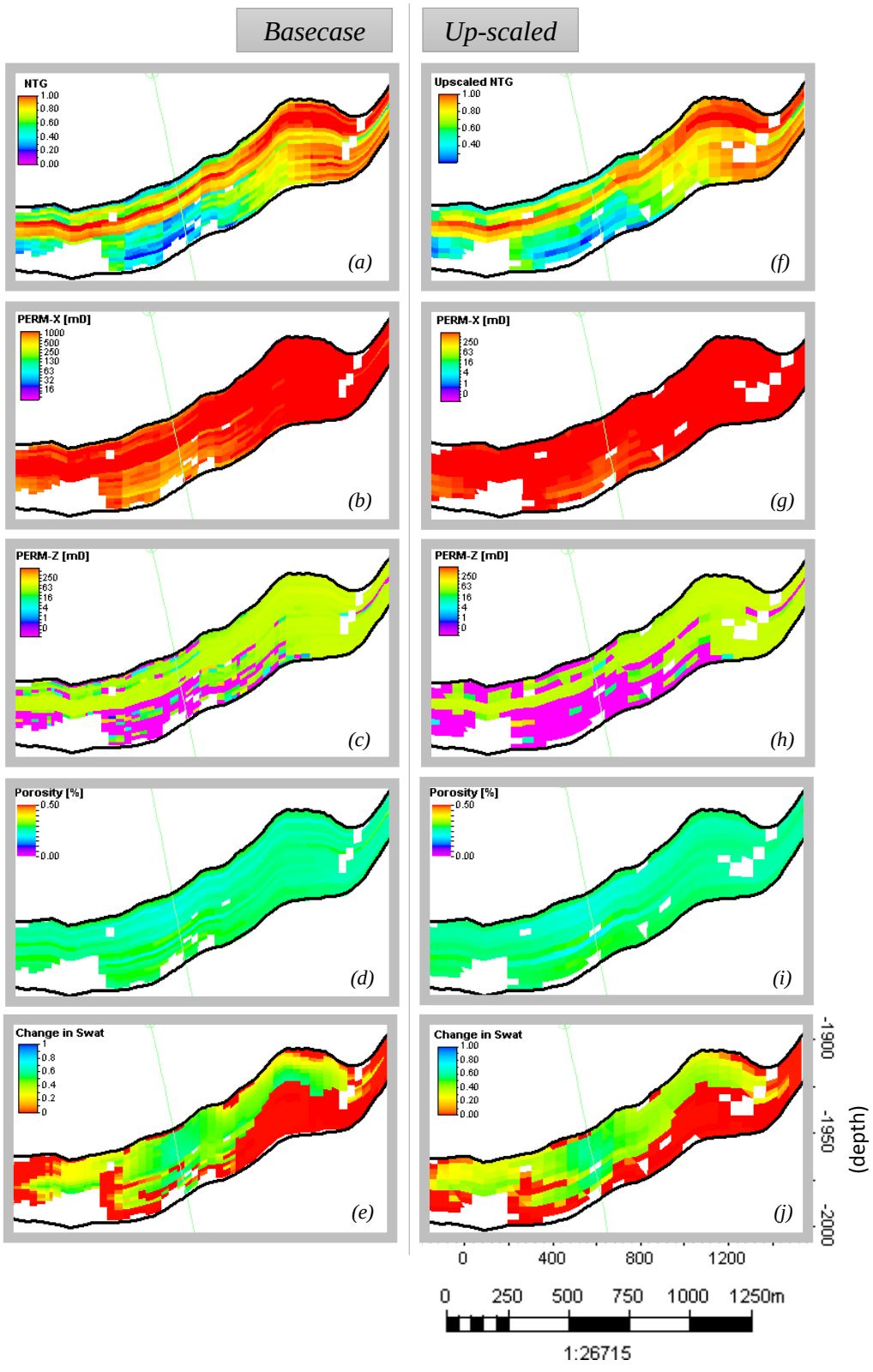

Figure 2.12: Basecae and upscaled properties of NTG, Permeability X and Y, porosity and dynamic saturation change. Basecase: (a) - (e), Upscaled (f) – (j).

Resampling the upscaled simulation model properties to the same basecase grid for comparison, Figure 2.13 shows that the predicted 4D seismic signals for both models

show a good correlation of the magnitude of amplitudes of the base-case scale and its upscaled equivalent (correlation coefficient of 0.87). Qualitatively, the vertical seismic resolution for the *Base-case* scale with grid cell thickness ≈ 2m compared to the *Up-scaled* case with cell thickness ≈ 8m is not vastly different with regards to signal architecture, as the thin bed structure again falls below resolution limits. For a thin reservoir with sand- shale interbedded layers less than tuning thickness of 32m, sand containing injected volumes cannot be accurately resolved by seismic and is thus underestimated.

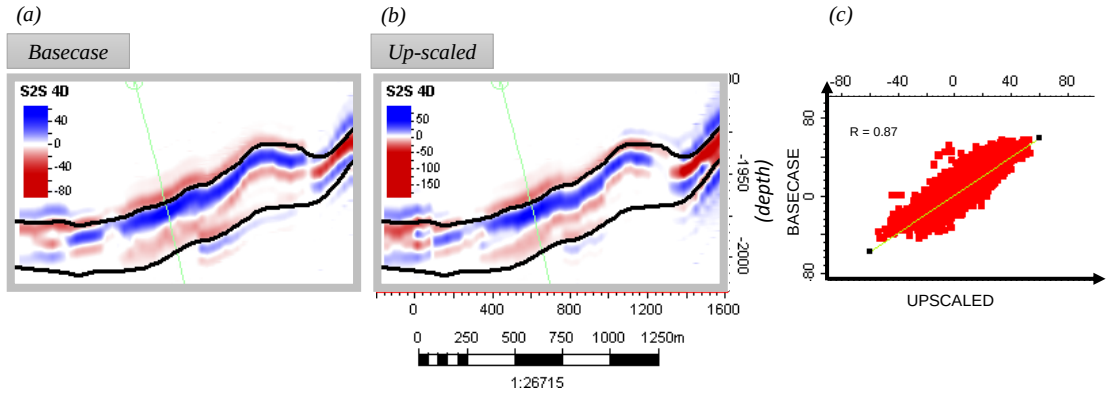

Figure 2.13: Well-centric 4D seismic sections of Finescale and Upscaled models (a and b). (c): Correlation between both scales

2.5.3 The Petroelastic Model and the Seismic Match

The Petroelastic model (PEM) determines the dynamic elastic properties in response to the pressure and saturation changes as a result of reservoir production. In using seismic forward modelling as part of our reservoir surveillance and monitoring system, good accuracy of synthetic and observed seismic signal match is essential. Generation of synthetic seismic using *Sim2Seis* from the simulation model yields a relatively good replication of the observed as seen in Figure 2.14, with the seismic polarities, main sand bed structures and orientation preserved. However, with known variable influence of an assumed well-calibrated PEM (Briceno, 2017), it is important to understand the degree to which the uncertainties and variations in the PEM could affect the final 4D seismic interpretation. This is even moreso in the case of a waterflooding study given the increase

in pore pressures with injection. The PEM describes the reservoir rock stress sensitivity which governs the reservoir's response to the increased injection pressures.

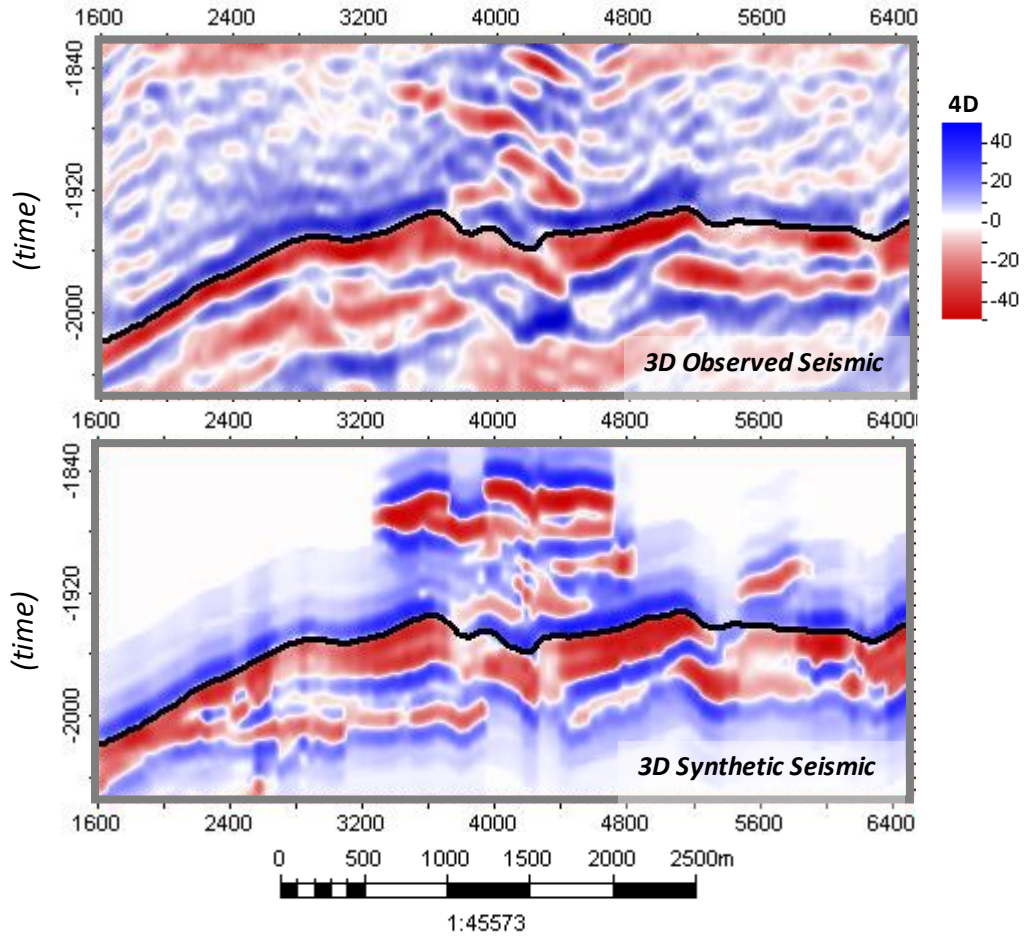

Figure 2.14: Petroelastic model analysis - Comparison of observed (left) and synthetic (right) 3D seismic sections.

Rock stress sensitivity

The challenge of accurately describing the in-situ rock stress sensitivity of the formation with production of hydrocarbon fluids is well-established. This concerns the discrepancy between the rock stress sensitivity estimates from confining pressures recorded from cores samples in the laboratory, as opposed to the in-situ reservoir field-scale conditions (Furre et al., 2009, Alvarez and MacBeth 2014). The MacBeth (2004) equations based on reservoir and outcrop core samples for sandstones from a variety of depositional environments and geographical locations, describe the rock sensitivity relationship for sandstones. They define the bulk modulus, k_{dry}, and shear modulus, μ_{dry}, for the dry rock as:

$$k_{dry} = \frac{k_{\infty}}{1 + E_k e^{\left(\frac{-P_{eff}}{P_k}\right)}} \tag{2.5}$$

$$\mu_{dry} = \frac{\mu_{\infty}}{1 + E_{\mu} e^{\left(\frac{-P_{eff}}{P_{\mu}}\right)}} \tag{2.6}$$

with E_k and E_{μ} as constants calibrated from dry cores isotropic loading which determines the rock's sensitivity to changes in effective stress in the producing reservoir, P_{eff} . P_{μ} and P_k determine the degree of curvature of the curve, while μ_{∞} and k_{∞} are the maximum moduli when the rock loses its sensitivity and thus is the point of the curve's asymptote, all described by the curve of the trend seen in Figure 2.15. Effective stress, P_{eff} is defined as the difference between overburden stress, σ_{ob}, related to the weight of the rock above the reservoir (typically 1psi/ft,) and the reservoir pore pressure, P_{pore}:

$$P_{eff} = \sigma_{ob} - nP_{pore} \tag{2.7}$$

where, n is the effective stress coefficient.

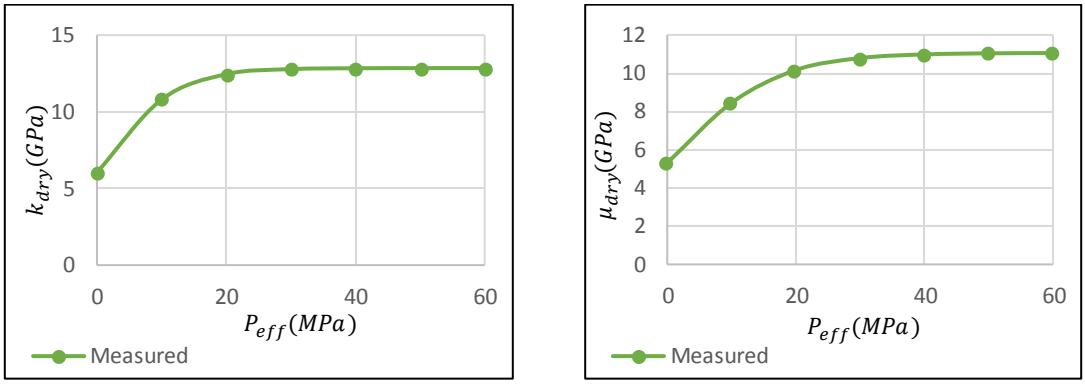

Figure 2.15: MacBeth stress sensitivity curves for dry bulk and shear moduli.

Increase in pressure from waterflooding would trigger rock stress variations in the formation influenced by the pressure increase. Using the MacBeth (2004) stress sensitivity constants for a West Shetland sandstone, the in-situ sensitivity of the rock stress sensitivity to reservoir production for the Schiehallion field can be investigated. This would allow for an understanding of possible uncertainties in the rock stress sensitivity equations or a calibration of the rock stress sensitivity given the well-centric reservoir heterogeneity. Following Amini and MacBeth (2015), a comparative qualitative analysis of the synthetic and observed seismic signals is done by perturbing the stress sensitivity curves around its calibrated values, providing a range of possibilities of reservoir sensitivity to the injected pressure as shown in Figure 2.16. Honouring the

laboratory measurements describing stress sensitivity pre-production at 20MPa, the bulk and shear moduli for production pressures are derived using the modifications to the equations in (2.8) and (2.9) and the parameters listed in Table 2.2.

Table 2.2: Stress sensitivity Parameters for measured, P1 and P2 curves

:

	Measured	P1	P2
Ek	1.1277	0.7	1.8
Pk	5.62	5.02	6.24
Eμ	1.0833	0.68	1.4
Pμ	7.97	6.8	8.5

$$k(P) = k_{calib}(P)\left(\frac{1 + E_k e^{-P_r/P_k}}{1 + E_k e^{-P_{eff}/P_k}}\right) \qquad (2.8)$$

$$\mu(P) = \mu_{calib}(P)\left(\frac{1 + E_\mu e^{-P_r/P_\mu}}{1 + E_\mu e^{-P_{eff}/P_\mu}}\right) \qquad (2.9)$$

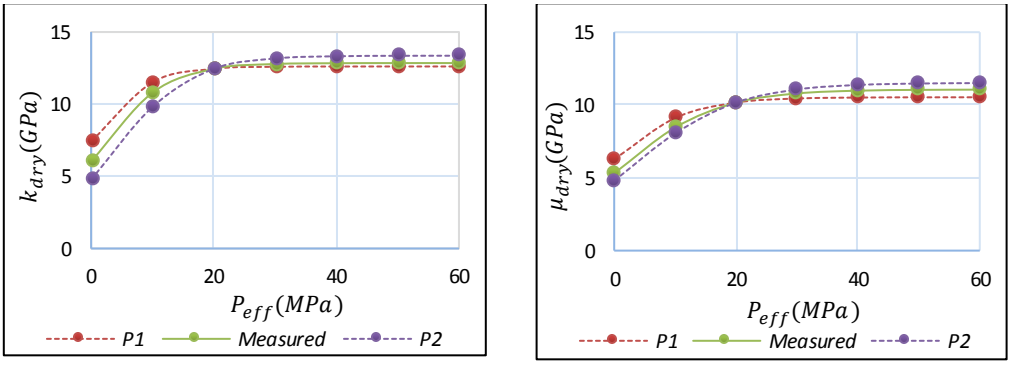

Figure 2.16: Perturbations of the MacBeth stress sensitivity equations: P1 and P2 curves

For the range of stress-sensitivity curves between perturbations, *P1* and *P2, shown in Figure 2.16*, the 3D and 4D synthetic seismic signals were generated to test for improvement of match quality to the observed seismic. These variations did not result in favourable results as evidenced by the corresponding example sections *(P1)* and *(P2)* in Figure 2.17. This improves the confidence in the calibration of the stress sensitivity curves

applied in the seismic forward modelling using the original MacBeth measurements, with which the top right section in Figure 2.17 is generated.

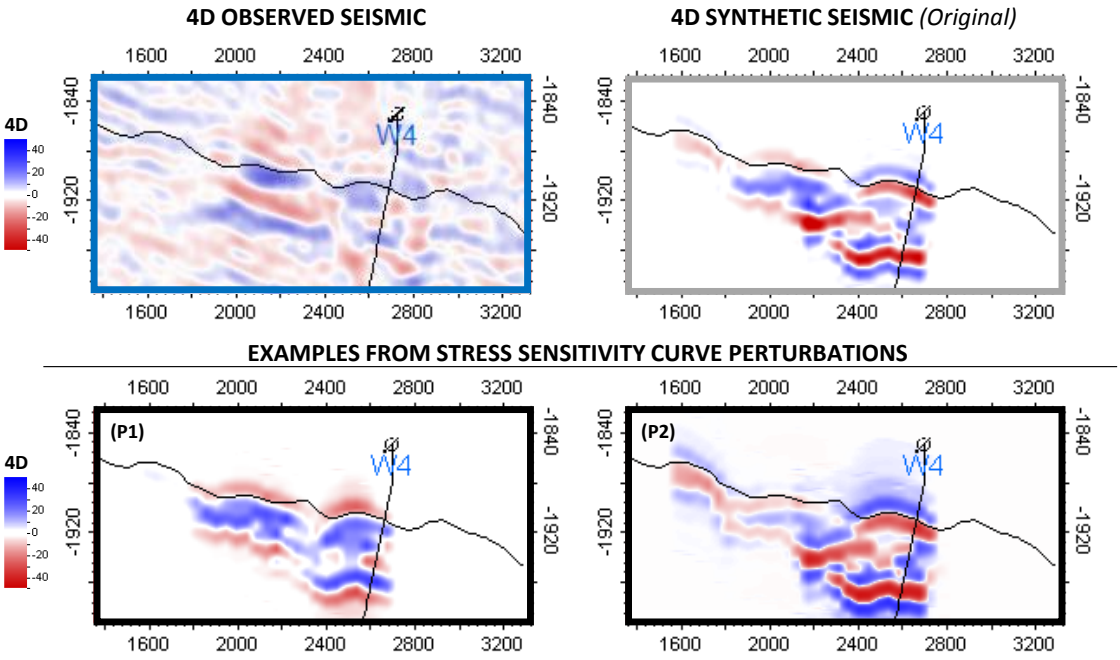

Figure 2.17: Petroelastic model analysis - Perturbation of the stress-sensitivity curves aiming at an improvement of the observed and synthetic seismic match. Top row: 4D observed (left) and synthetic seismic section (right). Bottom row: examples of results of variations with stress-sensitivity curves, P1 and P2.

2.6 Individual Effects of Salinity and Temperature Changes on the Waterflood Seismic Signal

With increased importance of low salinity waterflooding following its recorded improvement of oil recovery, effects of salinity on recovery factor have been investigated thoroughly at the core scale and explored extensively using reservoir simulation. Smith (1942) showed recovery of crude oil in sandstones resulted in a lower recovery factor for fresh water compared to brine and attributed the results to clay swelling. Studies by Jadhunandan and Morrow (1995) and Yildiz et al. (1999) showed how the differences in ion concentration in the brine and crude oil could cause spontaneous imbibition during waterflooding, thus affecting the recovery factor. The effect of brine on the recovering factor of crude oil during waterflooding is a confirmed complex process dependent on the brine, rock, oil relationship - how it affects the wettability of the rock, volume of connate water and clay content present.

Salinity is known to increase the density and viscosity of brine, with a velocity inversion as temperature increases (Batzle and Wang, 1992). Increase in temperature, irrespective of salinity or pressure, results in a decrease in density and bulk modulus. For Sodium Chloride solutions, the relationship between brine densities and increasing temperature estimated using empirical equations are shown in Figure (2.18).

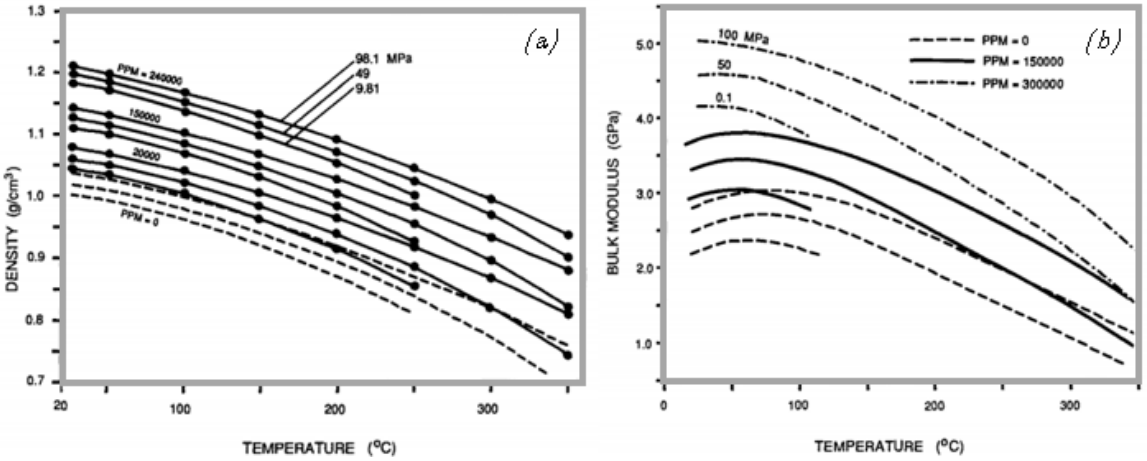

Figure 2.18: (a) Brine density and (b) Bulk modulus, both as functions of pressure, temperature and salinity for sodium chloride concentration in parts per million (Batzle and Wang, 1992).

Borges and Landrø, (2017) with results shown in Figure 2.19, demonstrated the impact of accounting for salinity in injection scenarios. Using a simple reservoir model to obtain time series of pressure, salinity and saturation, they simulated a well injecting sea water in a homogeneous isotropic reservoir with formation brine concentration of 100,000 ppm injecting in the water leg. Synthetic reflectivity was modelled and inverted for simulated reservoir changes. To determine noise sensitivity, noise was added to the synthetic data and inverted again. They determined that direct estimations of salinity are very sensitive to seismic noise but including sensitivity to salinity contributes to better estimation of the dynamic reservoir properties.

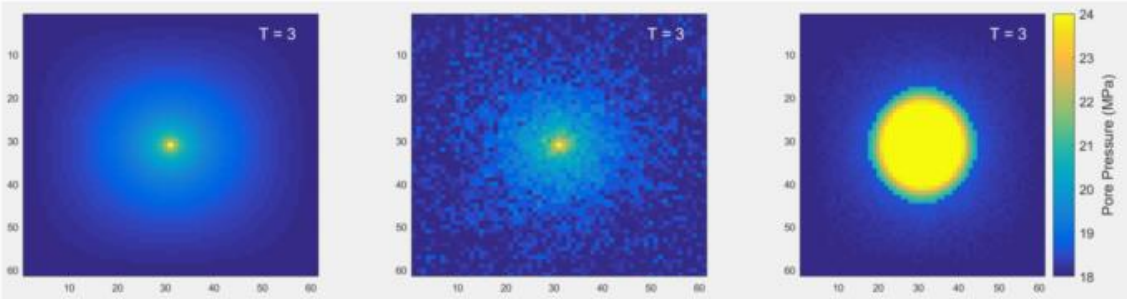

Figure 2.19: Left: Map view of modelled pore pressure in a given time frame. Centre: Inverted pore pressure, considering the salinity of the injected water. Right: Inverted pore pressure, neglecting the contribution (Borges and Landrø, 2017).

In Figure 2.19, inverted results without incorporation of salinity effects (right) for a modelled source of pressure (left) is shown to over-estimate the pore-pressure magnitude and diffusion radius, compared to the more accurate inverted results with salinity effects incorporated (middle).

Sensitivity of Salinity and Temperature changes

To understand the range of salinity and temperature changes as a result of waterflooding (in the case of the oil-water fluid substitution which is the focus), the study of these changes is specific to formation properties of the well centric area of the water injectors. The injectors completed in the oil leg in the Schiehallion field are mostly completed in sand beds with average net-to-gross ratios with higher mud content from ~0.6 to cleaner sands with net-to-gross ratios of ~0.8. The sensitivities to salinity and temperature changes for: i) the containing saturation alone (excluding pressure effects), ii) for the pressure effects alone and iii) the total acoustic impedance of saturated sands, for flooded beds with sand-shale ratios of 0.63 and 0.82 are analysed. For these sand-shale ratios, two fractions of water saturated states – 0.2 and 0.8, and two observed pressure scenarios of well injecting (pressure increase of 12MPa) and well shut-in with proximal producing well (pressure decrease of 4.5MPa) were analysed. All combinations of the salinity and temperature ranges listed in Table 2.3 were investigated to estimate the possibilities of impedance change due to salinity and temperature. The normalised percentage change for all the conditions are shown in Figure 2.21 for water saturation fractions of 0.2 and 0.8.

NTG	Salinity	Temperature	Water Saturation	ΔPressure
0.63	5,000 ppm	10°C	0.2 & 0.8	4.5MPa Decrease & 12MPa Increase
	18,000 ppm	15°C		
	30,000 ppm	30°C		
	120,000 ppm	60°C		
0.82	5,000 ppm	10°C	0.2 & 0.8	4.5MPa Decrease & 12MPa Increase
	18,000 ppm	15°C		
	30,000 ppm	30°C		
	120,000 ppm	60°C		

Table 2.3: Sensitivity Scenarios

For increased temperature, brine velocity increases while density decreases. On the other hand, with increasing temperature, velocity and density of oil both decrease (Batzle and

Wang, 1992; Johnston, 2013). Considering a two-phase oil-water reservoir for the scenarios listed for injection of cold, higher salinity water into a hot oil reservoir, and in agreement with the analysis by (Salako, 2015), the trends in Figure 2.21 show that for 12MPa increase in pressure and 4.5MPa decrease in pressure, salinity and temperature changes collectively do not affect the total impedance by more than 2% in the approximate life cycle of a waterflooded reservoir: from partially waterflooded at Sw = 0.2, until approximate economic limit at Sw = 0.8.

This sensitivity analysis estimates percentage total impedance changes for a broad range of possible salinities and temperatures. Specific to the Schiehallion however, and in the case of seismic amplitude interpretation, the real salinity and temperature scenario describing the waterflooding operation of injecting seawater of salinity of 30,000ppm and temperature of 15°C into the reservoir with formation water salinity of 18,000 ppm and temperature of 57°C is modelled using *Sim2Seis* in the next section.

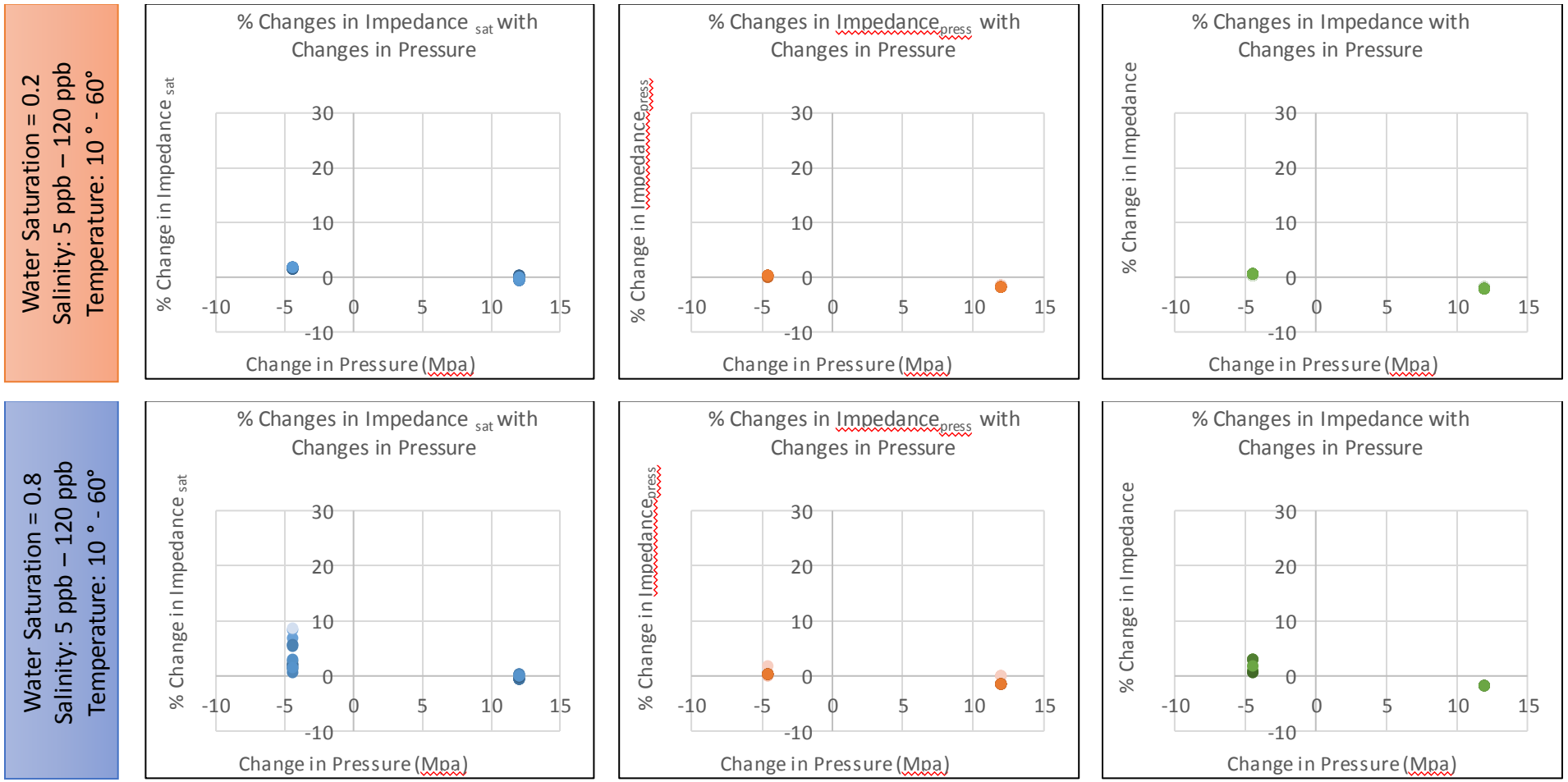

Figure 2.20: Charts of normalised percentage changes for varying NTG, percentage saturation, salinities and temperature. Top row: % changes in impedance due to saturation only, % changes in impedance due to pressure alone and % changes in total impedance for 20% water saturation and Bottom row: Same as top row, but for 80% water saturation.

2.6.1 Synthetic Seismic Results with Salinity and Temperature Tracking

To track the effects of salinity and temperature changes in the 4D seismic signal using seismic forward modelling, the salinity and temperature changes with waterflooding are first tracked in the simulation model. The salinity and temperature changes are then captured as grid cell properties, for which the seismic impedance are calculated.

Salinity Tracking in the Reservoir Simulation Model

Jerauld et al., (2008) demonstrated a practical method for modelling salinity tracking in reservoir flow simulators. By changing the shape of the relative permeability curves to imitate wettability changes corresponding to the different salinities, the industry simulator Eclipse 100 was used to model the effects of brine in injected water using the *Brine Tracking* feature.

The calculations for salinity tracking, interpolating between high and low-salinity relative permeability curves (Figure 2.21) is modelled after Jerauld et al. (2008) and illustrated in Figure 2.22.

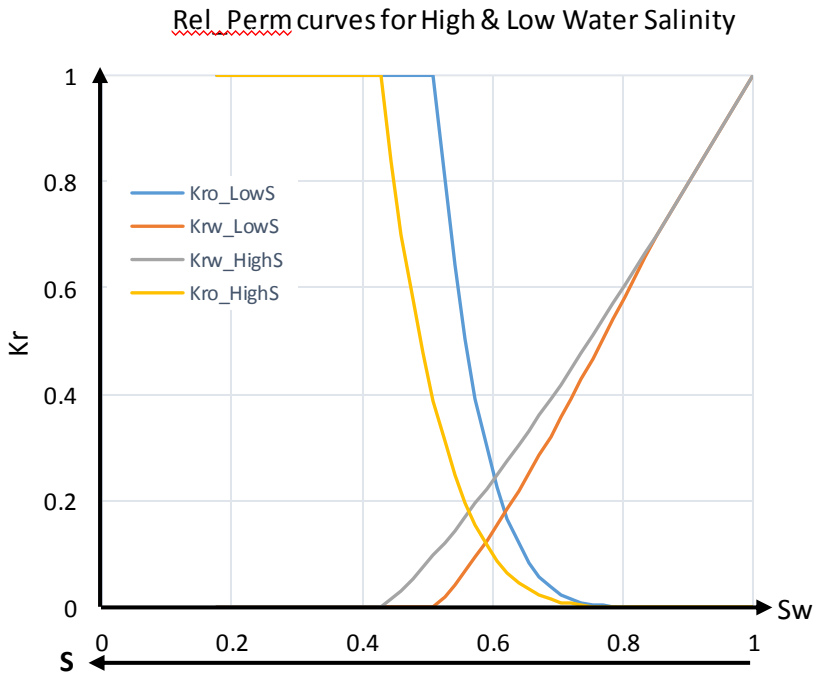

Figure 2.21: Relative permeability curves for high and low water salinities. LowS: Low salinity, HighS: High salinity

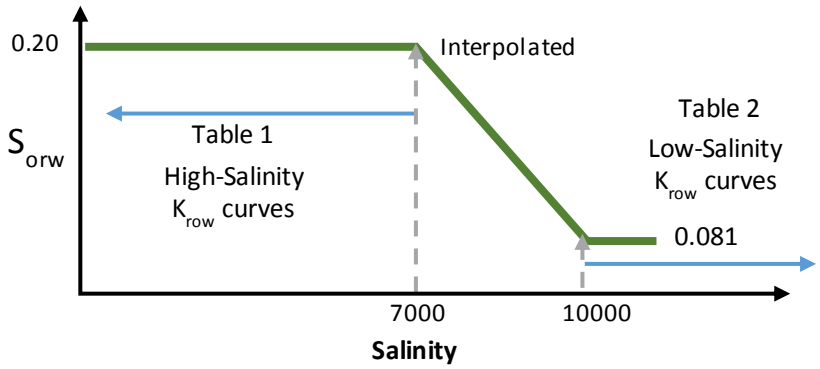

Figure 2.22: Schematic of salinity dependence of residual oil saturation (Jerauld, 2008)

.
$$k_{rw} = \theta k_{rw}^{HS}(S^*) + (1-\theta)k_{rw}^{LS}(S^*) \quad (2.10)$$

$$k_{row} = \theta k_{row}^{HS}(S^*) + (1-\theta)k_{row}^{LS}(S^*) \quad (2.11)$$

with,
$$\theta = (S_{orw} - S_{orw}^{LS})/(S_{orw}^{HS} - S_{orw}^{LS}) \quad (2.12)$$

$$S^* = (S_o - S_{orw})/(1 - S_{wr} - S_{orw}) \quad (2.13)$$

where, *LS* and *HS* denote low salinity and high salinity, and θ is a dimensionless measure if *LS:HS*, S_{orw} is residual oil to waterflood, S_{wr} is irreducible water saturation, S_o is oil saturation, k_{row} is oil relative permeability and k_{rw} is water relative permeability

Considering the water injection scenarios in the North-sea and the salinity contrasts obtainable (for salinities of 18,000 ppm formation water and 30,000 ppm injected water), salinity and temperature differences between the Schiehallion formation water and injected sea water were modelled tracking the changes in salinity by the resulting differences in density and viscosity. To effectively model salinity and temperature diffusion with waterflooding using the reservoir simulation model brine tracking feature, representative values of the reservoir brine salinity, injected water salinity and the oil and water viscosities are specified. The salt concentration mass conservation equation for each simulation grid cell is described in equation (2.14):

$$\frac{d}{dt}\left(\frac{VS_wC_s}{B_w}\right) = \sum\left[\frac{Tk_{rw}}{B_w\mu_{s(eff)}}(\delta P_W - \rho_w g D_z)\right]C_s + Q_w C_s \qquad (2.14)$$

where:

- S_w - *Water saturation*
- C_s - *Salt concentration*
- B_w - *Water Formation volume*
- T - *transmissibility*
- $\mu_{s(eff)}$ - *effective viscosity of salt*
- ρ_w - *water density*
- D_z - *cell centre depth*
- Q_w - *Water production rate*
- P_w - *water pressure*
- V - *block pore volume*
- K_{rw} *Relative permeability*
- $\sum$- *Sum over neighbouring cells*
- g- *Gravity due to acceleration*

With the flow simulation results reflecting waterflooding salinity changes, using *Sim2Seis* (Amini, 2014), the synthetic seismogram is created to analyse the influence of tracking salinity changes

Temperature Tracking in the Reservoir Simulation Model

Heat flow obeys the law of conservation of energy; therefore, injection of cold sea water into a hot reservoir facilitates an absorption of heat by the injected water and a release of heat by the reservoir (rock matrix and hydrocarbon combination).

Injecting cold sea water into a relatively warmer reservoir cools the formation in the well-centric drainage area. The reduced temperature within the drainage area increases the viscosity of the reservoir fluids and this phenomenon is tracked using ECLIPSE 100 and specifying representative values for reservoir temperature, injected water temperature as well as thermal conductivities and specific heat capacities for both oil and water. For each timestep, the three-dimensional energy conservation equation (*2.15*) is solved and new grid cell temperatures calculated for the next timestep.

$$c \cdot \rho \cdot \frac{dT}{dt} = k\left(\frac{\partial^2 T}{\partial x^2} + \frac{\partial^2 T}{\partial y^2} + \frac{\partial^2 T}{\partial z^2}\right) + Q_{(x,t)} \qquad (2.15)$$

where: c - specific heat capacity, T - temperature at x, y, z; t – time, k - thermal conductivity and Q - heat energy.

Figure 2.23 shows plan and cross-section views of the simulation model results with salinity and temperature tracked for the North Sea water injection scenario with properties listed in Table 2.4. The gradients of the salinity and temperature from the point of injection at the well to the front in the reservoir is evident in both views, with the cooling effects of injecting seawater concentrated around the well. The injected water is heated up by the formation towards the waterfront, resulting in a less significant temperature change. Salinity of the injected water, on the other hand, extends to the entire drainage area, with the high to low gradient from well to saturation front.

Table 2.4: Properties of reservoir and injected brine

	Reservoir Brine	Injected Brine
Salinity	18,000 ppm	30,000 ppm
Temperature	57.7 °C	15 °C

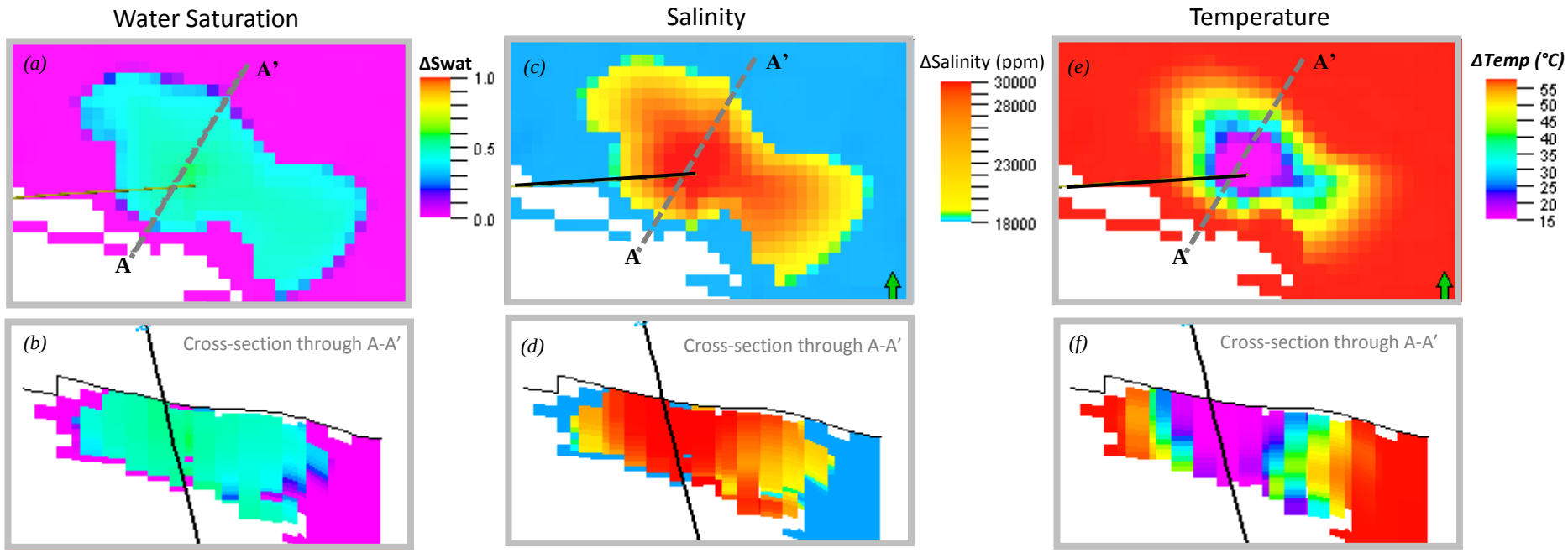

Figure 2.23: (a) and (c) salinity and temperature distribution modelled after injection scenario. (b) and (d) cross-sectional view through intersection A-A'

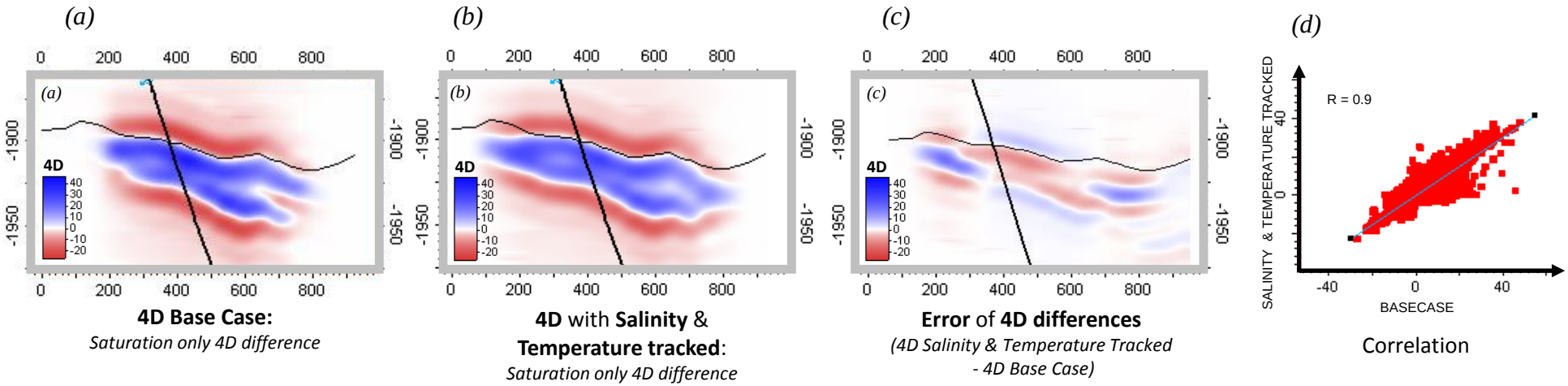

Figure 2.24: Synthetic Seismic sections for an injecting well showing the signal differences (b) with and (a)without tracking salinity and temperature. Error of 4D differences in (c) shows the qualitative interpretation lost when these effects are not tracked. (d) Crossplot of the seismic amplitudes with the salinity and temperature tracked against the basecase with no tracking shows the quantitative signal difference with the correlation coefficient describing the degree of correlation.

Excluding the time-lapse pressure response, saturation only 4D seismic sections with both salinity and temperature injection effects tracked are shown in Figure 2.24. (a) shows the 4D seismic saturation signal without these individual effects accounted for and (b) shows the section with effects incorporated. The section (c), shows an error difference of both 4D sections, with errors of up to ±3% amplitude.

Temperature effects in the immediate injector vicinity have led to the decreased amplitudes in the seismic section with salinity and temperature effects incorporated, compared to the base case. The salinity effects, on the other hand, due to the increased sensitivity to the brine tracking, appears to extend the waterfront further than the seismic signal in the base/untracked case. These slight signal extensions in the signal show up on a difference of 4D base-case – tracked section as errors of up to 15% amplitude. We can infer from this that the modelled 4D seismic is more sensitive to the flood with the tracked salinity, and thus the observed 4D seismic signal is in fact influenced by even small salinity and temperature changes.

2.7 Summary

This chapter investigates the effects of grid and geological scale on the seismic forward modelling interpretation and estimates the influence of individual effects of the salinity and temperature gradients introduced by waterflooding on the 4D seismic signal. Varying effects of vertical and lateral refinement as well as coarsening of the numerical grid on the predicted 4D seismic signal were compared to the base-case predicted seismic. Results indicated that while the vertically refined scale showed the best correlation to the predicted base-case seismic, the laterally refined scale produced a higher resolution of the geology with increased water saturation signal. The increased resolution compared to the base-case was reflected in the slightly lower correlation coefficient of 0.67 given the difference in spatial extent

The salinity and temperature changes on the waterflooding seismic signal led to an estimation of errors of $\pm 3\%$ amplitude change while the salinity tracking extended the character of the seismic signal, increasing the errors to $\pm 15\%$ amplitude change when differenced from the base-case. The errors of $\pm 3\%$, however, are for a noise-free synthetic seismic data and is not practically significant in this dataset with an average

NRMS noise metric of 29%, meaning 29% of the 4D seismic signal regarded as noise would encapsulate the salinity and temperature changes for this field characteristics and waterflooding scenario.

Chapter 3

Volumetric Calibration of the Seismic Signal

The comparison of reservoir simulation errors to 4D seismic uncertainties involved in a 3D volumetric seismic calibration procedure for waterflooding volumes is demonstrated in this chapter for the Schiehallion field. Calibration of the seismic response to actual reservoir volumes is an important process in quantitaive 4D seismic interpretation. For waterflooding, net water volumes estimated from 3D seismic geobodies are used calibrated to actual net water volumes from production data. For the simulation model, synthetic seismic and observed seismic interpretations of waterflooded reservoir volumes, the calibration process is repeated and the evolving error magnitude calculated. Results showed increase in errors from 4% to 67% from the simulation model calibrated volume to observed seismic interpreted volume.

3 Volumetric Calibration of the Seismic Signal

3.1 Quantitative Calibration of the Seismic Signal

Interpretation of the 4D seismic signal has evolved with improved technology to the point where quantitative attributes can be derived. For the use in reservoir characterization, waterflooding evaluation or seismic history matching, the seismic signal is typically calibrated to the real reservoir changes. To calibrate the seismic signal would mean to evaluate the volume of seismic response that is equivalent to the volume of reservoir change causing the response. In the case of waterflooding performance evaluation, the seismic geobody resulting from the injection of water into the reservoir would be calibrated to the net volume of injected water. Accurate calibration of the seismic signal is driven by the reservoir's response to the injected water and how these reservoir changes translate to different seismic attributes based on an understanding of the rock physics of the reservoir. The choice of seismic attribute to calibrate is related to reservoir characteristics, the reservoir condition to be calibrated, and the availability and quality of the seismic data. Methods of calibration of the seismic signal, therefore, are simply dependent on using the most appropriate data and are field and production scenario-specific.

Different methods of seismic signal calibration have been applied in the literature. Huang (2001) proposed a data-based integration of rock physics and log analysis, seismic modelling and 4D seismic processing, culminating in production data reconciliation for the seismic signal calibration cycle. On 2D attribute maps, an optimisation process is carried out to determine the threshold or seismic signal cut-off that matches the seismic anomaly to production data using conditions of the material balance of fluid production. This was exhibited using a gas saturation example, where the decrease of the seismic signal corresponding to the replacement of gas accumulation by water was calibrated to the produced gas volume. Acknowledging the ambiguity that exists between seismic amplitude and saturation change, best estimate thresholds were iteratively determined as signal cut-offs. In another example, Eiken and Tøndel (2005) used 4D seismic data with good sensitivity to small pore pressure changes and high repeatability to calibrate the changes in time shifts to the depleting gas column, thus deriving an expression for pressure sensitivity. Floricich et al. (2006) used well data to calibrate the time-lapse

changes in saturation and pressure in the reservoir to corresponding seismic responses, establishing a relationship for changes in seismic attribute ΔA over an elapsed time from pre-production to the time of monitor survey. Alvarez and MacBeth (2014) on the other hand, derived a simple balance between the overall change in seismic attribute to relative contributions of changes in saturation and pressure. Davolio et al. (2012) for a synthetic dataset, used the reservoir simulation model to constrain dynamic saturation and pressure properties estimated from a petroelastic inversion of seismic impedances. Volumes from estimated 4D seismic water saturation maps, products of the inversion, were then calibrated to known injection volumes by updating the volumes using a correction factor estimated from feasible ranges of water volumes predicted from multiple simulation models. Pluchery et al. (2013), for the Dalia field, a sandstone reservoir with unconsolidated sands, generated 4D seismic PLTs for multi-completed wells using high-quality 4D seismic with vertical resolution of 6-7 metres. The monitor and base surveys were warped and relative changes of the P-wave velocity as a result of increased water saturation calculated. Velocity relative changes were calibrated to the volumes injected along with injection anomalies in the form of seismic geobodies propagated along the wells. The geobodies, change in water saturation and effective porosity were used to calculate injected volumes per reservoir interval at the time of the reservoir interval.

Following a volumetric approach, a study to calibrate 4D seismic waterflooding volumes for the previously described Segment 1 of the Schiehallion field is carried out, utilizing the available multiple seismic surveys, aiming to understand the magnitude of possible errors encountered and the consequent impact across domains.

3.2 The Volumetric Calibration Error Evolution

Three-dimensional seismic data provides a volumetric realisation of the subsurface and illuminates the reservoir geology - stratigraphy and structure and hydrocarbon deposit characteristics. However, seismic data is typically visualised in two-dimensional planes of maps or cross-sections, yielding to the constraints of high data volume processing and computational costs and missing out on the main advantages of 3D seismic data. Two-dimensional visualization data is based on the mapping of individual subsurface attributes (horizons, contacts, faults) and converting the interpretation into a 3D volume (Figure 3.1). In contrast, three-dimensional volume visualisation is based on the fact that the seismic reflectivity of the earth model already exists in 3D space, allowing the application of different levels of transparency to the seismic data to reveal characteristics of the subsurface. Three-dimensional volume visualization through co-rendering, various attribute analysis, and automatic reservoir facies detection, facilitates the interpretation of seismic data (Kidd, 1999b; Gao, 2003, 2008). Volume visualization utilises the maximum amount of the 3D seismic data and reduces the two-step interpretation process undergone in two-dimensional visualisation.

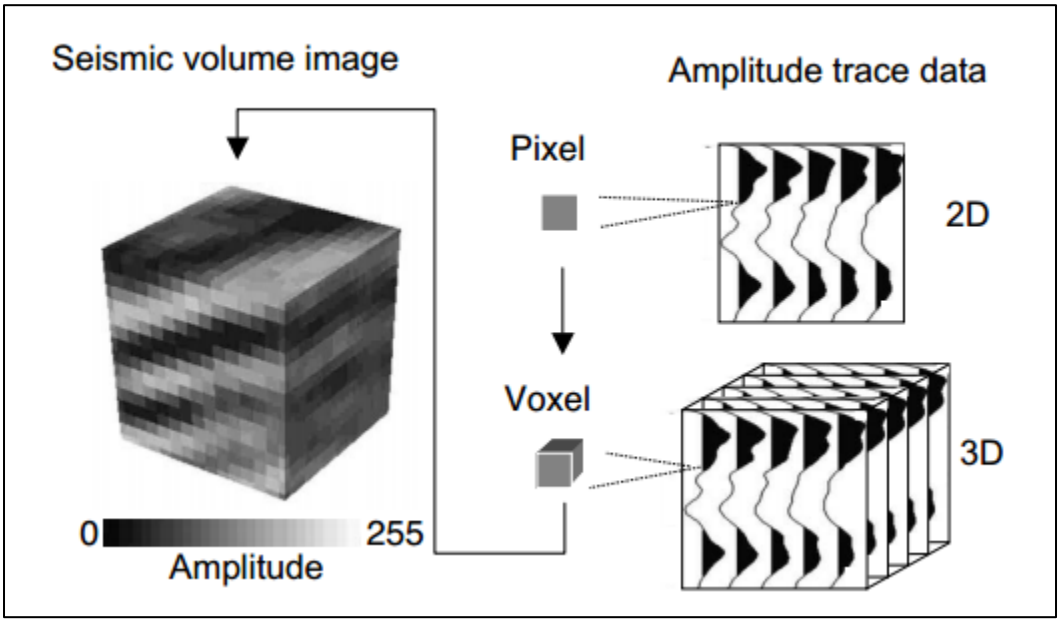

Figure 3.1: Visual depiction of seismic traces of amplitude samples as an array of volumetric pixels - voxels in 3D space. Voxel grayscale denotes the amplitude intensity of the sample (Kidd, 1999a).

In the three-dimensional volume visualisation, each seismic data sample is converted to a three-dimensional pixel (voxel) of bin and interval spacing dimensions with data values corresponding to the original seismic data. A seismic trace is therefore equivalent to a voxel column. The data in eight to thirty two bit colour scales (proportional to the level of technology) are represented in a histogram distribution of the voxel values. The voxel values are related to the seismic wiggle trace as shown in Figure 3.2a). The histogram distribution of voxel values, corresponding to the amplitude (or seismic attribute) values, can be thresholded according to the degree of opacity that is the magnitude of the amplitude (Figure 3.2b).

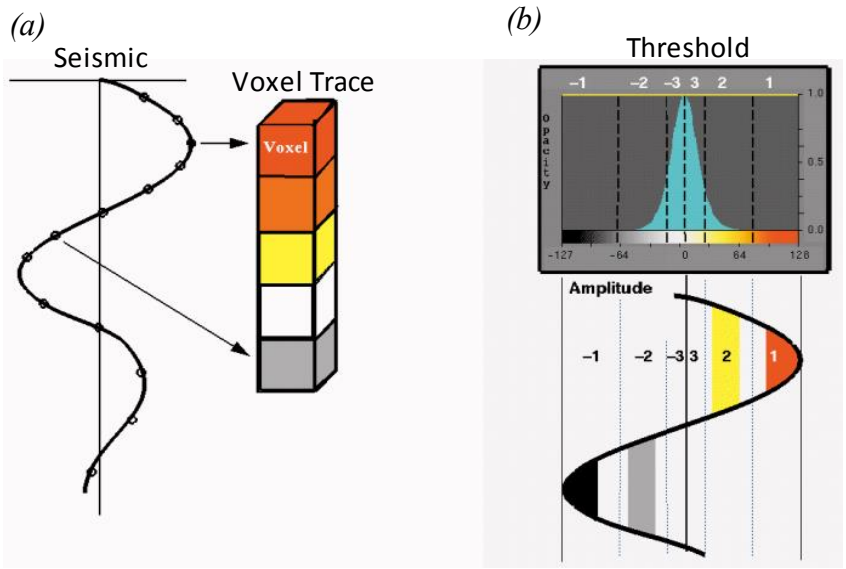

Figure 3.2: (a) Seismic sample to voxel relationship and (b) opacity editor and its relationship to seismic (Kidd, 1999).

In 4D seismic interpretation using three-dimensional volumetric visualisation, the amplitude signal responses to time-lapsed reservoir changes are rendered as 3D volumes in space called geobodies. For the waterflooded scenario, connected increased impedance (hardening) 3D volumes around the wells represent the volumes of injected volumes of water.

Using the available seismic attribute, seismic amplitudes, the seismic volume rendering feature in the geomodelling software Petrel™ is used to extract seismic 3D geobodies in a visual volumetric representation containing amplitude variation corresponding to injected water (or influx from aquifer). Varying the geobody opacity using amplitude magnitude as a filter criterion in the opacity editor (Figure 3.2) leads to a clipping of the hardening signal with the high amplitudes of the fully saturated regions more proximal to

the injector and the partly saturated regions further away from the well. The variations of the opacity of the geobody do not only reveal the volumes of water, geological architecture and net-to-gross of the volume occupied by the injected water but indicate the direction of water propagation via amplitude flow: from high to low.

Extracting a water volume geobody involves:

1) Converting the seismic volume from time to depth.
2) identifying the 3D flood volume with integrated interpretation of well activities and an understanding of the expected seismic anomalies related to waterflooding,
3) isolating the geobody related to the flood volume assisted by amplitude, size and connectivity criteria, and
4) extracting the 3D geobody from the seismic data. These geobodies are then calibrated to the known water volumes from engineering well data.

Constraining the volumetric calibration with engineering data is achieved with the help of the reservoir simulation and synthetic seismic models, by relating known injected volumes in the reservoir simulation model to the increased water saturation seismic signal. The net injected water volumes in the simulation model reflects an equivalent 4D hardening signal in the generated synthetic seismic model, just as the actual injected volumes trigger a seismic response in the observed 4D seismic data. An approximately equal estimate of net volumes calculated from the respective flood area is then expected across all three domains of (1) Simulation model, (2) Synthetic Seismic model and (3) Observed seismic, Figure 3.3. This is with the assumption that the product of the 4D geobody gross rock volume – that is, the i) 3D volume of waterflooded rock, ii) average net-to-gross ratio, iii) average porosity, iv) time-lapsed change in saturation and v) water formation volume factor would accurately estimate the net water volume, ΔV_{w4D}. This is expressed in equation (3.1) as:

$$\Delta Vw = \Delta GBV * \bar{\varphi} * \overline{NTG} * \overline{\Delta S_w} * B_w \qquad (3.1)$$

where ΔVw= the estimated net volume of water, ΔGBV= the 4D geobody gross rock volume, $\bar{\varphi}$ = mean porosity, $\overline{NTG}$ = the mean net-to-gross and $\overline{\Delta S_w}$ = the mean change in water saturation, all for the waterflooded area with B_w = water formation volume factor.

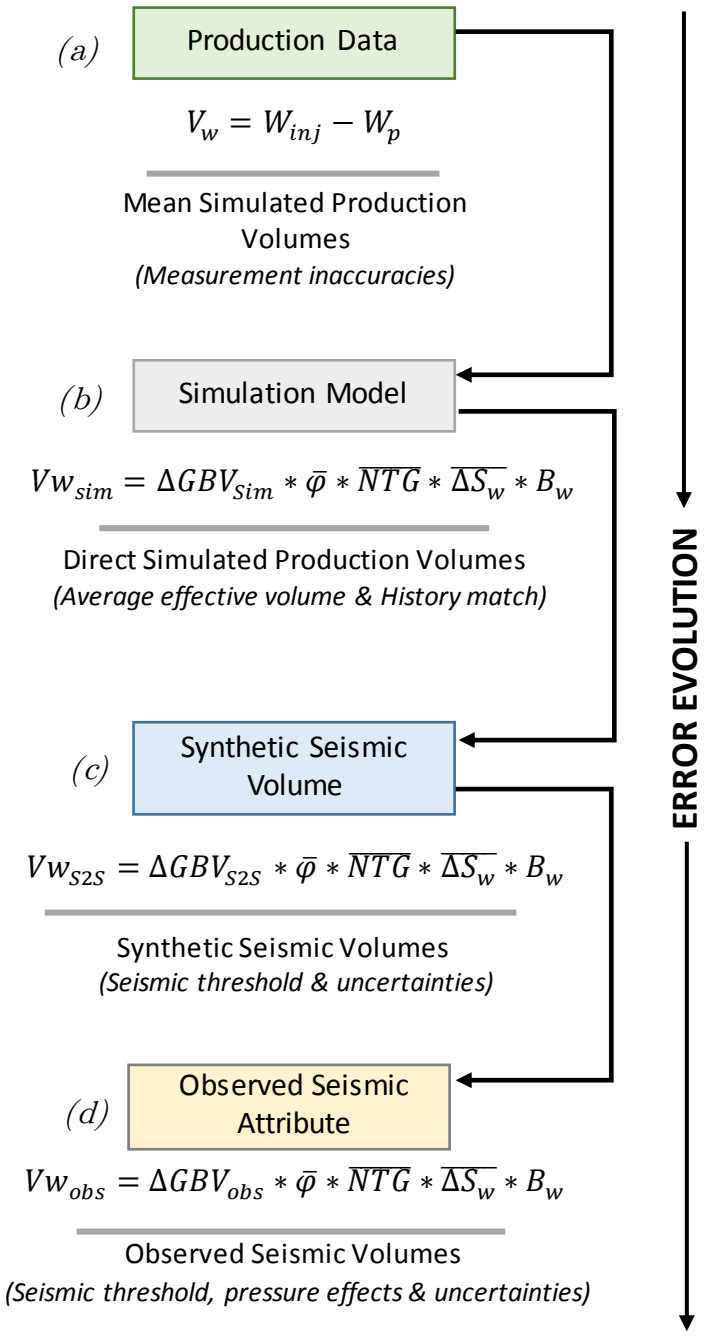

Figure 3.3: Error evolution through the different domains showing expressions for net water volume for (a) production, V_w (b) simulation, Vw_{sim} (c) synthetic seismic, Vw_{S2S} and (d) observed seismic, Vw_{obs}. Possible sources of errors in parenthesis.

3.3 Calibration in the Simulation Model

To aid our transition from production data to seismic data, we rely on an understanding from calibration of volumes in the history matched simulation model and its accompanying seismic forward model. For the available ten years production period in

the Schiehallion dataset considered, the water injection campaign ran from 1998 at the start of production to 2008, with 10 injectors completed in either the aquifer located in one-third of the North-west of the field, the oil leg or both the oil and water legs. Figure 3.4 shows the field-wide pre-production saturation distribution and the increased water saturation distribution following the years of injection.

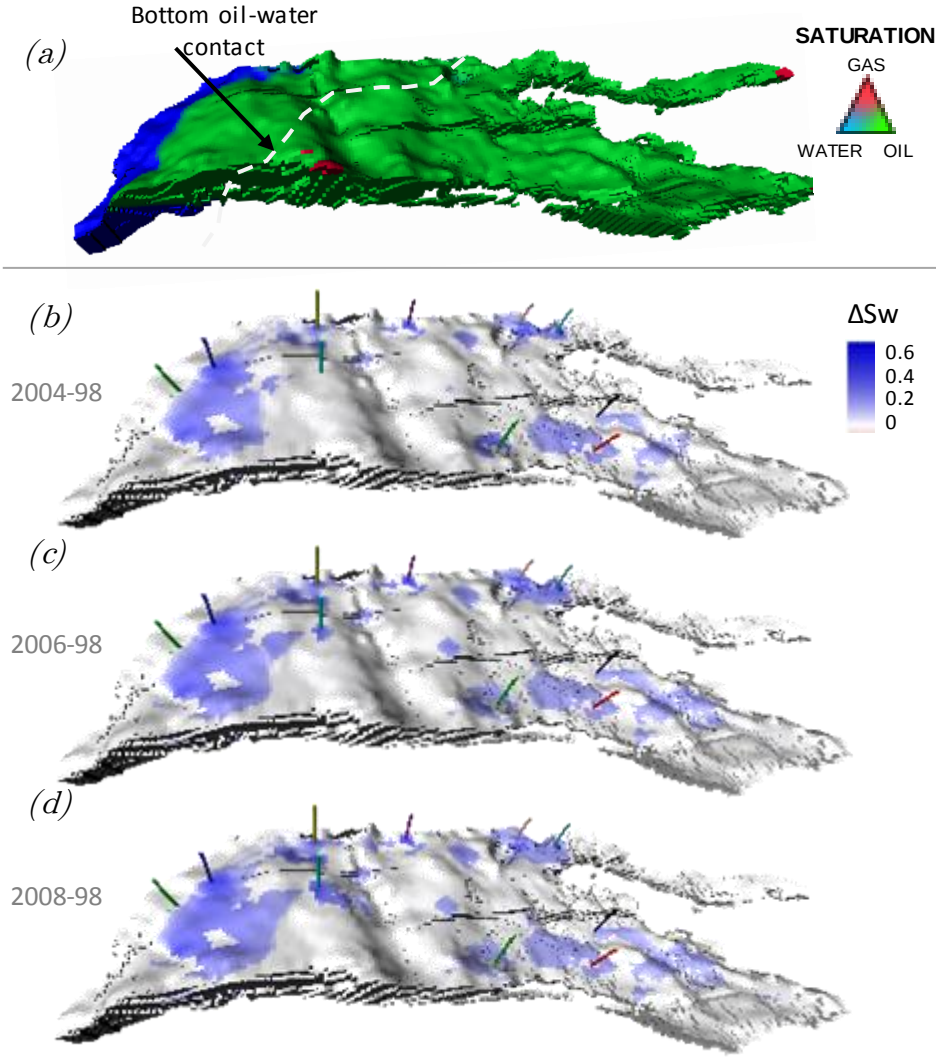

Figure 3.4(a) Saturation distribution of reservoir segment studied. (b - d):4D water saturation changes for the survey years: 2004, 2006, 2008.

Using the coefficient of determination, R^2, as a measure of match between the simulation model and observed data, the model has an average match quality of 92.48% for the field production rates and illustrated in Figures 3.5 – 3.7, allowing an assumption that the simulation model closely replicates the observed data, equalling a close approximation of the historical net volumes by the simulation model.

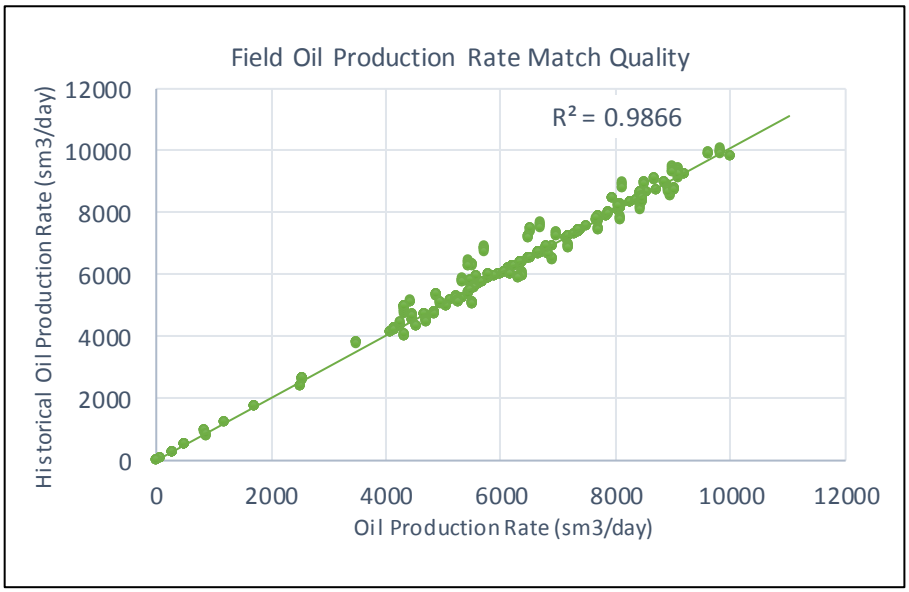

Figure 3.5: History Match Quality indicated by correlation coefficient of crossplot of historical and model field oil production rates.

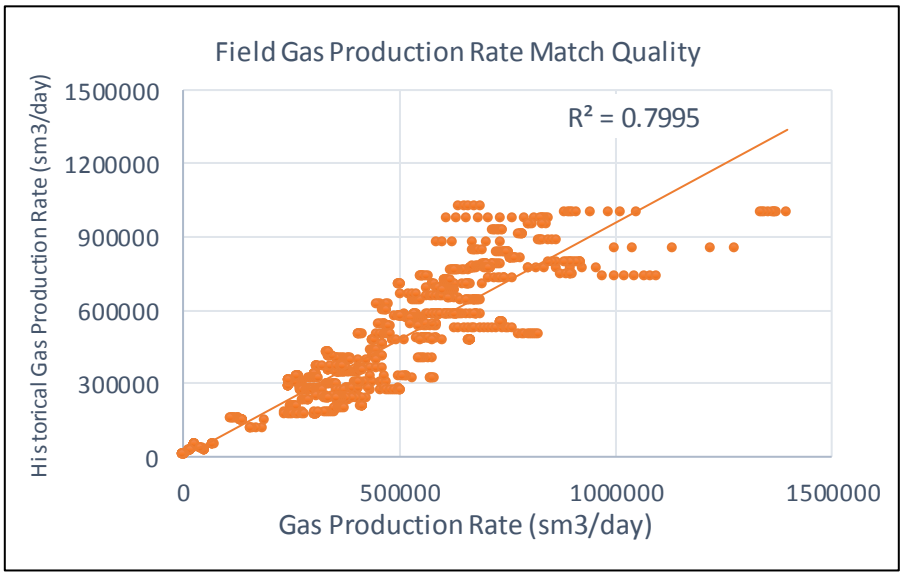

Figure 3.6: History Match Quality indicated by correlation coefficient of crossplot of historical and model field gas production rates.

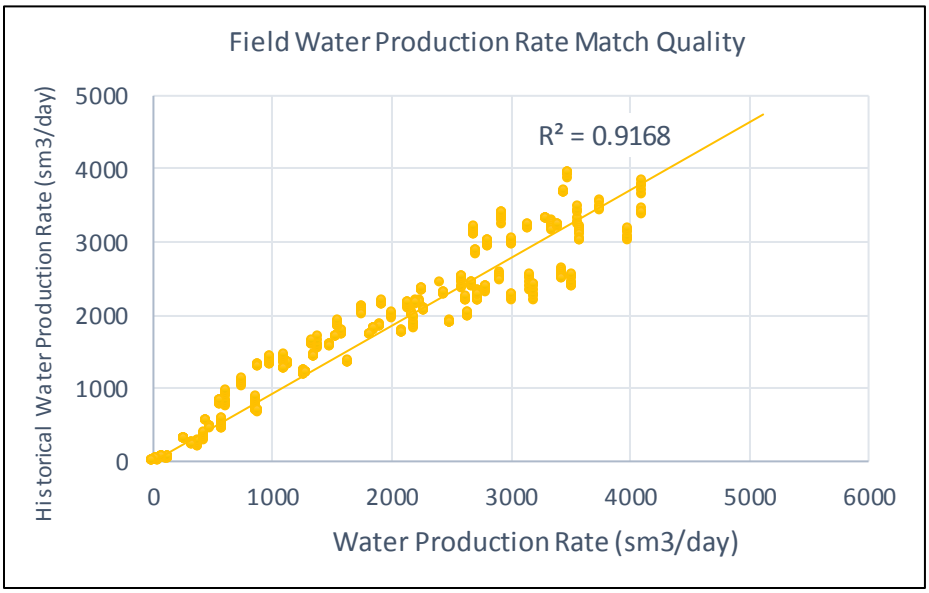

Figure 3.7: History Match Quality indicated by correlation coefficient of crossplot of historical and model field water production rates.

3.3.1 Simulation Model Geobody Material Balance Analysis

To resolve the observed net water volumes and the simulation model calculated volumes, material balance conditions of equation 3.2 must be satisfied, taking into consideration the presence of an aquifer (Figure 3.8) and the possibility of aquifer efflux or influx

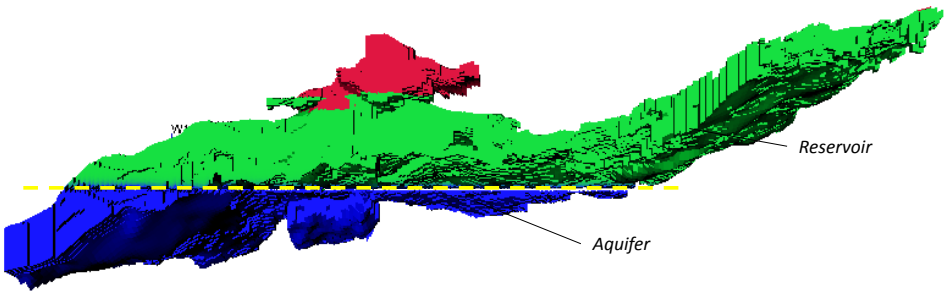

Figure 3.8: Side view of reservoir simulation model showing oil water contact and aquifer

$$\frac{V_{p1}S_{w1}}{B_{w1}} - W_p + W_i + W_e = \frac{V_{p2}S_{w2}}{B_{w2}} \qquad (3.2)$$

$$Net\ Volume, \Delta V_w = W_i + W_e - W_p = \frac{V_{p2}S_{w2}}{B_{w2}} - \frac{V_{p1}S_{w1}}{B_{w1}} \qquad (3.3)$$

where V_p = pore volumes, S_w = water saturation, W_p = produced water, W_i = injected water, W_e = aquifer influx and B_w = formation volume factor. The subscripts *1* and *2* denote the initial and post-production conditions.

Production data of water injected volumes and aquifer influx input into the simulation (Eclipse keyword AAQR), is regarded as the real data and is the benchmark against which volumes from all three domains (simulation, synthetic seismic and observed seismic) are compared. Real net water volumes calculated are therefore referred to as *"Actual Net Volumes"*.

For a field-scale calibration with an occurrence of an aquifer, there are additional material balance scenarios to be considered. For an expanding aquifer being injected into (efflux) for reservoir pressure support and flowing into the reservoir for water sweep (influx), the change in aquifer pore volume, ΔV_p, is expressed as:

$$\Delta V_p = c_p V_{pi} \Delta P \qquad (3.4)$$

where V_{pi} is the initial aquifer pore volume, c_p is the formation compressibility and ΔP is the reservoir pressure gradient.

Further consideration is to be given to:

- The transition zone which has a bearing on the calibration process given the average water saturation value, $\overline{\Delta S_w}$, in equation (3.1). This is because, for every average reservoir pressure gradient, there would be a change in the oil-water contact, a growth in the transition zone and hence an increase in the gross rock volume experiencing a change in water saturation. For determination of the waterflooded gross rock volume (GRV), a threshold must be applied to avoid including the entire reservoir experiencing minute increases in water saturation as a result of pressure gradient.
- Production activities, aquifer influx and resultant drop in pressure in the aquifer leads to an aquifer pore volume expansion defined in equation (3.4). The interpretation of these changes in pore volume should be considered in the estimation of net water volumes.

- Adjustments to net volumes should include volumes of aquifer efflux from injectors completed in the aquifer.

Given the expansive rock volume of the transition zone, for each 4D timestep considered, the histogram distribution of the predicted change in saturation in the simulation model is analysed, and a threshold of 0.01% of the maximum change in water saturation, $\overline{\Delta S_w}$, is applied as a cut-off to exclude the transition zone gross rock volume. For the years 1998 – 2008, the waterflooded geobodies were extracted from the simulation model and the net volumes, ΔVw_{sim} estimated using equation (3.1). For each year, the same cut-off was applied to determine the mean static properties and average water saturation fraction to calculate the field net water volume according to equation (3.1). The extracted field geobodies are shown in the first column of Figure 3.13.

Figure 3.9 shows a chart of the net water volumes for the period of production and the calculated net volumes from the simulation model, ΔVw_{sim}. The calculated volumes are shown in Table (3.1), with the percentage errors between the actual net volumes and computed reservoir simulation net water volumes, ΔVw_{sim}, shown in the last column.

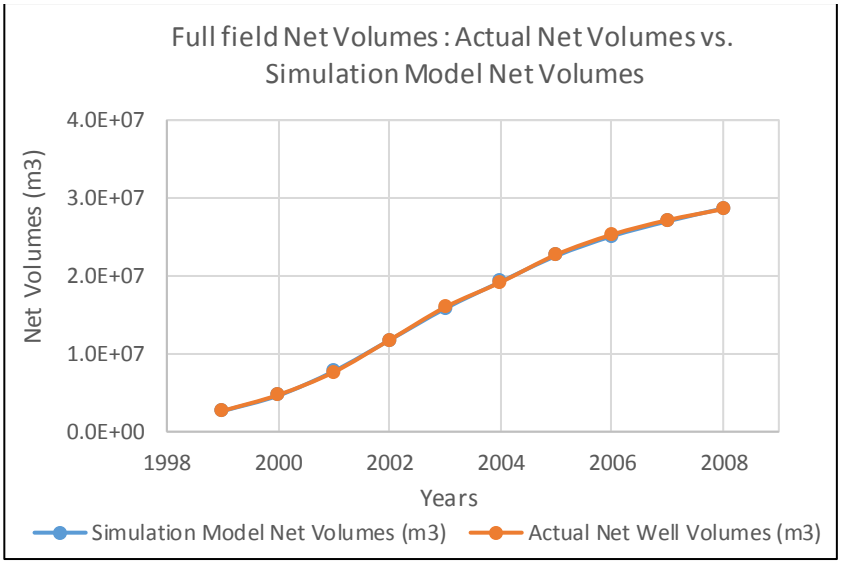

Figure 3.9: Chart showing the simulation net volumes compared to the actual net volumes for each year.

Year	Net Well Volumes	Aquifer Influx	ΔAquifer Pore volume	Total Actual Net Volumes	Model Net Volumes (ΔVw_{sim})	Percentage error (Actual/ Model) %
	(m3)	(m3)	(m3)	(m3)	(m3)	(%)
1999	3.17E+06	-5.17E+05	3.59E+04	2.67E+06	2.64E+06	1.18
2000	5.53E+06	-8.43E+05	5.84E+04	4.72E+06	4.63E+06	1.97
2001	9.06E+06	-1.47E+06	1.02E+05	7.64E+06	7.77E+06	-1.60
2002	1.40E+07	-2.30E+06	1.59E+05	1.18E+07	1.17E+07	0.12
2003	1.88E+07	-2.98E+06	2.06E+05	1.60E+07	1.58E+07	1.18
2004	2.23E+07	-3.20E+06	2.22E+05	1.92E+07	1.93E+07	-0.36
2005	2.61E+07	-3.45E+06	2.39E+05	2.27E+07	2.26E+07	0.74
2006	2.91E+07	-3.93E+06	2.72E+05	2.53E+07	2.51E+07	0.80
2007	3.16E+07	-4.57E+06	3.16E+05	2.72E+07	2.70E+07	0.56
2008	3.34E+07	-5.03E+06	3.48E+05	2.86E+07	2.87E+07	-0.32

Table 3.1: Simulation model net volume estimates compared to actual net volumes and calculated percentage error ((Model-Actual)/Actual)×100)

As seen in Figure (3.9), the use of mean static properties and averaging effects from grid cell dimensions of 50m × 50m × 2m, does not significantly affect the net water volume estimates from the simulation model.

Over the ten years, and for a threshold of 0.01%, net volumes calibrated from the simulation model, Vw_{sim}, had an error range of -0.32 – 1.97% (Table 3.1). We acknowledge that even for a history matched simulation model, production volumes captured in the simulation model are subject to measurement inaccuracies at the pumps and gauges, possible numerical errors from the flow simulation computations, a less than precise history match of the simulation model, approximations of model grid dimensions and orientation, lost volumes as a result of threshold to exclude transition zone, and the use of average values for the reservoir properties - static properties (porosity, net-to-gross) and average values for change in water saturation. The simulation results and accompanying errors and uncertainties, however are carried along as input to the seismic forward modelling process. The close replication of the actual net water volumes within an error of <±2% (Table 3.1) validates the process of extraction of the waterflooded geobody with the assumptions made. An awareness of the <±2% error transmitted to the synthetic seismic model allows compensation and a better understanding of the uncertainties in the synthetic seismic results.

3.4 Calibration of the Synthetic Seismic Data

Waterflooding triggers the main effects of increased water saturation and pressure; two contrasting effects of hardening and softening in 4D seismic interpretation. The response of the reservoir to waterflooding, however, is dependent on the reservoir's sensitivity to these effects. To better understand the resultant seismic signal with waterflooding, a primary step is a test of the reservoir sensitivity to expected changes.

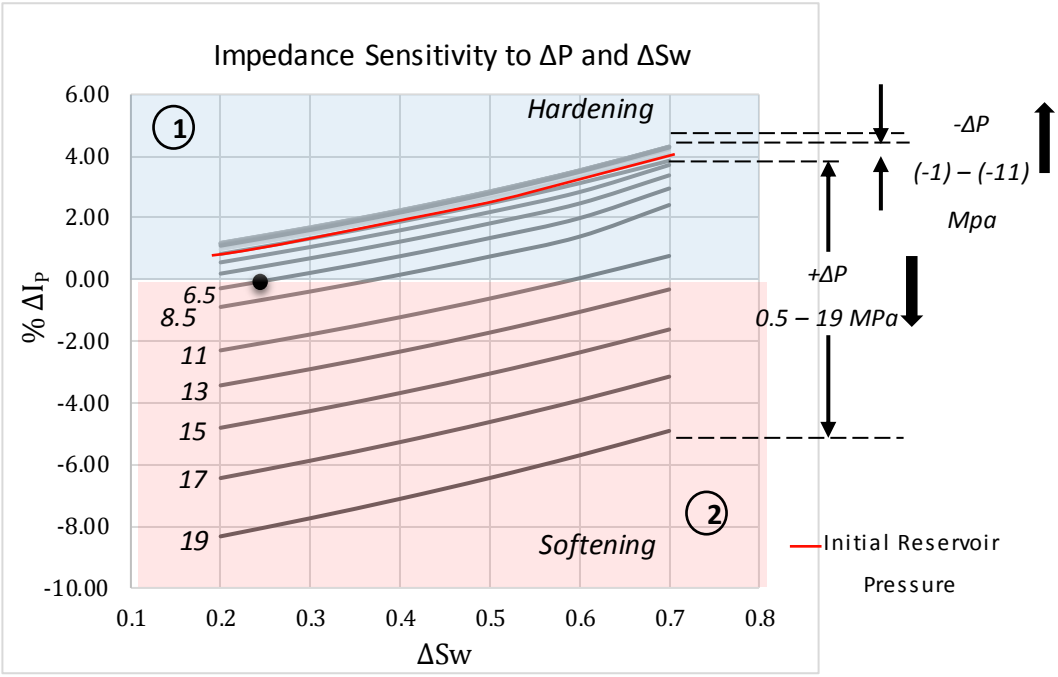

Figure 3.10: Percentage change in P-Impedance for a range of pressure changes for increasing change in water saturation.

Assuming a reference of initial water saturation: S_{wi} = 0.17 and initial reservoir pressure = 200 bar, expected percentage changes in impedance for a range of percentage pressure increases/decreases at different degrees of water saturation occurring in the Schiehallion dataset were analysed and estimated. This is to enable a more informed hardening and softening signal classification. Figure (3.10) shows the balance of hardening and softening signals. The black point indicates the cut-off at which an increase in water saturation, Sw = 0.25 would dominate all pressure increases less than 35% (progressing south from the reservoir pressure (red line)). This means that the hardening signal of flood fronts with a 25% increase in water saturation and less would be obscured by softening signals of pressure increases greater than 35%.

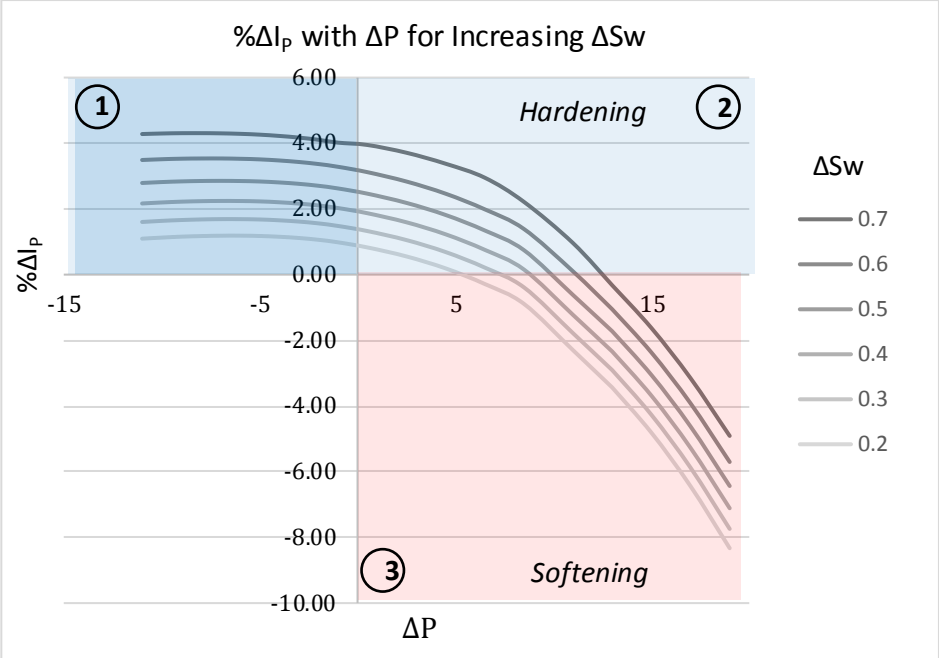

Figure 3.11: Percentage change in P-Impedance with percentage change in pressure for increasing change in water saturation.

As both increase in water saturation and decrease in reservoir pressure (depletion) cause a 4D seismic hardening effect, Figure 3.11 shows the proportion of the hardening signal attributable to increased saturation alone, and the proportion resulting from both increased saturation and pressure depletion (section (1)).

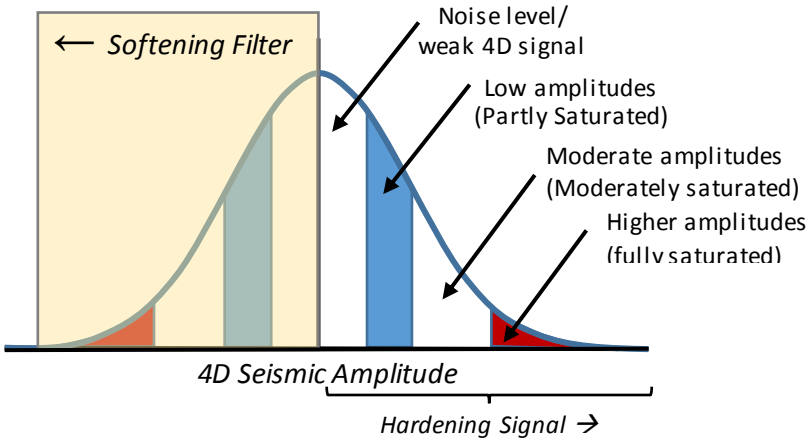

Figure 3.12: Gaussian distribution of 4D seismic data consisting of signal and noise (After Castanié et al. 2005)

For calibration of the waterflooded geobodies from seismic data, investigation is restricted to the the hardening signal. 4D seismic signal amplitude data is a Gaussian distribution consisting of 4D signals and noise. Majority of the noise and weak 4D seismic

signals occur about the histogram mean (Figure 3.12). These weak signals correspond to partly saturated areas of the reservoir and propagate towards higher magnitude amplitudes corresponding to the most saturated parts of the reservoir at the distribution's minimum frequencies.

The synthetic seismic model used in the calibration does not contain noise, allowing an application of a softening signal filter from the least possible amplitude threshold. To investigate the sensitivity of thresholds to calibration volumes and the possible degree of influence of noise amplitude clipping typically occurring in an observed seismic data interpretation, extraction of the waterflooded geobody volume, ΔGRV, is obtained at a range of cut-off thresholds. Starting with a least threshold, T, which assumes no noise at a cut-off of T = 0.01% of the maximum amplitude, to a cut-off that excludes noise up to 20% of the maximum, the extracted geobody volumes as shown in the second column of Figure 3.13 are then used to estimate Synthetic Seismic Net Volumes, ΔVw_{S2S} using equation 3.1.

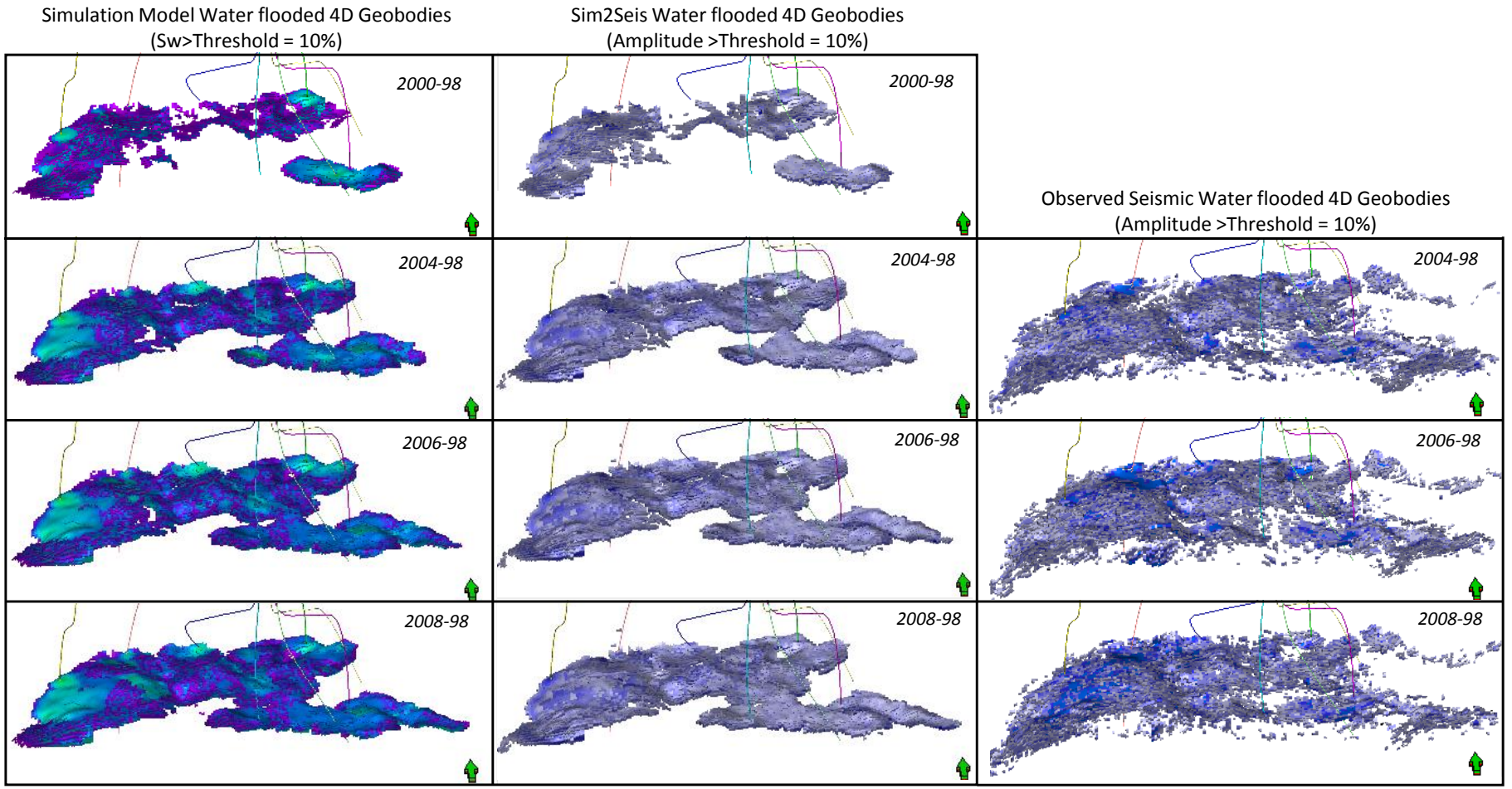

Figure 3.13: Extracted Field waterflooded geobody volumes for simulation model, synthetic seismic and observed seismic. All geobodies shown extracted with a threshold, T = 10%

Estimated volumes from the *Sim2Seis* saturation-only (excluding the pressure effects) extracted geobodies for all four thresholds are shown in Figure (3.14). Actual net volumes are plotted in black on the same chart for comparison. From the chart, the estimated volumes for the range of thresholds between 0.01% - 20% of the maximum amplitude vary only minimally and are seen to not have significant effects on the estimated volumes.

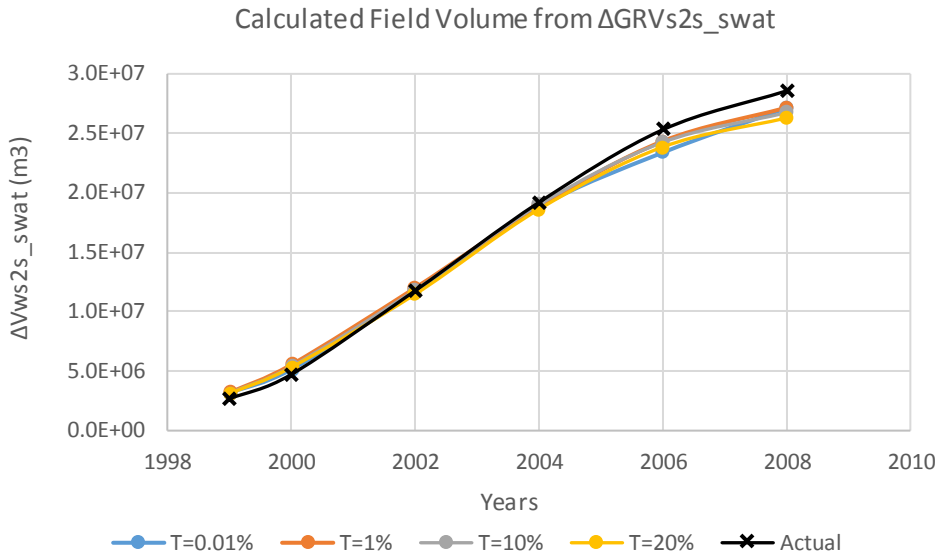

Figure 3.14: Estimated net water volumes from Sim2Seis saturation-only seismic signal for all surveys and for thresholds, T = 0.01%, 1%, 10% and 20%.

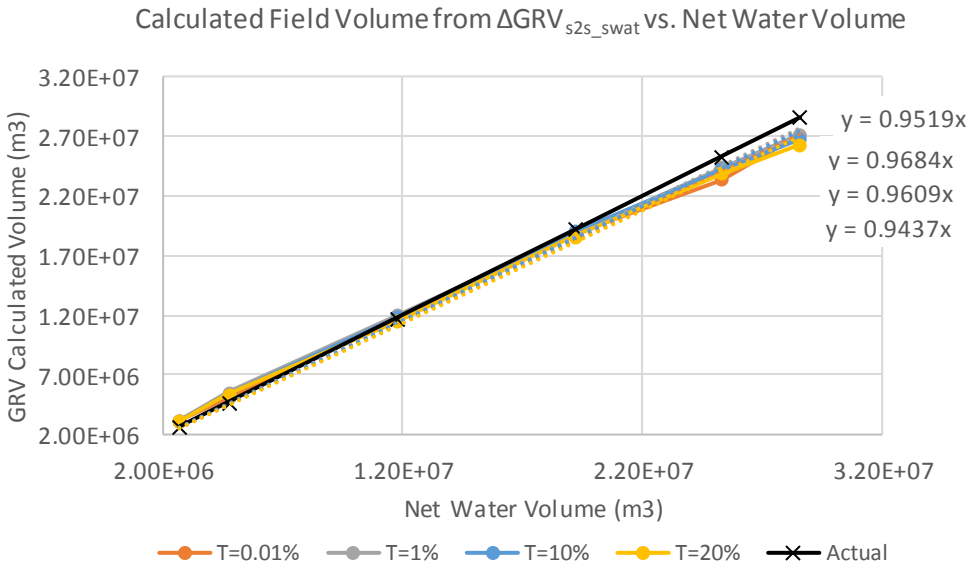

Figure 3.15: Cross-plot of ΔVw_{S2S_Swat} and Actual Volumes showing direct proportionality. Expressions of relationships between volumes from top to bottom for thresholds, T=0.01%, 1%, 10% and 20%.

S2S Swat %Errors				
Year	T=0.01%	T=1%	T=10%	T=20%
1999	18.51	19.27	17.88	16.34
2000	8.89	17.25	13.92	12.65
2002	-1.01	2.01	0.47	-2.54
2004	-2.13	-1.74	-1.06	-3.00
2006	-7.58	-3.80	-4.18	-5.73
2008	-5.06	-4.93	-6.40	-7.96

Table 3.2: Percentage Errors between actual net water volumes and net water volumes estimated from synthetic seismic saturation-only data for four thresholds, T= 0.01%, 1%, 10% and 20%. Errors given as (100 × (actual volume – estimate volume)/actual volume)

Table (3.2) shows the percentage errors, with volumes from threshold T=10% with the least average error. The initial large error for all thresholds could be as a result of inefficient aquifer influx/efflux estimation and uncertain aquifer pore volume reconciliation as the seismic characteristics of the aquifer are uncertain. In addition, the largest errors from the simulation model calibration were noticed in the first three surveys. These errors would have been carried over to the seismic forward modelling exercise and are contributing factors to the initial larger errors. Seismic uncertainties associated with the amplitude interpretation also extend the errors noticed in the synthetic seismic calibration. Figure (3.15) is a cross-plot of net water volumes calculated from extracted seismic saturation-only geobodies and the actual volumes. For the trendlines for all plots, calibration factors, y/x, range between 0.944 and 0.968 showing an almost one-to-one relationship. In spite of the errors, this calibration exercise increases confidence in the direct proportionality relationship between the seismic increased water saturation signal and actual net water volumes. This is for a case considering the saturation-only seismic signal, neglecting the pressure effects. A true waterflooding scenario, however, is always accompanied by a counteracting increased pressure signal, which would be investigated in the next section.

3.4.1 Including the pressure effect

Given our understanding of the sensitivity of the reservoir (Figures 3.11 and 3.12) and with confidence from the near 100% direct proportionality between the saturation-only signal of the 4D synthetic seismic and actual net water volumes, calibration of the full

synthetic seismic signal is executed. This is continuing with the same workflow and equation (3.1) to estimate volumes, ΔVw_{s2s_full}, from geobodies extracted from the hardening signal under the possible influence of the counteracting pressure signal.

Similar to published examples of geobody calibration (Byerley et al., 2009) and in line with Alvarez and MacBeth (2013), the seismic amplitude is expected to be directly proportional to the injected volume and this is maintained even with inclusion of pressure effects. In Figure 3.16 and 3.17, for thresholds T=0.1%, 1%, 10% and 20% the trends indicate good correlation and direct proportionality for thresholds T=0.01% and T=1%. In Figure 3.17, crossplots between estimated and actual net volumes for the thresholds T =10% and 20% are correlated, with calibration factors, y/x, of 0.53 and 0.12 respectively. The decreasing calibration factors as the threshold increases reflects expected pressure counter-effects which are concentrated at the wells, thereby impacting the extracted gross rock volume. Higher thresholds of T=10% and T=20% exclude amplitudes with partial saturations occurring further away from the wells thereby reducing the gross rock volume. Gross rock volumes of water geobodies around the wells are however jeopardised by the high pressures occurring at the wells (see Figure 3.18). The softening signals around the wells by countering the hardening water signal, contribute to the rock volume and this is reflected in the estimated net water volumes with poor calibration factors.

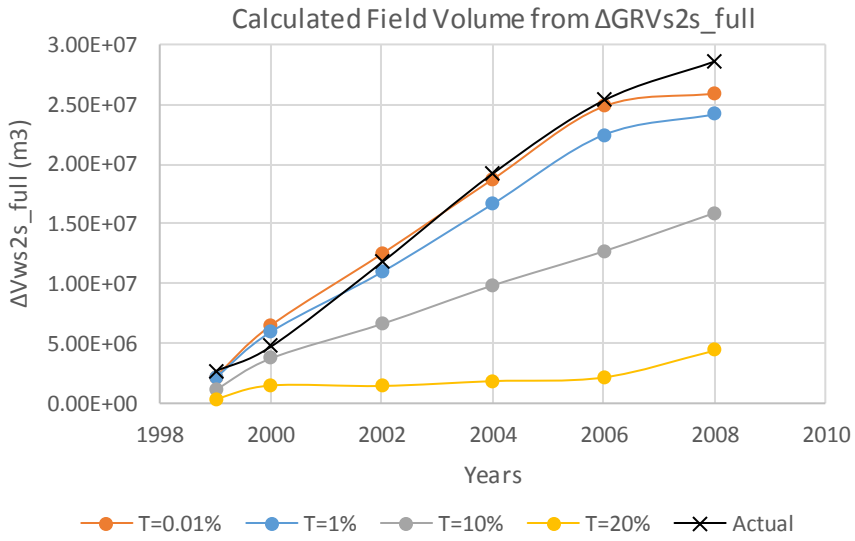

Figure 3.16: ΔGRVs2s_full - Estimated net water volumes from full synthetic seismic signal for all surveys and for thresholds, T = 0.01%, 1%, 10% and 20%.

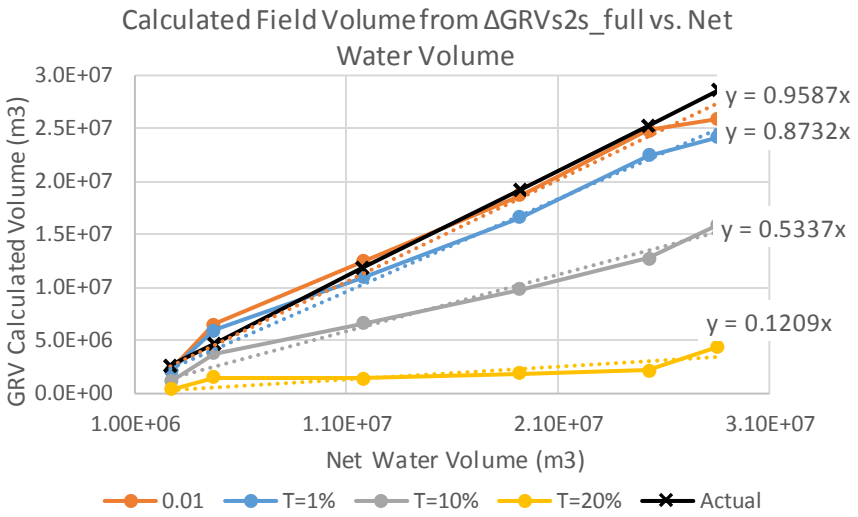

Figure 3.17: Crossplot of estimated net volumes from full synthetic seismic and actual net volumes for thresholds, T= 0.01%, 1%, 10% and 20%.

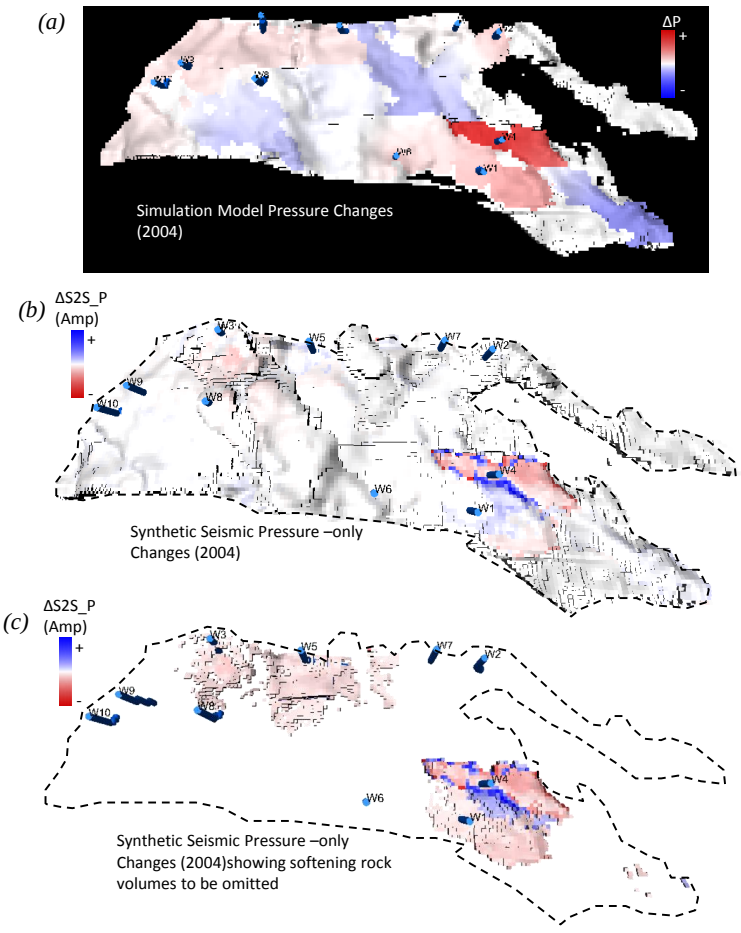

Figure 3.18: Top view of simulation model showing time-lapsed pressure changes for the year 2004. (b) Corresponding synthetic seismic pressure-only signal with softening signals surrounding injectors and (c) isolated softening signal geobodies around injectors.

3.5 Calibration of the Observed Seismic Data

With built confidence in direct proportionality between the 4D seismic response to increased water saturation and actual net water volumes, a calibration to the observed seismic can now be attempted. The four 4D co-processed seismic surveys available (1998, 2004, 2006 and 2008) have an average non-repeatability normalised root mean square noise metric (Kragh and Christie, 2002) of 29%, which means that 29% of the 4D seismic signal can be attributed to non-production related changes (e.g. seismic acquisition and processing elements like acquisition geometry and velocity models). Extending the approach from the synthetic seismic case, geobodies from the waterflooded zones are extracted for thresholds T= 0.1% of the maximum amplitude, T = 1%, 10% and 20%. Figure (3.17) shows the crossplot of the observed seismic estimate values with calibration factors of 0.1 – 0.5. The slight difference between the plots for T=0.1% and T = 1% infers the limit of the thresholds, thus implying that the discrepancy between the estimated volumes and the actual volumes is indeed related to noise and pressure effects.

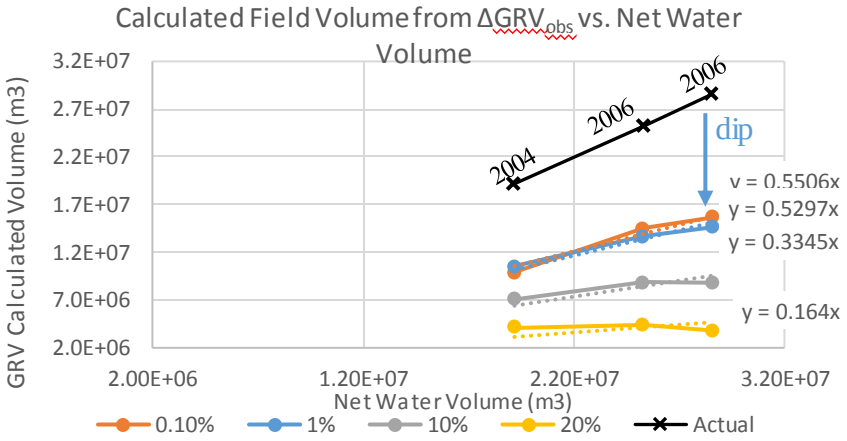

Figure 3.19: Cross-plot of observed seismic net volumes and actual volumes showing direct proportionality for thresholds, T= 0.1%, 1%, 10% and 20%.

Table 3.3: Percentage errors between the net water volumes estimated from the extracted field geobody compared to actual net water volumes for thresholds, T= 0.1%, 1%, 10% and 20%.

Observed Seismic % Errors - Field			
T= 0.1%	T=1%	T=10%	T=20%
-48.30	-44.90	-63.20	-78.60
-42.70	-45.90	-65.20	-82.60
-45.20	-48.80	-69.10	-86.70

In the observed seismic case, with an NRMS noise metric of 29%, the process of noise clipping to reveal more of the relevant hardening signal jeopardizes the volume-seismic proportional relationship as a substantial amount of the peripheral water volume's lower amplitudes were truncated as noise. This led to significant errors of up to -48.30% for a threshold T=0.1% and an error of -86.7% for T=20%. In addition to the muted increase in pressure around individual injectors, the dip in the trend (indicated in Figure 3.19) or all the thresholds for the third survey is as a result of the field-wide increase in average reservoir pressure given ten years of waterflooding and increasing reservoir support, severely reducing the seismic signal calibrated volume accuracy. Although the net volume estimation capability from observed seismic data is compromised, there is still a clear correlation between the estimated volumes and the actual volumes. This means that with the right choice of threshold and determined calibration factors via material balance, the extracted observed 4D seismic geobodies can be used in estimating injected volumes by applying the seismic-production data calibration factor. The high error levels highlight the importance of accounting for the pressure effect as part of the field-wide waterflooding seismic calibration exercise using seismic amplitudes, or applying a seismic calibration as a subsequent exercise to saturation-pressure separation.

3.6 Well-Centric Volumetric Seismic Signal Calibration

To mitigate the infiltration of complex field-wide interactions of counter-acting softening effects of pressure increase on the waterflooding hardening signal volumetric seismic calibration is carried out for an individual injector well. A well-centric seismic signal calibration allows for a controlled interpretation of the hardening signal related to waterflooding, omitting additional possible hardening effects of pressure depletion from producers nearby. The injector considered in this case was shut off after five years of continuous injection, one year before the first available monitor survey was shot in 2004 (see Figure 3.20). The well's operation activity ensures that it has a relatively isolated flood pattern and mostly dissipated injection pressure following a year of being shut-in. This leaves the total net injected volume approximately constant through the years the last two monitors 2006 and 2008 were shot. With the well completed in the oil leg outside the direct influence of the aquifer and given the short period of injection, the net volumes can be estimated from extracted geobodies of the hardening signal around the well.

Well-Centric Volumes from Synthetic Saturation-Only Seismic Data: Net volumes are estimated for the synthetic seismic signal case, to enable a calibration of the seismic signal based on the actual water-seismic response relationship. Following the field scale study for the saturation-only seismic signal calibration, estimates of volumes using thresholds of 0.01%, 1%, 10% and 20% of the maximum amplitude only varied slightly amongst all four thresholds. For the well-centric case, thresholds of T= 1% and T=10% are tested for volume estimate accuracy. Equation (3.1) and the corresponding mean properties from the simulation model are again used to calculate the net volume of water, $\Delta^{Vw_{s2s\_sw}}$.

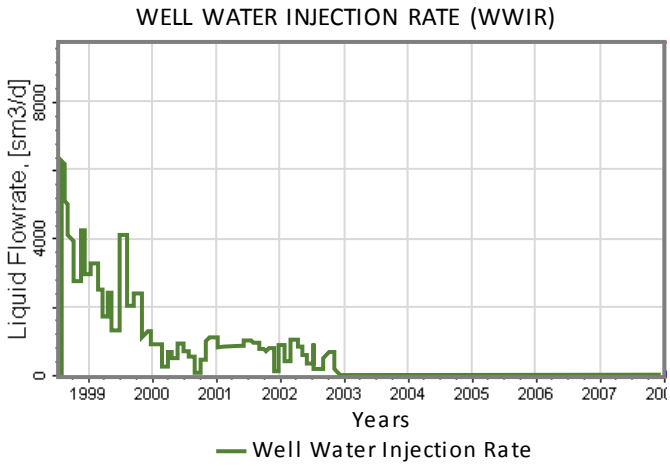

Figure 3.20: Well water injection rate

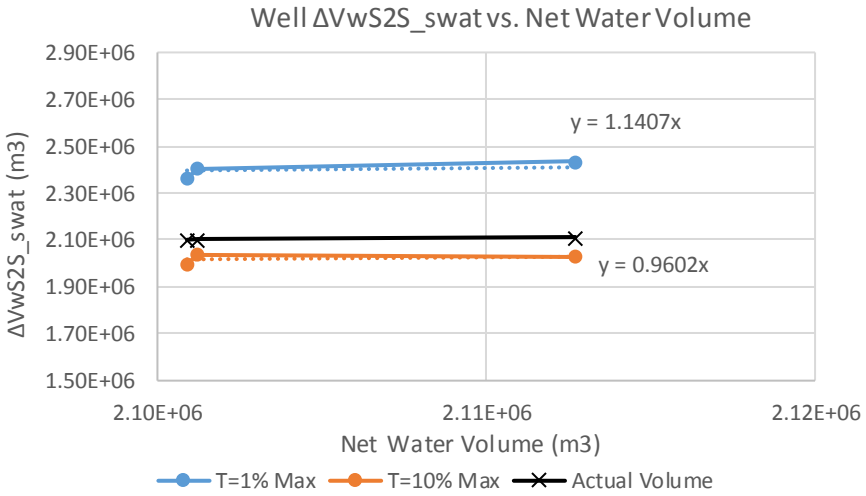

Figure 3.21: Crossplots of net water volume estimated from saturation-only geobody, ΔVw_{S2S_swat} and actual net water volumes for thresholds, T=1% and T=10%.

Figure 3.21 shows the crossplot of net volumes estimated from the synthetic seismic saturation-only geobody and the actual net water volume for the three available surveys. As the well stops injecting by the first survey, the volumes remain constant for both thresholds. Volumes from threshold T=10%, however, has a calibration (y/x) of 0.96 compared to 1.14 for T=1%. This indicates that the threshold of 10% of the maximum amplitude eliminates a realistic level of uncertainties associated with the seismic signal response (see section 3.4) such that the extracted geobody approximates the net volumes more accurately.

Well-centric volumes from observed seismic data: To define the spatial characteristics of the well-centric geology of the reservoir and probable limits of the sand bed(s) to be occupied by the waterflood, an analysis of the reservoir geology from the 3D seismic baseline and monitor volumes is carried out. This gives an understanding of the sand connectivity, faults or barriers and sand-shale laminae and how these evolve over time with the injection of water. Figure 3.22(a) 4D seismic map with the well location and intersection indicated. Figure 3.22 (b) shows the injector well cross-section views of the 3D seismic with clear depiction of the two relatively clean layers of sand (red troughs) interbedded with shale layers Figure 3.22(c) of the 4D cross-section, at the time of monitor 2004, shows the increased water saturation hardening signal at the perforations confined within the horizon and identified sand layers. This hardening signal is extracted as a volumetric seismic geoblob *(*visual seismic geobody object*)* shown in Figure 3.22(d). For water volume computation, the geoblob is depth-converted extracted and resampled to a very fine grid with cell dimensions of 3m by 2m by 1.4m (Figure 3.22(e)) in a bid to minimise the errors associated with grid orientation and grid size/shape. 4D seismic geobodies of the hardening signal corresponding to the water volume are then extracted with minimum thresholds of 5 – 10%.

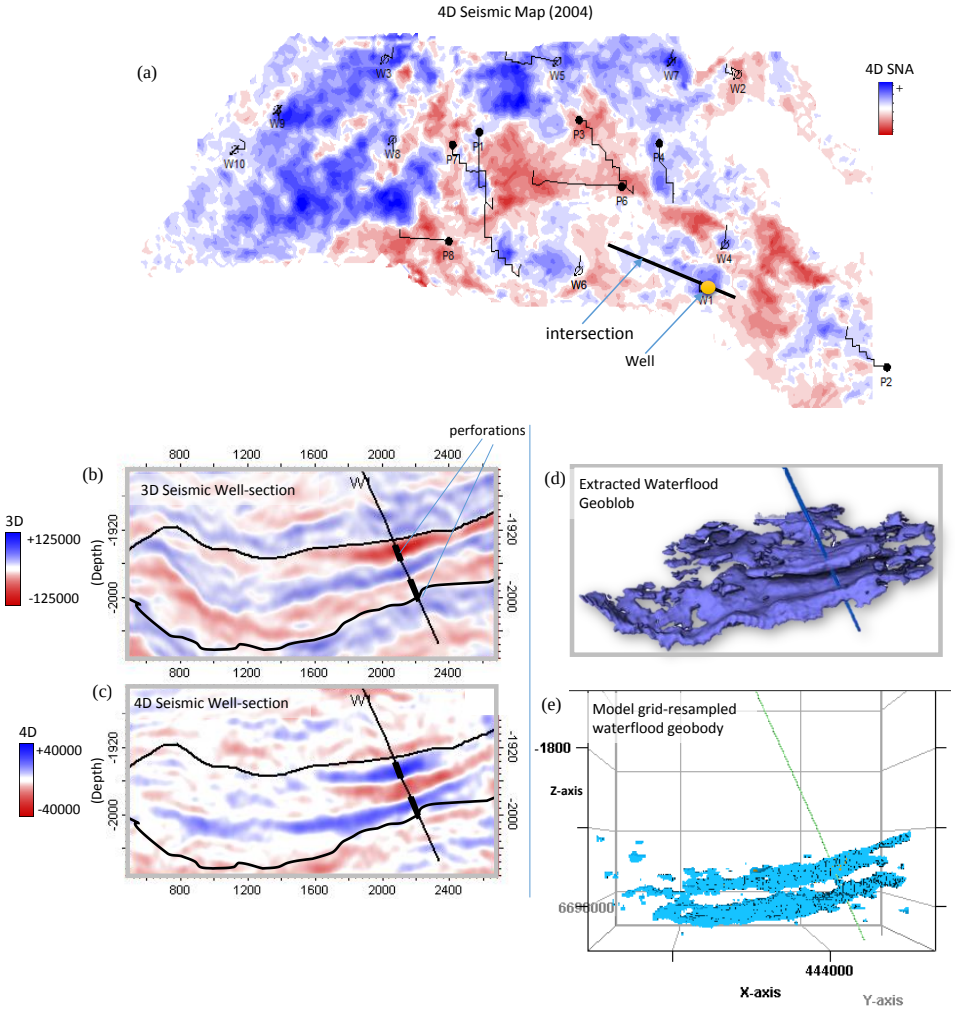

Figure 3.22: (a)4D seismic map showing well location and intersection (b)3D observed seismic cross-section showing sand layers - red peaks, (c) 4D seismic well cross-section showing well-centric hardening signal indicating injected water volumes (d) Extracted observed seismic geobody of waterflood from injector (e) Depth converted 4D seismic geobody resampled to fine grid for net water volume estimation.

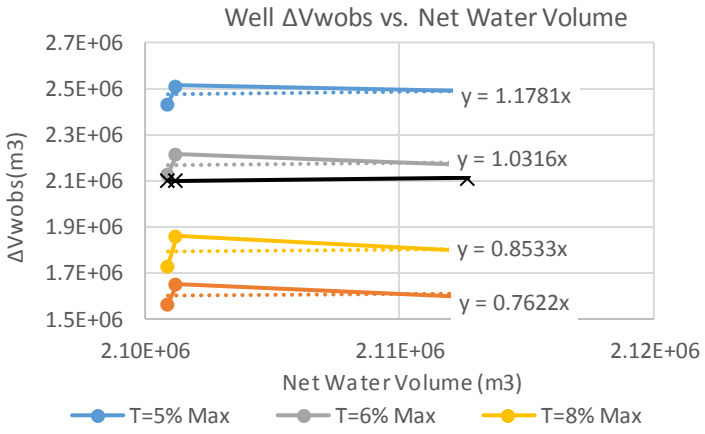

Figure 3.23: Crossplots of net water volume estimated from saturation-only geobody, ΔVwS2S_swat and actual net water volumes for thresholds, T=5%, 6%, 8% and T=10%.

As seen in Figure 3.19, the process of noise clipping to reveal more of the seismic signal jeopardized the volume-seismic proportional relationship as too much of the peripheral water volume's lower amplitudes were truncated as noise in the field-scale scenario. In the well-centric case, with a test of thresholds between 5 - 10%, the prescribed use of the 3D seismic sand-body filter for the waterflood allowed for more interpretation of the partly flooded areas, leading to estimated ΔVw_{obs} volumes with errors of only 1.26 – 5.16% for threshold T=6% as shown in Table 3.4.

Observed Seismic %Errors - Well				
4D survey	T= 5%	T=6%	T=8%	T=10%
2004	13.72	1.26	-21.30	-34.27
2006	16.44	5.16	-12.91	-27.24
2008	15.15	2.69	-17.65	-32.26

Table 3.4: Percentage errors between the net water volumes estimated from the extracted well-centric geobody compared to actual net water volumes for thresholds, T=5%, 6%, 8% and T=10%.

The exaggerated dip in the trend for all the thresholds for the third survey is again as a result of the field-wide increase in reservoir pressure as a result of 10 years of waterflooding and increasing reservoir support.

3.7 Uncertainties in the Seismic Signal Calibration

Seismic amplitude, a measure of acoustic impedance contrast between two layers is the most commonly used seismic attribute. In the case of a zero-offset trace, and where the reservoir characteristics apply (reservoir beds of a larger thickness than tuning thickness for example), the amplitude measured at the maximum peak or trough and its magnitude would give indications of the layer properties. In addition to the ambiguity in the timing of the towed streamer seismic survey with respect to the measurement of the exact net volumes of water in the reservoir when the seismic survey is shot, interpretation of the seismic signal and its subsequent calibration is subject to a number of uncertainties. Summarily, these are:

- Sensitivity of 4D seismic to changes in water saturation.
- Competing 4D signals like accompanying counteracting increased pressure effect or gas exsolution obscuring the water saturation signal.

- Wavelet interference effects, varying bed thicknesses and tuning possibilities.
- Accuracy of the velocity model used in time-to-depth conversion.
- Static reservoir parameters (i.e. variations reservoir characteristics like sand-shale balance, porosity and permeability and how they influence the waterflooded pattern), as average values of these are used in the calibration calculations.
- Processing/imaging effects: for the post-stack data, the convolutional model applied in the processing of the seismic zero-offset traces does not accurately transform migration artefacts or multiples.
- 4D seismic noise.
- Assumptions behind thresholding and the chosen thresholds.

Given the breadth and variation of these uncertainties, calibrating the seismic signal to a fine precision is challenging. However, with a physics-driven approach and an application of engineering judgment/efficiency as demonstrated in this chapter, reasonable approximations and quantitative correlations between the seismic signal and reservoir volumes can be achieved.

3.7.1 Temporal Seismic Resolution in Volumetric Calibration

Reservoir geological changes (lithology, pressure, changes in pore fluid, cementation, porosity changes) influence seismic impedance and ultimately, the seismic amplitude. Using amplitudes in 4D seismic interpretation and volumetric calibration, however, subjects interpretation to the limits of seismic vertical resolution. As seismic signal is an interaction of the wavelet and the reflecting interfaces, the seismic bandwidth and wavelet shape defines the limits to which reservoir strata thicknesses can be resolved.

A sand bed is defined as thin when its thickness is less than a quarter of the seismic wavelength, $\frac{\lambda}{4}$ (Widess, 1973). Contrasts in the lithology can result in misinterpretation as reflections from the interface where the wavelet length is larger than the length of impedance contrasts would cause interference of the seismic signal. With this phenomenon, different combinations of impedance and thickness could be resolved into the same seismic response for thin beds. In addition to possible interference, the natural decrease in frequency in seismic data and the increase in velocity with depth all contribute

to uncertainties in volumetric three-dimensional seismic calibration. The Wedge model (Widess, 1973) is typically used to analyse tuning thickness, vertical resolution and wavelet interference for a wedge shaped low impedance section. The seismic response for a wedge model of a sand layer encased in shale, with reflection coefficients at the top and bottom of the wedge of equal but opposite polarity, is shown in Figure 3.21(a). The positive standard polarity wavelet used to model the seismic response is shown in (b) with the tuning curves in (c). The red and blue curves show how the amplitude changes with actual and apparent sand thickness. While the amplitude decreases as the sand thickness reduces, the apparent sand thickness remains constant below the tuning thickness (15ms in the figure). Conversely, interpretation of apparent thickness using peak-to-trough separation for bed thicknesses above tuning thickness would be underestimated (between 15ms – 28ms in (c)).

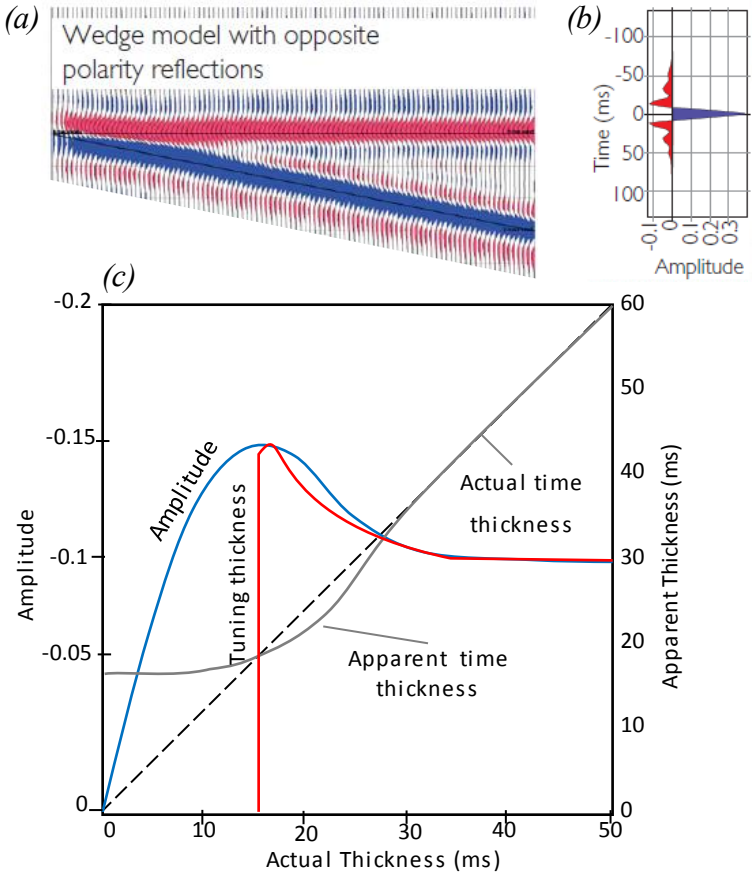

Figure 3.24: (a) Wedge model with opposite polarity reflections (b) applied wavelet (c) tuning curves showing apparent thickness relationship to true thickness (After (Simm et al., 2014).

Given the presence of relatively thin beds in this field, a survey of the average resolution of the waterflooded sand beds was carried out. Excluding the aquifer, the waterflooded sand bed thicknesses range between 25 – 50 m. The expected resolution of the layers given the low-frequency seismic signal was investigated to analyse how the apparent seismic thickness compares to the true thickness of the reservoir beds. This was done by convolving the extracted Schiehallion wavelet with predicted acoustic impedance differences. The Schiehallion coloured inversion extracted wavelet is a quadrature phase wavelet of 24Hz peak frequency and wavelength 128m. As shown in Figure 3.26 and following the tuning curves interpretation in Figure 3.25, for bed thicknesses of 10m and 25m, there is an overestimation of the apparent thickness compared to the true thickness, and an underestimation of amplitudes for beds of thickness 50m – 150m.

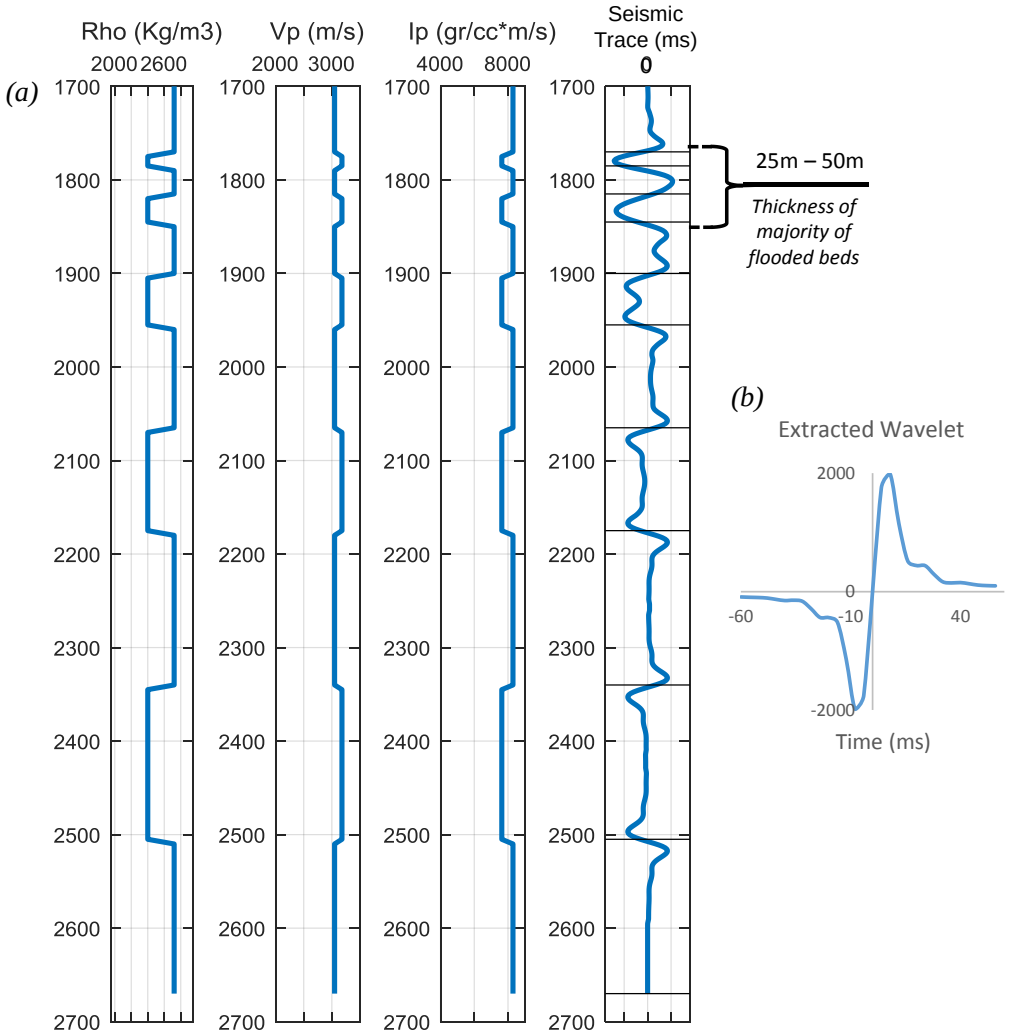

Figure 3.25: (a) Density, velocity and impedance logs with corresponding seismic trace to demonstrate tuning potential for a range of sand bed thicknesses occurring in dataset (b) extracted wavelet used to generate trace.

The over- and underestimation of the amplitude of the sand bed layers contribute further uncertainties in the estimation of volumes using the interpretation of seismic amplitudes for waterflooded rock volumes.

3.8 Summary

The success of volumetric seismic signal calibrations using seismic amplitudes in addition to being dependent on the level of experience of the interpreter is subject to the nature of the dataset and the quality of the seismic data. It produces more detailed seismic interpretation of the subsurface but can be data intensive and time-consuming. The use of 4D seismic data quantitatively is greatly influenced by defined simulation-synthetic seismic model relationships as a bridge to understanding the observed seismic and in setting signal thresholds and consequent clustering algorithms. The study highlights the composite errors that evolve through these processes and directly play a role in the interpretation of the observed seismic volumes. An understanding of these errors, their magnitudes and relationships are important for accurate quantitative interpretations and incorporating these would effectively improve the involved reservoir management activities like history matching and model updating.

Net water volumes computed by the reservoir simulation model differed from the actual net water volumes by $\pm 2\%$. This begins the evolution of error propagation from actual net injected water volumes to the seismic interpreted water volumes. For a saturation-only seismic signal, errors of estimated net volumes double to an average of $\pm 4\%$, with increasing error as net volume of water increases given the spatial growth of partially saturated rock volumes eliminated by the threshold. The proportional relationship of amplitudes to increased water saturation however, was validated with an average calibration factor of 0.96 for a range of thresholds for the synthetic seismic saturation-only signal. For the full seismic signal including the counter-acting pressure signal, the calibration factors for the estimated net water volumes from the synthetic seismic signal decreased as the threshold increased. This aligned with the understanding that the injected pressure effects are concentrated at the wells and thus with the increased water saturation more of the saturation signal is truncated as the threshold increases. The well-centric seismic signal calibration method of pre-defining the near well sand facies significantly reduced errors from the field scale calibration by an average of 67% and gave indications

of suitable thresholds (T=6% - 7%). Seismic signal volumetric calibration, however, requires field specific interpretation with careful accounting of the effects of propagated errors on the final 4D seismic interpretation.

In addition to the uncertainty in the timing of the seismic survey with respect to the exact measurement of net volumes of water in the reservoir at a particular time, interpretation of the seismic signal and its subsequent calibration is subject to other uncertainties like: 1) Degree of sensitivity of the 4D seismic to changes in water saturation. 2) Competing 4D signals (especially the counteracting increased pressure effect dimming the water saturation signal), 3) Wavelet interference effects, 4) Accuracy of the velocity model used in time-to-depth conversion and uncertainties in the horizon picking. 5) Averaged static reservoir parameters, 7) Processing/imaging effects, 8) 4D seismic noise. The breadth and variation of these uncertainties make calibrating the seismic signal to a fine precision challenging. However, with 3D seismic geology interpretation, a physics-driven approach and an application of engineering judgment/efficiency, reasonable approximations and quantitative correlations between the seismic signal and reservoir volumes can be achieved.

Chapter 4

Waterflooding Performance Evaluation

In this chapter, waterflooding performance metrics to measure displacement efficiency and directionality are defined using 4D seismic data. The performance metrics are applied to the Schiehallion dataset and used to gain an understanding of the field wide displacement efficiencies. Further interpretation of the performance metrics is done using the Capacitance Model, leading to improved waterflood performance management on the field.

4 Waterflooding Performance Evaluation

4.1 Reservoir Surveillance to Monitor Waterfloods

A waterflood campaign is considered successful when it achieves its designed objectives despite high costs of implementation and within economic limits. This is in addition to increasing production by maintaining reservoir pressure and oil sweep and minimising water production handling costs while optimising environment safety (Palsson et al., 2003). The engineering success of waterflooding is typically measured in terms of the overall recovery factor which is dependent on even volumetric and displacement sweep efficiencies. The uniformity of these sweep efficiencies is inhibited by reservoir heterogeneity. This means that with the uncertainty of the heterogeneity of the subsurface, the accuracy of achieving waterflooding objectives is not as high as hoped. This could stem from – lower permeability zones less exposed to flooding leading to large remaining volumes or bypassed zones, water injectivity decline as a result of the failure in water injection facilities or poor water quality; water injecting conditions causing high-permeability streaks and fractures thus re-directing the water propagation or a loss of water volume caused by injecting pressures breaching the reservoir limits. Given these conditions, reservoir surveillance for reservoirs under waterflooding is a necessity to improve the understanding of the waterflooding, allowing for timely, optimum decision making regarding diverting the waterflood from preferential flow zones or possible modifications of the present waterflooding strategy to improve targeted objectives, development of infill drilling plans or alternative hydrocarbon recovery processes.

In the industry, statistical and analytical methods of evaluating waterflooding performance using the historical injection data and reservoir simulation model are typically applied at different levels: well, pattern or field evaluation (Atabay et al., 2012). Waterflooding recovery efficiency is a good performance indicator and describes the volume of oil produced from the reservoir by injected water (Chierici, 1995; Smith and Cobb, 1997). For a full field and a reservoir that has not yet fallen below reservoir bubble point pressure (hence there has been no gas exsolution), the cumulative volume of oil produced via waterflooding, N_p, at a particular time, t, is given as (Chierici, 1995),:

$$N_p(t) = V_v(t)\varphi\left\{\frac{1 - S_{wi}}{B_{of,i}} - \frac{\overline{S_{or}}(t)}{B_{of}[p(t)]}\right\} \quad (4.1)$$

where Np is Volume of oil produced, V_v is swept rock volume, φ is porosity, S_{wi} is initial water saturation, $B_{of,i}$ and $B_{of,i}[p(t)]$ are initial oil formation volume factor and oil formation volume factor at pressure, p, at time, t, and S_{or} is oil saturation.

If initial volume of oil, *N*, is given as:

$$N = V_R\varphi\frac{1 - S_{wi}}{B_{of,i}} \quad (4.2)$$

Recovery efficiency, E_R at time, t, is:

$$E_{R,o}(t) = \frac{N_p(t)}{N} = \frac{V_v(t)}{V_R}\left\{1 - \frac{B_{of,i}}{B_{of}[p(t)]} \times \frac{\bar{S}_{or}(t)}{1 - S_{wi}}\right\} \quad (4.3)$$

where, V_R, is the gross rock volume and volumetric efficiency, E_v, the fraction of reservoir pore volume swept by the injected water at time, t, is:

$$E_v(t) = \frac{V_v(t)}{V_R} \quad (4.4)$$

and displacement efficiency, E_D, is the fraction of oil that existed in the pore space prior to the waterflood which has been displaced from the swept volume at time, t:

$$E_D(t) = \frac{1 - S_{wi} - \bar{S}_{or}(t)}{1 - S_{wi}} \quad (4.5)$$

so that the field recovery efficiency, E_R, becomes:

$$E_{R,o}(t) = E_V(t) \times E_D(t) \quad (4.6)$$

The displacement efficiency depends on the relative permeability and capillary forces of the reservoir formation and the contrasting viscosities and densities of water and oil.

4.2 Quantitative Seismic Sweep Efficiency

The qualitative capability of 4D seismic signal in evaluating waterflooding sweep is well published, detailing the attributes of determining areas of bypassed oil or lost volumes (Kolstoe et al., 2008) as well as the shape of waterflood drainage pattern and field-scale

sweep efficiencies. The quantitative characteristics of 4D seismic in determining waterflooding performance, however, are less common given the challenges of accurately calibrating the resolved seismic signal to production volumes. With signal calibration from Chapter 3, and using reservoir simulation and seismic forward modelling tools, estimates of waterflood pattern and propagation direction towards a quantitative performance evaluation can be obtained from 4D seismic data.

The change in dynamic properties of the reservoir as water is injected in the reservoir is reflected as seismic attribute contrasts between the baseline pre-production and the time-lapsed monitor seismic surveys. This correlation drove the studies by (MacBeth et al., 2006), Falahat et al. (2011), and Alvarez and MacBeth (2014) leading to the formulation of relationships between seismic and 4D seismic data. These relationships describe the proportionality of dynamic changes in seismic amplitudes to the dynamic changes in production volumes and is reliably done via a reservoir simulation model with a high history match quality. Falahat et al. (2011) for gas exsolution, derived the relationship between change in-situ gas volumes, S_g within an area, $\sum$, and the time-lapsed time-shift, Δt, as a result of the presence of S_g as:

$$\Delta V_{gas} = \left\{ S_g \times \phi \times NTG \frac{VV'}{2(V - V')} \right\} \Delta t(x, y) \Delta x \Delta y \qquad (4.7)$$

with:

V: *seismic wave velocity with no gas*

V': *seismic wave velocity with gas saturation, S_g, present.*

φ: *porosity*

NTG: *Net-to-gross*

Integrating equation (4.7) over the defined area, $\sum$, an estimate of the total time-lapsed volume of injected gas is derived. This applies in reservoirs that are relatively homogenous with geological properties varying only slightly within the area, $\sum$, so the average of φ and S_g can be approximated by their spatial integration. Integration of the time-lapsed time-shift changes, Δt, at a certain time is then shown to be directly proportional to volume of injected gas at the same elapsed time in the equation:

$$V_{gas} = V_{gas}(initial) + \left\{ S_g \phi_{eff} \frac{VV'}{2(V - V')} \right\}^{mean} \iint_{\Sigma} \Delta t(x,y) dxdy \tag{4.8}$$

For a waterflooding scenario, Alvarez et al., (2014) defined the change in seismic attribute, ΔA, as:

$$\Delta A = C_s \Delta S_w - C_p \Delta P \tag{4.9}$$

with ΔS_w and ΔP as changes in water saturation and pore pressure, and C_s and C_p as constants describing the relationship of pore pressure and saturation changes with the gross change in seismic amplitude. Extending this relationship, for a saturation dominating seismic signal where the pressure effects are not significant (in equation (4.9) $C_p \Delta P = 0$), the change in seismic amplitude ΔA as a result of water injection is shown to be directly proportional to the water saturation change, ΔS_w.

$$\Delta A \propto \Delta S_w \tag{4.10}$$

This relationship also detailed in Chapter 3 is the basis on which the waterflood performance metrics are formulated.

4.2.1 The Seismic Displacement Efficiency Metric

Water injected into the oil leg of a reservoir forms a drainage pattern around the injector well that is visible in a 4D seismic amplitude map as an impedance hardening event. The spatial extent of this drainage pattern visible on the 4D seismic data defines a boundary within which the efficiency of the water injection can be evaluated (Figure 4.1(a)). This efficiency measure is achieved by linking the integral of amplitudes evaluated within this boundary at the time of the baseline survey (A), with the amplitude level change at the time of the monitor surveys ($A + \Delta A$). Thus, for a well-centric drainage pattern, the displacement efficiency around the well within the swept volume would be defined as the fraction of oil displaced from the pores within the defined drainage area:

$$E_D = \frac{Fraction\ of\ Oil\ Displaced}{Volume\ of\ Oil\ before\ flooding} = \frac{1 - S_{wi} - S_o}{1 - S_{wi}} \tag{4.11}$$

where S_{wi} is initial water saturation and ROS is remaining oil saturation. This allows us to connect the average amplitudes within the defined drainage boundary directly to the displacement efficiency of the reservoir within the same boundary, following the proportionality of the change in water saturation, equation (4.10) to the integral of the change in amplitude within the same boundary:

$$E_D \propto \frac{(A + \Delta A) - A}{A} \propto \frac{\Delta A}{A} \tag{4.12}$$

and the change in saturation within the boundary then is proportional to the integral of the change in amplitudes within the boundary:

$$\Delta S_w \propto \beta \int \Delta A \, dxdy \tag{4.13}$$

where, E_D is displacement efficiency, ΔS_w is change in water saturation, A is amplitude and β is the calibration factor for the relationship between amplitude and water saturation.

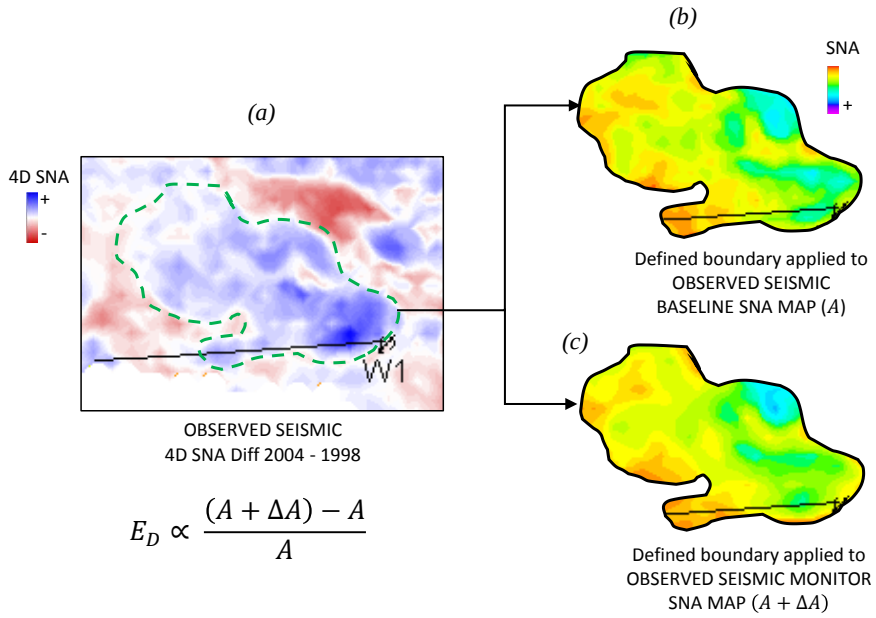

Figure 4.1: Evaluation of seismic displacement efficiency using the flood pattern boundary defined from 4D seismic. (a) 4D hardening response around the injector in observed seismic (b) and (c) application of the boundary to the baseline survey.

To obtain a precise reservoir measure, the effects of seismic wavelet interference must be eliminated. This process is achieved by reservoir simulator to seismic calculation. (Falahat et al. (2011); Falahat (2012)), proved the relationship between pressure and saturation changes to 4D seismic signals interpreted from seismic attribute maps, by describing the

strong correlation of the adaptive scaled 4D seismic signal. His work showed that 4D seismic signatures scaled by reservoir pore volumes are better correlated to reservoir changes interpreted by 4D seismic, following the principle that the reservoir thickness occupied by reservoir changes of pressure, gas and water saturation vary according to the nature of the reservoir. As effective pore volume, PV eff= $h \times \varphi \times NTG$, where h is the depth of the reservoir, φ is the reservoir sand porosity and NTG the sand-shale ratio of the reservoir, scaling the 4D seismic signature by the pore volume in map attributes thus relates the 4D seismic signal to the actual reservoir volume of change effecting the 4D seismic signal. He went on to show the correlation between the pore volume scaled changes in pressure, water saturation and gas saturation from the simulation model to the corresponding seismic forward modelled amplitude changes shown in Figure 4.2. Coefficients of determination, R2 = 0.76, 0.72 and 0.78 for the correlation of amplitude changes to pore-volume-weighted changes for pressure, water saturation and gas showed improvements compared to coefficients of determination of R2 = 0.64, 0.59 and 0.66 and R2 = 0.59, 0.51 and 0.62 for depth-averaged and thickness scaled maps respectively. This established the pore-volume-weighted maps as the most representative surface average of reservoir changes which is well correlated to the 4D seismic attribute maps.

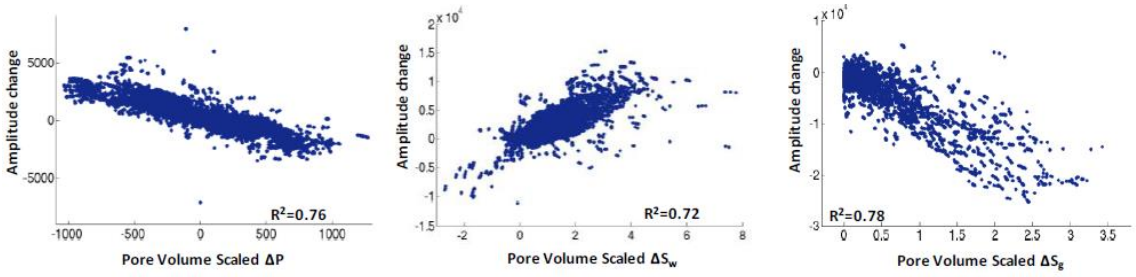

Figure 4.2: (a), b) and c) Crossplots for Synthetic seismic amplitude change versus the pore volume scaled pressure, water saturation and gas saturation change respectively (Falahat, 2012).

Since the volume of water injected is known and is an input to the simulation model, the same theory of drainage pattern boundary efficiency as applied for the seismic maps can also be applied to pore-volume weighted saturation maps from the simulator and the corresponding synthetic seismic amplitude maps at the baseline and monitor times (Figures 4.3(a), (c) and (b), (e)), to give the corresponding displacement efficiencies E_D *(syn) and* E_D*(sim).* This defines the relationship between the seismic and the simulation model in the form of a correction factor:

$$\alpha = E_{D(sim)} / E_{D(syn)} \tag{4.14}$$

The derived factor is then used to correct the observed seismic displacement efficiency to the true value of $E_{D(obs)}$.

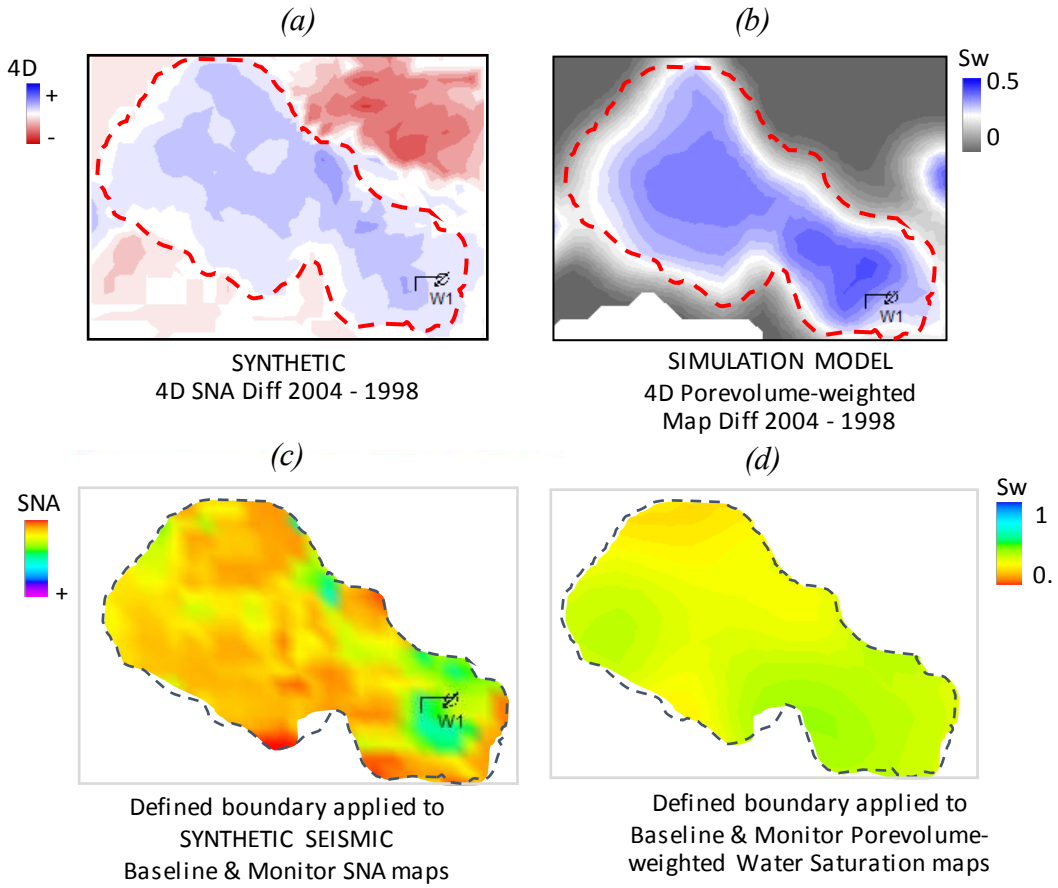

$$\frac{1 - S_{wi-}S_{orw}}{1 - S_{wi}} = \frac{S_{w-}S_{wi}}{1 - S_{wi}}$$

Figure 4.3: Calculation of relationship between displacement efficiency in the synthetic seismic and simulation model using the defined flood pattern boundary.(a) and (b) Time-lapsed flood pattern around the injector in synthetic seismic and simulation model, (c)

4.2.2 Flood pattern shape and directionality Metric

A common concern in waterflooding scenarios is premature water breakthrough. Timely mitigation of this ensures optimized reservoir pressure support and water flooding. The waterflood drainage pattern is heterogeneous and propagates in the direction of least resistance influenced by the static properties of geological architecture (eg. turbidite

channel character, permeability distribution) and dynamic properties like relative permeability and in response to well pressure gradients. A measure of the drainage pattern heterogeneity in the form of an estimated direction of the preferential flow path is a useful performance metric that immediately provides information about the reservoir heterogeneity and how that injector would interact with producers. From a thresholded, saturation-dominating, 4D seismic amplitude map such as that in Figure 4.4, the aspect ratio of the delineated flood pattern (A:B) and the angle, θ, of the dominant direction can be determined as a fast waterflood propagation direction indicator.

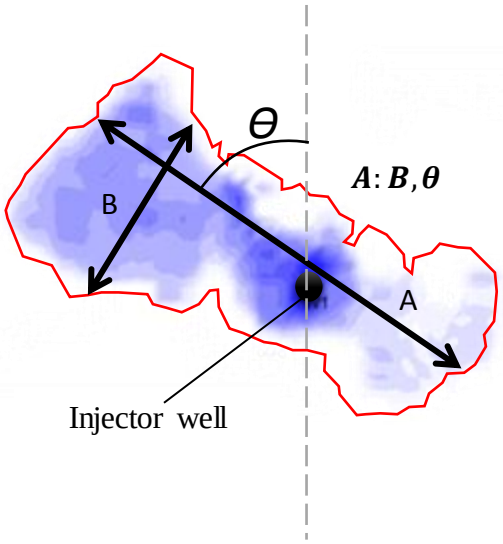

Figure 4.4: Seismic Pattern Directionality - aspect ratio and angle of preferential propagation direction.

The validity of the application of both metrics depends on:

1) Early water injection - Flood pattern from injector is relatively isolated;
2) Visible and continuous flood pattern interpretation from seismic;
3) Injection wells are at a distance that ensures that flood patterns are not interconnecting;
4) Increased saturation seismic signal dominates contrasting increased pressure signal;
5) Quality of seismic data sufficient to allow 4D drainage pattern interpretation;
6) All injector well completions are functioning as designed.

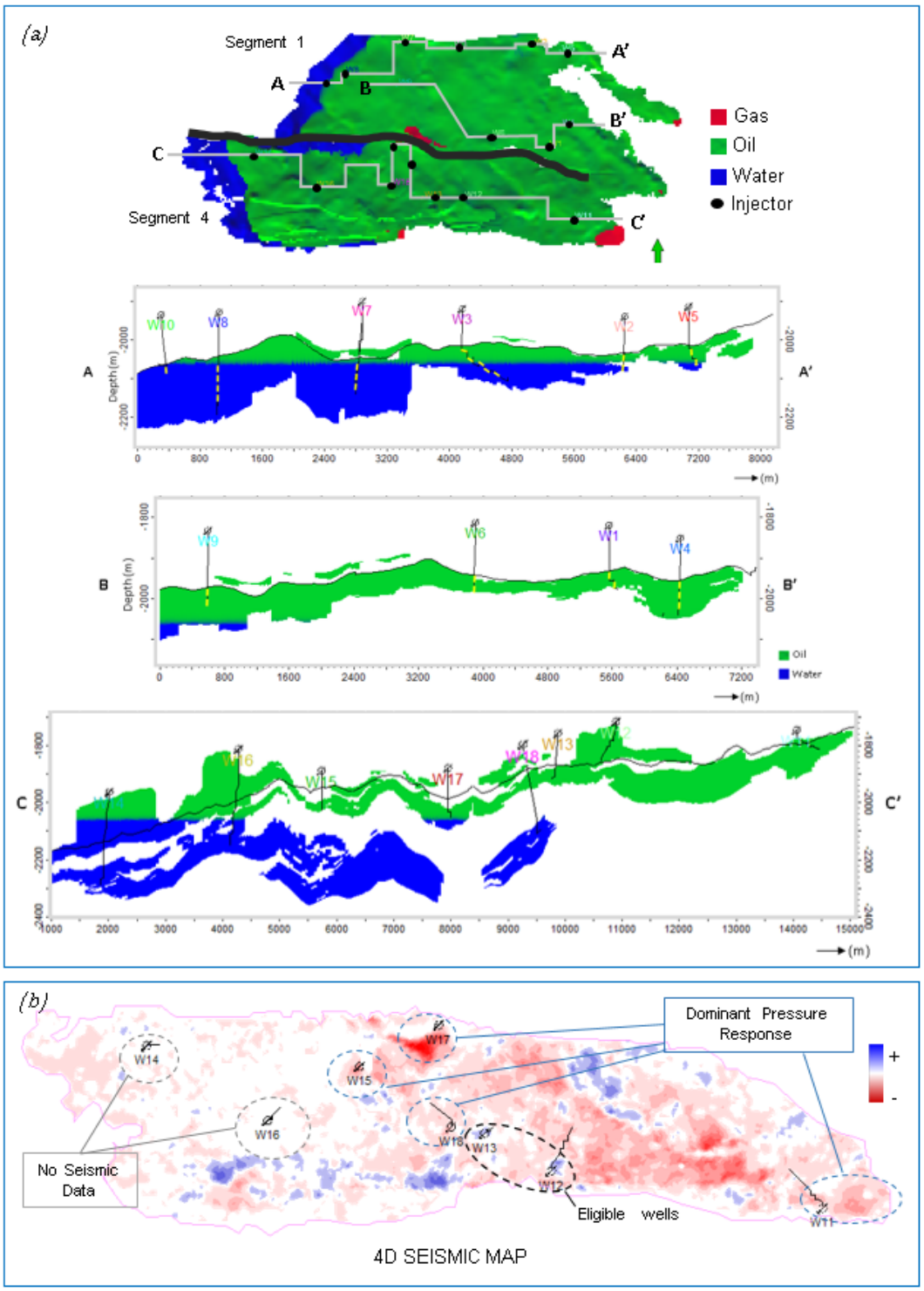

Figure 4.5: (a) Simulation model showing oil and/or water leg in which injectors were completed via cross-sections of injectors through planes A-A', B-B' and C-C'. (b) 4D Seismic map showing Segment 4 injectors with noncompliant conditions of being over-pressured, lacking data.

4.3 Calculating the Performance Metrics

The water flooding performance evaluation was carried out on the previously described Schiehallion field. The Schiehallion field is divided into four segments by E-W faults. Divided between the available two of the four segments are twenty injection wells that are analysed. The injectors were analysed for compliance to the performance metrics conditions. Of all twenty injectors in the field, In Segment 1, shown in Figure 4.6(a) through intersection A-A', Wells W7, W8 and W10 are totally completed in the aquifer, while Wells W3, W2 and W5 are completed in both the oil and water legs. The cross-section through intersection B-B' shows Wells W6, W1, Well W9 and W4 completed in the oil leg. As this metrics are based on the hardening response as a result of the fluid substitution - oil to water, wells completed in the aquifer do not show an obvious seismic response, thus eliminating Wells W7, W8 and W10 which are in the aquifer, leaving 7 wells in Segment 1. This highlights that for an amplitude map-based study, we may expect possible exaggerations of the hardening response around wells also completed in the water leg. In Segment 4, most of the water injectors were completed in the oil leg, however, wells W11, W15, W17 and W18, were strongly pressured, creating a counteracting impedance softening response that is completely dominated the water saturation response and as a consequence had incomplete data sets. The entire Segment 4 within 10 years of injection was significantly pressured (>150bar pressure gradient from Baseline). This limited the wells assessable using these "seismic performance metrics" to Wells W12 and W13 which have heavily pressure dominated 4D flood patterns.

Well	Monitor Survey	Comments
W1	2004	Injection from 1998 – 2003, 2004 is the earliest available survey
W2	2004	Proximal producer began producing water at end of 2003
W3	2004	Completed in both oil and water legs, water breakthrough at nearest producer in 2003
W4	2004	Nearest producer water cut in 2005
W5	2004	Completed in both oil and water legs and flood pattern intersects with Well W2. Water breakthrough at nearest producer in 2003
W6	2004	Injected from 2003 – 2004
W9	2008	Injection only began in late 2007
W12	2004	Injected from 1998 – 2008. Water cut in nearest producer in 2003
W13	2004	Injected from late 2003 – 2008

Table 4.1: List of wells assessed and 4D seismic surveys used to assess performance.

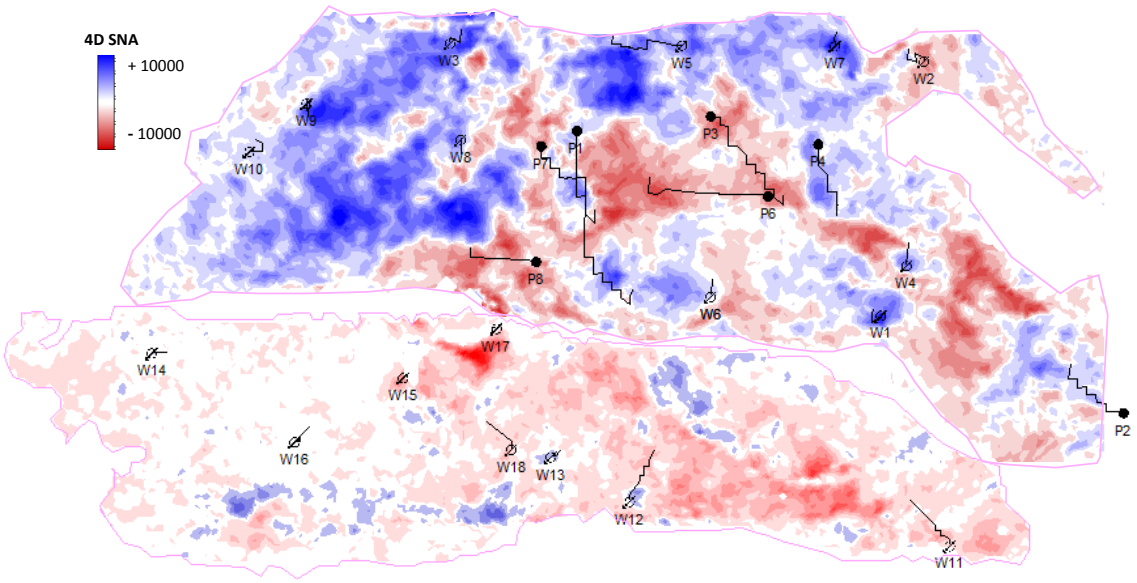

Figure 4.6: 4D Seismic Map showing waterflood patterns around injectors at timestep 2004 -1996.

The Seismic Performance Metrics are dependent on strong hardening signals defining the drainage pattern around injectors on 4D seismic amplitude-maps. As water injection triggers these contrasting effects, instances where pressure dominates and where there is gas exsolution would counter the validity of the metrics. Therefore, the metrics would only be applicable where the water saturation signal dominates and other individual effects (see Chapter 2) are sufficiently small and can be considered as noise. The top and base horizons for the main T31 reservoir were used to create seismic attribute surface maps for the respective 4D seismic data volumes (Figure 4.7 shows the 4D seismic map for 2004 - 1998). The corresponding simulation maps were generated along the same horizons, tying the 4D seismic maps to representative layers in the simulation model. According to equation (4.12) – (4.14), Displacement efficiency for the synthetic and observed seismic cases are calculated for the nine applicable wells listed in Table 4.1 from the integrals of amplitudes for both baseline and monitor surveys, as well as the displacement efficiency for the simulation model using the water saturation equation. For calibration, the relationship between the seismic and simulation values is estimated with the calibration factor, α, with which the observed seismic displacement efficiency value is corrected. The calculated Seismic Displacement efficiencies are shown in Table 4.2. Figure 4.8 and 4.9 show how the trends compare for observed seismic, synthetic seismic and simulation model displacement efficiencies, and how the calibrated displacement efficiency compares to the simulation model (considered the "known" displacement efficiency).

WELL	DISPLACEMENT EFFICIENCY			Corrected ED	COMMENTS
	OBSERVED	SYNTHETIC	SIMULATION		
W1	0.22	0.20	0.30	0.32	Completed in oil leg
W2	0.32	0.17	0.58	1.12	Completed in oil & water leg
W3	0.22	0.25	0.37	0.32	Completed in oil & water leg
W4	0.22	0.18	0.33	0.38	Completed in oil leg
W5	0.14	0.15	0.37	0.36	Completed in oil & water leg
W6	0.18	0.11	0.38	0.63	Completed in oil leg
W9	0.32	0.21	0.32	0.78	Completed in oil & water leg
W12	0.08	0.36	0.32	0.09	Saturation signal severely dampened by high pressure
W13	0.08	0.02	0.30	0.18	Saturation signal severely dampened by high pressure

Table 4.2: List of injectors showing calculated Observed seismic, synthetic seismic and simulation model displacement efficiencies as well as derived seismic displacement efficiencies for the wells.

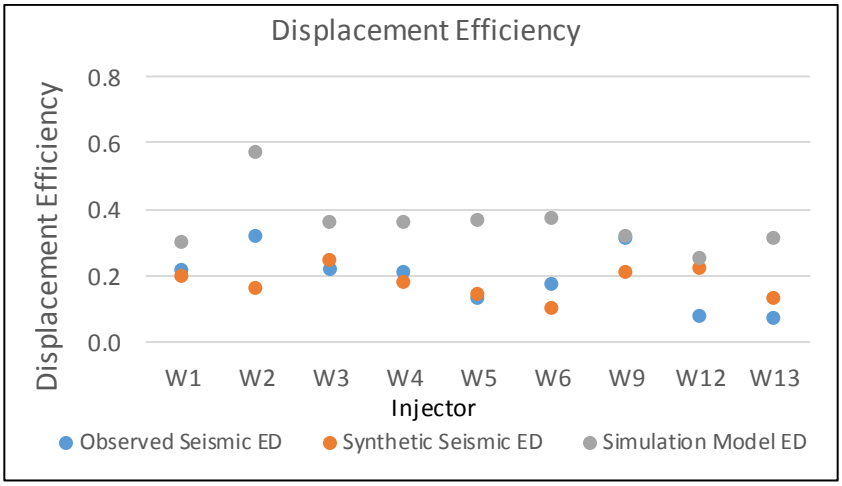

Figure 4.7: Observed seismic, synthetic seismic and simulation model displacement efficiency for all wells (a). Blue – observed seismic, Orange – synthetic seismic, Grey – simulation model.

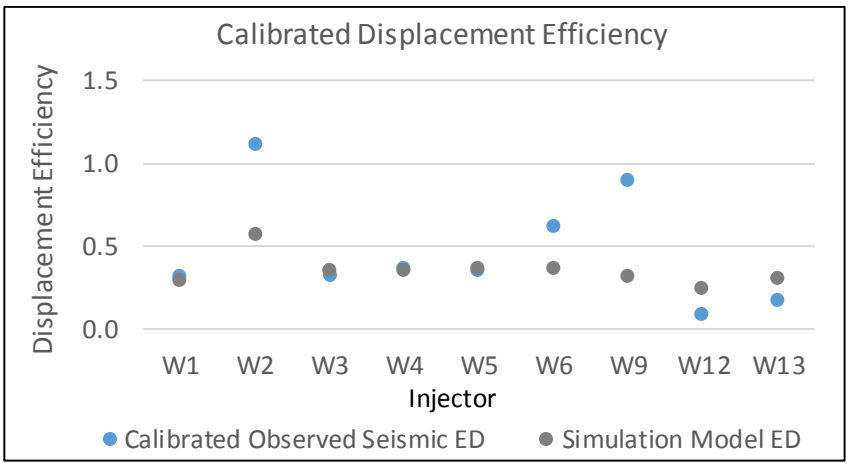

Figure 4.8: Corrected displacement efficiency for observed seismic and simulation model.

	WELL	Aspect Ratio, Θ
1	W1	1.94, -78°
2	W2	1.06, -63.46°
3	W3	1.85, -59°
4	W4	1.45, -72°
5	W5	2.46, -147°
6	W6	1.01, -43°
7	W9	3.36, 90°
8	W12	-
9	W13	-

Table 4.3: Calculated seismic directionalities

Charts in Figure 4.8 and 4.9 show reasonable agreement between observed, synthetic and simulation model displacement efficiencies (Figure 4.8), with some disagreement in wells W2, W3, W5, W9, W12 and W13. Wells W2, W3, W5, and W9 were completed in both water and oil legs. The presence of the aquifer in wells completed across the oil-water contact increase the wells susceptible to uncertainties in the well-centric 4D seismic interpretation due to impedance change contributions unrelated to the water injected from the injector, from the depth averaged map effects of aquifer changes (changes in pressure or influx from injector). Wells W12 and W13 have dominating pressure responses which significantly obscure the increased water saturation response and thus the seismic displacement efficiency. Information from all the derived metrics (shown in *Table 4.2 and 4.3)* are superimposed on the field map, together with seismic amplitude in Figure (4.9). This helps to understand the relation between the pattern of sediment deposition and injector performance. There is a consistency between the direction of the water flow and channel alignment. The relatively low values of efficiency (approximately 9-18% after nearly six years of injection) in wells of the highly pressured segment of the reservoir are a clear indication of the counteracting pore pressure effects.

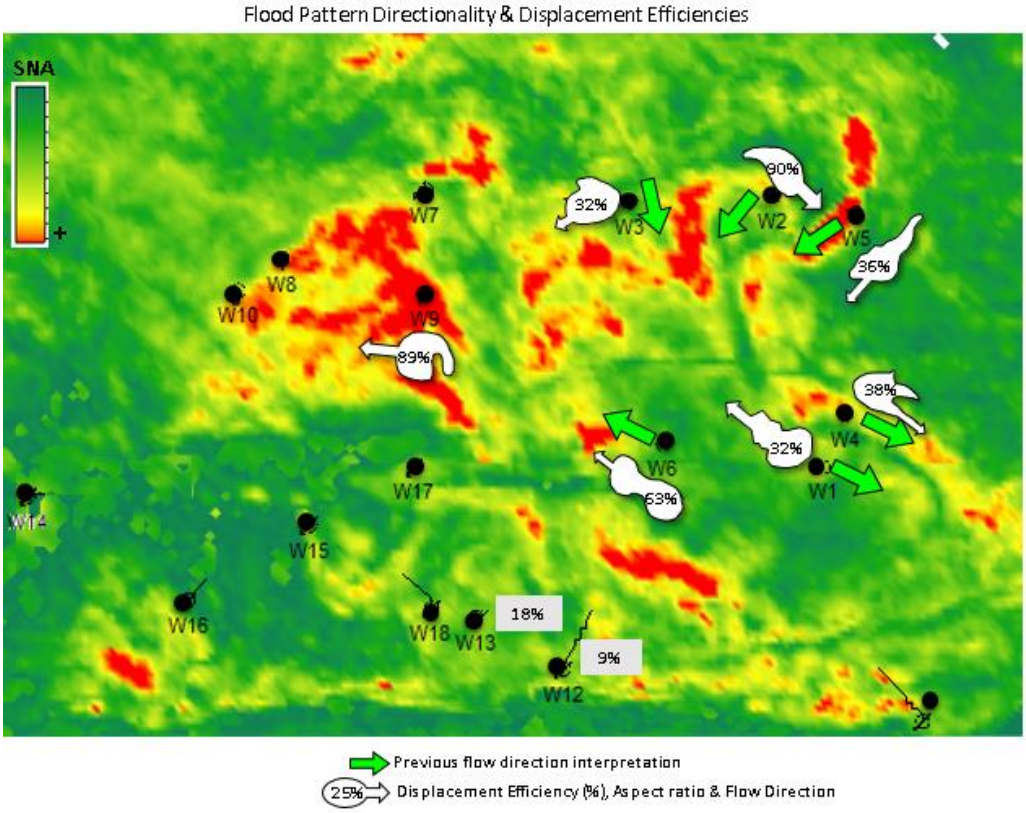

Figure 4.9: Combined Seismic Displacement Efficiencies and Seismic Directionalities shown on a 3D seismic attribute map depicting net-to-gross distributions with sands illuminated. Green arrows display previously interpreted waterflood directionalities (Floricich, 2009)

4.4 Further Interpretation of the Performance Metrics

4.4.1 Waterflooding Induced Fractures

Waterflooding typically leads to injectivity decline unless it is occurring at an injection pressure above reservoir fracture pressure. Thus, fractures are almost always guaranteed when injecting into the reservoir (van de Hoek et al., 2000; Gadde and Sharma, 2001; Noirot et al., 2003; Van den Hoek et al., 2008). Fracture creation can be designed as part of a waterflooding scheme where water injection at fracture propagation pressure is employed targeting the improvement of the water injectivity to combat injectivity declines as a result of formation damage, rock and fluid characteristics, or poor injected water quality containing particles of oil droplets or suspended solids. Fractures could also be unintentionally induced hydraulically or thermally as a result of the naturally increased pore pressure (or pressure increase resulting from particulate plugging) and high temperature gradients which leads to reductions in effective stresses around the injector. These reductions in effective stress could induce new fractures, activate naturally

occurring fractures, change the permeability character around the well or continuously grow existing fractures over time.(Gadde and Sharma) High conductivity fractures within injector area of influence affects the shape of the waterflood pattern, hence the sweep efficiency which could lead to premature water breakthrough or reduced pressure support in targeted producers. This implies that monitoring the changes in reservoir heterogeneity, fracture orientation and rate of fracture growth are key factors in improving recovery efficiency.

As most injectors are not fractured prior to the start of injection, time-lapsed seismic can be utilized as a fracture monitoring tool, where the initiation of a new fracture, growth of fracture over time and influence of the fracture on the sweep efficiency is captured by changes in the 4D seismic anomaly over time. Understanding the pre-injection state of the reservoir by interpretation of the seismic data in comparison to the monitor seismic surveys could first determine if the injection has resulted in a fracture, and with subsequent monitors, determine the dynamic development of the fracture as it affects the waterflood.

Heffer and Lean (1993); Heffer et al. (1997, 2002) analysed the flood breakthrough characteristics in 80 cases of naturally fractured and unfractured reservoirs and confirmed that for either set of reservoirs, the anisotropy of the initial water breakthrough was strongly correlated to the azimuth of the maximum horizontal stress as seen in Figure 4.11.

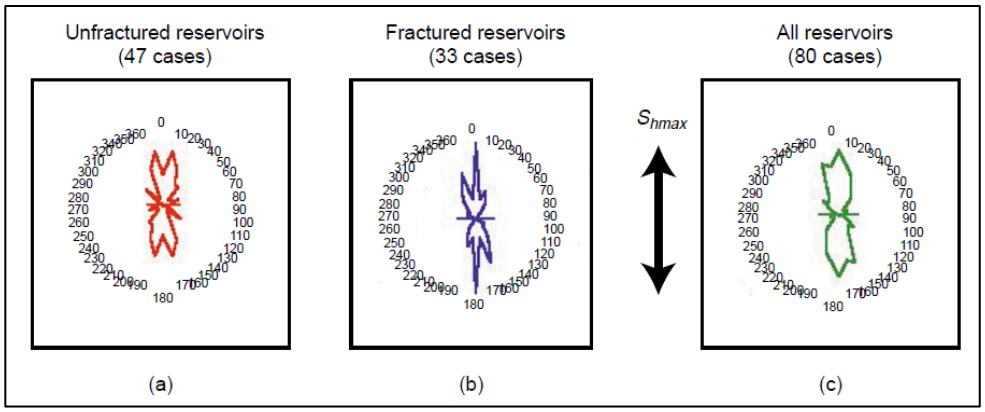

Figure 4.10: Flood directionality and fractures showing the bias in the major azimuthal axes of breakthrough towards Sh_{max} for both unfractured and fractured reservoirs.

For a section of formation therefore, with the maximum, minimum and vertical stresses acting in the directions as shown, the conditions of magnitude where the maximum horizontal stress is greater than the vertical stress and greater than the minimum horizontal

stress, a fracture would be propagated from the perforation as shown in Figure 4.12 – along the maximum horizontal axis in the plane of the vertical stress and opening along the minimum horizontal stress axis.

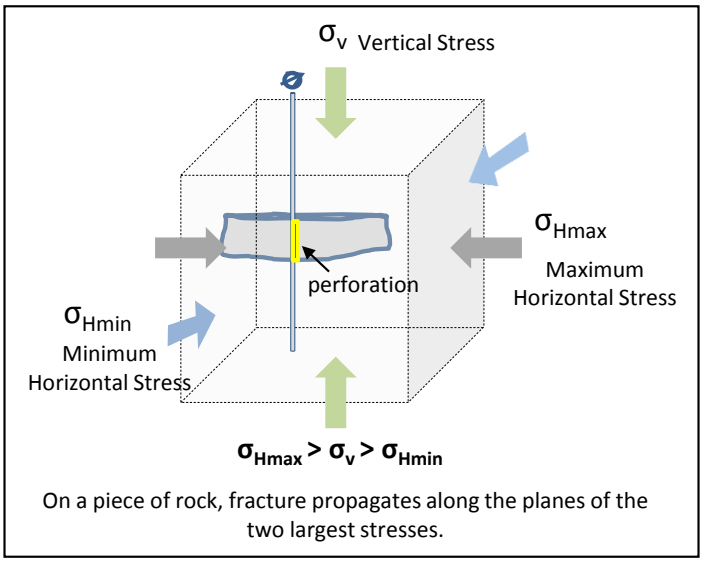

Figure 4.11: Illustration of fracture propagation orientation along the planes of the two largest stresses.

As shown in Figure 4.13a, the Seismic directionality symbols for injectors W1, W5, W7 and W8 all deviate from or go against the interpreted direction of the reservoir channel geology as illustrated in Figure 4.13(b) (Leach et al., 1999). For example, well W1 (within the red and white squares) indicates a north-westerly directional flood at an angle of 78 degrees, but not parallel to the expected interpreted channel direction. This directionality of the flood could be a definition of the sand body around the well or an indication of the permeability direction. The seismic interpretation of the geology around the well in Figure 4.13(b) suggests a more Northern flood propagation than indicated by the seismic directionality metric. Fracture pressure information from Roy et al. (2004) for a similar water injector in this segment states that the theoretical fracture pressure is about 317 bar. The Well bottomhole pressure for the injector is shown in Figure 4.14a and from this, it is evident that the well begun injection well above the fracture pressure with initial injection pressures of 400 bar and can thus be confirmed as fractured.

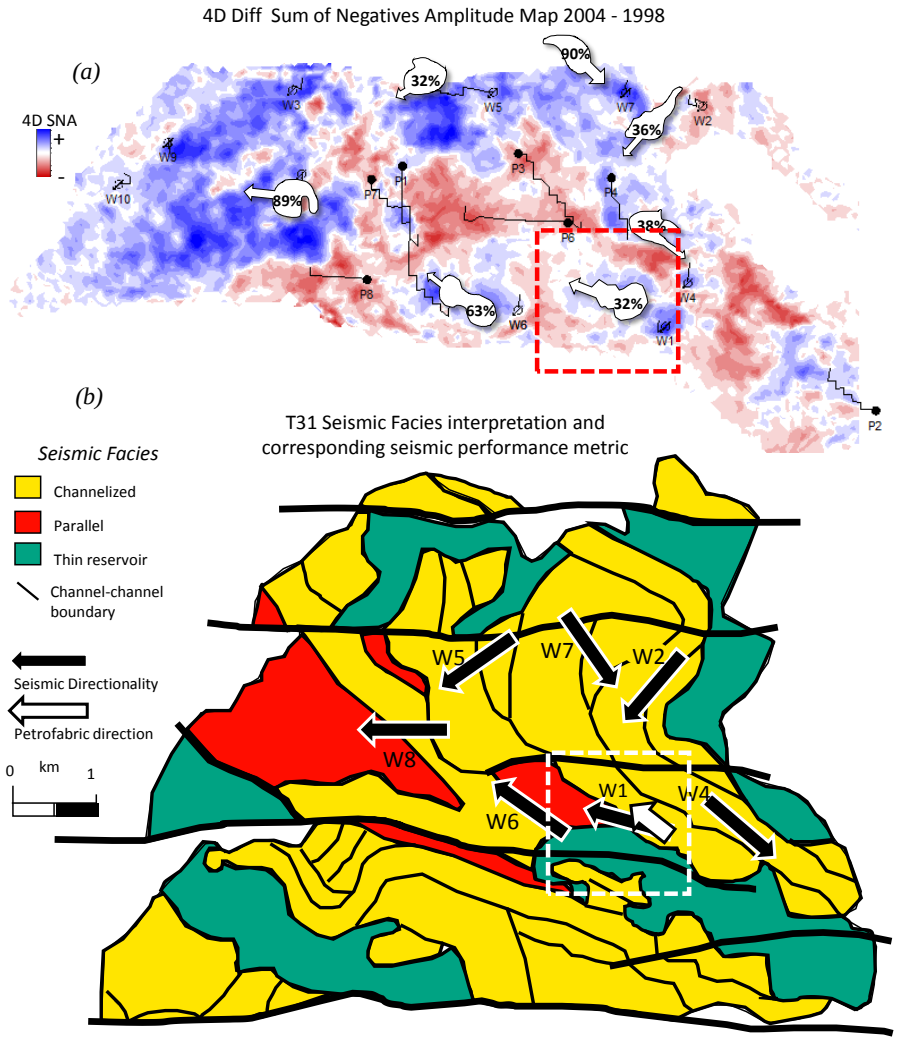

Figure 4.12: (a) Interpreted Seismic Displacement Efficiency and directionality correlated to 4D seismic map and (b) Seismic facies interpretation showing channel architecture and petrofabric direction. (After (Leach et al., 1999))

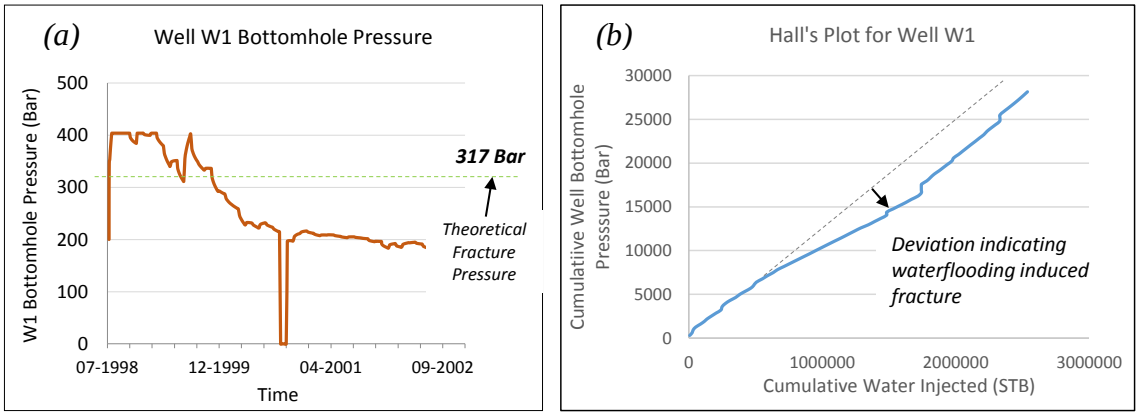

Figure 4.13:(a)Well bottomhole injection pressure for Well W1 with highlighted Fracture propagation pressure (b) Hall's plot for injector W1 showing deviation of trend downwards, indicating waterflooding induced fracture after initial injection at pressures higher than fracture propagation pressure.

Analysis of the North Sea stress map in Figure 4.15, shows that the Central Graben area data generally has NW-striking S_{Hmax} orientations. Drilling-induced tensile fractures from image logs are used to determine the orientation of S_{Hmax} and orientations determined via this source have no depth dependence. Considering this, though there is sparse horizontal stress data in the West of Shetlands region where the Schiehallion is located an interpretation can be derived from the stress orientation. Proximal maximum horizontal stress data to the Schiehallion indicate a North-west direction. This means that waterflooding induced fractures would propagate in the direction of the maximum horizontal stress, a direction that aligns with the waterflood orientation indicated by the Seismic Performance Metric and could be the consequence of waterflood induced fractures. It can therefore be inferred that the seismic directionality metric could serve as an indication of the presence of a fracture and the fracture influenced waterflood direction.

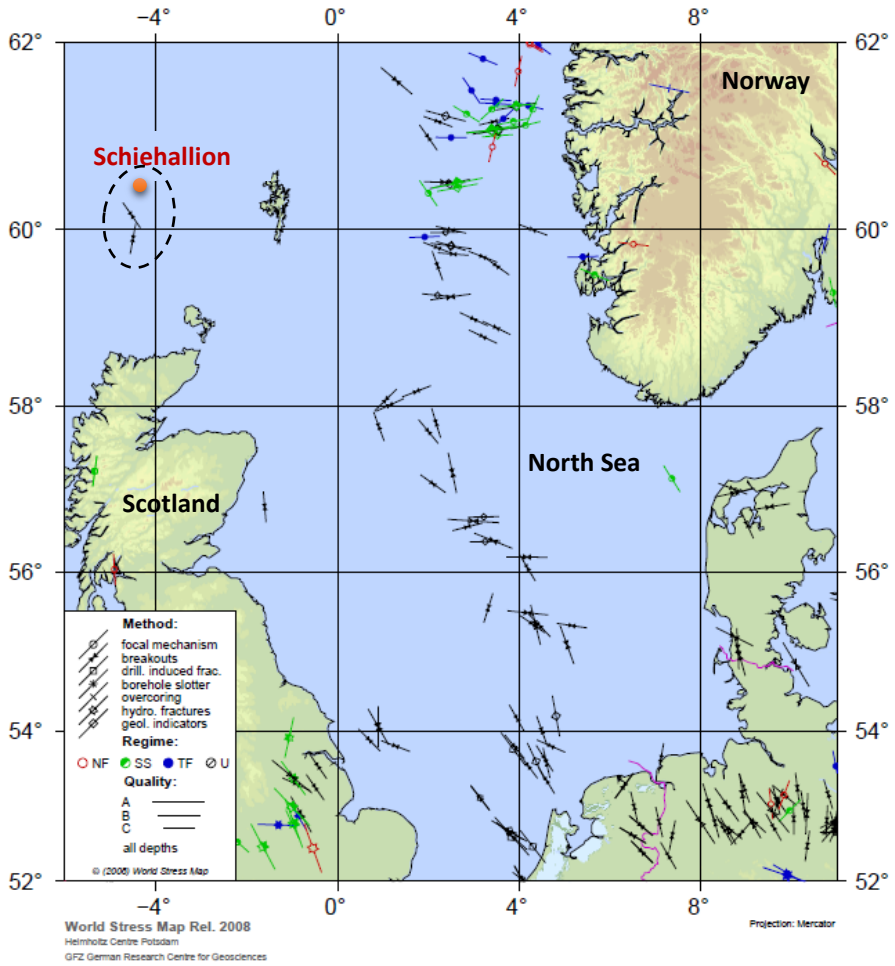

Figure 4.14: World Stress map of North Sea showing Schiehallion field area (World Stress Mapp Rel. 2008. Helmholtz Centre Potsdam, GFZ German Research Centre for Geosciences).

4.4.2 Validating Seismic Displacement Efficiency with Well-Well Connectivity

The performance metrics provide information about the injector well performance itself, immediate geology around the well and the flood directionality, but so what? How valid are the metrics as an indication of injector interaction with surrounding producers?

Accurately characterizing the injector-producer connectivity is directly connected to optimizing waterflood operation and forecasting performance. Interwell connectivity evaluation though achievable with reservoir flow simulation models can be complex and time-consuming. There are several methods of evaluation of interwell connectivity: for example, Spearman's rank correlation, Multivariate Linear Regression, Capacitance Model (Yousef et al., 2005a; Al-Yousef, 2006; Yin et al., 2015). The Capacitance Model has been proven as a reliable technique in determining inter-well connectivity between a producer and injectors (Albertoni, 2002; Yousef et al., 2005a; Yousef et al., 2009). It is based on material balance and is a data-driven method that calculates the connectivity between injectors and producers using nonlinear regression on historical production data. It characterizes properties of the reservoir using production data, where the injection rate is converted to an output signal (total production rate) and the output response is a result of the time-lag and attenuation between the injector and producer. Two coefficients, weight and time constant, are determined for each injector producer pair. The weight quantifies the connectivity between both wells and the time constant quantifies the degree of fluid storage between wells. Incorporating effects primary production, multiple injectors and bottom hole pressure change for the producers, equation (4.15) describes an estimate production rate, $\hat{q}_j(t)$ as:

$$\hat{q}_j(t) = \lambda_{pj} q_j(t_0) e^{-\left(\frac{t-t_0}{\tau_{pj}}\right)} + \sum_{j=1}^{i=I} \lambda_{ij} w'_{ij}(t) + \sum_{k=1}^{k=K} v_{kj} \left[\left(p_{wfk}(t_0)\right) e^{-\left(\frac{t-t_0}{\tau_{kj}}\right)} - p_{wfkj}(t) + p'_{wfkj}(t) \right] \qquad (4.15)$$

$$\text{where } w'_{ij}(t) = \sum_{m=1}^{n} \left(e^{\left(\frac{t_m - t}{\tau_{ij}}\right)} - e^{\left(\frac{t_{m-1} - t}{\tau_{ij}}\right)} \right) w_i(t_m) \qquad (4.16)$$

$$\text{and } p'_{wfkj}(t) = \sum_{m=1}^{n} \left(e^{\left(\frac{t_m - t}{\tau_{kj}}\right)} - e^{\left(\frac{t_{m-1} - t}{\tau_{kj}}\right)} \right) P_{wfkj}(t_m) \qquad (4.17)$$

Giving $\hat{q}_j(t)$ as the estimated production rate at time, t for producer,j, λ_{pj} and τ_{pj} are the weighting factor and time constant respectively for the primary production contribution to the rate of producer, j. λ_{ij} is the weight that indicates the productivity between the injector i and the producer, j and τ_{ij} is the time constant between the injector-producer, i-j. v_{kj} is a coefficient that determ

ines the effect of changing the BHP of producer,k on the production rate of producer j. $\left(p_{wfk}(t_0)\right)e^{-(\frac{t-t_0}{\tau_{kj}})}$ accounts for the initial production condition of producer k at time $t = t_0$. Equations (4.16) and (4.17) are used to calculate the convolved injection and pressure terms. $w'_{ij}(t)$ is the convolved injection rate for injector i, indicating the influence of injector i on producer j. It is calculated from the injection rate $w_i(t)$ at time, t. $p'_{wfkj}(t)$ is the convolved BHP for producer, k on producer j and τ_{kj} is the time constant between producer pair k-j. n describes the number of discrete timesteps at time,t.

The interwell connectivities between injector-producers pairs are determined for wells in operation during the same intervals. For the intervals in Figure 4.16 showing the well groups of producers and proximal injectors of possible influence, the interwell connectivity coefficient, λ_{ij} is interpreted in reverse as connectivity between injector W1 and producers P1, P2 and P4 and between injector W9 and producers P1 and P2.

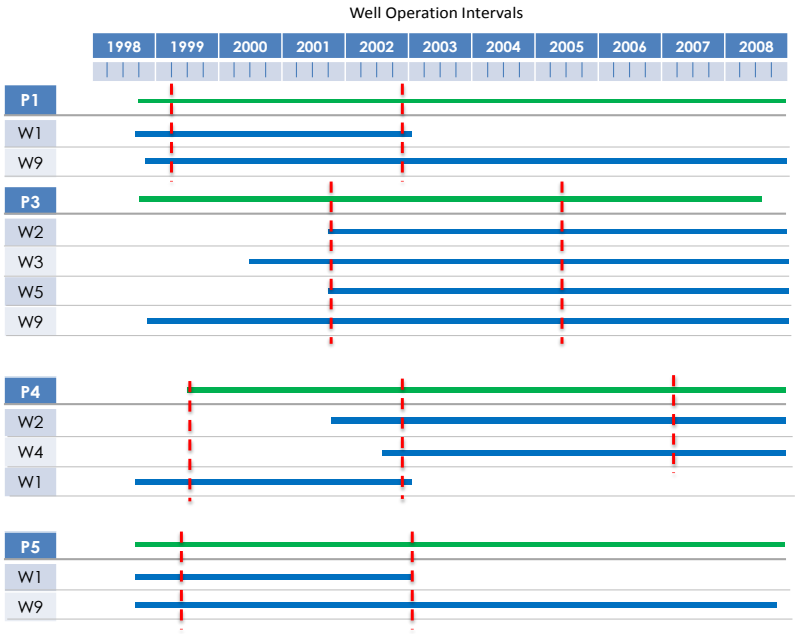

Figure 4.15: Well operation intervals for determination of inter-well connectivity

The calculated coefficients shown in Figure 4.17 indicate the waterflood preferential direction. The red arrows are drawn characterising the injector-producer connectivity and for the analysed 4D seismic 2004 survey (2004 – 1998), we notice that the interwell connectivity indicators align with the performance metric directions such that:

- Well W1 has the strongest connectivity with Producer P1
- Well W1 has the least connectivity with Producer P2, which is across the mud baffle identified in the geology.
- The resolution of the 3 vectors with Producers P1, P2 and P4 would give an approximate North-west directional flood as indicated by the performance metric.

The same applies for injector Well W2 which shows the strong interconnectivity with Producer P4, propagating along the sand channel as indicated by the seismic directionality metric.

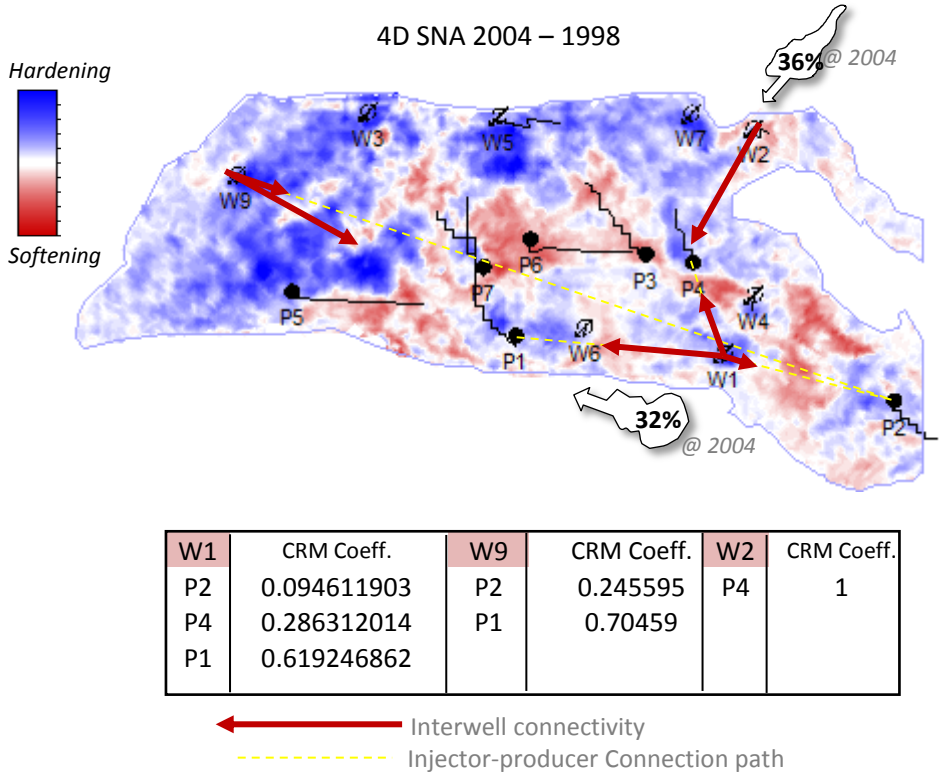

W1	CRM Coeff.	W9	CRM Coeff.	W2	CRM Coeff.
P2	0.094611903	P2	0.245595	P4	1
P4	0.286312014	P1	0.70459		
P1	0.619246862				

Figure 4.16: Seismic Displacement efficiencies and directionalities showing alignment with interwell connectivity determined with the Capacitance Resistance Model.

4.5 Summary

The study highlights the quantitative abilities of 4D Seismic Data in evaluation of waterflood displacement efficiency and directionality. Seismic Waterflood Performance metrics based on 4D seismic data and calibrated with the reservoir simulation model and forward modelled seismic were defined. Successful application of the metrics is dependent on:

- Good quality seismic data
- Reservoir with characteristics sensitive to seismic waves.
- Presence of strong increased water saturation signal
- Agreeable injection pressures that do not obscure the hardening signal

After calibration to the simulation model, the seismic measures provided a reasonable indication of the well-centric behaviour of injectors across the field. The Seismic performance metrics not only improved the well-centric geology understanding but identified the fracture exaggerated flow by indicating unexpected strong flood directionality in wells W1, W5, W7 and W8. The usefulness and validity of the metrics were confirmed via a good correlation with the interwell connectivity coefficients. Such measures can support permeability and connectivity methods for injection pattern design, injection rates or volumes injected. In addition to all previously mentioned benefits, application of the seismic performance metrics could ease expensive sub-sea PLT logging and well surveillance. Multiple surveys and improved data quality, however, would improve the robustness of the information. Ideally, localised high repeatability data acquired around each injector would be of benefit to field development and reservoir monitoring strategy for well planning, in-fill drilling programmes or waterflood surveillance decisions.

Chapter 5

Local Automatic Seismic History Matching

This chapter introduces local automatic seismic history matching. Characteristics of the reservoir simulation are modified to obtain the best configuration of properties that accurately replicates the well-centric 4D seismic interpreted flood pattern. Binary image representations of the seismic signal are used in the formulation of the seismic objective function. Two methods of seismic misfit formulation, *Currents Measurement Metric* and *Hamming Distance* are tested for applicability and accuracy. The methods are validated through a history matching exercise on a synthetic reservoir model. Results show that though both methods of formulation efficiently handle the seismic misfit function in the history matching workflow, the Hamming Distance method was more sensitive to improving the match quality between the truth and basescase local flood patterns.

5 Local Automatic Seismic History Matching

5.1 Seismic History Matching

History matching of the reservoir model is defined as the process of improving the ability of a reservoir model to honour real reservoir static and dynamic behaviour. Mathematically, it involves inversely solving for the best configuration of parameters of a reservoir flow simulation model that reduces the misfit between simulated and observed data, matches historical dynamic behaviour and can reliably forecast reservoir behaviour (Oliver and Chen, 2010). This effectively calibrates the reservoir model to the observed reservoir behaviours. The reservoir flow simulation model is defined by a numerical finescale geological model, based on geoscientists' interpretation of depositional environment and combined data from well logs, seismic, core analysis and well tests. This describes the initial reservoir static properties which may be modified over time as a result of production activity (eg., injection-induced fractures, reservoir subsidence, etc). History matching aims to find the reservoir model with minimized discrepancies in both static and dynamic characteristics from the observed reservoir at a given production time.

History matching has evolved over the years from the determination of areal permeability distribution in verifying reservoir data by matching historical reservoir conditions (Kruger, 1961) to the inclusion of time-lapsed seismic information as in recent use of binary equivalents of 4D seismic data in a probabilistic reservoir model update by Davolio et al., 2018. The domain of Automatic seismic history matching has shown significant development over the years, expanding from qualitative 4D seismic data inclusion to increasingly quantitative use of seismic data (O'Donovan et al., 2000; Huang, 2001; Huang et al., 2001; Gosselin et al., 2003; Kazemi and Stephen, 2011; Roggero et al., 2012; Trani et al., 2012; Davolio et al., 2013; Obidegwu et al., 2015; Obidegwu et al., 2016; Trani et al., 2017; Davolio and Schiozer, 2018).

Updating the reservoir properties in the injector well-centric drainage area to better match the observed 4D seismic flood-pattern depicted by a mapped hardening signal, would rely on a high-resolution local perturbation of the properties to ensure that as much geological character of the reservoir is maintained. As discussed in Chapter 2, however, the resolution of the seismic signal, far lower than resolution of well logs, restricts the limits of flood pattern heterogeneity captured by the 4D seismic signal. Simultaneously,

computational cost of history matching regulates the number of reservoir model grid cells that can be efficiently used in a history matching exercise without compromising the solution and is dependent on computer processing power. To arrive at a realistic trade-off for flood-pattern match and efficient history matching using 4D seismic, the approach of a *Local Automatic History Matching* is taken. This entails local parameterization of the drainage area as part of the seismic history matching process of matching the simulated flood-pattern to the seismically mapped hardening pattern.

There are various forms of integrating dynamic reservoir changes information from 4D seismic data - direct seismic attributes or seismic impedances from inversion workflows in seismic grid or reservoir model grid form. These forms are highly reliant on good seismic quality, reservoir model with a high accuracy and a well-calibrated rock physics model to convert impedances to reservoir properties (Jin et al., 2012a; Jin et al., 2012b; Tillier et al., 2012; Obidegwu et al., 2016; Obidegwu et al., 2017). The inversion process required to generate seismic impedances is a time-consuming process with accompanying uncertainties tied to the inversion workflow, petroelastic model, rock physics model, etc. Given the intricacies of converting seismic data to a format compatible with production data time-constraints involved in history matching detailed reservoir models, the use of binary images in representing the seismic anomaly in an assisted seismic history match has been adapted as a fast, direct alternative (Jin et al., 2012b; Tillier et al., 2012; Obidegwu et al., 2015; Trani et al., 2017; Davolio and Schiozer, 2018). Converting the 4D Seismic signal to binary requires converting the mapped seismic anomaly into a two-component *signal/no-signal* form of ones and zeros, with ones corresponding to areas with signal and zeroes corresponding to everywhere else. Conversion to binary can be achieved with filtering by a defined threshold following calibration of the seismic signal to reservoir properties as described by Huang et al. (2001), and discussed in Chapter 3, or with a widely used clustering method like the *K-means clustering* (MacQueen, 1967) which has been applied in Automatic seismic history matching studies (Tillier et al., 2012; Obidegwu et al., 2015; Trani et al., 2017). Chassagne et al. (2016) and Obidegwu (2016) present a detailed analysis on the quantification of misfit for different threshold levels from a one-threshold converting data into binary form of two parts, to a no-threshold using the full complement of the data. For a range of synthetic models, results showed no significant difference in the misfit calculation for all four threshold levels both in misfit calculation and in the character of the optimisation search space landscape. This confirms

the use of single threshold binary images as a fast, practical method of representing seismic signal of a heterogenous reservoir.

Determining a computationally realistic scale that conforms to available seismic quality and resolution and captures the heterogeneity of the reservoir, ultimately improves the reservoir accuracy. This is a crucial prerequisite to a local history matching exercise. Building off the geological and numerical scale study in Chapter 2 and the speed and efficiency of using binary images in history matching alternative (Jin et al., 2012b; Tillier et al., 2012; Obidegwu et al., 2015; Obidegwu et al., 2016; Trani et al., 2017; Davolio and Schiozer, 2018), a local seismic history matching study using binary images is adopted. Binary images of the 4D seismic flood pattern would be derived using a one-threshold level, with a threshold determined from the material-balanced calibrated seismic signal.

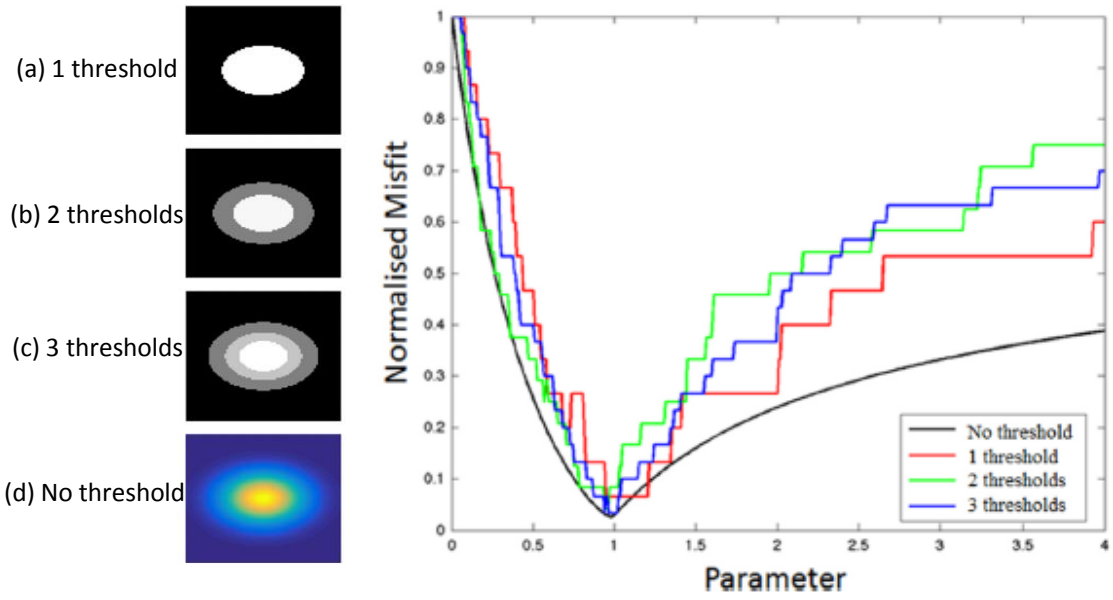

Figure 5.1: Cross-section of the normalised search space applied to different threshold levels from one (binary map) to no-threshold (adapted from Chassagne et al., 2016)

5.2 Local Seismic History Matching of the Water Signal

As discussed previously, for a saturation dominated waterflood signal, (no significant contrasting pressure signal obscuring the saturation signal), the degree of injected water resolved into the observed 4D seismic hardening, is not only dependent on the quality and resolution of the seismic data, but also on the reservoir petroelastic properties (sand-

shale distribution, effective porosity, pressure sensitivity). Binary images, however, convert the waterflood patterns to homogenous representations of the flooded area (signal exceeding determined threshold equated to ones) reducing the heterogeneity of the flood to variations in the flood front. Using binary images in seismic history matching evades the petroelastic model, thus eliminating the need for perturbing elastic properties as part of the history matching loop. However, as characteristics of waterflood patterns are influenced by the volume of water injected, and geological and petrophysical properties of the drainage area, uncertainties in the heterogeneity of the flood pattern in the history matching are instead addressed by perturbation of the appropriate reservoir static properties (eg. Net-to-gross, porosity, permeability). This captures the variations in heterogeneity which affect water volume distribution in a bid to match the shape, extent and character of the 4D observed seismic flood pattern.

5.3 The History Matching Loop

Given the complexity of static property update and the volume of data of different formats, the most feasible method of local seismic history matching is a combined reservoir simulation and a geostatistical-stochastic approach that incorporates various forms of data. Limited success of achieving accurate history matched models for complex fields through parameter adjustment of a single model (which does not accurately incorporate the possible uncertainties in the model itself), has led to the increase in the importance of generating a set of realistic good models. This is achieved via multi-parameter adjustments in Automatic history matching and converts the process of history matching to an optimisation problem. Automatic history matching simply refers to the use of software programs and computers in manipulation and update of reservoir parameters, rather than single-factor-at-a-time manual adjustments subject to the reservoir engineer's experience and interpretation.

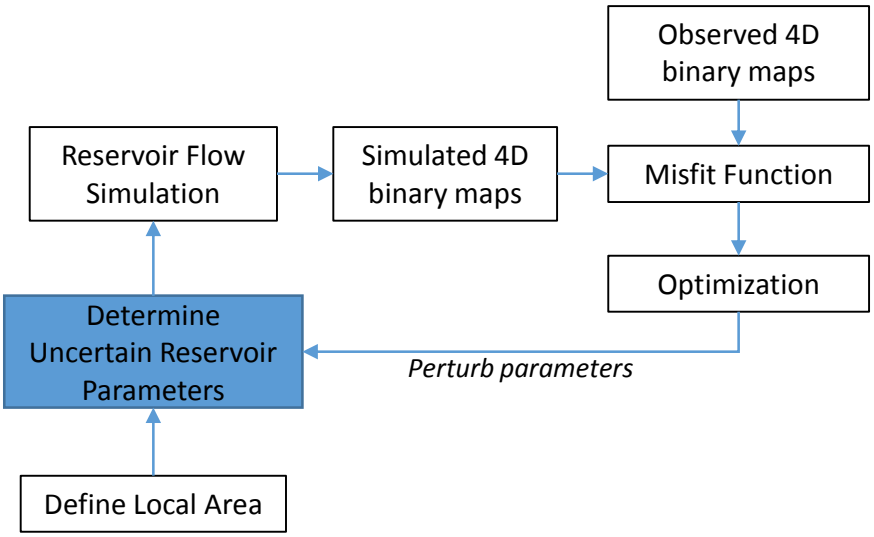

Figure 5.2: General Local Seismic History Matching workflow

The local seismic history matching loop shown in Figure 5.2 iteratively solves the non-linear optimisation problem through the stages of: (1) definition of the local area to be history matched, (2) determining uncertain reservoir parameters and following flow simulation and (3) optimisation of parameters by evaluating the mismatch of simulated and observed binary maps against a defined misfit function.

5.3.1 The History Matching Optimisation Algorithm

Optimisation is a concept applicable to various engineering disciplines. Defined as *"an act, process, or methodology of making something (such as a design, system or decision) as fully perfect, functional or effective as possible;"* in the Merriam-Webster Dictionary, describing history matching as an optimisation problem translates to optimizing the objective function by selecting the configuration of input parameters that achieve the most effective solution, thus improving the match between the simulation model and observed data using optimisation algorithms. The selection of an effective optimisation algorithm is not trivial. There are several algorithms used in automated history matching processes proposed in the literature, expanding from the gradient-based methods where the computation of derivatives in calculation of the gradient of the object-function within the flow simulation is a requirement (Wu and Datta-Gupta, 2001; Feraille et al., 2003; González-Rodríguez et al., 2005; Maschio and Schiozer, 2005) to direct search methods for which global optimisation is based on direct evaluation of the objective function.

Application of direct optimisation methods with parallel computing has been identified as an efficient way to tackle large numbers of simulation in history matching. Reservoir flow simulations involve a multi-dimensional solution space containing numerous local minima, therefore, in the history matching problem with a geological, heterogeneous and thus rugged solution space landscape, gradients are not directly accessible and the search space is multimodal, noisy and mostly non-smooth. The evolutionary algorithm (EA) applied extensively in history matching problems in the literature and found to be insensitive to nonlinearities and the combined continuous and discrete domain of the reservoir simulation solution space is a direct search method which only utilizes the objective function value to calculate the subsequent search step without requiring gradient information. It is inspired by the process of descent with modification in the biological evolution of reproduction, mutation, recombination and natural selection where population individuals are candidate solutions striving to survive an environment defined by the fitness function, in a cycle illustrated by the flowchart in Figure 5.3.

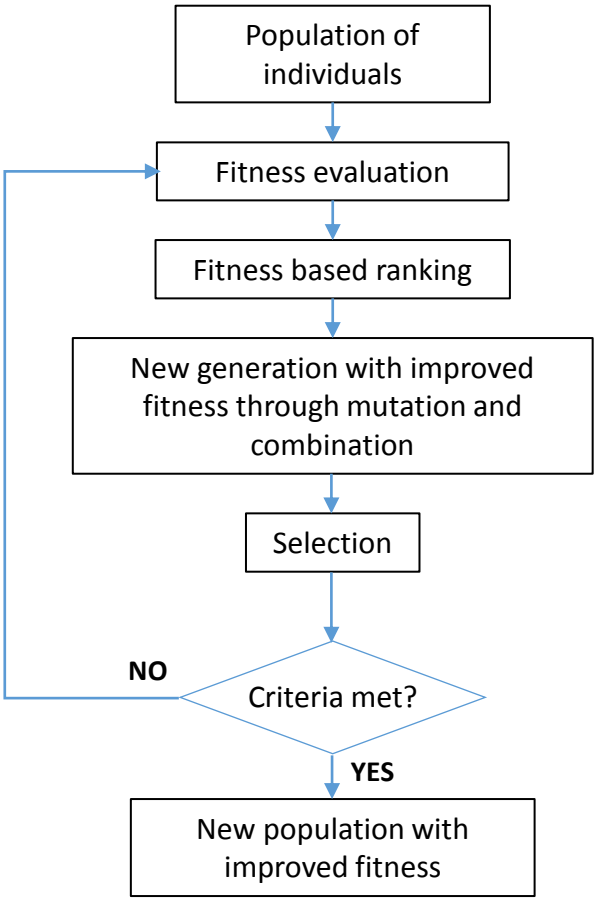

Figure 5.3: Evolutionary Algorithm Flowchart

In history matching terms, the population transitions from one generation to another through mutation of members selecting only the best-ranked objective function values and revealing parameter combinations in the search space that create reasonably matched solutions (Schulze-Riegert et al., 2002; Schulze-Riegert and Ghedan, 2007; Aranha et al., 2015)). A randomly selected initial point begins the evolutionary cycle with surrounding points evaluated for improved cases. The point with a decreased objective function defines the linear direction of the next search where an evaluation of surrounding points is again conducted. This continues until a minimum value of the objective function is derived. The quality of the history match, defined by the value of the objective function, is evaluated by misfit minimisation between observed and simulation values.

5.4 Uncertainty estimation and Parameterization

Irrespective of positive results achievable using Evolution Strategies in Automatic History Matching, the non-uniqueness of the reservoir renders the search for improved solutions dependent on engineering judgment constraints and heuristic strategies based on a priori observed production information. For selection of input parameters, detailed analysis of uncertain properties and trends in the reservoir is required. Expansive and complex reservoirs could have a high number of uncertain parameters which directly increases the complexity of optimizing the inverse problem. It is therefore important that input parameters with an influence on the history match quality are prioritised. These influential parameters are determined with a selected Design of Experiment technique which would be discussed in the next chapter. Of the five uncertain parameters, only the three most sensitive parameters were selected as input parameters. This was in a bid to replicate the true history matching workflow that would be followed in a real field case.

5.5 Defining the Binary Objective Function

The objective function is a mathematical expression that quantifies the difference between the simulated and observed data. Direct application of seismic data via grid-based elastic property assimilation has been explored by several authors (Stephen and Macbeth, 2008; Tillier et al., 2012). The use of binary images to represent 4D seismic anomaly eliminates the need for CPU-expensive seismic forward modelling utilizing uncertain petroelastic properties, time-to-depth conversion, etc., and has been explored

in recent times (Jin et al., 2012b; Tillier et al., 2012; Trani et al., 2017; Davolio and Schiozer, 2018). Inclusion in a history matching loop, however, requires an applicable seismic misfit formulation.

Conversion of seismic interpreted images of dynamic changes in the reservoir to binary images is achieved via definition of a seismic threshold which quantifies the calibrated seismic image in reservoir terms. Obidegwu et al. 2016 and Chassagne et al., 2016 compared the sensitivity and efficiency of several binary image disparity measurements, revealing the *Currents Measurement Metric* and the *Hamming Distance* as the two most suitable metrics in terms of sensitivity and applicability. The *Currents Measurement Metric* determines the difference between two closed images using the linear expression of the norm on curves by measuring the circulation of these norms through the image. Chesseboeuf et al. (2015) extended the original method introduced by Vaillant and Glaunès (2005) by using a theorem to circumvent the intricate curve extraction involved in currents metric application for 3D images. The modification of the method for 2D images is the method used in this research. The *Currents Measurement Metric*, M_{Curr}, is expressed as (Chassagne et al., 2016):

$$M_{Curr} = \sum_{i,j=1}^{N} \left\{ (i^2 + j^2)^2 \left(1 + \sqrt{i^2 + j^2}\right)^{-p} \right\} \left| \hat{A}_{ij} - \hat{B}_{ij} \right| \qquad (5.1)$$

Where A and B are two binary images with coordinates i, j and dimension N. $\hat{A}_{ij}$ and $\hat{B}_{ij}$ denote the (i,j)-th Fourier coefficients of A and B and p is a smoothing parameter that controls the resolution of the norm.

The *Hamming Distance* (Hamming, 1950) first defined as the number of bits that vary between two codewords in error detection within codes, quantifies the dissimilarity between pixels of two images and has been used extensively in image matching scenarios (Landré and Truchetet, 2007; Pele and Werman, 2008). Though Fuzzy Hamming Distance (Ionescu and Ralescu, 2004) is the advanced adaptation of the Hamming Distance for real numbers, this research only utilizes the original Hamming Distance which applies to dissimilarities between two binary vectors. The Hamming Distance, M_{Hamm}, between two binary images A and B with coordinates i and j and of dimension N is calculated with the equation:

$$M_{Hamm} = \sum_{i=j}^{N} |A_i - B_j| \qquad (5.2)$$

Hamming Distance and *Currents Measurement Metric* can be used as the seismic misfit formulation method in seismic history matching (Obidegwu et al., 2015; Obidegwu et al., 2016; Obidegwu et al., 2017). To assess applicability and efficiency in *local* automatic seismic history matching, both methods are tested on a synthetic case. The global seismic objective function, SOF, to be optimized would be a summation of the calculated misfit for the partial objective function, $PSOF$, calculated for each base-case – history misfit pair of each survey, for the number of available surveys, $nseis$. Both Hamming Distance and Currents Measurement Methods were used to calculate the misfit between each available observed and simulated binary map.

$$SOF = \sum_{i=1}^{nseis} PSOF \qquad (5.3)$$

5.6 Binary images in Local Automatic Seismic History Matching - Synthetic case

5.6.1 The Synthetic Model

The synthetic model is a black oil heterogeneous reservoir with a grid of 54 × 23 × 12 cells in the i-j-k direction, modelled after a North Sea turbidite reservoir with similar geological description and rock physics description. The synthetic model static properties are as shown in Figure 5.4. The model is a relatively thin reservoir with a thickness of 45m and defined facies distribution consisting of seven discrete facies interconnected via different degrees of transmissibility. The reservoir is drilled by a vertical injector-producer pair perforated along the full extent of the reservoir and both in operation for 885 days. To ensure 4D seismic flood pattern is unadulterated by aquifer influx, gas exsolution or pressure depletion, the injector is operating in the fully oil-saturated reservoir at an injection pressure sufficiently above the reservoir pressure to allow pressure support and sweep, but below pressures that would dominate the injection hardening signal. This ensures a saturation dominated flood pattern in the seismic signal. For this model, the true model is referred to as the "history" and the initial model as the "base-case".

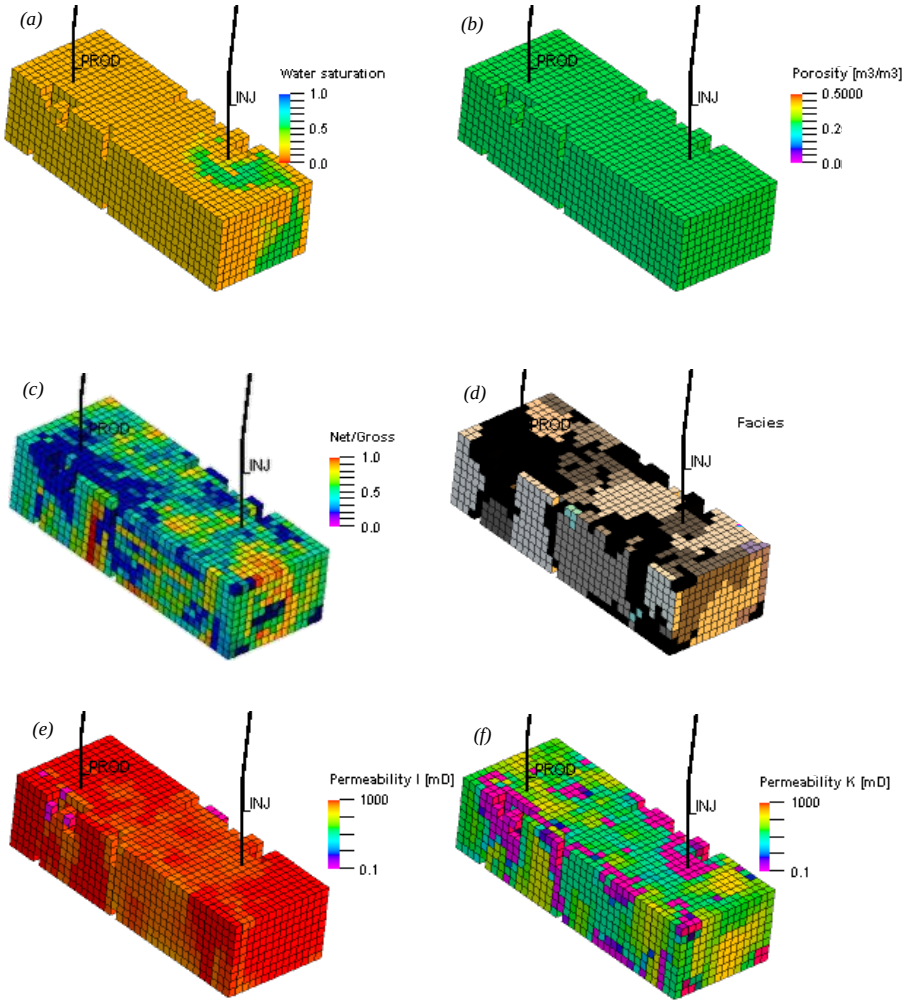

Figure 5.4: Synthetic Model Reservoir Properties: (a) Water Saturation at 735 days. (b) Porosity (c) Net-to-gross (d) Facies (e)Horizontal Permeability (f) Vertical Permeability

A base-case model to be history matched is created by varying inter-facies connectivities via the transmissibility multipliers. The variation in these geobody transmissibilities which ultimately affect the well-centric waterflood pattern are the only differences between the base-case model and the true model. The wells in both models are liquid rate-controlled and Figure 5.5(a) & (b) show the Well Bottom Hole pressures (WBHP) of both the original model "History" and the Base-case model, along with the timesteps at which monitor seismic surveys are generated (in addition to the pre-production survey) indicated with the red dashed line.

Increases in saturation are determined from differences between the initial preproduction timestep and two post-production timesteps after 185 days and 735 days of injection/production (Survey 2 – Survey 1 and Survey 3 – Survey 1). Using (Amini,

2014) and a calibrated petroelastic model, synthetic seismic surveys for these timesteps are generated via seismic forward modelling. The time-lapsed simulation and synthetic seismic maps are shown in Figure 5.7 for the two timesteps in Figure 5.6.

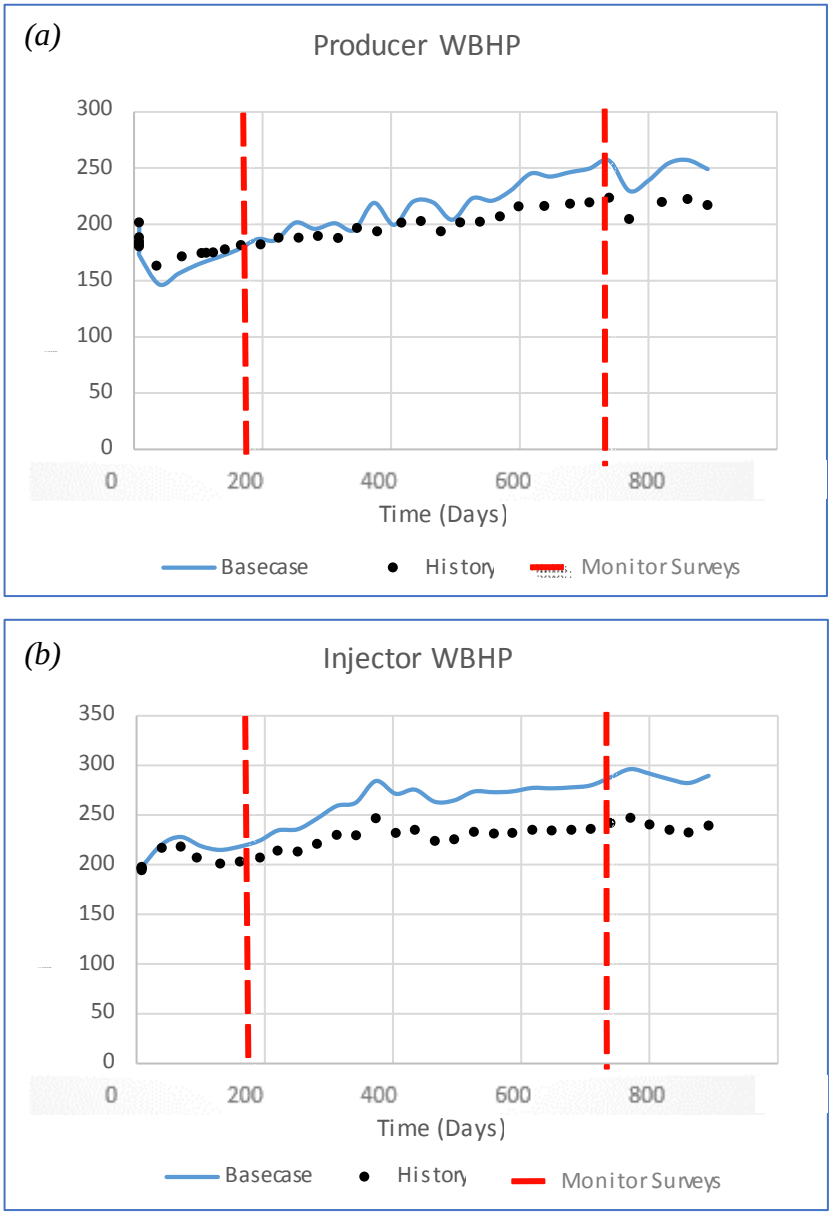

Figure 5.5: Charts showing well bottomhole pressures for (a) producer and (b) injector for base-case and observed models. Survey times indicated in red dashed lines

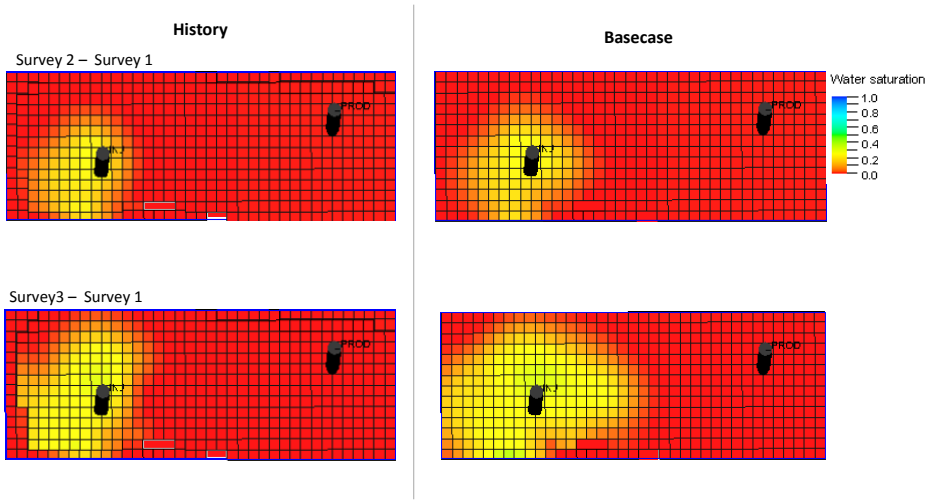

Figure 5.6: Time-lapsed simulation water saturation maps resampled into the reservoir model grid for two time periods (survey 2 -1 and survey 3 -1) for Base-case and history models.Flood patterns evident around injectors.

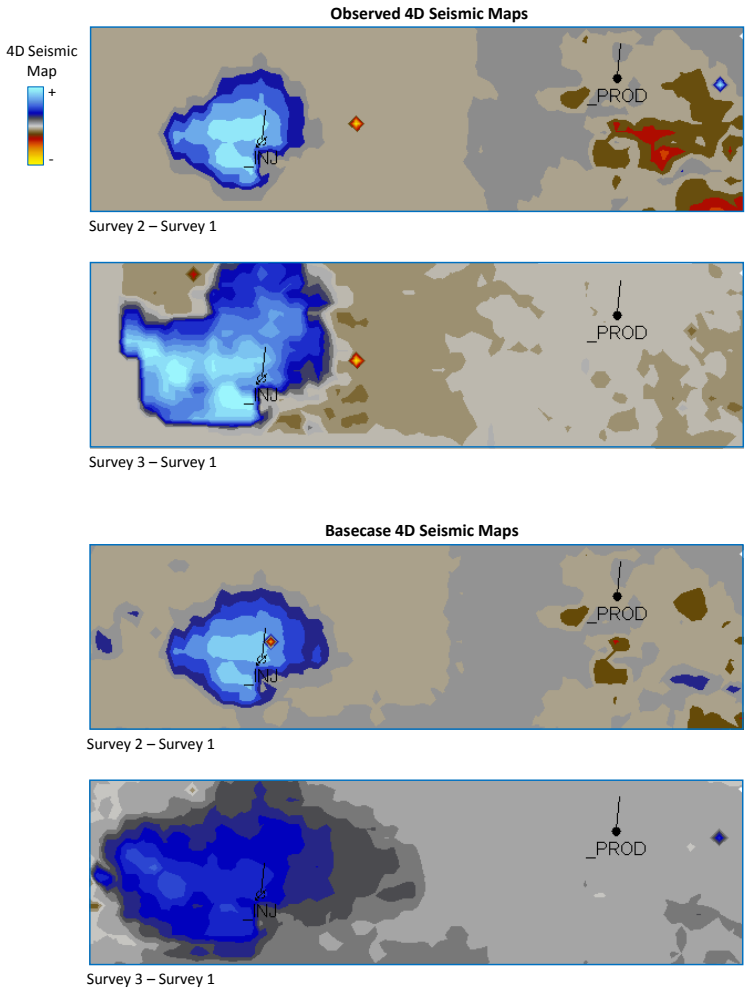

Figure 5.7: Synthetic time-lapsed seismic attribute maps for observed and base-case models showing hardening anomaly corresponding to the flood pattern around injector.

With set variations in the facies transmissibilities, thus altering the connectivity in the reservoir, the simulation maps show distinct differences in magnitude, extent and shape of the flood patterns through progressive time periods: from Survey 2 to Survey 3. These characteristics of the flood patterns are replicated in synthetic seismic maps, in Figure 5.7. The objective of the seismic history match is to match the shape of the binary representation of the flood pattern by perturbing sensitive parameters.

5.6.2 Conversion of the Waterflood Pattern Maps to Binary

Conversion to binary, referred to as *binarization*, is an efficient image segmentation processing technique used to extract information automatically from a picture. Applied to seismic maps, binarization converts the seismic responses to binary images by filtering the seismic data through a defined threshold into a monochrome image of foreground representing the seismic signal and background. Converting to binary helps eliminate irrelevant signal and noise and highlights the main signal. There are several methods of achieving this, including using either bi-level or multi-level thresholding (Stathis et al., 2008; Huang and Wang, 2009) in conjunction with clustering or neural networks (Khashman and Sekeroglu, 2008; Chamchong et al., 2010) on a local or global scale. These methods essentially employ algorithms in the analysis of the histogram distribution of the image, optimising a defined criterion to separate specific images from the background.

For a waterflooded reservoir, the 4D seismic signal is influenced by a combination of the: volume of water injected, magnitude of injected pressure, porosity of flooded area, sand-shale ratios, pressure sensitivity of flooded area, cementation, compartmentalisation or barriers, etc. In reference to the calibration of the seismic signal to the reservoir volumes, the distribution of these influencing factors of the waterflooded signal play a major role. Following this reason, an integrated data interpretation consisting of well data, production operations information and an understanding of the rock physics model is applied for appropriate tuning and conversion to binary of the seismic signal. To determine the appropriate threshold for binary conversion, the waterflooding 4D seismic hardening signals are reconciled to the injected water volumes using an iterative volume balancing method (Huang, 2001). Following the map-equivalent for the process detailed in Chapter 3, the relationship of direct proportionality is first established between the 4D seismic

maps and the material-balanced well injection volumes. The seismic threshold that approximates the material-balanced waterflood volume within the defined boundary is determined, such that the heterogeneity of the seismic resolved flood front is preserved as shown in Figure 5.8. This threshold determination method can be applied to maps (time-lapsed reservoir simulation or seismic) for all reservoir volume and pressure changes.

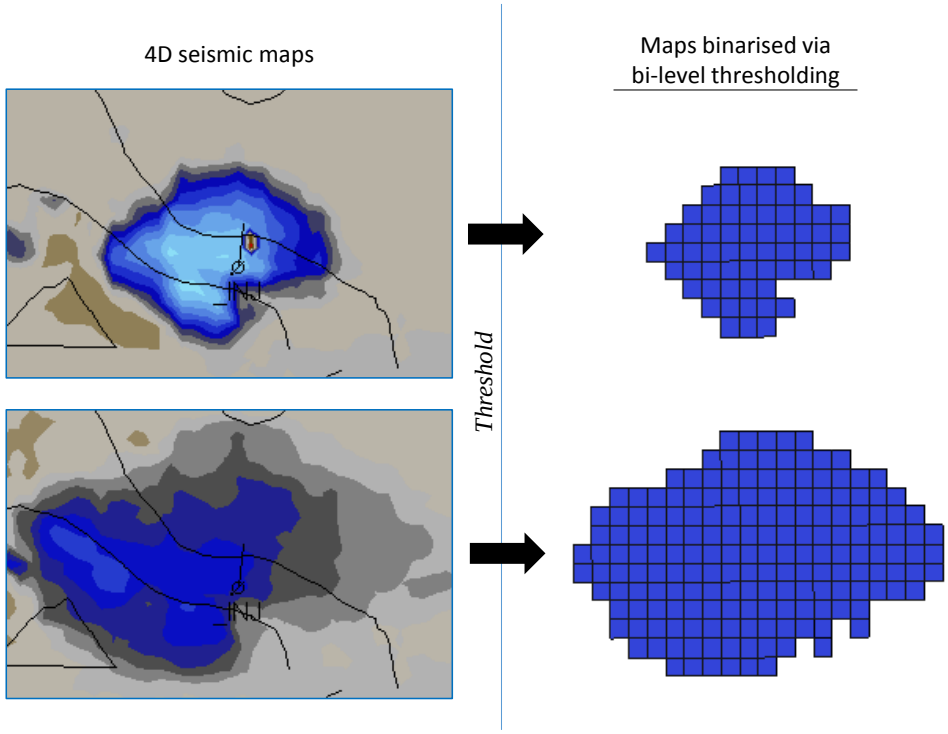

Figure 5.8: Thresholded 4D seismic waterflood patterns.

5.6.3 Running the History Matching Loop

The seismic history matching loop is an automated flow simulation and optimisation system used to locally match the injector flood pattern. To test the sensitivity and efficiency of the seismic objection function formulation methods, Hamming Distance and Currents Measurement Metrics are incorporated into the loop such that the computed seismic misfit value is the index for optimisation ranking. Figure 5.9 shows the binary versions of the observed and base-case maps input to the history matching process. The seismic signal threshold filter was determined by calibrating the injected volumes to the interpreted flood patterns. On visual inspection, the binary maps created closely represent the flood patterns observed in the history and base-case scenarios shown in Figure 5.6

and Figure 5.7, with reasonable discrepancies between the history and base-case maps to allow for misfit minimisation. The first set of maps for Survey 2-1 though of similar spatial extent, differ in the shape of the front and for the later maps, (Survey 3-1), the fronts differ in extent and front characteristics. Misfits from both timesteps would be summed to make up the global objective function towards minimising the combined attributes of mismatch.

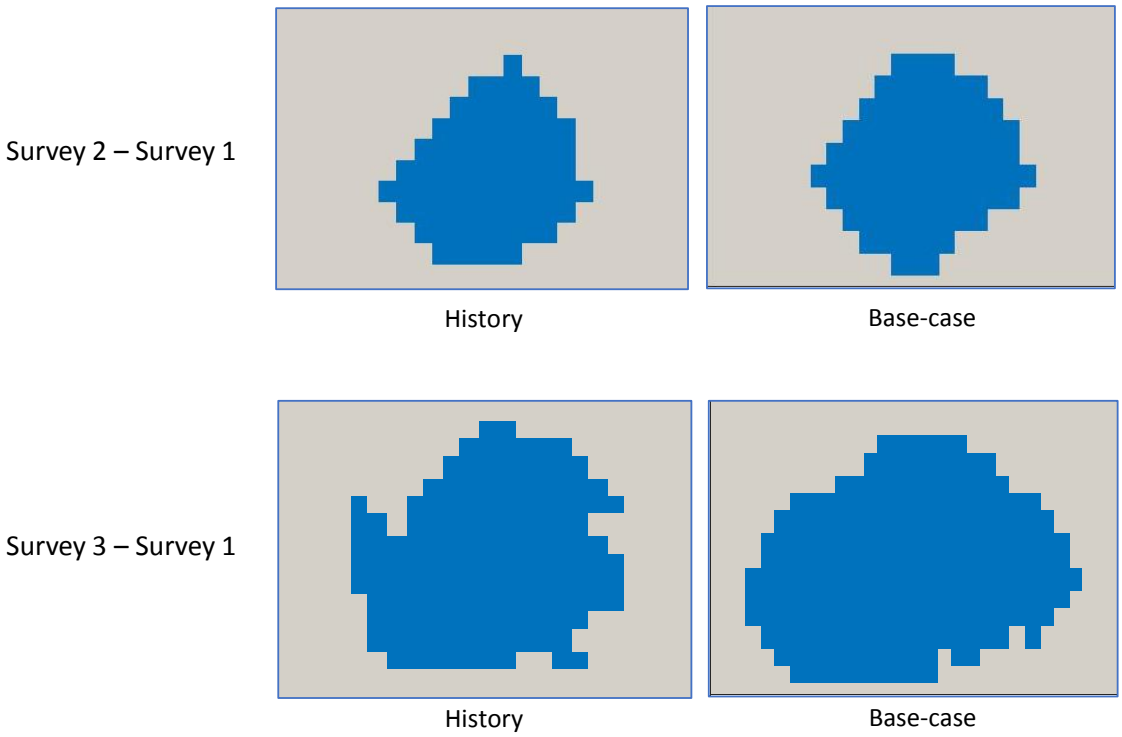

Figure 5.9: Binary maps for the true (history) and base-case models

The facies transmissibility factors are the history matching input parameters. The loop was then run using the Hamming Distance method of computing the seismic objective function. Figure 5.10 and 5.11 show charts of the injector and producer WBHP with the basecase, history and initial ensembles.

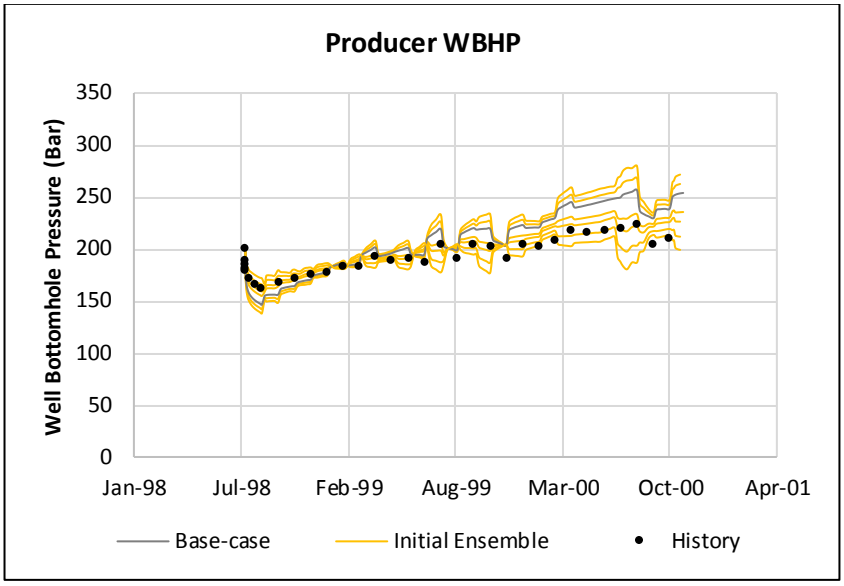

Figure 5.10: Well Bottom Hole Pressure profile for producer well for the basecase, initial ensemble and observed models

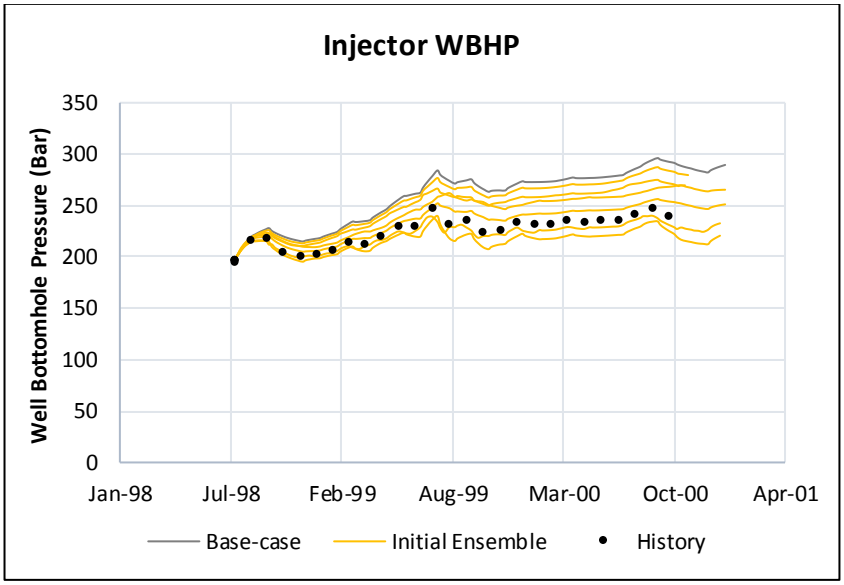

Figure 5.11: Well Bottom Hole Pressure profile for injector well for the basecase, initial ensemble and observed models.

5.7 Results

5.7.1 Hamming Distance Formulation

Matching to seismic alone using the binary maps as the only misfit function and using Hamming distance for the seismic objective function formulation, the objective value decreased by 80% to converge to an objective function value of 0.18. This is with respect to the initial value after 25 iterations. For this non-unique optimisation problem, it honours the evolution stopping criterion of convergence, thus arriving at the best possible

set of solutions for the problem. The evolution of the objective function for the history matching process is shown in Figure 5.12.

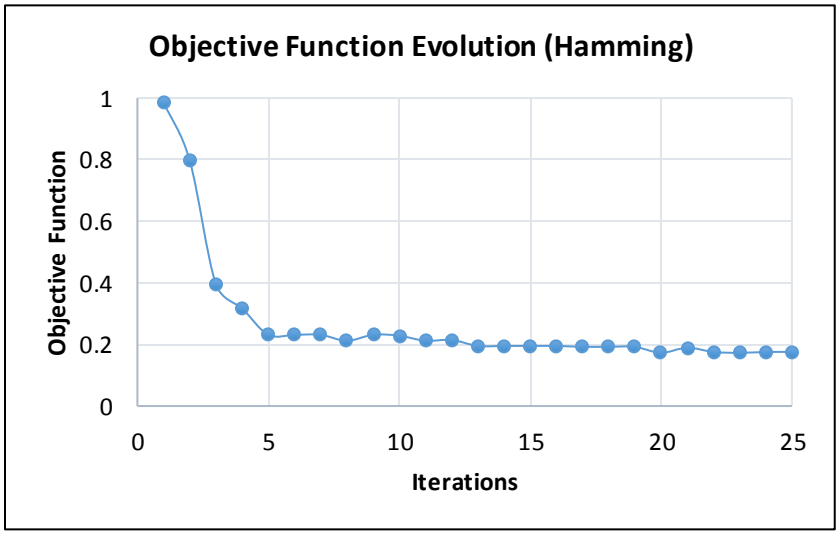

Figure 5.12: Evolution of the objective function with number of iterations using Hamming Distance method of seismic misfit formulation

Despite the exclusion of well production data from the history match, the impact of matching to the 4D seismic binary maps alone for the fluid-rate controlled wells in the model results in the exact match of well bottomhole pressures for the injector and producer shown in Figures 5.13 and Figure 5.14 for all five best-case models.

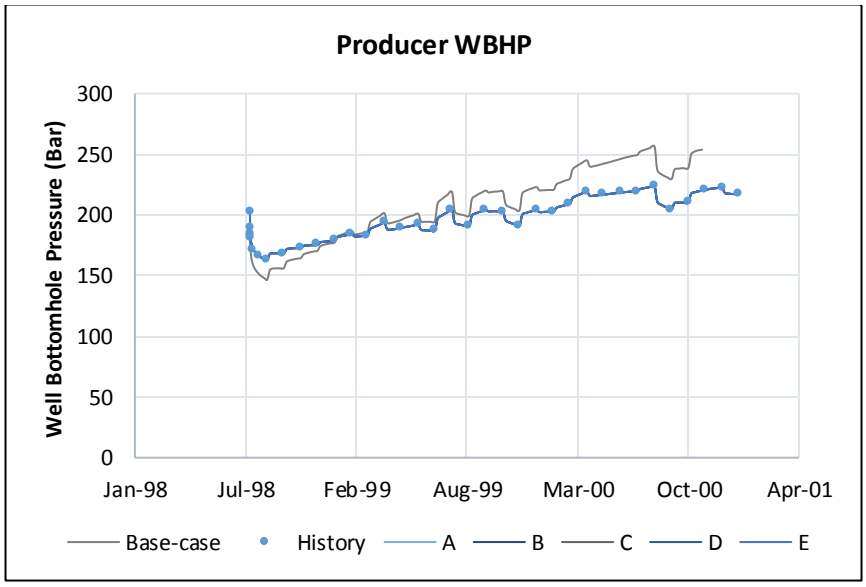

Figure 5.13: Well Bottom Hole Pressure profile for producer well showing observed, predicted and best-case using Hamming Distance. A, B, C, D and E are best-case models.

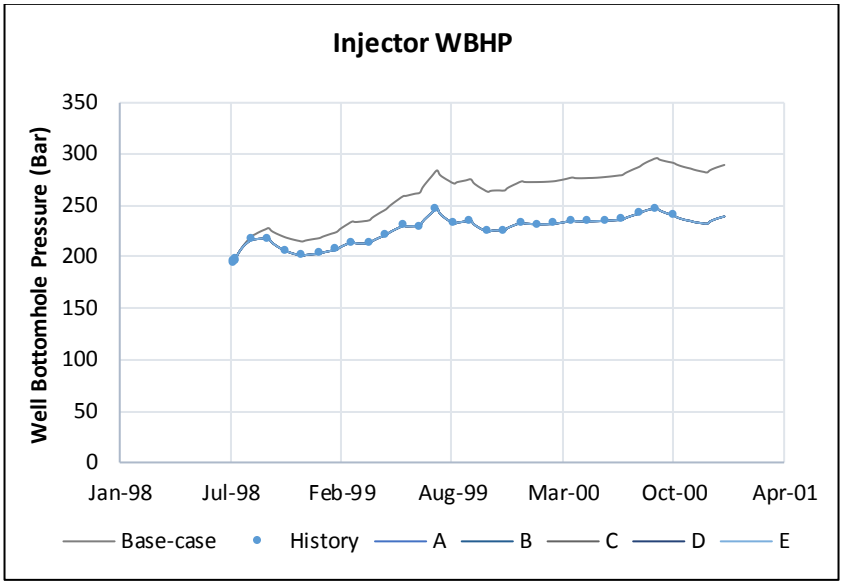

Figure 5.14: Well Bottom Hole Pressure profile for injector well showing observed, predicted and best-case using Hamming Distance. A, B, C, D and E are best-case models.

The 100% production data match differs from the binary maps match as can be seen in Figure 5.15. From the best-case solution population ensemble, five best-case candidate binary maps with the lowest misfits: A – E (objective function value = 0.176 – 0.192) show a marked improvement in replicating the flood pattern, reducing the mismatch between observed and base-case maps for both time-lapsed time periods, survey 3 – survey 1 and survey 2 – survey 1. Figures 5.15 (a) and (b) show the true model (history) and base-case (initial) model binary maps for corresponding time period (3-1 and 2-1) and Figure 5.15 (c) shows the binary maps of five best-case models. The root-mean-square (RMS) error between the history and base-case binary maps compared to the RMS error between the history binary map and average of best-case models reduces from 140 to 0. The spatial difference between history and best-case models, however, is illustrated in the mapped $d = m_{hist} - \overline{m_{best}}$ difference where $\overline{m_{best}}$ is the average of binary maps of the best-case models and m_{hist} is the binary map of the history model. These difference maps are shown in Figure 5.15 (d), where the blue areas depict $d = 0$, areas of the best-case map exactly matched to the history map, the green areas depict $d = -1$, areas where the best-case models extends past the history maps and the red areas depict $d = 1$, areas where the best-case map falls short. Following this convention, the first time period, (2-1), shows an exact match of the binary map to the history, with a reasonable 80% match of the second time period, (3-1).

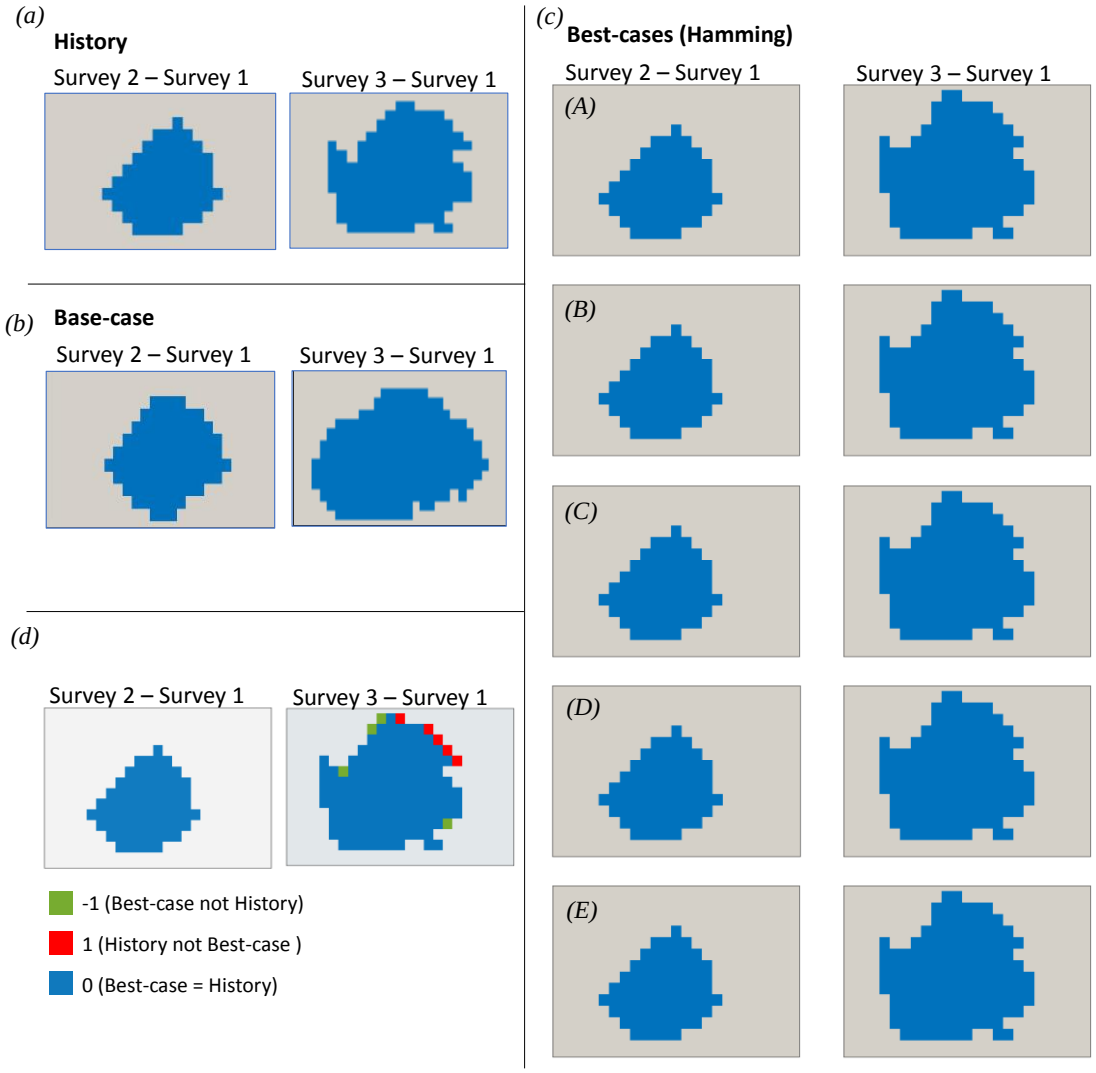

Figure 5.15: Binary maps comparing the maps from the observed (history) and base-case maps to maps from five best-case models as a result of history matching using Hamming Distance.

5.7.2 Currents Measurement Metric Formulation

Following a test of a suitable smoothness factor appropriate for this system of flood pattern maps, the *Currents Measurement Metric* was used to compute the seismic objective function. The objective function, after 25 iterations converged to approximately zero (0.07), (Figure 5.16).This history matching run produced results similar to the Hamming Distance method with respect to accurate matches of the production profiles shown in Figures 5.17 and 5.18.

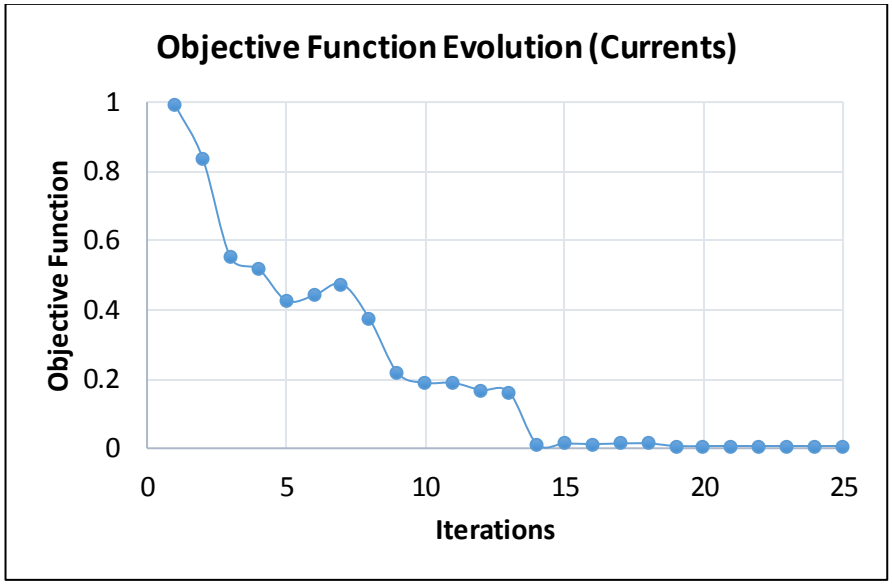

Figure 5.16: Normalized evolution of the objective function with number of iterations using Currents Measurement Metric method of seismic misfit formulation

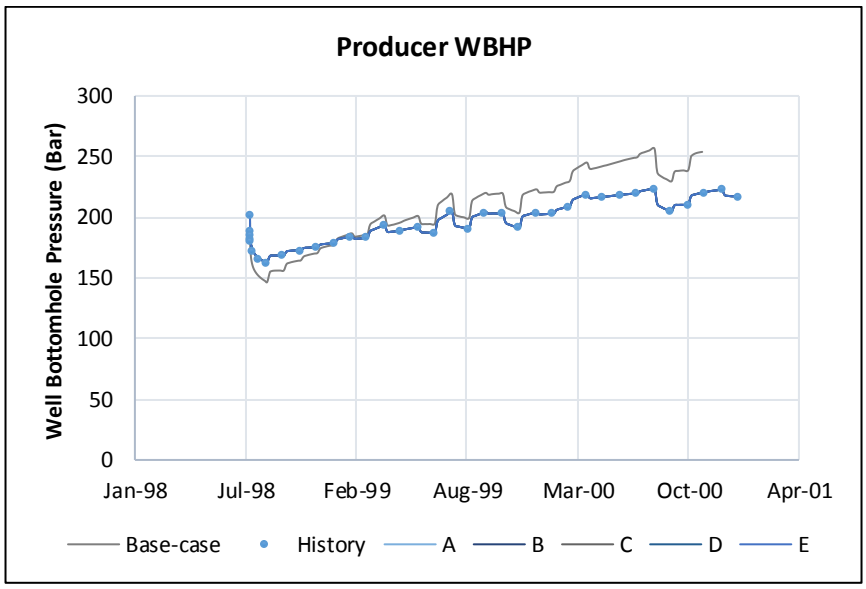

Figure 5.17: Well Bottom Home Pressure profile for producer well showing observed, predicted and best-case using Currents Measurement Metric. A, B, C, D and E are best-case models.

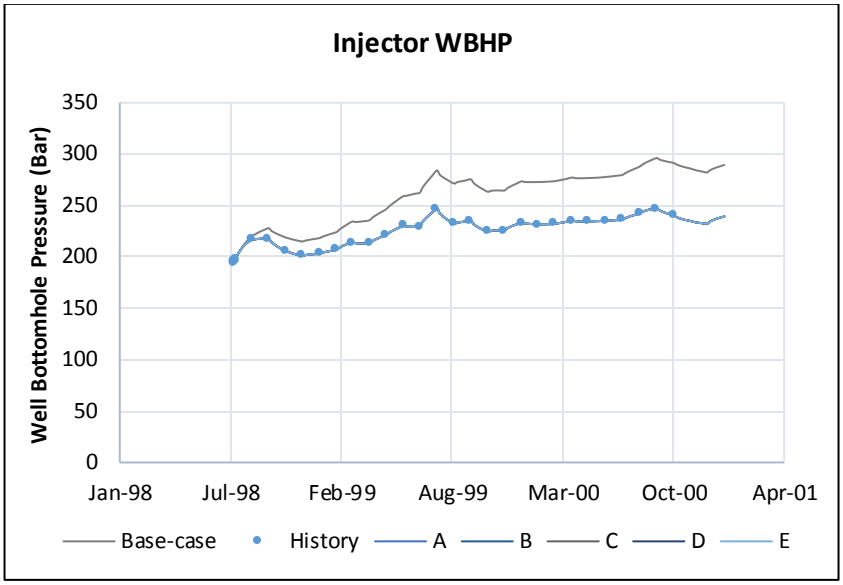

Figure 5.18: Well Bottom Home Pressure profile for the injector well showing observed, predicted and best-case using Currents Measurement Metric. A, B, C, D and E are best-case models.

Analysing the binary maps in Figure 5.19, the flood patterns for both time periods very closely mirror the maps of the best-case map using the Hamming Distance method. The residual misfits in the best-case model binary maps, however, are not commensurate with the near 100% misfit convergence rate. Though the RMS error between history and best-case maps is also reduced to zero as in the Hamming distance case, for differences between an average of the history and the best-case maps given as: $= m_{hist} - \overline{m_{best}}$, the difference of maps shown in Figure 5.19(d) illustrates the spatial difference between the history maps and the average of the best-case maps.

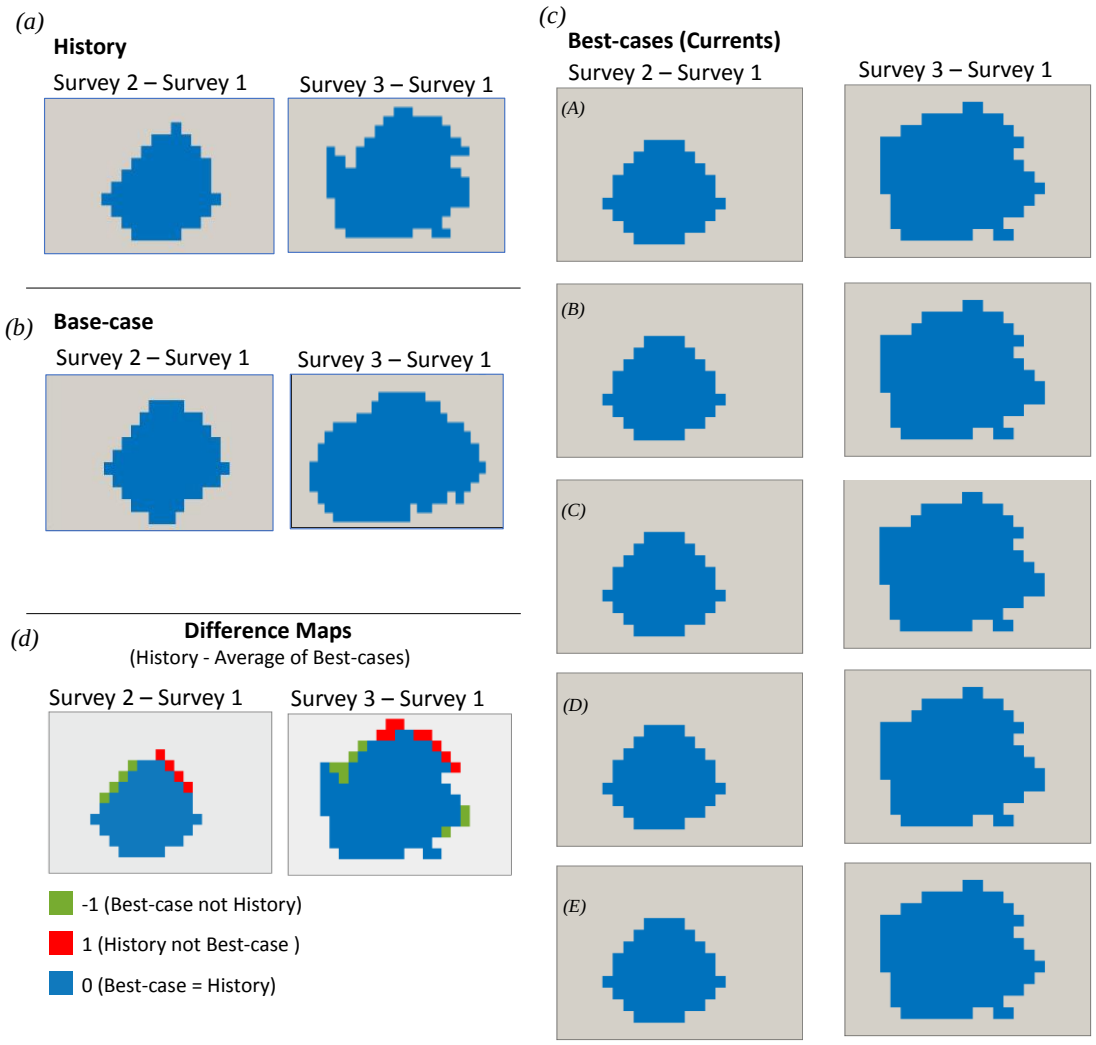

Figure 5.19: Binary maps comparing the maps from the observed (history) and base-case maps to maps from the best-case model as a result of history matching using Currents Measurement Metric method.

Both methods of measuring dissimilarity between binary maps, Hamming Distance and Currents Measurement Metric, are sensitive to local seismic history matching of the well-centric waterflood pattern. In addition to the exact match of the first time period, comparison of match quality using the sum of difference squares $\sum(x_i - \bar{x}_i)^2$ shows the Hamming Distance as the more accurate formulation with a sum of difference squares of 9 compared to 17 for the Currents Measurement Metric method.

5.8 Summary

The results of a local seismic history match using an Evolutionary Algorithm and two seismic misfit formulation methods to match binary map representations of the flood

pattern exhibit the validity of this approach. For the two misfit formulation methods tested: Hamming Distance and *Currents Measurement Metric*, the convergence rates and improved match quality indicate a satisfactory handling of the seismic representation for both methods. While both methods match the production data to a high degree of accuracy, the 80% objective function convergence rate for the Hamming Distance seismic misfit function formulation directly refers to a more realistic degree of match to the binary maps achieved (<100% match). Conversely, the Currents Measurement Metric had a higher convergence rate of 99% for the best-case maps with reduced match quality. The Hamming Distance method therefore appears better suited to a local seismic history matching of flood patterns using binary maps, a consequence of the direct spatial computation of the Hamming Distance method. The success of this approach leads to its application to real field data in the next chapter.

Chapter 6

Local Seismic History Matching: Application to Field Data

A workflow to improve the well-centric waterflood pattern using geostatistical simulation and local seismic automatic history matching is proposed. Using the Hamming Distance method to calculate dissimilarities between maps, the seismic objective function is computed from binary images of the 4D seismic data. The methodology is applied to a sector in Schiehallion field. Results show that the combined geostatistical simulation of static properties and dynamic properties update guided by history matching to seismic data alone introduces a reasonable degree of variability allowing improvement of the flood pattern characteristics match to the 4D seismic resolved flood pattern.

6 Local Seismic History Matching: Application to Field Data

6.1 Applying Methodology to Real field data

Following the same philosophy of improving reservoir characterisation, especially within the well-centric flooded area, by history matching using the binary representation of 4D seismic signal as in Chapter 5, a local seismic history match is applied to real field data. Unlike a synthetic reservoir model, the plethora of uncertainties accompanying a complex reservoir would have to be considered through sensitivity analysis and careful application of best-fit methods.

As previously discussed, a saturation dominated flood pattern largely reduces the uncertainty of the degree of seismic increased pressure signal interference, allowing for proper interpretation of the increased water saturation signal. It is also important that the flood pattern is distinct, and material-balanced in the case of produced water through seismic signal calibration to well production data as discussed in Chapter 3. Although a high-resolution reservoir model if accurately characterised improves the reservoir validity and accuracy, it is computational expensive to effectively carry out a history matching process for fine-scale simulation models. Grid coarsening of the reservoir model results in simulation computation speed gains, with a loss of high resolution as a trade-off. In a well-centric approach with a focus on the characteristics of the injector well drainage pattern, an appreciable resolution permitting the conservation of reservoir heterogeneity is important.

Considering combined conditions of a well-centric injection analysis of an interpretable drainage pattern and reasonable model resolution, a local automatic seismic history matching is carried out on a sector model of the Schiehallion field. This allows direct update of a reservoir simulation model of relatively higher resolution than would be the typical history matching case considering history matching computation cost and increasing the chances of retaining a degree of reservoir accuracy.

6.2 The Schiehallion Data for History Matching

The Schiehallion field dataset extends through ten years of production from 1998 to 2008. Four 4D processed seismic surveys were used: 1998 Baseline and monitor surveys shot in 2004, 2006 and 2008. The available 4D seismic-processed seismic surveys were shot

preproduction in 1998, and in 2004, 2006 and 2008. The six years interval between the baseline in 1998 and first monitor survey in 2004 with continuous injection and production has resulted in interconnected flood patterns around some wells in sections of the reservoir and other nearly field-wide flooded areas.

Further away from the perimeter of the aquifer, the south-east sector of Segment 1 of the reservoir retains a discrete 4D seismic flood pattern around three wells (2 injectors and one producer) by the time the first monitor survey is shot in 2004. Major faults with minimal to no hydraulic communication, separating this section from the rest of the reservoir, is further justification for an application of the proposed *Local History Matching* methodology to this section of the reservoir. The use of this section as a sector model fulfils the prerequisites:

- Avoiding well completions extending across faults and different flux regions,
- Waterflood in the oil leg (excluding area of direct aquifer influence),
- Improvable history match quality, and
- Available seismic & production data.

6.2.1 Reservoir Sector Model Setup:

The reservoir simulation model used in this study is of Segment 1 of the Schiehallion field and a product of a partial history matching process. This model subsequently referred to as the *Base-case model*, is the initial model to be improved through the Local Seismic History Matching methodology. Excluding the degree of history match quality, it is similar to the Segment 1 Schiehallion model introduced in earlier chapters (Chapter 2 & 4). Charts comparing well fluid and pressure rates of the base-case model and the observed historical data in Figures 6.2 –6.11 show the degree of mismatch. Following the seismic only local history matching process detailed in Chapter 5, the use of local seismic history matching, in this case, is towards an improvement of the resolved seismic flood pattern match using binary images for real field data. This is applied with an automatic history matching framework, including simultaneous geostatistical update of the reservoir static properties, alongside the use of binary representation of the 4D Seismic data.

The full Schiehallion Segment 1 simulation model is a 237,440 cell model with approximately 70,000 defined cells and an average runtime of 4 hours. A "full field" flow simulation was first run to capture pressure and saturation flux across the sector boundary

thus delineating the sector flux region. This ensures that the sector boundary conditions are maintained and material balance between the sector and the remaining field is fulfilled. The sector model with the preserved boundary conditions is subsequently configured as an independent simulation model for the history matching cycle. Given the prerequisite for reasonable simulation model resolution to preserve seismic-resolvable reservoir heterogeneity, using a sector model eliminates the need to further upscale the model and decreases simulation runtime from 4 hours to 9.5 minutes.

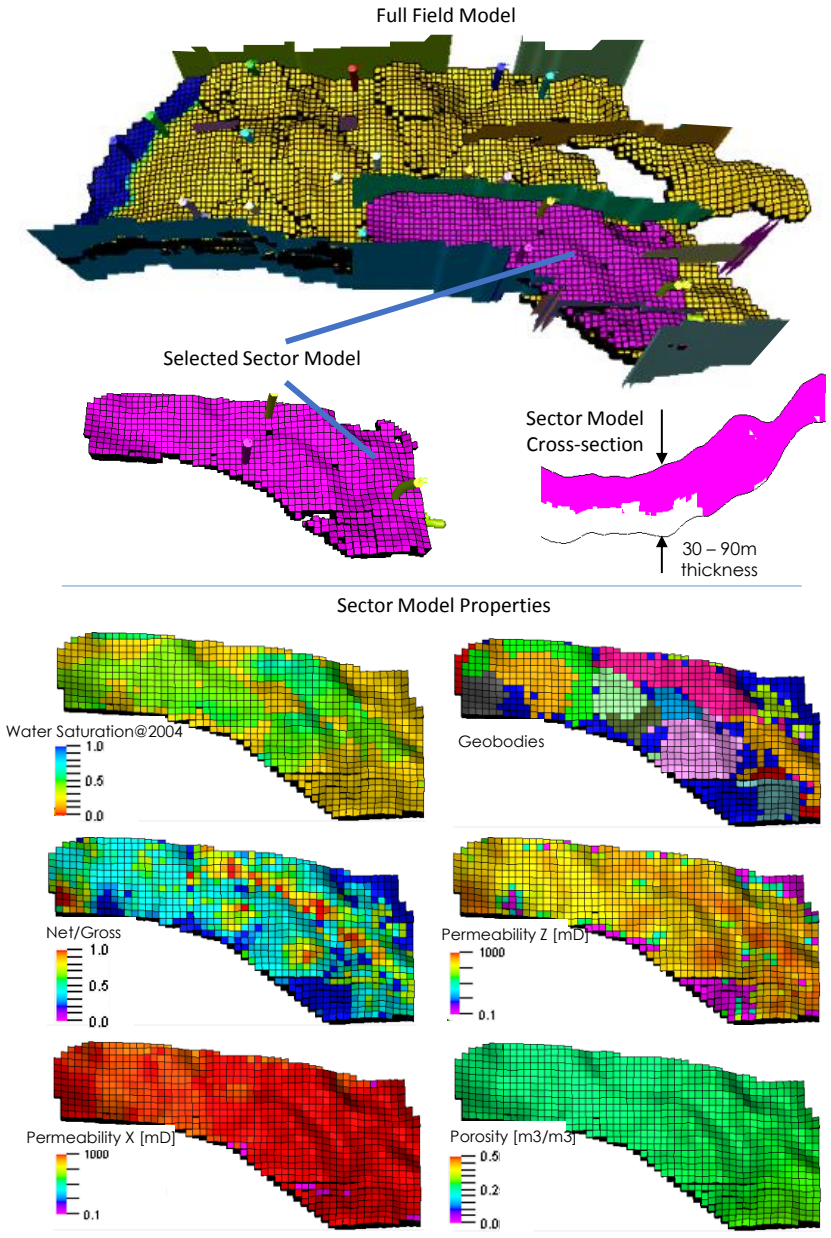

Figure 6.1: Selected reservoir simulation model sector to be history matched showing static properties and top layer view of water saturation distribution at the end of production period.

6.2.2 Integrated 4D Seismic and Production Data of the Sector Model

Production Data: Wells within the sector were operated between 1998 and 2008. The three wells, two injectors and one producer, were drilled and completed in the oil leg above the oil-water contact. Producer P2 was flowing throughout the period of ten production years, 1998 – 2008 (Figure 6.4). No significant water production occurred until 2005 (Well Water Production Rate, Figure 6.5), peaking between 2006 and 2007. Due to over-estimated reservoir connectivity, injected water from Well W1 could not properly support Well P2 leading to a decrease in reservoir pressure and gas exsolution between 1999 and 2003 as shown in the Well Gas Production Rate chart in Figure 6.6. The injector W1 (Figure 6.7) was injecting from 1998 to 2003 but was shut-in by 2003 after its pressure support was determined to be insufficient, a few months before the first monitor seismic survey was shot in 2004. The adjacent injector well, W4, was drilled in mid-2003 (Figure 6.8), providing reservoir pressure maintenance, immediately leading to reduced gas production and gas going back into solution. It was in operation from two years after the first monitor was shot and injected through to the end of 2008.

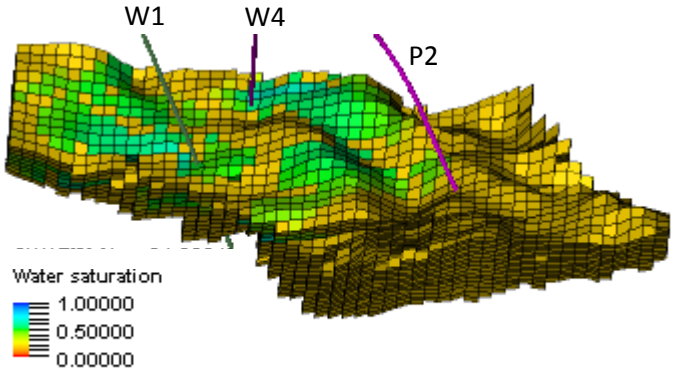

Figure 6.2: 3D view of Sector Model showing water saturation distribution at 2004 and producer (P2) and injectors (W1 & W4) drilled in oil leg.

While the estimated sector boundary flux from the full field model had minor discrepancies in the field pressure profile (Figure 6.3), the sector model correctly predicts the field model flow rates for the well of interest, Producer P2, as shown in Figures 6.4 – 6.6.

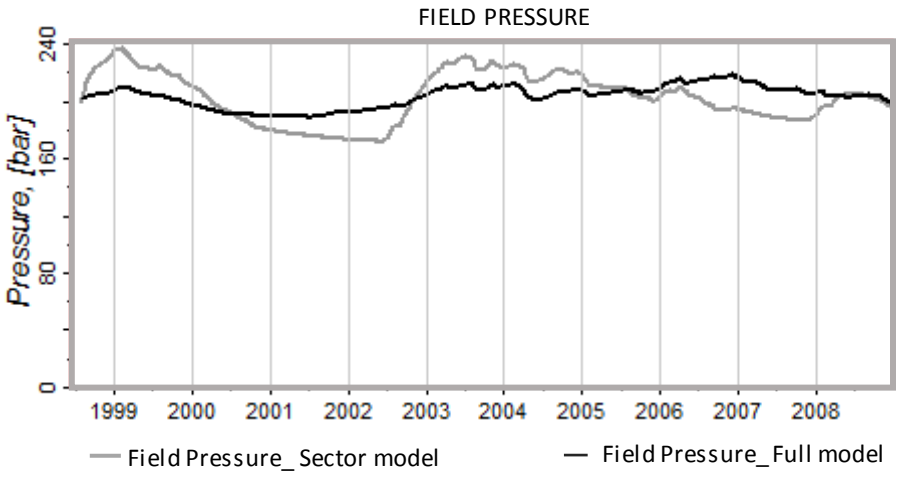

Figure 6.3: Field pressure for sector model and full field model

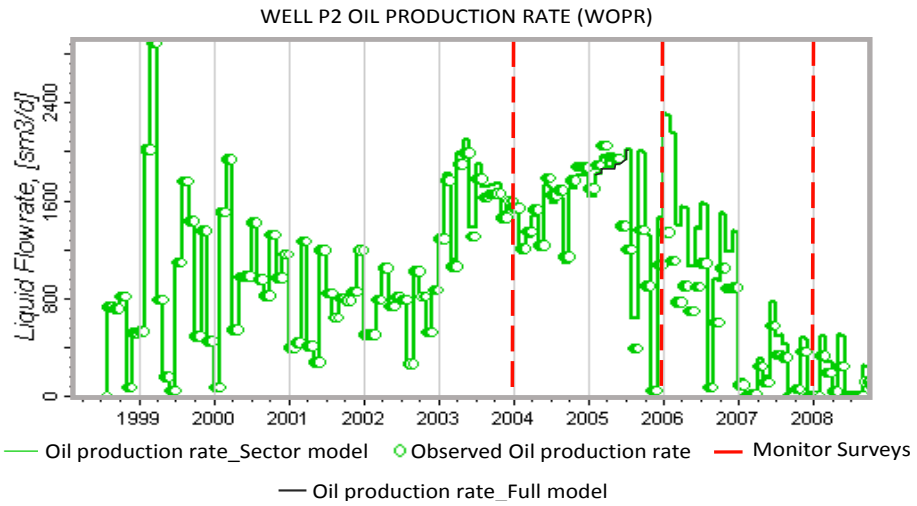

Figure 6.4: Well P2 oil production rate profile for sector model and full model including corresponding years seismic surveys were shot

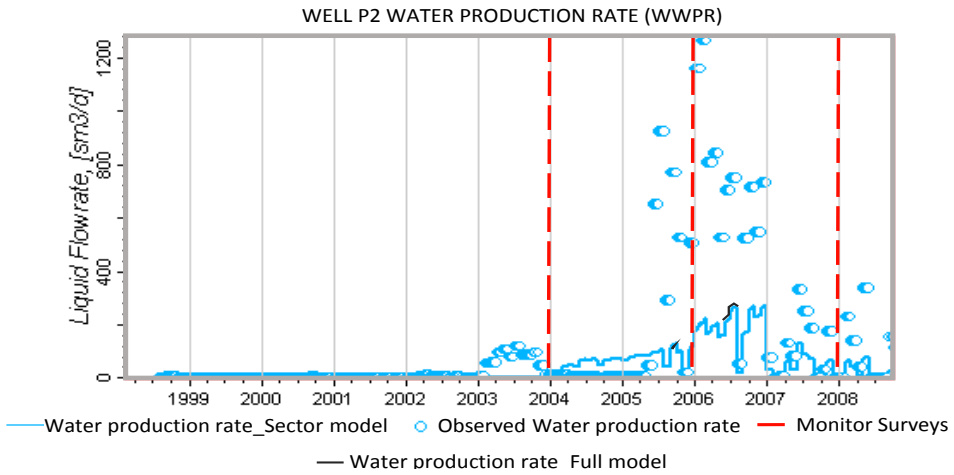

Figure 6.5: Well P2 water production rate profiles for sector model and full model including corresponding years seismic surveys were shot.

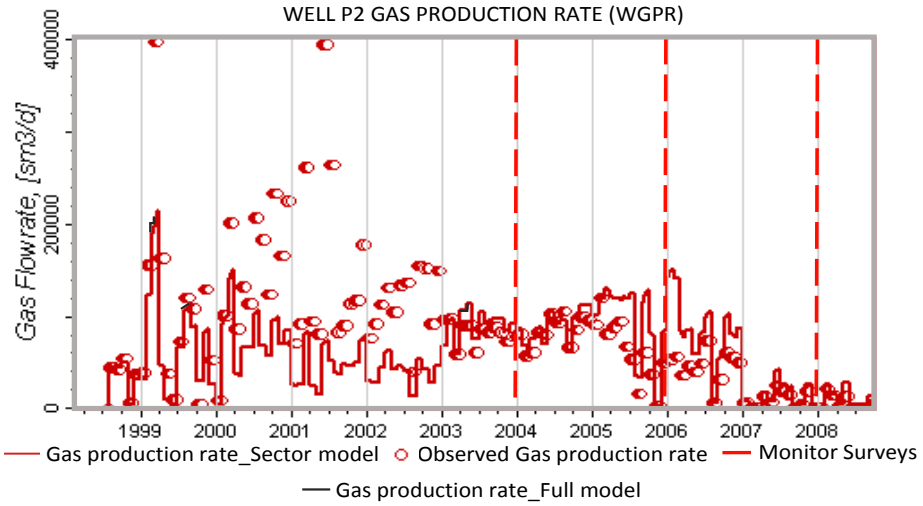

Figure 6.6: Well P2 gas production rate profile and corresponding years seismic surveys were shot.

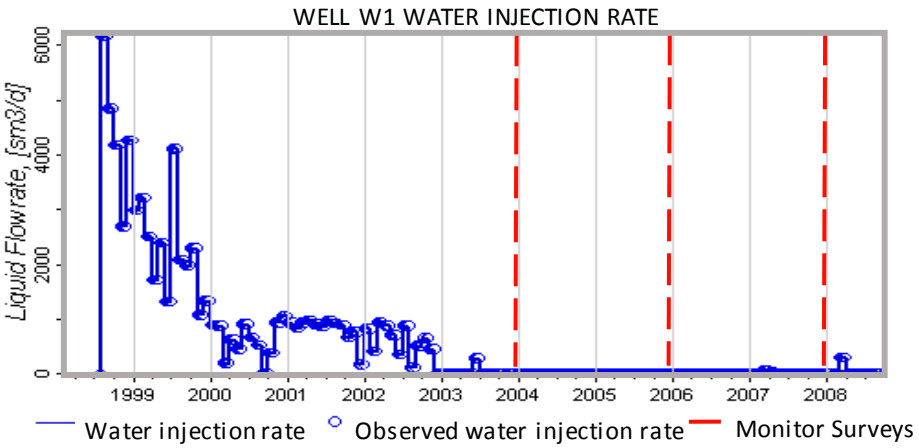

Figure 6.7: Well W1 water injection rate profile and corresponding years seismic surveys were shot.

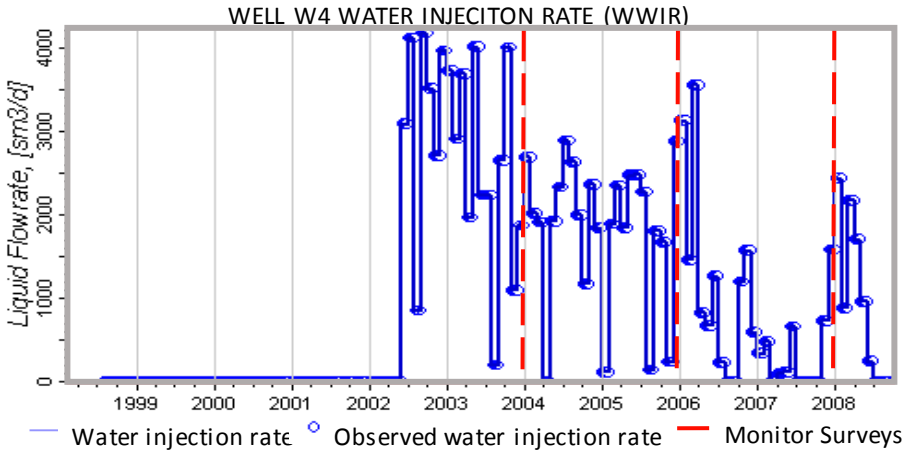

Figure 6.8: Well W4 water injection rate profile and corresponding years seismic surveys were shot.

Seismic Data: The observed 4D seismic attributes (sum of negative amplitude) were extracted for the T31 interval and are shown in Figure 6.9(a). The three 4D seismic maps indicate softening signals which propagate from the origin of well W4 in all three 4D maps for 2004, 2006 and 2008. A comparison to the synthetic seismic maps generated using *Sim2Seis* (Amini, 2014), from the base-case reservoir simulation model and shown in column (b) of Figure 6.9, indicates a mismatch in the softening and hardening signals characteristics of shape and magnitude. The increased water saturation signal illuminates the facies attributes and the water volume variations contained within the facies influenced by the net-to-gross ratios. These hardening signal heterogeneities are dependent on the seismic velocity sensitivity to the varied combinations of sand-shale ratios and water saturation content. Disparities between the well centric flood patterns of wells W1 & W4 from the observed and base-case 4D seismic maps, therefore, indicate uncertainties in the geological architecture of the facies in the base-case model as well as in the static properties defining the lithological composition of the well-centric formation. The volume of injected water determines the extent of waterflood propagation, and thus is proportional to the size of the flood pattern. As discussed in Chapters 3 and 4, the proportionality of the net volume of water in the reservoir to increased seismic impedance indicates that the magnitude of the increased amplitudes seen on the 4D seismic maps is proportional to the volume of water distributed within the flood pattern and directly linked to the dynamic flow properties of the reservoir.

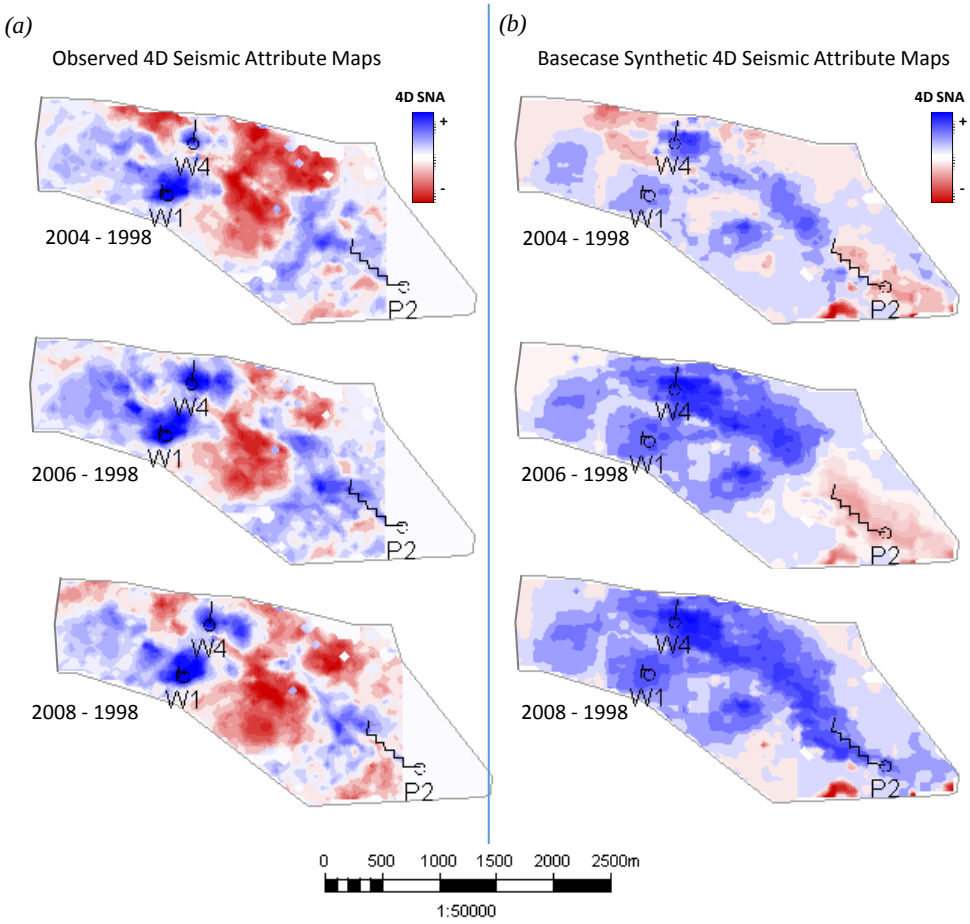

Figure 6.9: Observed and synthetic seismic attribute maps for the three time-lapsed periods, 2004-1996, 2006-1996 and 2008-1996.

Interpreting the 4D seismic signal:

The 4D seismic signals are validated by applying prior engineering judgment to filter expected reservoir conditions given the production activities at each monitor survey time. Main accompanying effects of reservoir water flooding are increased water saturation and increased reservoir pressure. These effects result in conflicting hardening and softening seismic signals with the ability to obscure each other depending on magnitude of pressure, presence of compartmentalisation, volume of water injected or petroelastic properties of the formation. The 4D seismic attribute maps in Figure (6.10a) show interacting hardening and softening signals around the two injector wells W1 and W4 through 2004 – 2008. The softening signal, however, is divided by a sealing fault into a compartment around well W4 and a relatively clean sand body (indicated in Figure 6.10c). Given the production history of significant gas exsolution in the years prior to the first monitor survey in 2004, the unvarying shape and magnitude of the softening signal within the high net sand region as well as the structural high location, the softening signal within the boundaries indicated in Figure 6.10(b) and (c) is interpreted to be decreased impedance

as a result of gas exsolution. The decrease in reservoir pressure prior to 2003 relative to pre-production reservoir pressure caused gas to come out of solution. Some gas is interpreted to have exsolved and risen to this high net sand region at a time coinciding with the shut-off of injector well W1. The shut-in of well W1 prevented pressure increase that could force the gas back into solution, causing the gas to be trapped in the local high through the years 2004 – 2008. The gas signal residing at a depth higher than the waterflooded sand bodies compromises a part of the waterflood pattern from well W1.

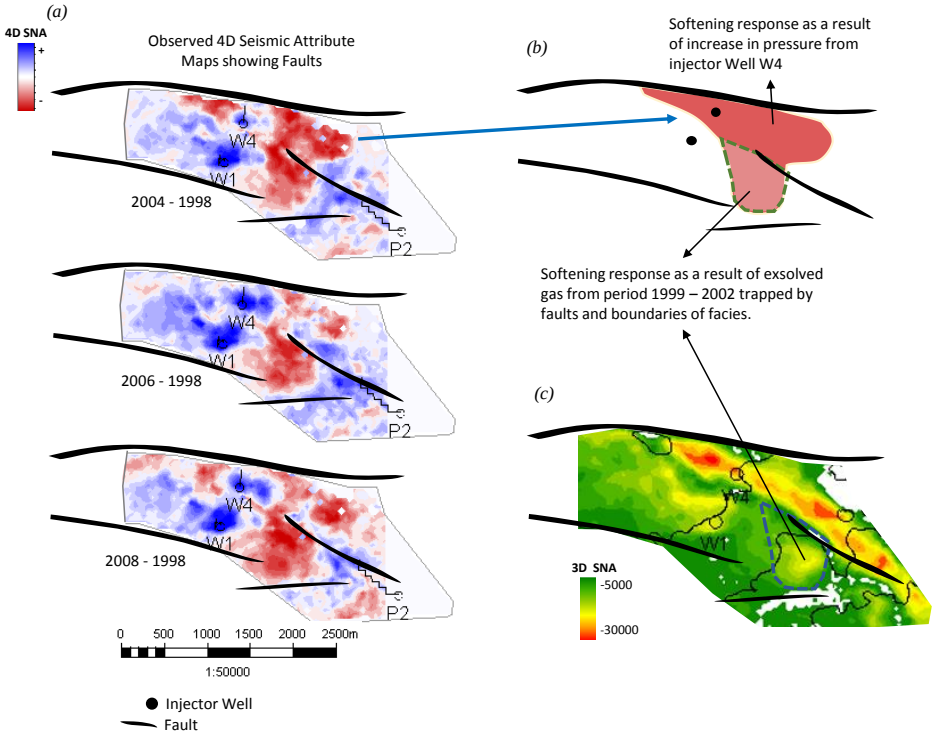

Figure 6.10: (a) 4D seismic attribute maps 2004-1998, 2006-1998 and 2008-1998 showing hardening-softening interaction. (b) illustration of pressure and exsolved gas signal (c) 3D seismic attribute map showing sand distribution and barriers.

Compartmentalisation of the geobody around well W4 appears to mainly restrict the high injection pressures to within the geobody. This has led to high injection pressures which have obliterated the water saturation signal from well W4 everywhere within the geobody but at the well. Fast, efficient pressure and saturation separation is still a challenge in the industry, especially with regards to the uncertain petroelastic model. Given the nature of the dataset, to successfully apply a local seismic history matching framework, a two-part hardening and softening binary approach is employed. This modifies the history matching objective to improving the combined match of the hardening waterflood pattern and the softening signal.

The size, pattern or magnitude of the section of waterflood hardening pattern obscured by the softening signal is uncertain. As the trapped gas signal is prior to the 2004 when the first monitor seismic was shot, it would be challenging to replicate this signal with the reservoir simulation, thus excluding this area from the objective function formulation. An intersection of signals as illustrated in Figure 6.11 would be defined as the binary signal, such that the waterflood pattern is restricted to only the waterflood pattern resolved by the 4D seismic signal excluding the uncertain areas. For the softening pressure signal, heterogeneity variations within the pressure signal, for example, the strong hardening signal around well W4 in spite of the strong pressure increase, is influenced by the petroelastic model. As the use of binary images aims to eliminate the uncertainties of using the petroelastic model, geostatistic variations that best match the *known* hardening signal of the waterflood pattern would have the same effects and apply to the improving the pressure signal heterogeneity match.

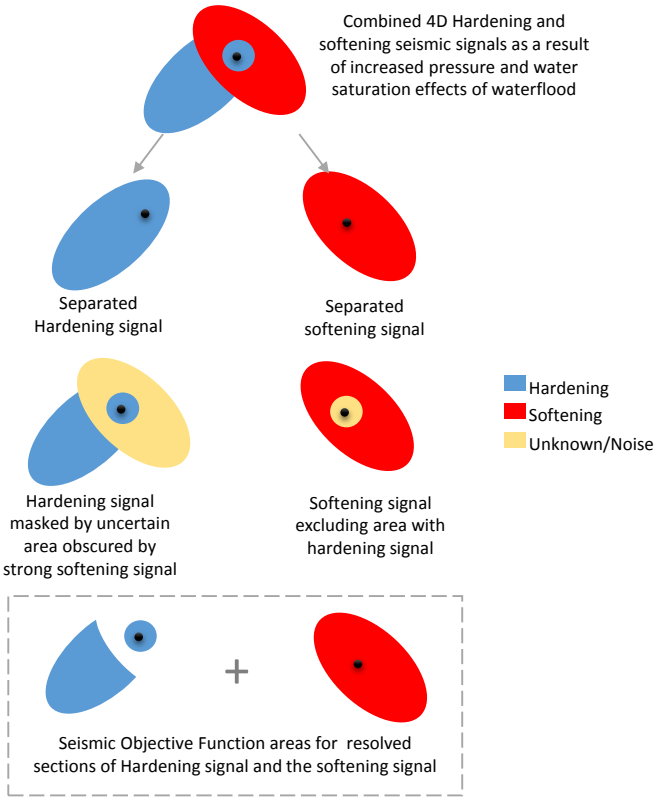

Figure 6.11: Illustration of the decomposition of the hardening and softening signals of a waterflooding well.

6.3 Noise Analysis

4D seismic data is made up of the 4D seismic signal and the non-repeatability noise. Following Kragh and Christie (2002) the normalised root mean square non-repeatability

noise metric (NRMS) can be used to quantify this seismic data uncertainty using the equation:

$$NRMS = \frac{2 \times \text{RMS(M-B)}}{RMS(M) + RMS(B)} \qquad (6.1)$$

where, RMS is the root mean square and M and B are the Monitor and baseline seismic surveys respectively.

The full segment of the Schiehallion under study has an average NRMS of 29% calculated from a 500 ms window of the overburden (Figure 6.12). This is excluding the south-east local high area of the sector with high NRMS values of up to 80% (Figure 6.12). Derived seismic noise-to-signal ratio based on the NRMS (Grion et al., 2000; Behrens et al., 2002) defines the level of resolvable true seismic signal given the noise with the Equation:

$$NSR = \frac{NRMS}{\sqrt{2} - NRMS^2} \qquad (6.2)$$

where NSR is the noise-to-signal ratio and NRMS is the non-repeatability noise metric.

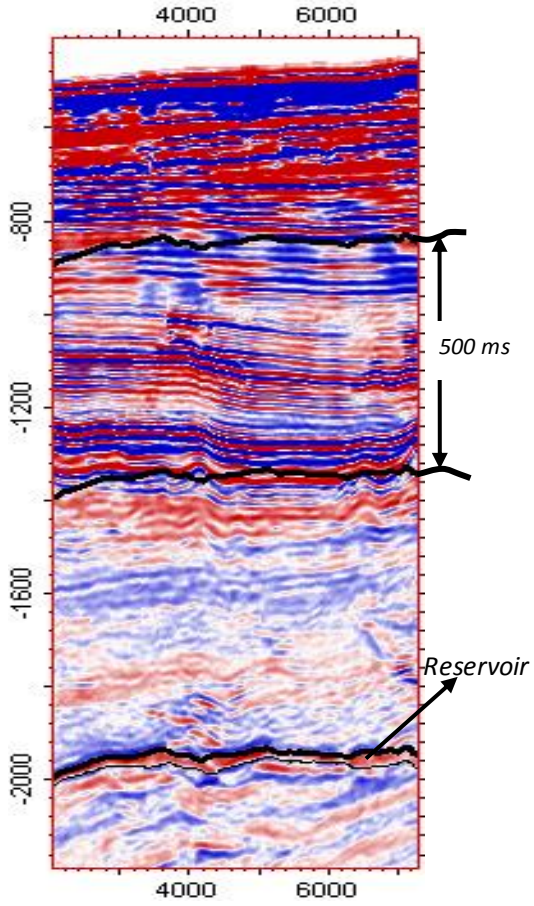

Figure 6.12: Seismic section showing 500ms window of overburden NRMS noise calculation.

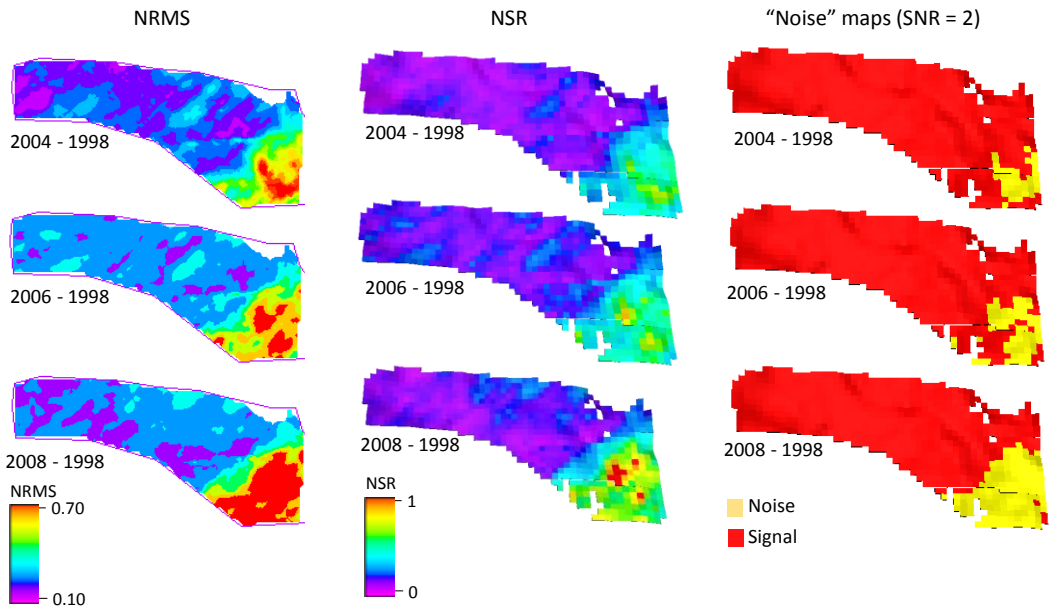

Figure 6.13: Noise maps for sector model showing NRMS, NSR (inverse of SNR) and binary images of thresholded NSR areas (threshold: SNR=2)excluded from seismic objective function.

A local seismic history match and update of waterflood patterns is dependent on good heterogeneity resolution which would be jeopardised by high noise. For this reason, the Signal-to-noise (SNR) is calculated to exclude areas of over 70% NRMS and with noise-to-signal ratios greater than 50% (SNR < 2). This high noise area, for which its binary equivalent is depicted in the last column of maps in Figure 6.13 as the yellow cells, is excluded from the seismic objective function in the history match loop.

6.4 Description of Reservoir Heterogeneity using Geostatistics

The study is applied to a clastic reservoir in a turbidite depositional environment. As reservoir heterogeneity exists at different scales of complex geological architecture following deposition, formation migration or production induced modification, a turbidite reservoir, therefore, largely tends to possess easily observable sand channels of meandering form on a larger scale, with interbedding, fractures and layer discontinuities within the channel on a smaller scale (Middleton and Hampton, 1973). A further microscale scale observation would reveal variations in porosity, pore size and pore connectivity, and different wettabilities evidenced by different contact angles leading to variations in permeability and relative permeabilities. This multi-scale characteristic of the reservoir combines to affect the reservoir's production capabilities, recovery and

ultimately increases the challenge of accurately predicting performance and forecasting production.

Data on multi-scaled reservoir characteristics is collected using varied tools in different formats. Core analysis provides high-resolution information of pore-scale rock and fluid interactions, well-logs provide sparsely located downhole information of geology and petrophysics at well locations, and lower resolution seismic provides information on large scale reservoir structure and changes to reservoir conditions following production. The reservoir properties from seismic data are typically derived from the inverse modelling of seismic signal to seismic velocities and impedances. Together, combined large scale inter-well heterogeneity data from seismic and finer scale downhole heterogeneity well data provides a complementary wholistic reservoir description.

To reduce reservoir evaluation uncertainties and improve production forecasting, it is important that the reservoir model is consistent with all available information at different scales. Incorporating 4D seismic data as part of the history matching process of characterising reservoir heterogeneity such that dynamic reservoir behaviour is replicated, improves the reliability of the updated reservoir model as it is conditioned to two forms of integrated data: sparse higher resolution well data and spatially extensive lower resolution seismic data. Time-independent static geological properties like lithology, porosity and sand-shale ratios, however, influence the time-varying dynamic fluid-properties resolved by 4D seismic data. This means that for realisations of petrophysical and geological properties to effectively match the integrated data in a history matching reservoir update cycle, constraints to dynamic data are applied to achieve realistic reservoir representations.

Roggero and Hu (1998) and Le Ravalec et al. (1999) developed the Gradual Deformation method that creates reservoir realisations matching both geological and dynamic data by continuously modifying the realisations while maintaining consistency with geological data. Spatio-temporal Gaussian random functions representing realisations of the reservoir are built by combining independent standard Gaussian random functions to generate a new realization preserving all geostatistical properties ((Roggero and Hu, 1998; Ding et al., 2007; Ding and Roggero, 2009)). Using the structural parameters of the

reservoir stochastic model, Gradual Deformation allows realisations to be deformed with an algorithm that modifies the covariance operator simultaneously with realization generation while honouring set dynamic data constraints. This method has been applied successfully in general seismic history matching (Roggero and Hu, 1998; Roggero et al., 2007) and in local seismic history matching cases (Ding and Roggero, 2009). Though the Gradual Deformation method has been successfully applied in several cases, the unavailability of key statistical parameters of the available dataset, a prerequisite for the Gradual Deformation method, eliminated this approach as a history matching geomodelling update option in this study. The Collocated Co-kriging method of integrating well log data and seismic data in reservoir property prediction is considered instead.

6.4.1 Gaussian Simulation with Collocated Cokriging:

Considering well-logs data as 'hard' data and seismic data as 'soft' data, multiple possible generations of the reservoir properties are achieved with geostatistical simulation in a combination of a regression algorithm and stochastic simulation, honouring the variation in vertical resolution between well logs and seismic data. The Gaussian Simulation with Collocated Cokriging algorithm proposed by Xu et al. (1992) as a more stable alternative to full cokriging, efficiently deals with 3D complex reservoir systems (See Appendix B).

For the history matching loop in this study, the specified parameters employed in the collocated cokriging are a product of 3D and 4D seismic data analysis regarding the reservoir compartments with dynamic changes of water flooding and pressure variations. The Schiehallion field reservoir simulation model used is as described in Chapter 2, section 2.5.1. As the net-to-gross property closely represents the seismic data (Figure 2.8) it is deemed to be a reliable seismic interpretation of the combined reservoir compartments and sand-shale distribution for the reservoir in this study. For a waterflood, variations in the shape of the drainage pattern are influenced by the geology of the reservoir, static properties of net-to-gross, porosity, and geobody transmissibility. As a result, all potential barriers to flow or pressure are factors of interest. The mapped sand geobodies in the Schiehallion are interspersed with shale deposits, resulting in varying levels of interaction and connectivity between geobodies. This resulted in the seismic-interpreted geobodies being identified as the most uncertain property affecting

connectivity in the Schiehallion (Govan et al., 2006). The significant uncertainties of the geobody transmissibilities was thus identified as a main parameter important for perturbation and update in the history matching process. Given the inaccessibility of the deterministic geological modelling step of creating the geobody distribution, iteratively perturbing the shape and structure of the geobodies as part of the history matching loop was a challenge mitigated by utilising transmissibilities of all geobodies in the reservoir sector as input parameters to the history matching loop.

The net-to-gross distribution is a major contributing factor that influences the waterflood pattern attributes and is closely correlated to the geobodies (Figure 2.8). Using the Gaussian Random Function Simulation approach, available well logs as the primary variable (hard data) and the seismic interpreted NTG distribution as the secondary variable, (soft data), the Collocated Cokriging method was used to generate net-to-gross realisations. Following analysis of the seismic geological properties, the collocated cokriging was set up using correlation lengths of 600 m in the x-direction with an azimuth of -69, 400 m in the y-direction and 8 m in the z-direction.

6.5 The History Matching Framework

The history matching loop, for a multi-objective optimisation allowing more than one simulation output to be optimized, is designed as an automatic chain of geostatistical and petrophysical property perturbation, flow simulation and seismic data objective function calculation. The workflow is shown in Figure 6.16 and describes the seamless process flow chain connected to simultaneously carry out each step in parallel through iterations, with the result of each run ranked relative to the objective function. The history matching process facilitated by the loop follows the flow of:

- Definition of the objective function to measure the mismatch between the reservoir simulation models and the observed history.
- Model analysis to determine potential parameters for perturbation using knowledge of the field characteristics and uncertainties.
- Identification and selection of the most influential parameters for input to the optimisation problem, using the design of experimental design method to get the maximum amount of information through the lowest number of samples.

- Generation of an ensemble of models incorporating selected parameters within the defined model constraints, accounting for uncertainties and eliminating bias.
- Activation of the history matching process to determine the ensemble of improved models with the least objective function value.

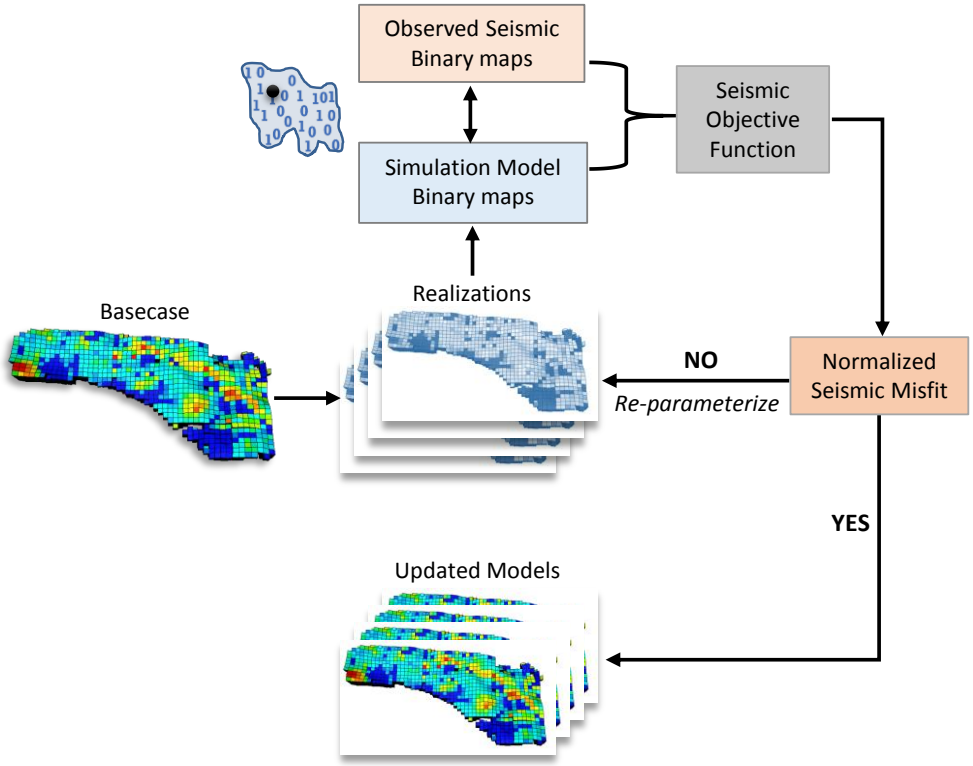

Figure 6.14: Automatic seismic history matching loop for static property update using geostatistics and matching to 4D seismic data using binary images.

A suite of Schlumberger industry software consisting of Petrel, Eclipse and MEPO and connected to a combined objective function calculator written in Python programming language, was used to facilitate the history matching workflow:

i) **MEPO** - A multiple realisation optimiser, creates an initial ensemble with configurations governed by the latin hypercube method and the input parameters. A correlation coefficient within the defined range is randomly generated for each ensemble member. The correlation coefficient is fed to ii) **Petrel** - for generation of petrophysical properties using geostatistical simulation. Each Petrel pass involves the simulation of a new NTG property using collocated cokriging between well logs and seismic (in the form of a reservoir property) and using the generated correlation coefficient from MEPO. The new NTG property completes the ensemble member which is then run using iii) **Eclipse** – a black oil simulator. The outputs from Eclipse are dynamic saturation and pressure properties for each report step. The report steps in this case correspond to available

seismic survey years. iv) **Python** programming – a python code analyses the Eclipse result and extracts the relevant information to create the water saturation maps depicting waterfloods. These maps are then converted to binary images following the methodology outlined in Chapter 5. A linear model of contributing seismic objective functions constitutes the misfit function computation between observed and simulation maps. The calculated misfits for the ensemble loop back to MEPO to be optimised using an evolutionary algorithm.

6.5.1 Formulating the Seismic Objective Function

Figure 6.17 shows the 4D observed seismic attribute maps for the three 4D surveys and its corresponding binary images. For scale comparability, the 4D seismic maps are rescaled to the simulation model grid, prior to conversion to binary images. Appropriate thresholds were determined using the material balanced iterative method discussed in Chapter 3 and the seismic maps converted to binary maps of ones and zeroes with the value one representing areas of strong water saturation or pressure signal by filtering the maps through the predetermined seismic thresholds, the hardening and softening signals are decomposed into respective binary images of pressure and saturation for the three available 4D seismic surveys: 2004, 2006 and 2008.

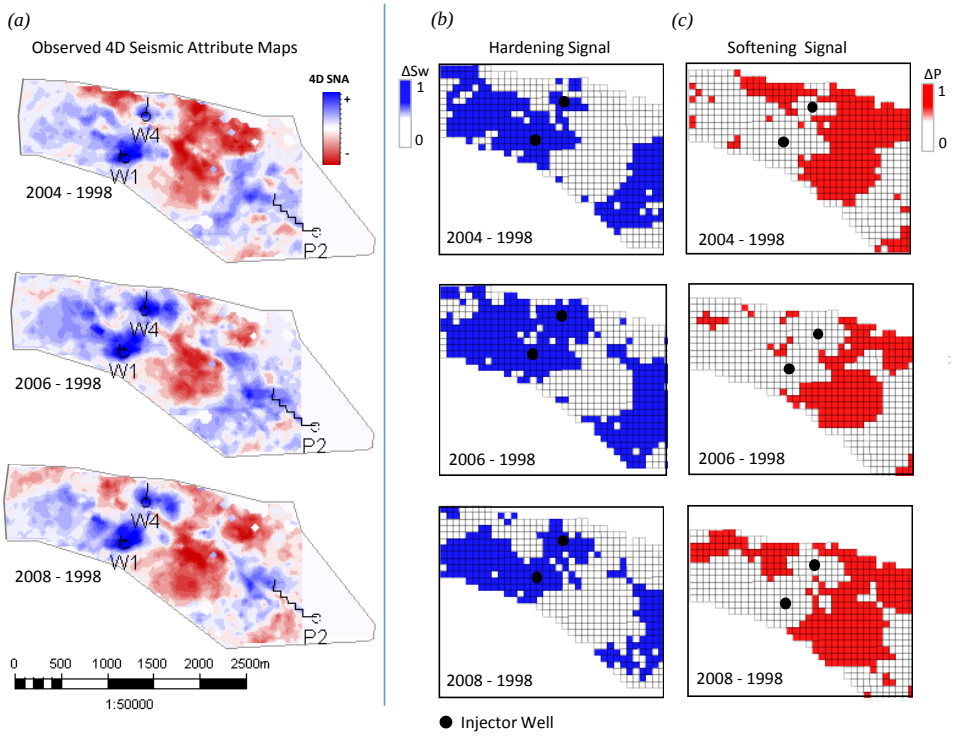

Figure 6.15: Observed 4D seismic attribute map decomposed into binary hardening and softening signals

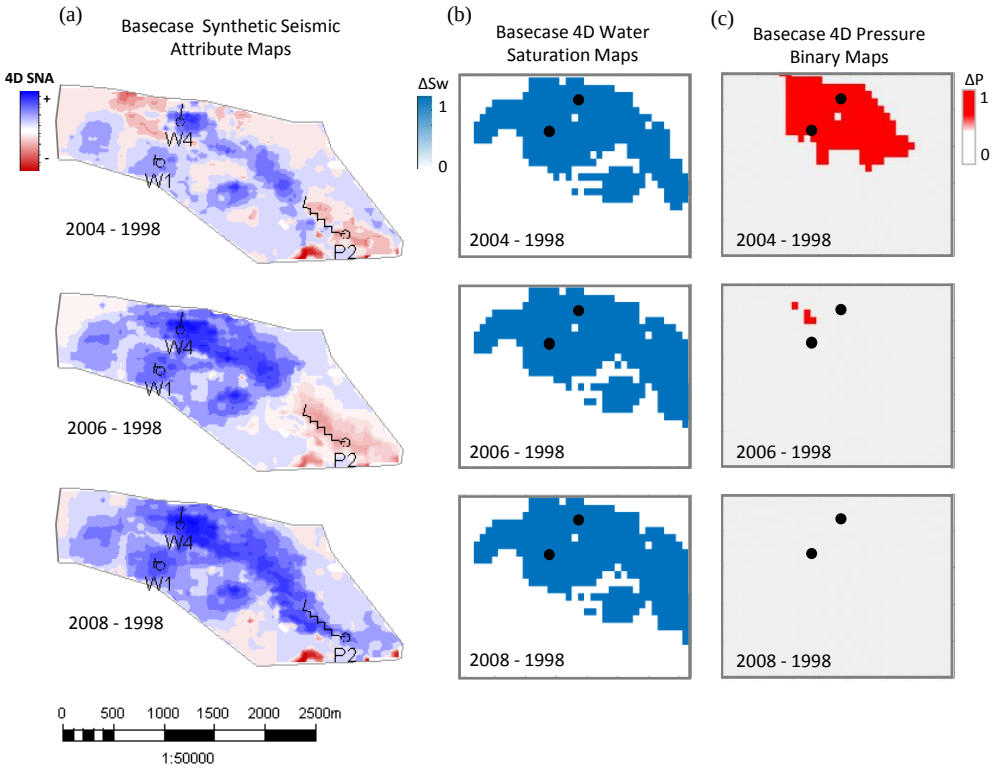

Figure 6.16: Base-case 4D synthetic seismic attribute map showing hardening and softening signals alongside the binary maps from 4D pore-volume weighted water saturation and pressure maps from the base-case simulation model.

The main objective is to determine the best values of the well-centric reservoir static and dynamic properties which replicates both the observed 4D seismic interpreted signals by minimizing the mismatch between the composite binary maps, with a combined improvement of the production data match. The Hamming Distance method introduced in Chapter 5 which exhibited better results with regards to binary map match accuracy, is used to formulate the seismic objective function formulation. The global seismic objective function, SOF, is defined as a summation of all the misfit contributions of the water saturation and pressure signal map pairs for each survey:

$$SOF = \frac{1}{2}\left\{ w_{sw} \sum_{i=1}^{nseis} \left| \left(m_{i,j}^{obs} - m_{i,j}^{sim} \right) \right| \right\}_{sw} + \frac{1}{2}\left\{ w_{pr} \sum_{i=1}^{nseis} \left| \left(m_{i,j}^{obs} - m_{i,j}^{sim} \right) \right| \right\}_{pr} \quad (6.3)$$

where $nseis$ is the number of seismic surveys to be matched, $m_{i,j}^{obs}$ and $m_{i,j}^{sim}$ are the observed and simulated binary maps and the coefficients, w_{sw} and w_{pr} are the weights assigned to the water or pressure binary maps. In this case, both the saturation and pressure data are assigned equal weights.

The base-case model Well Bottomhole Pressure (WBHP) profiles and correlations to the observed WBHP as a measure of match quality for the three wells are shown in Figures 6.19 – 6.24. For the fluid-rate controlled wells, the well bottomhole pressures for the producer, P2, and two injectors, W1 & W4, in the sector model show poor match qualities between the simulated initial model and observed production data with correlation coefficients of 0.04 – 0.46. It is expected that the local seismic history matching exercise using binary images would result in improvements of these production data match qualities.

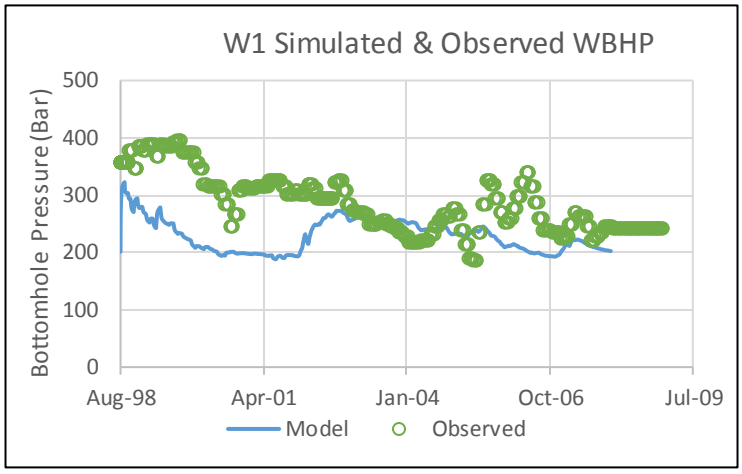

Figure 6.17: Well W1 simulated and observed well bottomhole pressure profiles

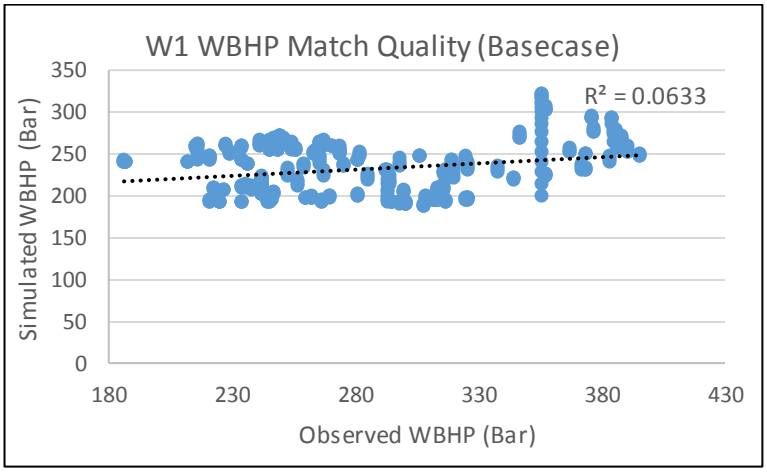

Figure 6.18: Well W1 simulated-observed crossplot indicating well data match quality

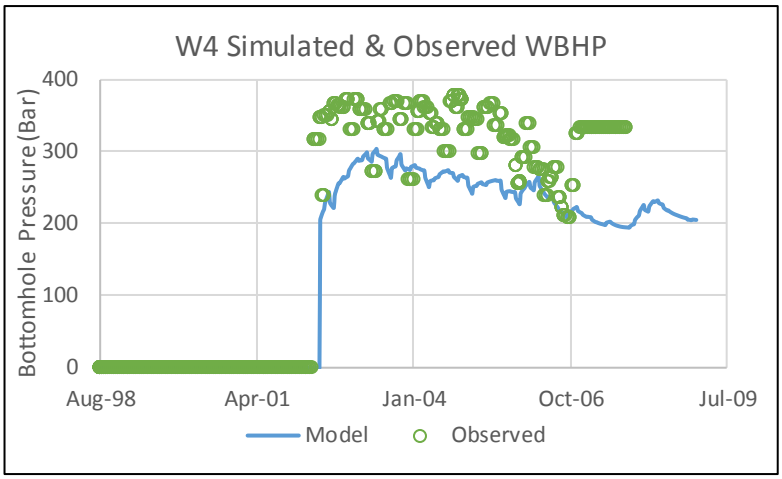

Figure 6.19: Well W4 simulated and observed well bottomhole pressure profiles

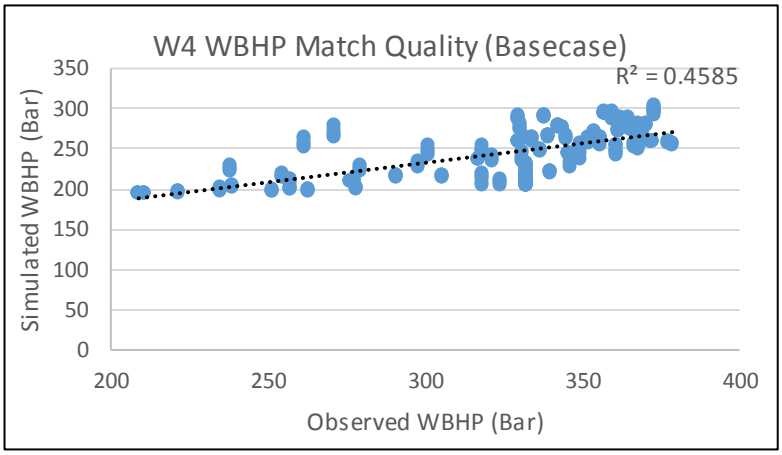

Figure 6.20: Well W4 simulated-observed crossplot indicating well data match quality

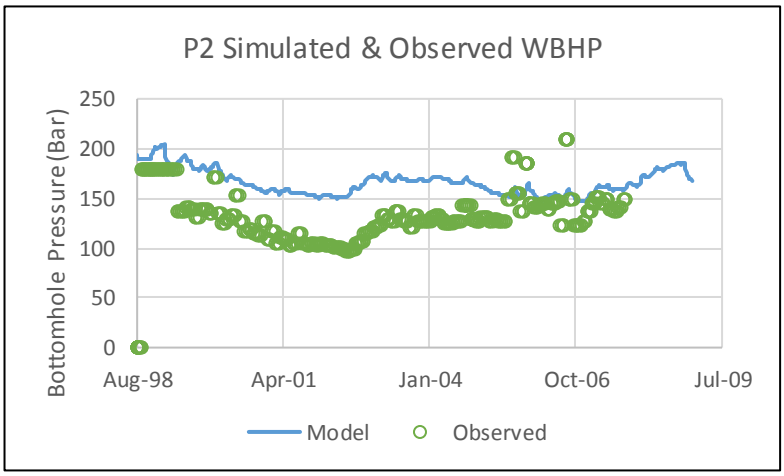

Figure 6.21: Well P2 simulated and observed well bottomhole pressure profiles

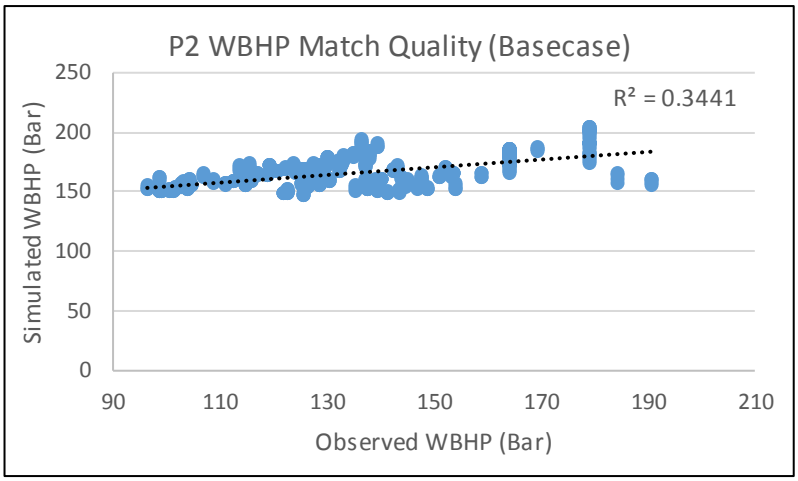

Figure 6.22: Well P2 simulated-observed crossplot indicating well data match quality

6.5.2 Parameterization and Sensitivity

Initializing a history match begins with identifying the factors that could influence the simulation flow responses. These factors could be static, dynamic reservoir properties, or engineering properties. Sensitivity analysis on flow simulations of different configurations of input factors is used to assess the uncertainty related to the objective function. This helps quantify how the uncertainties of the input factors affect the uncertainty of the simulation response, identifying and maximising parameters with the greatest impact on the reservoir behaviour. Experimental Design, a formula that describes the configuration of each factor in a series of simulation runs such that maximum information is obtained from an optimum number of simulation runs analyses the impact of input parameters on a process (White et al., 2001; Shams, 2016). It is therefore, an efficient way of guiding the choice of samples where a lower number of samples are chosen in the design space to achieve the maximum amount of information - ultimately reducing the number of simulations that would typically be required for a sensitivity study by about 30-40% (Egeland et al., 1992). There are different kinds of Experimental Design. In the simplest linear design, varying one parameter at a time, if factors which influence the flow responses (response variable), y, are given as $x_1, x_2, x_3, \ldots x_n$, the function that relates these factors to the response variable is the relationship computed by the reservoir simulator. If $y = f(x_1, x_2, x_3, \ldots x_n,)$, for n factors, the Experimental Design formula approximates the function with a polynomial, $y = b_0 + b_1 x_1 + b_2 x_2 +$

$b_3x_3 + \cdots + b_nx_n$, determining the appropriate coefficients from a number of experiments and minimising the misfit between the reservoir simulator and polynomial.

Experimental Design is used to obtain sensitivities of the reservoir simulation model to the input factors. It also allowed for an analysis of a reasonable range of feasible parameter combinations to determine the level of interaction and dependencies between factors on the reservoir flow response. Tornado plots in Figure 6.24 show the most sensitive input factors in order of decreasing influence for the partial objective functions of seismic water and pressure for the series of 4D seismic surveys: 2004, 2006 and 2008. A combination of sector-wide and reservoir compartmentalised input factors were considered. These are distinguishable by the nomenclature where 'GEOB' refers to a geobody specific parameter and 'SEC', a sector wide parameters. Properties such as porosity, permeabilities in the x, y and z directions, pore volumes and critical water saturation were included in the sensitivity study. Each geobody is labelled by its unique number, shown in Figure 6.23, such that the porosity of a geobody with the label *219* would be 'GEOBPORO219'. For transmissbilities across geobodies, the transmissibility between geobody 219 and geobody 227 would be defined as 'GEOB219227'.

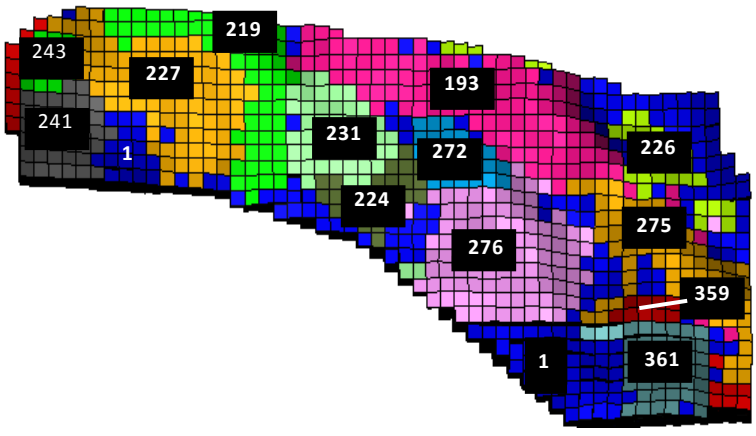

Figure 6.23: Reservoir simulation sector showing geobodies and their corresponding labels

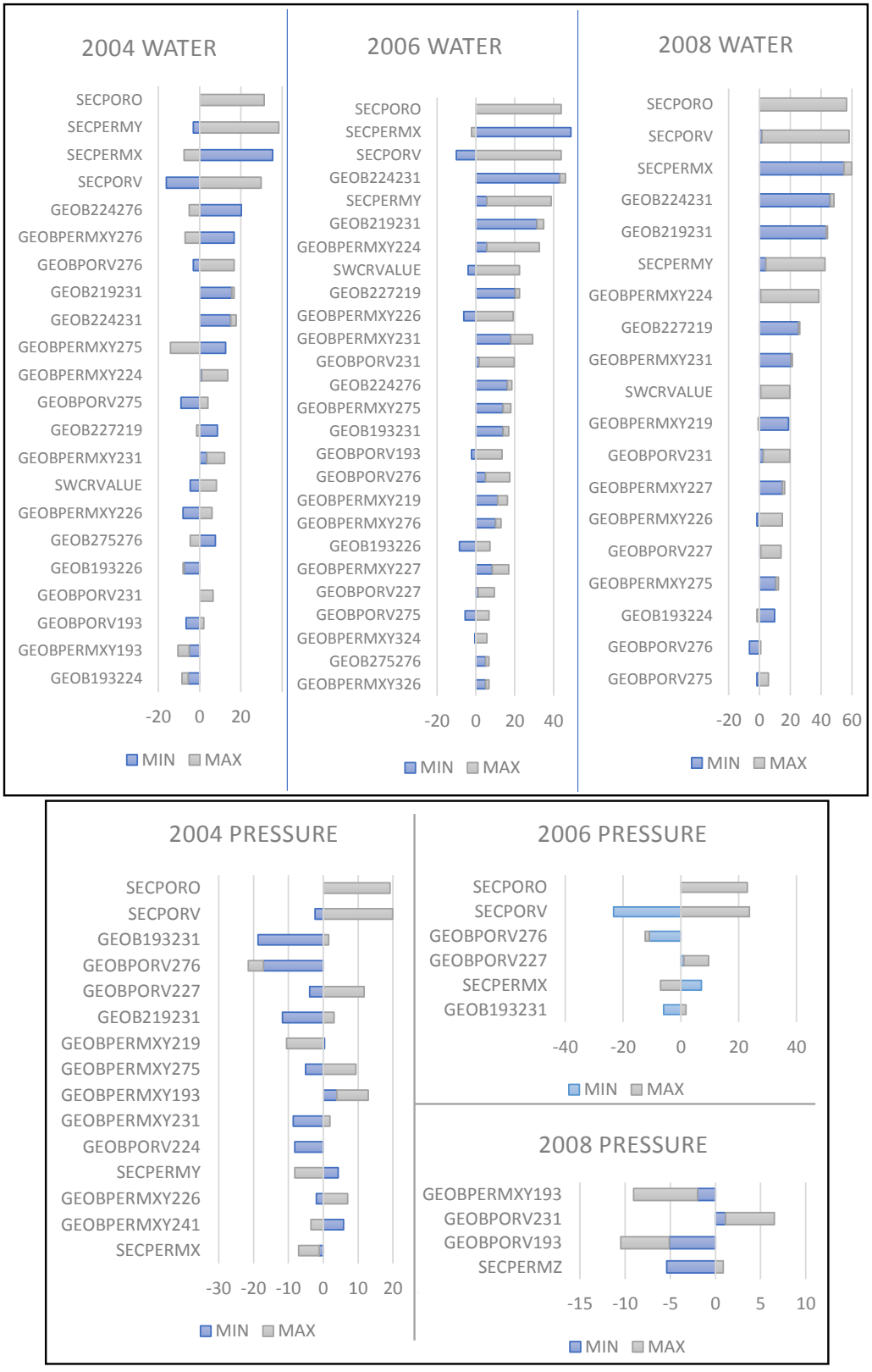

Figure 6.24: Potential input parameters in order of decreasing influence on the partial seismic objective function for top- water saturation and bottom-pressure for surveys 2004, 2006 and 2008

For 55 uncertain parameters, the 34 most influential parameters for all contributing responses of increased water saturation and pressure for the three 4D seismic surveys considered we selected as input parameters.

Following selection of input parameters, and similar to the approach of quantifying uncertainties of reservoir description in history matching in (Zabalza-Mezghani et al., 2001; Maschio and Schiozer, 2005; Schulze-Riegert and Ghedan, 2007; Maschio and Schiozer, 2016), the Latin Hypercube Experimental method was used to sample the parameter space ensuring that the breadth of the uncertainty domain was explored without bias. Latin Hypercube Experimental method is considered one of the most efficient statistical methods of generating samples of factor values from a multidimensional distribution (Maschio et al., 2008; Shams, 2016), and applied widely in history matching cases (Schulze-Riegert et al., 2002; Feraille et al., 2003; Roggero et al., 2007; Maschio et al., 2008). It essentially involves dividing the parameter space into intervals of the same length per factor so that the number of factor values from each interval is proportional to the probability of that factor value occurring in that interval.

For a population size of 16 and 34 uncertain parameters, a uniform probability density function was defined for the initial input parameter search space. This allowed for a wide search of possible solutions. The optimisation completion criterion was set at 992 models and 62 generations. Given the limited sector area and geologically unrealistic conditions that could arise from possible combinations of extreme input parameters (e.g. Zero transmissibility for main connected geobodies around an injector), termination conditions were specified to reject such inappropriate models from the search space. Table (6.1) lists the input parameters and their set ranges used in the history matching. Emphasis was placed on the over-estimated connectivity of the reservoir geobodies within the sector, specifying a range of 0 – 1.1 to allow a search between no and full geobody transmissibilities.

Parameter	Min	Max
GEOB193224	0	1.1
GEOB193226	0	1.1
GEOB193231	0	1.1
GEOB193272	0	1.1
GEOB193275	0	1.1
GEOB193276	0	1.1
GEOB219224	0	1.1
GEOB219231	0	1.1
GEOB224231	0	1.1
GEOB224276	0	1.1
GEOB226275	0	1.1
GEOB226324	0	1.1
GEOB227219	0	1.1
GEOB229241	0	1.1
GEOB231276	0	1.1
GEOB272276	0	1.1
GEOB275276	0	1.1
GEOB275361	0	1.1
GEOBPERMXY193	0.1	2
GEOBPERMXY201	0.1	2
GEOBPERMXY219	0.1	2
GEOBPERMXY224	0.1	2
GEOBPERMXY226	0.1	2
GEOBPORV227	0.5	1.1
GEOBPORV231	0.5	1.1
GEOBPORV272	0.5	1.1
GEOBPORV275	0.5	1.1
GEOBPORV276	0.5	1.1
NTG_CORR	0.7	1.1
SECPERMX	0.5	2
SECPERMY	0.5	2
SECPERMZ	0.5	2
SECPORV	0.5	1.1
SECPORO	0.5	1.1
SWCRVALUE	0.177	0.42

Table 6.1: Input parameters showing minimum and maximum limits used in history matching.

For each simulation run, a new net-to-gross realization is first generated by perturbing the correlation coefficient, *c*, for the collocated co-kriging between well logs and seismic interpreted facies and included for each generation member. The correlation coefficient range 0.7 – 1.1 was informed by a prior sensitivity test identifying a correlation coefficient of 0.7 as the limit below which correlation to the seismic interpreted geological architecture including sand channel characteristics are lost. Examples of NTG realisations with varying correlation coefficient, *c = 0.2 – 0.8*, are shown in Figure 6.25.

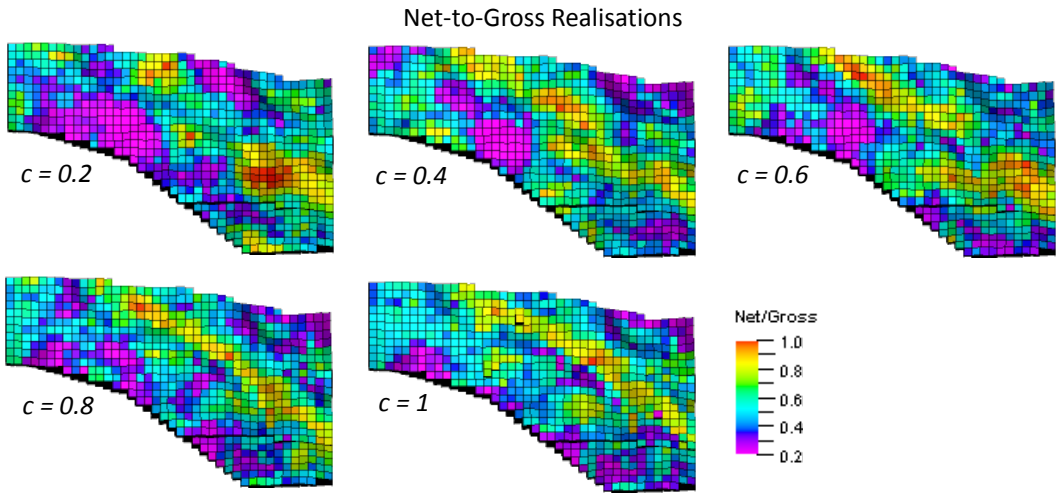

Figure 6.25: Net-to-gross realisations generated with collocated cokriging using correlation coefficient variation c = 0.2 – 0.8.

6.5.3 Running the History Matching

Outputs from each reservoir flow simulation run are processed by the bespoke Python code to:

- Generate pore-volume weighted maps of simulated increased pressure and increased water saturation.

- Convert pore-volume weighted maps to binary maps using predetermined thresholds.

- Compute the seismic objective function by determining the misfits between the simulation binary maps and observed binary seismic maps using the *Currents Measurement Metric* method. The partial objective functions are calculated independently for each water saturation and pressure survey within the defined objective function area. Normalised linear combinations of the partial objective

functions make up the global objective function which is looped back to the optimisation process for ranking according to least global misfit.

Figure 6.26 shows the comparison of the observed and simulated binary water saturation (a) and (b) and pressure maps (c) and (d). The water saturation maps are masked to only reveal flood pattern within the objective function area, while the pressure maps include areas within the softening signal that overlaps with the hardening signal. The ultimate objective of the history matching exercise is to determine the best configuration of select input parameters using optimisation and geostatistical simulation that provides the best match between maps Figure 6.26(a) and (b) and between Figure 6.26(c) and (d).

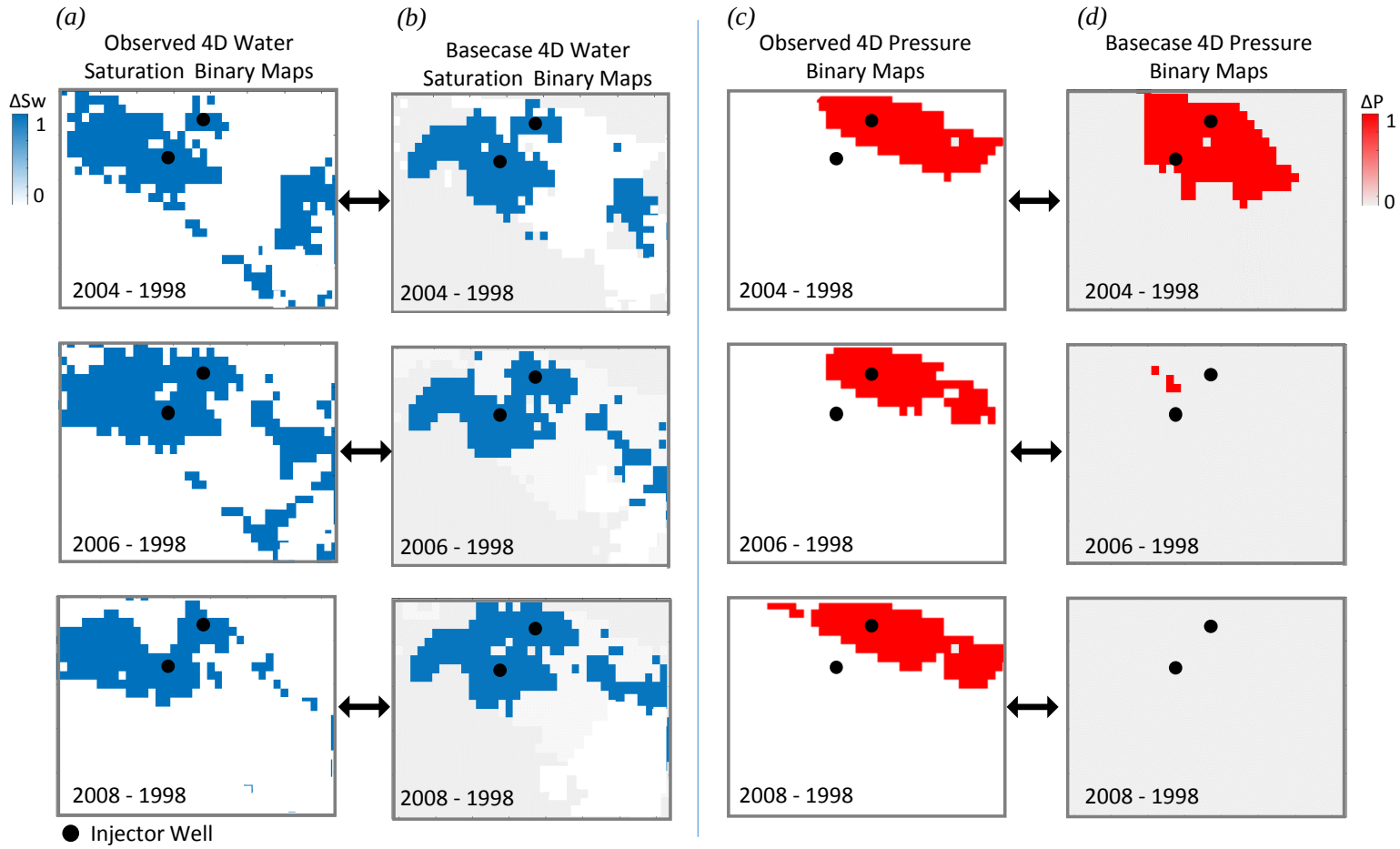

Figure 6.26: Base-case binary simulation maps compared to the observed binary seismic maps for water saturation (a) & (b) and pressure (c) & (d). Water saturation maps (a) and (b) are masked by excluding softening signal and high noise regions.

6.6 Results

Following the history match, updated maps from a member of the best-case models are compared to the observed binary maps and shown in Figure 6.28 and 6.29. Figure 6.30 compares improvement of the Well Bottomhole pressure profiles of the best-case model to the base-case model with the observed WBHP profile as a reference. Using the Hamming Distance in misfit computation, the normalised objective function evolution trend in Figure 6.27 shows a reduction in the objective function value by 50% after 21 iterations.

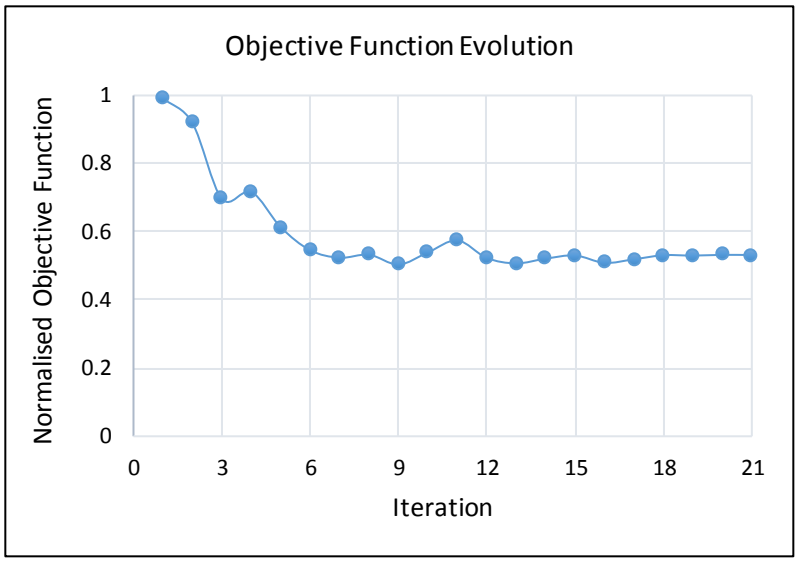

Figure 6.27: Objective Function Evolution showing 50% reduction in objective function value.

Update of the well-centric properties have modified the waterflood propagation such that the hardening binary maps (Figure 6.28 (a) & (b)) show an improvement in the general pattern shape to the observed binary maps. Excluding the masked area obscured by the softening signal, the "certain" waterflood pattern exhibits a more realistically matched waterflood pattern to the observed binary map. Updates in the transmissibilities have modified the flood pattern such that the flood does not extend past the pressure excluded area as in the history and base-case model maps. This could be as a result of the counterproductive pressure partial objective function influence, as updates to the model to match the pressure signals have impeded the waterflood.

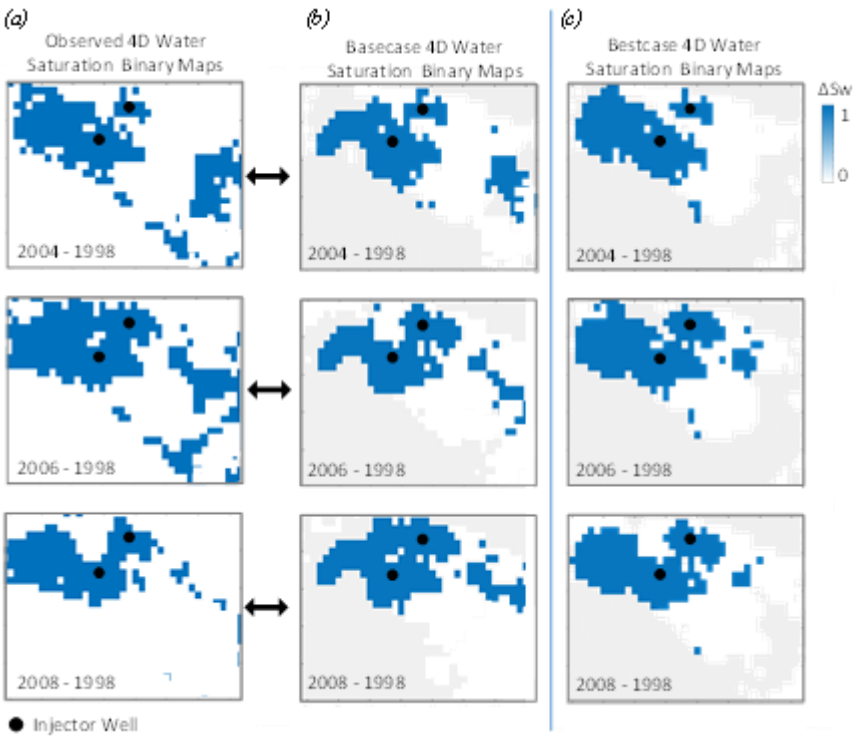

Figure 6.28: Binary hardening maps (masked) showing (a) observed maps, (b) base-case maps and (c) updated best-case maps.

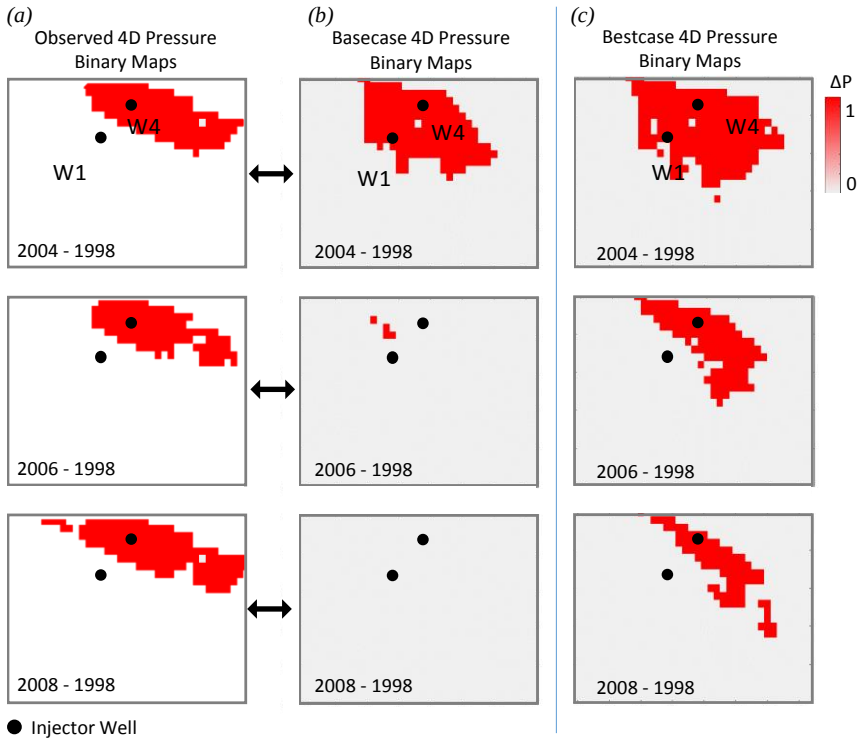

Figure 6.29: Binary softening maps (masked) showing pressure propagation for all surveys in (a) observed maps, (b) base-case maps and (c) updated best-case maps.

As the shape and structure of the geobodies could not be statistically modified as part of the history matching, limitations were placed on the achievable flood pattern shape as

variability was mainly confined to the boundaries of the geobodies. It was also a challenge to match the fine detail of the observed flood pattern boundary, as anomalies along the observed binary map boundary are possibly due to transition or seismic processing noise or higher resolution heterogeneity not captured by the geostatistical simulation of the net-to-gross property. In the case of the pressure maps (Figure 6.29), update of the well-centric properties have led to an increased reservoir pressure around both wells W1 and W4 in 2004 and gradually reducing softening responses between 2006 and 2008. This is a marked improvement from the base-case which had no significant softening response for 2006 and 2008 and thus did not replicate the observed 4D seismic signal.

From the observed WBHP profile, wells W1 and W4 begun injection at very high pressures of 150 - 180 bar greater than the preproduction average reservoir pressure of 200 bar. High injecting pressures were maintained at both wells until well W1 was shut-in in 2003 prior to the acquisition of the 2004 monitor survey, and injecting pressures at well W4 declined between 2006 and 2008. After approximately one year of the shut-in of well W1, we expect the injecting pressures to have dissipated by the time of monitor acquisition in 2004. The best-case model reasonably simulates a large area of increased pressure influence for well W4 which slightly decreases by 2006. The discrepancy between the observed softening response and the simulated pressure response is in part due to the 4D seismic signal filtering applied in definition of the objective function area. As softening signal from well W4 occurs adjacent to the softening signal caused by exsolved gas trapped in the high net sand structural high, areas of softening signal overlap are probable. Separation of the softening signals according to source of decrease in seismic impedance from seismic amplitude interpretation alone is challenging and introduces added uncertainty in the interpretation of the pressure results.

The best-case pressure maps also tie in with the well bottomhole pressure (WBHP) rates as seen in Figure 6.30. Though the main objective of the history match was reducing the mismatch between well-centric waterflood patterns, the WBHP profiles for wells W4 and P2 show an improvement in the match to observed production data, particularly in 2004 and 2006 (omitting spurious observed data at 2008). More improvements in the production data match to historical data would be expected in a combined production and seismic history matching scenario with binary images (Jin et al., 2012b; Tillier et al., 2012; Obidegwu et al., 2015; Trani et al., 2017; Davolio and Schiozer, 2018).

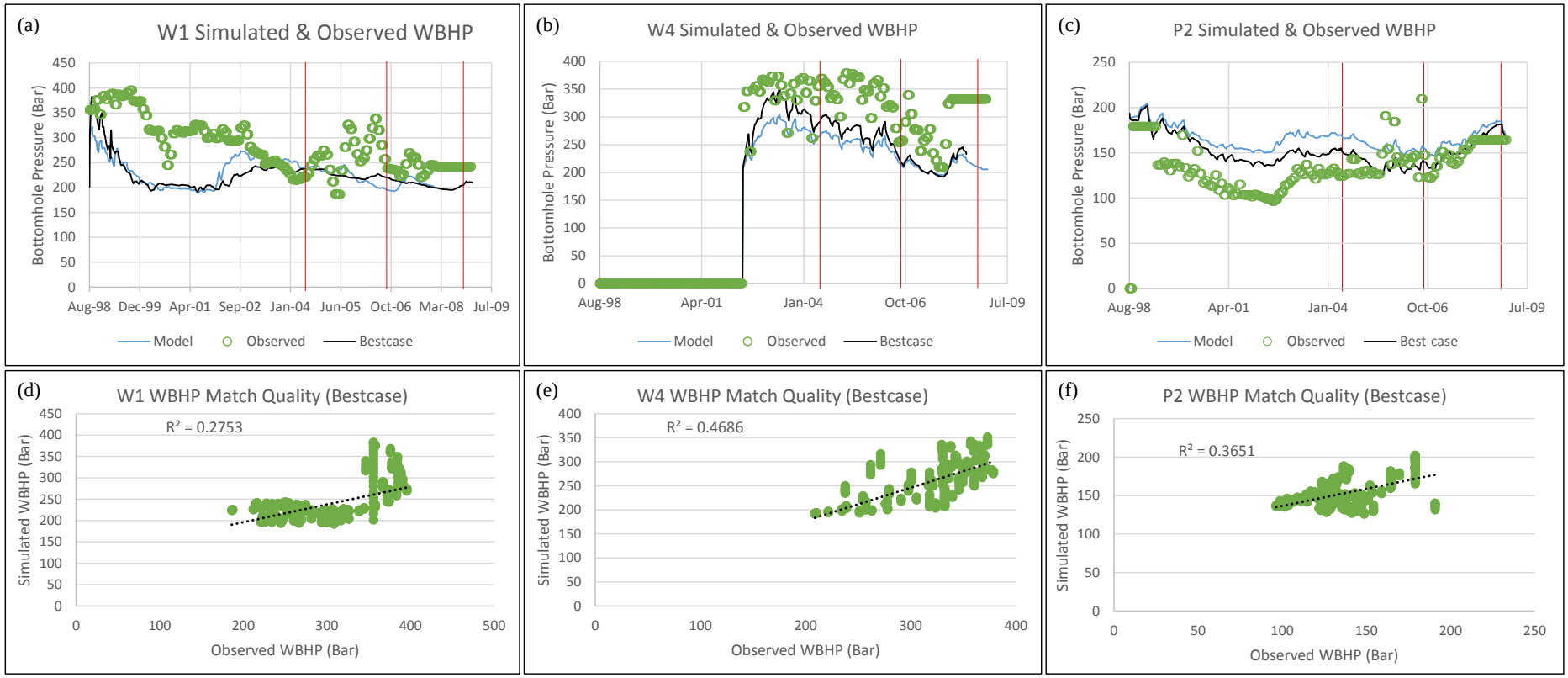

Figure 6.30: Production profiles showing base-case, observed and best-case well bottomhole pressure rates and cross-plots of best-case and observed rates for well W1 - (a) & (d), well W4 - (b) & (e) and well P2 - (c) & (f). Red lines show the seismic survey times.

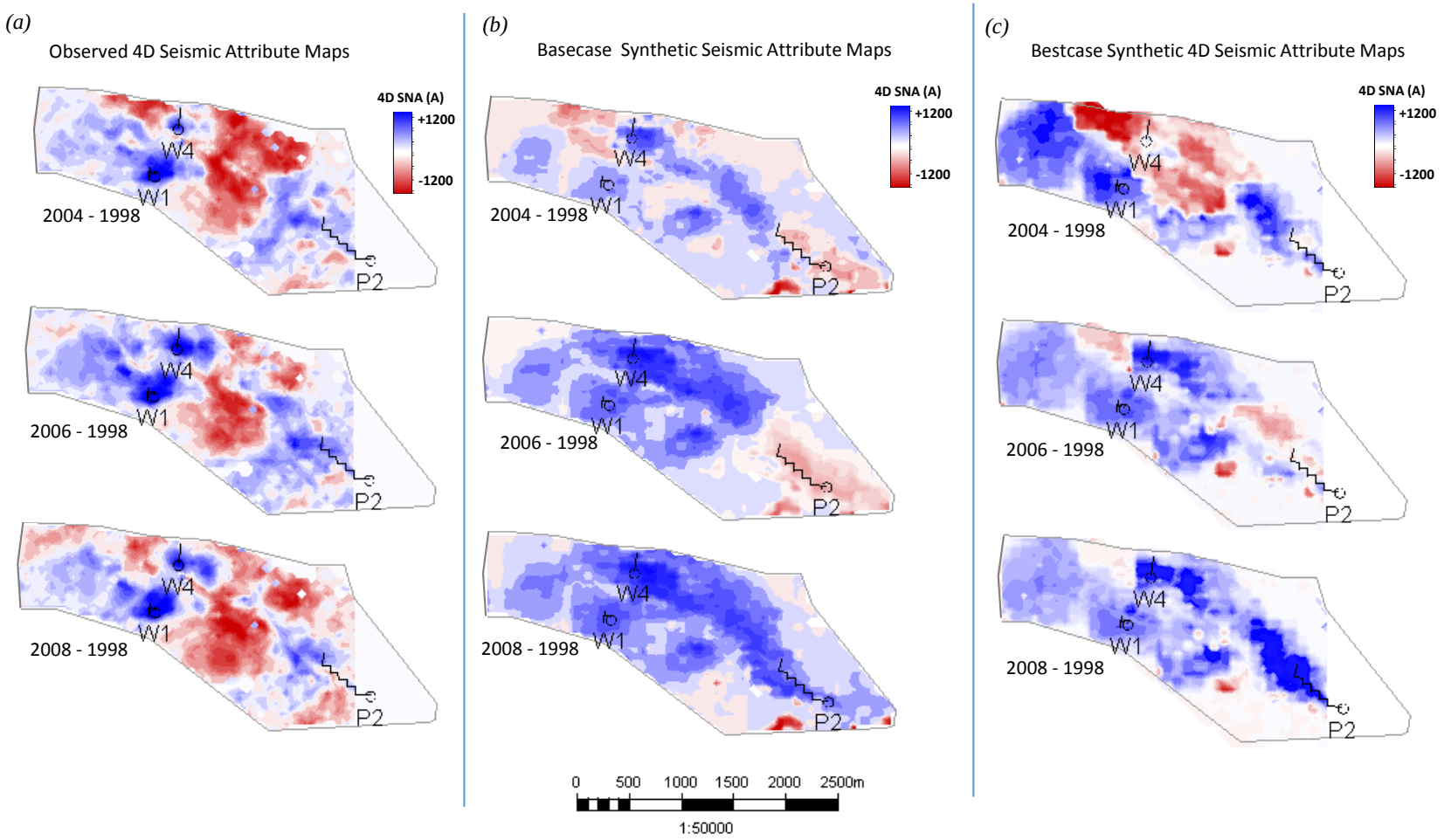

Figure 6.31: (a) Observed 4D seismic maps, (b) base-case synthetic 4D seismic maps and (c) best-case 4D synthetic 4D seismic maps for three surveys 2004, 2006 and 2008.

With *Sim2Seis* seismic forward modelling and the same petro-elastic model calibrated for the base-case model, synthetic 4D seismic maps are generated for the best-case reservoir simulation model and compared to the observed and base-case 4D seismic maps in Figure 6.31. In the 2004 survey, the softening signal around well W4 appears to replicate a similar shape of the observed softening response. As we know that there is no simulated trapped gas contributing to the softening response as interpreted in the observed seismic case, an increase in pressure from well W4 is solely responsible for the similar shaped softening signal. This is further confirmed by the dimming of the softening signal with increase in the volume of water injected in well W4. The increased water saturation with continued injection then creates a contrasting hardening signal which dominates the softening signal for the years 2006 – 2008.

Following high time-lapsed injecting pressure >200bar, there is a significant poorly matched section in the WBHP profile of well W1. This could be as a result of an injector induced fracture for which characteristics are not properly modelled using Eclipse 100. Additionally, the section around well W1 is relatively thin (30 m) which increases the chances of an incorrect geological architecture modelling given the seismic based modelling approach (Martin and MacDonald, 2010) and uncertainties in reservoir bed thicknesses with seismic resolution.

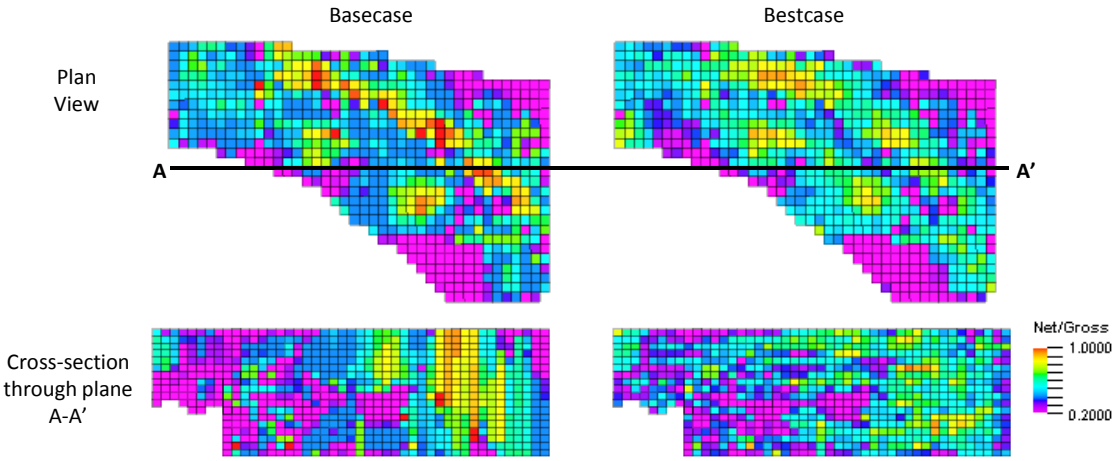

Figure 6.32: Base-case and best-case net-to-gross property comparison

The heterogeneity within the waterflood pattern is mostly influenced by the seismic velocity interaction with the sand-shale ratios. The best-case model net-to-gross property was generated with a collocated cokriging correlation coefficient of 0.846 and shown in

Figure 6.32. This, in conjunction with other updated dynamic properties, created increased lateral heterogeneity in the best-case net-to-gross property to a degree similar to the observed seismic map. Simultaneously, in the vertical direction, cokriging the well-logs and seismic data introduced higher resolution heterogeneity from the well-logs (cross-sections in Figure 6.32). As seen in Chapter 2, higher resolution reservoir heterogeneity better replicates the real waterfloods, which has helped minimise the disparity between the simulated and observed waterflood patterns.

6.7 Summary

In this chapter, a methodology is proposed for the application of local seismic history matching of well-centric waterflood patterns to a field dataset using geostatistical simulation for static property update and the use of binary images for 4D seismic data representation. The methodology was applied to a sector of the Schiehallion reservoir, preserving a higher degree of reservoir heterogeneity and eliminating the need for further upscaling of the model normally required for a practical history matching exercise. The Hamming Distance was used as the binary seismic objective function for combined matching of hardening signals and softening signals from the injector. Static and dynamic reservoir properties were explored to determine the most sensitive parameters as input to the history matching process. For static property perturbation, and to include finer detailed information, high-resolution downhole well-logs and low-resolution laterally extensive seismic data were interpolated using collocated cokriging to generate net-to-gross properties for each simulation run. This was integrated to run in parallel as part of the history matching loop. For a match to only seismic data using binary images, the history matching results showed good improvements of the well-centric flood pattern match to the observed binary flood pattern for both water-saturation and pressure, as well as improvements in the production data. The history match achieved a modest convergence rate of 50% which is attributable to the uncertainties presented by the strong contrasting pressure signal, limitations of the geobody facies architecture, noise and possible model errors. Despite the uncertainties encountered, the methodology highlights the benefits of a well-centric seismic history matching for waterflood patterns using geostatistical simulations for static property update and circumventing time consuming seismic forward modelling within the history matching loop via the use of binary images.

Chapter 7

Discussions and Recommendation

This chapter concludes the thesis with discussions and recommendations for future work.

7 Discussion and Recommendations

7.1 4D seismic to assess waterflooding

Waterflooding is a key field development strategy and is carried out for the main purpose of oil sweep and reservoir support and is a main improved oil recovery method given its accessibility, relative cost and wide applicability. The merits of successful waterflooding monitoring and management is, therefore, inexhaustible and can be further developed with improving technology. 4D seismic has been applied extensively on the field-scale in qualitative performance evaluation of waterflooding: indication of flooded areas and bypassed zones, identification of lost volumes, etc and more recently quantitatively as part of history matching and reservoir model update schemes. This thesis proposes waterflooding performance assessment from the perspective of understanding and maximising the local quantitative 4D seismic interpreted benefits of waterflooding towards improved reservoir characterisation and management, using data-integration and reservoir simulation. With a synergy of 4D seismic interpretation and reservoir simulation, the research was based on a well-centric study of 4D seismic with regards to waterflooding in a deep-water North Sea turbidite oil reservoir.

7.1.1 Accounting for the individual effects of waterflooding

Chapter 2 investigated the effects of the composite responses to waterflooding (salinity, temperature, etc) on the interpreted 4D seismic signal, by estimating the influence of properly including these effects as part of seismic forward modelling in the 4D seismic interpretation workflow. The qualitative interpretation effects of upgridding and upscaling the geological and reservoir models as related to the 4D seismic modelling and interpretation were tested for different scales, quantifying the 4D seismic signal errors. The influence of these individual effects is dependent on the reservoir characteristics and seismic data resolution and quality. The magnitude of the gradient-dependent salinity and temperature effects were relatively small and had no significant impact on the 4D seismic forward modelling interpretation given the combination of the salinity and temperature characteristics of the waterflooding scenario in the Schiehallion and the seismic data resolution and accompanied noise. While the impact of reservoir heterogeneity on waterflooding has a significant influence on the recovery factors especially in the presence of high permeability channels, in the studied case of the Schiehallion, improved

heterogeneity did not significantly improve the 4D seismic waterflooding interpretation. Higher resolution reservoir simulation and geological grid translated to increased detail in the 4D seismic interpretation of the geology of the reservoir and reservoir changes. However, determination of the benefits of improvement of additional heterogeneity compared to computational expense decreased the importance of finescale reservoir simulation in 4D seismic interpretation of the Schiehallion field.

7.1.2 Application of Seismic Signal Calibration

The 4D seismic signal is calibrated to the reservoir volumes across the different domains of observed seismic, synthetic seismic and reservoir simulation via data integration in Chapter 3. Utilising the reservoir simulation model and seismic forward modelling, the direct proportional relationship between actual reservoir volumes and the seismic resolved volumes was established. Model precision and accuracy. The aphorism "all models are wrong" acutely applies in the reservoir engineering and reservoir geophysics industry as the accuracy with which reservoir models can replicate the dynamic reservoir at a real-life scale is impossible. Successful seismic calibration, however, is dependent on a history matched reservoir simulation model and accompanying seismic forward modelling. This limits the precision to which the seismic signal can be quantitatively calibrated to production data as allowances would have to be made for errors of Measurement, seismic acquisition and processing, reservoir model upscaling, uncertainties in history match, seismic non-repeatability and noise, etc. Estimates for these errors should be included as part of the seismic calibration workflow, properly defining the uncertainty range.

Acknowledging the challenges associated with amplitude signal resolution for thin reservoirs, 3D volumetric calibration of the 4D seismic increased water saturation signal was calibrated to material-balanced production volumes. The errors of calibrating reservoir volumes in the different domains and effects of error evolution across domains were estimated and seen to grow from simulation model through to synthetic seismic and observed seismic, with increasing seismic signal uncertainty, pressure signal interference and noise. The study highlighted the requirement of a sufficient number of surveys to appropriately understand the seismic signal sensitivity to different reservoir scenarios for proper signal calibration.

7.1.3 4D Seismic Displacement Efficiency and Directionality

In Chapter 4, quantitative waterflooding performance metrics were defined using the 4D seismic signal to evaluate well-centric displacement efficiencies and infer waterflood directionality. The metrics provided a fast assessment of the waterflood performance with respect to pore-scale water-replacing-oil properties and characterises the well-centric flood heterogeneity. Interpretations from the Seismic performance metrics aligned with waterflooding sweep estimations from production operations, inter-well connectivity assessments using the Capacitance Model and indicated waterflooding induced formation changes.

7.1.4 Using binary images in a local seismic history matching

The expanded well-centric interpretation of the reservoir was applied to a local automatic seismic history matching process using binary image representation of the 4D seismic waterflooded signal. The aim was to improve the match between the 4D seismic waterflood and the simulation generated waterflood maps. For a synthetic simulation model with characteristics similar to the Schiehallion, the validity of the seismic objective function formulation was tested using Hamming Distance and *Currents Measurement Metric* for applicability and suitability given the well-centric approach and dataset characteristics. The Hamming Distance was seen to be the more sensitive method in computing the well-centric observed seismic and simulation model binary image dissimilarities and was applied in a Schiehallion local seismic automatic history matching workflow using Evolution Strategy as the optimisation algorithm. Along with dynamic properties of transmissibilities, static net-to-gross distributions of the reservoir were also updated simultaneously as part of the history matching loop using geostatistical simulation constrained by 4D seismic and well log data. This method improves on the net-to-gross update using multipliers by generating plausible realisations aiming to match the shape and magnitude of the well-centric waterflood pattern.

7.2 Comments and Recommendations for Future Research

7.2.1 Use of Alternative Seismic Attributes

The seismic attributes used for the entire research were post-stack coloured inversion volumes. For maps, the sum of negatives amplitude maps was used as they best

characterised the geology of the field with related 4D seismic reservoir dynamic responses. The surface maps were generated between horizons of the appropriate reservoir interval. The reliability of the amplitude signal in calibrating the 4D seismic signal is not high in the case of thin reservoirs given the susceptibility of constructive and destructive interference due to tuning. In this case, a calibration of the seismic impedance product from a seismic inversion could yield a more precise calibration. The accuracy of the 3D volumetric seismic signal calibration applied to thick reservoirs, however, is dependent on the characteristics of the reservoir and the seismic quality. A calibration was applied to a waterflooding well in the Girassol field. The Girassol field, a ~200m thick field located on the Angolan shelf in West Africa is a complex faulted turbidite reservoir with high-resolution seismic data. The inverted seismic impedance volumes were used to calibrate the seismic signal to the net water volumes. As observed in Figure (7.1), despite the thickness of the reservoir considered appropriate for a 3D volumetric seismic calibration and the high quality seismic data, it is challenging to appropriately extract the 3D volumetric gross rock volume of the seismic signal. An extraction of the seismic signal in the form of a seismic geoblob depicts the tortuous characteristics of the channel sands, but the unconsolidated sand beds render the sand bed definition and boundary extent identification challenging. The unconsolidated sands shown in different views in Figure (7.1) a, b and c, carry significant errors as indicated by the significantly low calibration factors (y/x), $0.03 - 0.13$, in the chart shown in Figure (7.2). The suitable seismic attribute for calibration, therefore, is dependent on the specific reservoir characteristics and seismic data quality and availability.

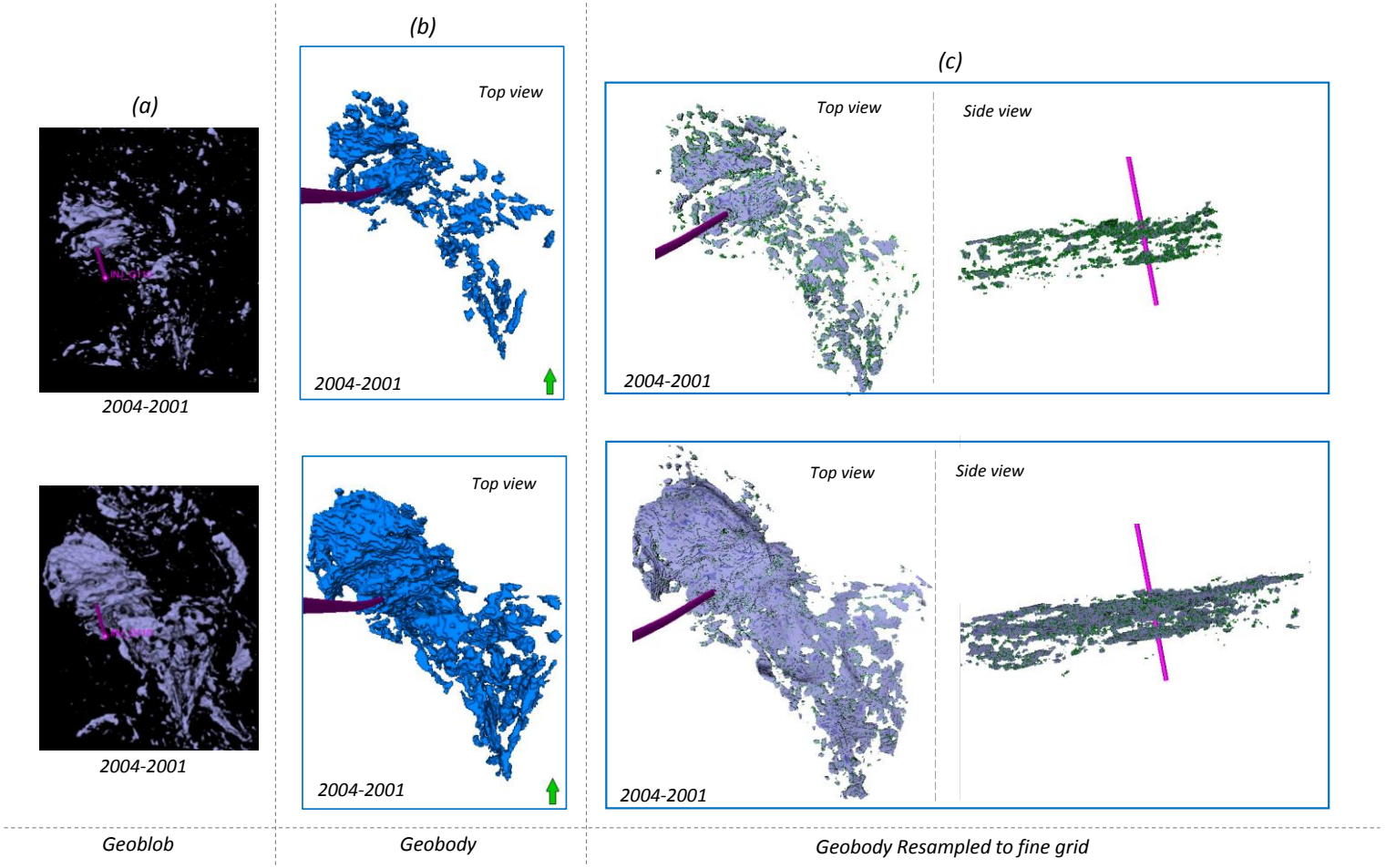

Figure 7.1: 3D volumetric seismic calibration showing (a) extracted seismic geoblob, (b) converted geobody and (c) plan and south-view of geobody resampled to reservoir grid.

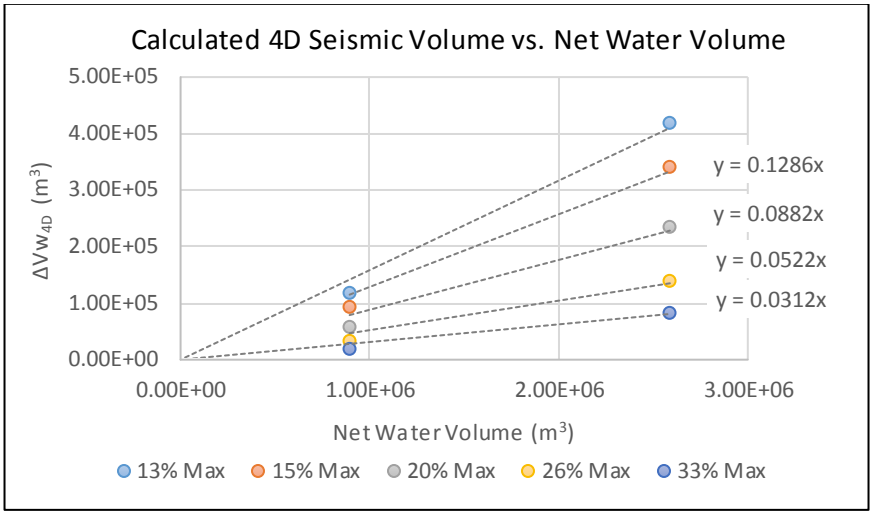

Figure 7.2: Crossplot of net water volumes estimated from extracted observed seismic gross rock volume and actual net water volumes for thresholds T=13%, 15%, 20%, 26% and 33%.

In 4D seismic performance metrics: Full angle stack seismic volumes were used in the entire seismic interpretation for this research. The merits interpreting waterflooding in the near, mid and far stacks (prestack data) however are well published and are bound to increase the breadth of interpretation of the waterflooding seismic performance metrics, especially regarding the difference in pressure signal resolution compared to the increased water signal in prestack data.

In local seismic history matching: Separating the counteracting increased pressure and saturation signals as a result of waterflooding is an industry-wide challenge. The use of the seismic amplitude interpretations for conversion to binary images in the history match as detailed in Chapter 6 introduces the uncertainty of the magnitude of the obscured signal and the transition zones between signals. In such cases, the binary image approach decreases in efficiency. Using a combination of elastic property attributes in the seismic history matching improves the constraint for the model parameters, leading to a more accurate history matching.

A seismic inversion product of separated saturation and pressures though tedious and time-consuming would be a more effective method of handling the combined signals. Seismic forward modelling as a part of the history matching loop, equally time consuming and dependent on the uncertain petroelastic model would also result in a more accurate handling of the combined signal. These attributes, however, are computational intensive and would require careful configuration to be included in a practical history matching

workflow. Synthetic seismic generation would also incorporate the geostatistically simulated net-to-gross property, thus accounting for the sand-shale ratio influences on the seismic signal.

7.2.2 Updating the Reservoir Simulation Model Structure

The undulating thickness of the Schiehallion field with thin sections of the reservoir ranging between 15 – 30 m could extend the reservoir adverse characteristics to include the question of structural accuracy, especially with the initial model build based on seismic interpretations. We ask the questions: Do we need to model more than just the reservoir? Could it benefit reservoir management if relevant sections of the underburden and/or over burden are modelled too?

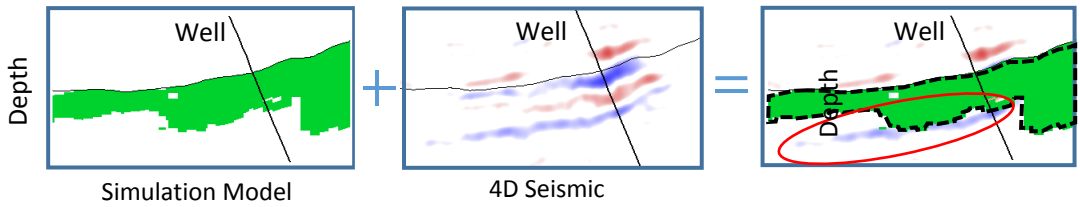

Figure 7.3: Cross section through a thin area of the field showing the simulation model - left, 4D seismic section showing hardening signals as a result of waterflooding (centre) and a cross-section with the seismic section with the model superimposed (right).

Figure (7.3) shows cross-sections through a thin section of the Schiehallion, showing the simulation model, depth-converted well-centric 4D seismic section showing waterflooding and a cross-section with the simulation model superimposed on the 4D seismic section. Subject to the accuracy of the velocity model used in the depth-conversion, there appears to be an inaccuracy in the structure of the field, leading to a misrepresentation of the well-centric area and leading to loss of injected water volumes. With integrated seismic, geological and engineering data interpretation, a structural model update could lead to improved reservoir simulation models.

7.2.3 4D Seismic Volumetric Displacement Efficiencies

The map-based approach of data integration has been successfully applied to seismically "thin" reservoirs in this work where depth and pore-volume averages of seismic signals can be appropriately approximated following calibration of the seismic signal. In the case of thick reservoirs, extended challenges of multiples, interference, side-lobes and tuning

are introduced, compromising the map-interpreted seismic signal. In this case, a volumetric approach to sweep efficiency would be the logical next step.

7.2.4 Improved Heterogeneity in the Local Seismic History Matching Loop

Thresholding Levels: Chapters 5 and 6 dealt with the local seismic history matching using binary images. Binary conversion of the 4D seismic and simulation model waterflood patterns were achieved through a bi-level thresholding into zeros and ones, with the waterflood patterns as ones and zeros everywhere else. The bi-level thresholding was used for a fast application of a local seismic history matching combined with geostatistical updates. However, the bi-level thresholding limits the achievable resolution of the waterflood patterns. As seen in Figure (7.4), while a bi-level threshold would capture the shape of the waterfront in detail subject to the size of the reservoir grid, the heterogeneity character of the waterflood is lost. Excluding the effects of 4D seismic noise, 4D seismic data resolves the waterflood within the flood pattern into a distribution governed by the reservoir sand-shale ratios, permeability and porosity and volumes of water injected. Although the net-to-gross update achieves a level of heterogeneity preservation, a more improved approach would be automatic conversion of the waterflood patterns into ternary or multinary images within the history matching loop.

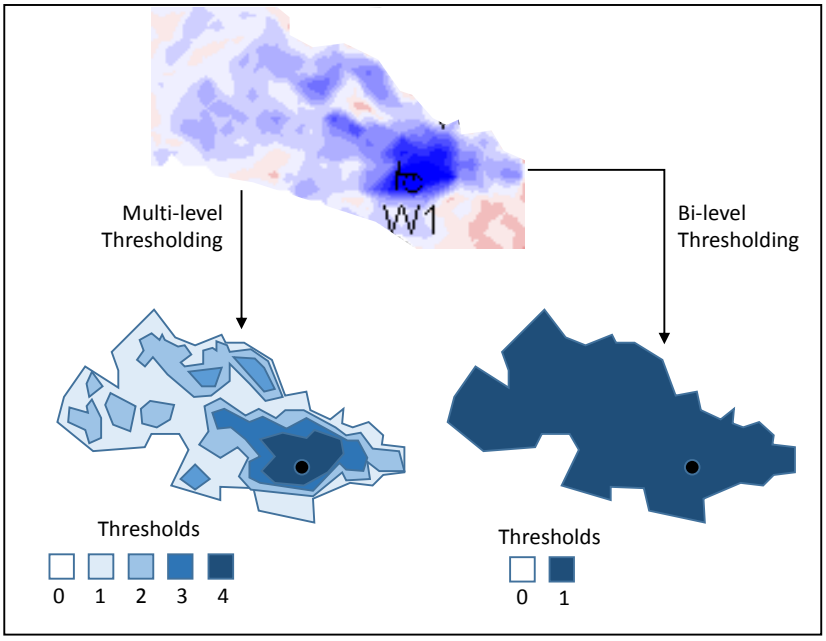

Figure 7.4: Waterflooding pattern converted to multinary and binary images by filtering through different level thresholds.

The multinary images could be achieved with a multi-cycle optimisation, where threshold gradients are applied for varying degrees of image resolution. That is, images are first filtered by one threshold to achieve general flood front characterisation and matching for a first map, and then image resolution is increased by passing the image through other thresholds to define the heterogeneity of the first map.

Stochastic Facies Perturbation: Matching the waterflood patterns in the local seismic history matching loop in Chapter 6 was restricted by the geobody facies definition. The Schiehallion geological model was built using a deterministic geomodelling approach constrained to 3D seismic, well-logs and core data (Martin and MacDonald, 2010), mapping the sand facies distribution to the seismically interpreted bright amplitudes interpreted as low impedance sands. Given the uncertainty of this approach, the inter-geobody transmissibilities were identified as a key input parameter to the history matching process, with good results. The Schiehallion, however, is a thin reservoir susceptible to tuning interferences, increasing the possible uncertainties in the structure and extents of the geobody facies. The deterministic method of facies distribution however restricted the levels of perturbation applied to the geobodies to transmissibility multipliers, thus limiting the possible solution of waterflood pattern match to the pre-defined boundaries of the geobodies. An improvement to this process would be a stochastic modification of the geobody structure within a tolerance defined by the tuning limits and applicable uncertainties, as part of the history matching workflow, extending the heterogeneity of the geobodies as suggested by illustration in Figure (7.5).

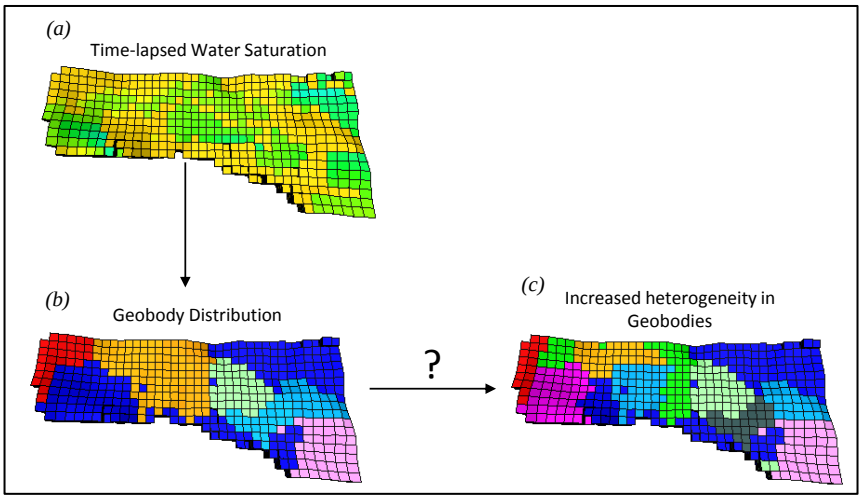

Figure 7.5: (a) Simulation model time-lapsed water saturation showing heterogenous flood map (b) and (c) geobody distribution of varying heterogeneities

7.2.5 Geological Modelling in the History Matching Workflow

Including a joint-inversion method simultaneously inverting for the stratigraphy of the reservoir, static properties and the elastic properties using direct seismic and well log constraints as part of the history matching workflow extends the geological model updating. The geological model is of a much finer scale than the simulation model and simultaneous updating in a history matching loop is presently impractical given the computing limitations. The local seismic history matching, however, limits the history matching exercise to the well-centric well radius and thus significantly reduces the computational expense.

7.3 Final Remarks

The research covered in this thesis has integrated reservoir simulation and 4D seismic interpretation in assessing the performance of early waterflooding by scrutinising the well-centric 4D seismic signal and accompanied integrated data. From a reservoir engineering perspective, it breaks down the typically less explored details of the finer scale 4D seismic signal as they relate to waterflooding an oil reservoir. The results of the well-centric study collectively inform the field-scale waterflooding assessment, using defined fast methods of displacement efficiency assessment and local history using binary images. The understanding of the waterflooding signal as interpreted by the 4D seismic signal has been improved, but room remains for further applications of the methods proposed to other datasets and alternative improved and enhanced oil recovery methods.

References

AL-YOUSEF, A. A. 2006. *Investigating statistical techniques to infer interwell connectivity from production and injection rate fluctuations.*

ALBERTONI, A. 2002. *Inferring interwell connectivity from well-rate fluctuations in waterfloods.* University of Texas at Austin.

ALLAN, P., FOWLER, S., HILL, C., MACDONALD, C. & CAMPBELL, S. 2011. A Decade of West of Shetland 4D Seismic – The Power of Consistency. *Devex*.

ALVAREZ, E. & MACBETH, C. 2014. An insightful parametrization for the flatlander's interpretation of time-lapsed seismic data. *Geophysical Prospecting,* 62**,** 75-96.

AMINI, H. 2014. *A pragmatic approach to simulator-to-seismic modelling for 4D seismic interpretation.* Heriot-Watt University.

AMINI, H. & MACBETH, C. Calibration of Rock Stress-sensitivity Using 4D Seismic Data. 77th EAGE Conference and Exhibition 2015, 2015.

AMINI, H., MACBETH, C. & SHAMS, A. Calibration of simulator to seismic modeling for quantitative 4D seismic interpretation. 73rd EAGE Conference and Exhibition incorporating SPE EUROPEC 2011, 2011.

ARANHA, C., TANABE, R., CHASSAGNE, R. & FUKUNAGA, A. Optimization of oil reservoir models using tuned evolutionary algorithms and adaptive differential evolution. Evolutionary Computation (CEC), 2015 IEEE Congress on, 2015. IEEE, 877-884.

ATABAY, S., DRONEN, O. M., FLO HVIDSTEN, J. M. & FAWKE, A. R. 2012. Developing a Toolbox for Evaluating of Water Injection Performance on the Norne Field. Society of Petroleum Engineers.

BATZLE, M. & WANG, Z. 1992. Seismic properties of pore fluids. *GEOPHYSICS,* 57**,** 1396-1408.

BEHRENS, R., CONDON, P., HAWORTH, W., BERGERON, M. & ECKER, C. 2002. 4D Seismic Monitoring of Water Influx at Bay Marchand: The Practical Use of 4D in an Imperfect World.

BORGES, F. & LANDRØ, M. Analysis of the Influence of Water Salinity On Time-Lapse Seismic Response. 79th EAGE Conference and Exhibition 2017, 2017.

BYERLEY, G., BARHAM, G., TOMBERLIN, T. & VANDAL, B. 2009. 4D seismic monitoring applied to SAGD operations at Surmont, Alberta, Canada. *SEG*

Technical Program Expanded Abstracts 2009. Society of Exploration Geophysicists.

CASTANIÉ, L., BOSQUET, F. & LÉVY, B. 2005. Advanced volume visualization techniques for seismic interpretation. *SEG Technical Program Expanded Abstracts 2005*. Society of Exploration Geophysicists.

CHAMCHONG, R., FUNG, C. C. & WONG, K. W. 2010. Comparing binarisation techniques for the processing of ancient manuscripts. *Cultural Computing*. Springer.

CHASSAGNE, R., OBIDEGWU, D., DAMBRINE, J. & MACBETH, C. 2016. Binary 4D seismic history matching, a metric study. *Computers & Geosciences*, 96**,** 159-172.

CHESSEBOEUF, C., BIERMÉ, H., DAMBRINE, J., GUILLEVIN, C. & GUILLEVIN, R. Non-rigid registration of magnetic resonance imaging of brain. Image Processing Theory, Tools and Applications (IPTA), 2015 International Conference on, 2015. IEEE, 385-390.

CHIERICI, G. L. 1995. The Injection of Water into the Reservoir. *Principles of Petroleum Reservoir Engineering*. Springer.

COLE, S., LUMLEY, D., MEADOWS, M. & TURA, A. Pressure and saturation inversion of 4D seismic data by rock physics forward modeling. 2002 SEG Annual Meeting, 2002. Society of Exploration Geophysicists.

COLLINS, R. & SIMONS, L. 1961. Calculation of water-flood sweep patterns for unit mobility ratio.

CRAIG, F. F. 1971. *The reservoir engineering aspects of waterflooding*, HL Doherty Memorial Fund of AIME New York.

CRAWFORD, P. B. & COLLINS, R. 1954. Estimated effect of vertical fractures on secondary recovery. *Journal of Petroleum Technology,* 6**,** 41-45.

DAKE, L. P. 2001. *The practice of reservoir engineering (revised edition)*, Elsevier.

DAS, O. P., ASLAM, M., BAHUGUNA, R., AL-ENEZI, K., HUSSAIN, A.-S. M. & TAHANI YOUSEF, A.-R. 2009. Water Injection Monitoring Techniques For Minagish Oolite Reservoir In West Kuwait. International Petroleum Technology Conference.

DAVOLIO, A., MASCHIO, C. & SCHIOZER, D. J. 2012. Pressure and saturation estimation from P and S impedances: a theoretical study. *Journal of Geophysics and Engineering,* 9**,** 447.

DAVOLIO, A., MASCHIO, C. & SCHIOZER, D. J. 2013. Local History Matching Using 4D Seismic Data and Multiple Models Combination. Society of Petroleum Engineers.

DAVOLIO, A. & SCHIOZER, D. J. 2018. Probabilistic seismic history matching using binary images. *Journal of Geophysics and Engineering,* 15**,** 261.

DE, A., SILIN, D. B. & PATZEK, T. W. 2000. Waterflood Surveillance and Supervisory Control. Society of Petroleum Engineers.

DING, Y., ARTUS, V., ROGGERO, F. & BERTHET, P. 2007. Upscaling on the Girassol Field: Comparative Tests and Impact of Near-well Upscaling. Society of Petroleum Engineers.

DING, Y. & ROGGERO, F. 2009. Local Parameterization of Geostatistical Realizations for History Matching. Society of Petroleum Engineers.

DURLOFSKY, L. J. Upscaling and gridding of fine scale geological models for flow simulation. 8th International Forum on Reservoir Simulation Iles Borromees, Stresa, Italy, 2005.

DYES, A., KEMP, C. & CAUDLE, B. 1958. Effect of fractures on sweep-out pattern.

EGELAND, T., HOLDEN, L. & LARSEN, E. Designing better decisions. European Petroleum Computer Conference, 1992. Society of Petroleum Engineers.

EIKEN, O. & TØNDEL, R. 2005. Sensitivity of time-lapse seismic data to pore pressure changes: Is quantification possible? *The Leading Edge,* 24**,** 1250-1254.

FALAHAT, R. 2012. *Quantitative monitoring of gas injection, exsolution and dissolution using 4D seismic.* Heriot-Watt University.

FALAHAT, R., SHAMS, A. & MACBETH, C. 2011. Towards quantitative evaluation of gas injection using time-lapse seismic data. *Geophysical Prospecting,* 59**,** 310-322.

FANCHI, J. R. 2005. *Principles of applied reservoir simulation*, Elsevier.

FERAILLE, M., ROGGERO, F., MANCEAU, E., HU, L. Y., ZABALZA-MEZGHANI, I. & REIS, L. C. 2003. Application of Advanced History Matching Techniques to an Integrated Field Case Study. Society of Petroleum Engineers.

FINCHAM, A., CHRISTENSEN, J., BARKER, J. & SAMIER, P. Up-gridding from geological model to simulation model: review, applications and limitations. SPE Annual Technical Conference and Exhibition, 2004. Society of Petroleum Engineers.

FLORICICH, M., MACBETH, C., STAMMEIJER, J., STAPLES, R., EVANS, A. & DIJKSMAN, N. 2006. Determination of a Seismic And Engineering Consistent Petro-elastic Model For Time-lapse Seismic Studies: Application to the Schiehallion Field. Society of Exploration Geophysicists.

GADDE, P. B. & SHARMA, M. M. 2001. Growing Injection Well Fractures and Their Impact on Waterflood Performance. Society of Petroleum Engineers.

GAINSKI, M., MACGREGOR, A. G., FREEMAN, P. J. & NIEUWLAND, H. F. 2010a. Turbidite reservoir compartmentalization and well targeting with 4D seismic and production data: Schiehallion Field, UK. *Geological Society, London, Special Publications,* 347**,** 89.

GAINSKI, M., MACGREGOR, A. G., FREEMAN, P. J. & NIEUWLAND, H. F. 2010b. Turbidite reservoir compartmentalization and well targeting with 4D seismic and production data: Schiehallion Field, UK. *Geological Society, London, Special Publications,* 347**,** 89-102.

GAO, D. 2003. Volume texture extraction for 3D seismic visualization and interpretation. *Geophysics,* 68**,** 1294-1302.

GAO, D. 2008. 3D seismic volume visualization and interpretation: An integrated workflow with case studies. *Geophysics,* 74**,** W1-W12.

GASSMANN, F. 1951. Elasticity of porous media. *Vierteljahrsschrder Naturforschenden Gesselschaft,* 96**,** 1-23.

GONZÁLEZ-RODRÍGUEZ, P., KINDELAN, M., MOSCOSO, M. & DORN, O. 2005. History matching problem in reservoir engineering using the propagation–backpropagation method. *Inverse Problems,* 21**,** 565.

GOSSELIN, O., AANONSEN, S., AAVATSMARK, I., COMINELLI, A., GONARD, R., KOLASINSKI, M., FERDINANDI, F., KOVACIC, L. & NEYLON, K. History matching using time-lapse seismic (HUTS). SPE Annual Technical Conference and Exhibition, 2003. Society of Petroleum Engineers.

GOVAN, A. H., PRIMMER, T., DOUGLAS, C. C., MOODIE, N., DAVIES, M. & NIEUWLAND, F. 2006. Reservoir Management in a Deepwater Subsea Field – the Schiehallion Experience. Society of Petroleum Engineers.

GRION, S., KEGGIN, J., RONEN, S. & CALDWELL, J. Seismic repeatability benchmarks. Offshore Technology Conference, 2000. Offshore Technology Conference.

GULICK, K. E. & MCCAIN, W. D., JR. 1998. Waterflooding Heterogeneous Reservoirs: An Overview of Industry Experiences and Practices. Society of Petroleum Engineers.

HALL, H. N. 1963. How to analyze waterflood injection well performance. *World Oil,* 157**,** 128-33.

HAMMING, R. W. 1950. Error detecting and error correcting codes. *Bell Labs Technical Journal,* 29**,** 147-160.

HEFFER, K. 2002. Geomechanical influences in water injection projects: An overview. *Oil & Gas Science and Technology,* 57**,** 415-422.

HEFFER, K. & LEAN, J. 1993. Earth stress orientation-a control on, and guide to, flooding directionality in a majority of reservoirs. *Reservoir Characterization III, PennWell Books, Tulsa***,** 799-822.

HEFFER, K. J., FOX, R. J., MCGILL, C. A. & KOUTSABELOULIS, N. C. 1997. Novel techniques show links between reservoir flow directionality, earth stress, fault structure and geomechanical changes in mature waterfloods. *SPE Journal,* 2**,** 91-98.

HELLAND, R., STRONEN, L. K., FESTERVOLL, K. & YOUNESS, E. O. 2008. Successful LOR Implementation At the Gullfaks Field. World Petroleum Congress.

HUANG, D.-Y. & WANG, C.-H. 2009. Optimal multi-level thresholding using a two-stage Otsu optimization approach. *Pattern Recognition Letters,* 30**,** 275-284.

HUANG, X. 2001. Integrating time-lapse seismic with production data: A tool for reservoir engineering. *The Leading Edge,* 20**,** 1148-1153.

HUANG, X., BENTLEY, L. R. & LAFLAMME, C. 2001. Seismic history matching guided by attribute zonation. *SEG Technical Program Expanded Abstracts 2001*. Society of Exploration Geophysicists.

IONESCU, M. & RALESCU, A. Fuzzy hamming distance in a content-based image retrieval system. Fuzzy systems, 2004. Proceedings. 2004 IEEE international conference on, 2004. IEEE, 1721-1726.

JADHUNANDAN, P. & MORROW, N. R. 1995. Effect of wettability on waterflood recovery for crude-oil/brine/rock systems. *SPE reservoir engineering,* 10**,** 40-46.

JERAULD, G. R., WEBB, K. J., LIN, C.-Y. & SECCOMBE, J. C. 2008. Modeling Low-Salinity Waterflooding.

JIN, L., VAN DEN HOEK, P. J., ALPAK, F. O., PIRMEZ, C., FEHINTOLA, T., TENDO, F. & OLANIYAN, E. E. 2012a. A comparison of stochastic data-integration algorithms for the joint history matching of production and time-lapse-seismic data. *SPE Reservoir Evaluation & Engineering,* 15**,** 498-512.

JIN, L., WEBER, D., VAN DEN HOEK, P., ALPAK, F. O. & PIRMEZ, C. 2012b. 4D Seismic history matching using information from the flooded zone. *First Break,* 30**,** 55-60.

JOHNSTON, D. H. 2013. *Practical applications of time-lapse seismic data*, Society of Exploration Geophysicists.

KAZEMI, A. & STEPHEN, K. D. Automatic production and seismic history matching by updating locally and by geological environment in the Nelson field. SPE EUROPEC/EAGE Annual Conference and Exhibition, 2011. Society of Petroleum Engineers.

KELKAR, M. G. & SHARIFI, M. Upgridding under multiphase flow conditions. SPE Improved Oil Recovery Symposium, 2012. Society of Petroleum Engineers.

KHASHMAN, A. & SEKEROGLU, B. 2008. Document image binarisation using a supervised neural network. *International Journal of Neural Systems,* 18**,** 405-418.

KIDD, G. D. 1999a. Fundamentals of 3-D seismic volume visualization. *The Leading Edge,* 18**,** 702-709.

KIDD, G. D. 1999b. Fundamentals of 3D Seismic Volume Visualization. *Offshore Technology Conference*. Houston, Texas: Offshore Technology Conference.

KOLSTOE, E., ROSTE, T., HUSBY, O., TYSSEKVAM, J. A. A., MOEN, A., ENDRESEN, T. & DAWODU, N. K. 2008. Using 4D Seismic for Understanding Drainage Pattern and Optimizing Infill Wells Placement in a Heterogeneous and Compartmentalised Reservoir - Cases From the Heidrun Field. International Petroleum Technology Conference.

KRAGH, E. & CHRISTIE, P. 2002. Seismic repeatability, normalized rms, and predictability. *The Leading Edge,* 21**,** 640-647.

KRETZ, V., VALLES, B. & SONNELAND, L. Fluid front history matching using 4D seismic and streamline simulation. SPE Annual Technical Conference and Exhibition, 2004. Society of Petroleum Engineers.

KRUGER, W. 1961. Determining areal permeability distribution by calculations. *Journal of Petroleum Technology,* 13**,** 691-696.

LANDRÉ, J. & TRUCHETET, F. Image retrieval with binary hamming distance. VISAPP (2), 2007. 237-240.

LANDRØ, M. 2001. Discrimination between pressure and fluid saturation changes from time-lapse seismic data. *Geophysics,* 66**,** 836-844.

LE RAVALEC, M., HU, L. Y. & NOETINGER, B. Stochastic reservoir modeling constrained to dynamic data: local calibration and inference of the structural parameters. SPE Annual Technical Conference and Exhibition, 1999. Society of Petroleum Engineers.

LE RAVALEC, M., TILLIER, E., DA VEIGA, S., ENCHÉRY, G. & GERVAIS, V. 2012. Advanced integrated workflows for incorporating both production and 4D seismic-related data into reservoir models. *Oil & Gas Science and Technology– Revue d'IFP Energies nouvelles,* 67**,** 207-220.

LEACH, H., HERBERT, N., LOS, A. & SMITH, R. The Schiehallion development. Geological Society, London, Petroleum Geology Conference series, 1999. Geological Society of London, 683-692.

MACBETH, C. 2004. A classification for the pressure-sensitivity properties of a sandstone rock frame. *Geophysics,* 69**,** 497-510.

MACBETH, C., FLORICICH, M. & SOLDO, J. 2006. Going quantitative with 4D seismic analysis. *Geophysical Prospecting,* 54**,** 303-317.

MACQUEEN, J. Some methods for classification and analysis of multivariate observations. Proceedings of the fifth Berkeley symposium on mathematical statistics and probability, 1967. Oakland, CA, USA, 281-297.

MANDAL, D., SUWARLAN, W., ABU MANSUR, R., ALI, K. & MASOUDI, R. 2011. 4D Seismics Improves Reservoir Management - A Case Study On Angsi. International Petroleum Technology Conference.

MARTIN, K. & MACDONALD, C. Schiehallion Field: applying a geobody modelling approach to piece together a complex turbidite reservoir. 7th European Production & Development Conference, Aberdeen, UK, 2010.

MASCHIO, C. & SCHIOZER, D. J. Development and application of methodology for assisted history matching. SPE Latin American and Caribbean Petroleum Engineering Conference, 2005. Society of Petroleum Engineers.

MASCHIO, C. & SCHIOZER, D. J. 2016. Probabilistic history matching using discrete Latin Hypercube sampling and nonparametric density estimation. *Journal of Petroleum Science and Engineering,* 147**,** 98-115.

MASCHIO, C., VIDAL, A. C. & SCHIOZER, D. J. 2008. A framework to integrate history matching and geostatistical modeling using genetic algorithm and direct search methods. *Journal of Petroleum Science and Engineering,* 63**,** 34-42.

MIDDLETON, G. V. & HAMPTON, M. A. 1973. Part I. Sediment gravity flows: mechanics of flow and deposition.

MIKKELSEN, P. L., GUDERIAN, K. & DU PLESSIS, G. 2008. Improved reservoir management through integration of 4D-seismic interpretation, Draugen field, Norway. *SPE Reservoir Evaluation & Engineering,* 11**,** 9-17.

NOIROT, J. C., VAN DEN HOEK, P. J., ZWARTS, D., BJOERNDAL, H. P., STEWART, G., DRENTH, R., AL-MASFRY, R., WASSING, B., SAEBY, J., AL-MASROORI, M. & ZARAFI, A. 2003. Water Injection and Water Flooding Under Fracturing Conditions. Society of Petroleum Engineers.

O'DONOVAN, A., SMITH, S. & KRISTIANSEN, P. Foinaven 4D seismic-dynamic reservoir parameters and reservoir management. Spe Annual Technical Conference And Exhibition, 2000. Society of Petroleum Engineers.

OBIDEGWU, D., CHASSAGNE, R. & MACBETH, C. 2015. Seismic Assisted History Matching Using Binary Image Matching. Society of Petroleum Engineers.

OBIDEGWU, D., CHASSAGNE, R. & MACBETH, C. 2017. Seismic assisted history matching using binary maps. *Journal of Natural Gas Science and Engineering,* 42**,** 69-84.

OBIDEGWU, D., MACBETH, C. & CHASSAGNE, R. Comparative Analysis of Binary and Conventional Seismic Assisted History Matching. 78th EAGE Conference and Exhibition 2016, 2016.

OLATUNBOSUN, O. Managing Waterflood in Deepwater Soft Rock: The Bonga Experience to Date. SPE Nigeria Annual International Conference and Exhibition, 2014. Society of Petroleum Engineers.

OLIVER, D. S. & CHEN, Y. 2010. Recent progress on reservoir history matching: a review. *Computational Geosciences,* 15**,** 185-221.

PALSSON, B., DAVIES, D. R., TODD, A. C. & SOMERVILLE, J. M. 2003. Water Injection Optimized with Statistical Methods. Society of Petroleum Engineers.

PELE, O. & WERMAN, M. 2008. Robust real-time pattern matching using bayesian sequential hypothesis testing. *IEEE transactions on pattern analysis and machine intelligence,* 30**,** 1427-1443.

PLUCHERY, E., TOINET, S., CRUZ, P., CAMOIN, A. & FRANCO, J. 2013. Intensive Use of 4D Seismic in Reservoir Monitoring, Modelling and Management: The Dalia Case Study. International Petroleum Technology Conference.

RICHARDSON, S. M., HERBERT, N. & LEACH, H. M. 1997. How Well Connected Is the Schiehallion Reservoir? : Society of Petroleum Engineers.

ROGGERO, F., DING, D. Y., BERTHET, P., LERAT, O., CAP, J. & SCHREIBER, P.-E. Matching of Production History and 4D Seismic Data--Application to the Girassol Field, Offshore Angola. SPE Annual Technical Conference and Exhibition, 2007. Society of Petroleum Engineers.

ROGGERO, F. & HU, L. Gradual deformation of continuous geostatistical models for history matching. SPE annual technical conference and exhibition, 1998. Society of Petroleum Engineers.

ROGGERO, F., LERAT, O., DING, D. Y., BERTHET, P., BORDENAVE, C., LEFEUVRE, F. & PERFETTI, P. 2012. History Matching of Production and 4D Seismic Data: Application to the Girassol Field, Offshore Angola. *Oil & Gas Science and Technology – Revue d'IFP Energies nouvelles,* 67**,** 237-262.

ROGGERO, F., LERAT, O., DING, D. Y., BERTHET, P., LEFEUVRE, F., PERFETTI, P. & BORDENAVE, C. Constraining reservoir models to production and 4D seismic data-application to the Girassol Field, offshore Angola. 19th World Petroleum Congress, 2008. World Petroleum Congress.

ROY, A., THRASHER, D., TWYNAM, A. & WILSON, A. Water Injection Completion Philosophy in a Deepwater Subsea Environment Requiring Sand Control: A Case

Study of 29 Injection Wells West of Shetland. SPE Annual Technical Conference and Exhibition, 2004. Society of Petroleum Engineers.

SALAKO, O. 2015. *The assessment of time lapse marine controlled-source electromagnetics (CSEM) for dynamic reservoir characterisation.* Heriot-Watt University.

SATTER, A. & THAKUR, G. C. 1994. *Integrated petroleum reservoir management: a team approach*, PennWell Books.

SAYARPOUR, M., KABIR, C. S. & LAKE, L. W. 2009. Field Applications of Capacitance-Resistance Models in Waterfloods.

SCHULZE-RIEGERT, R., AXMANN, J., HAASE, O., RIAN, D. & YOU, Y.-L. 2002. Evolutionary algorithms applied to history matching of complex reservoirs. *SPE Reservoir Evaluation & Engineering,* 5**,** 163-173.

SCHULZE-RIEGERT, R. & GHEDAN, S. Modern techniques for history matching. 9th International Forum on Reservoir Simulation, 2007. 9-13.

SHAMS, M. 2016. Reservoir Simulation Assisted History Matching: From Theory to Design. Society of Petroleum Engineers.

SHEHATA, A. M., EL-BANBI, A. H. & SAYYOUH, M. H. Proper Selection of Upscaling Techniques for Different Production Processes. North Africa Technical Conference and Exhibition, 2012. Society of Petroleum Engineers.

SIMM, R., BACON, M. & BACON, M. 2014. *Seismic Amplitude: An interpreter's handbook*, Cambridge University Press.

SMITH, J. T. & COBB, W. M. 1997.

STAPLES, R., STAMMEIJER, J., JONES, S., BRAIN, J., SMIT, F. & HATCHELL, P. Time-Lapse (4D) Seismic Monitoring-Expanding Applications. Joint Convention, What's Next, 2006.

STATHIS, P., KAVALLIERATOU, E. & PAPAMARKOS, N. 2008. An Evaluation Technique for Binarization Algorithms. *J. UCS,* 14**,** 3011-3030.

STEPHEN, K. D. & MACBETH, C. Reducing Reservoir Prediction Uncertainty Using Seismic History Matching. SPE Europec/EAGE Annual Conference and Exhibition, 2006. Society of Petroleum Engineers.

STEPHEN, K. D. & MACBETH, C. 2008. Reducing reservoir prediction uncertainty by updating a stochastic model using seismic history matching. *SPE Reservoir Evaluation & Engineering,* 11**,** 991-999.

SUGAI, K. & NISHIKIORI, N. 2006. An Integrated Approach to Reservoir Performance Monitoring and Analysis. Society of Petroleum Engineers.

SULEEN, F., OPPERT, S., CHAMBERS, G., LIBBY, L., CARLEY, S., ALONSO, D., DYGERT, T. & OLAYOMI, J. 2017. Application of Pressure Transient Analysis and 4D Seismic for Integrated Waterflood Surveillance- A Deepwater Case Study. Society of Petroleum Engineers.

TALASH, A. W. 1988. An Overview of Waterflood Surveillance and Monitoring. *Journal of Petroleum Technology,* 40**,** 1539-1543.

TERRADO, M., YUDONO, S. & THAKUR, G. 2007. Waterflooding surveillance and monitoring: Putting principles into practice. *Spe Reservoir Evaluation & Engineering,* 10**,** 552-562.

THAKUR, G. C. 1991. Waterflood surveillance Techniques - A Reservoir Management Approach.

TILLIER, E., LE RAVALEC, M. & DA VEIGA, S. 2012. Simultaneous inversion of production data and seismic attributes: Application to a synthetic SAGD produced field case. *Oil & Gas Science and Technology–Revue d'IFP Energies nouvelles,* 67**,** 289-301.

TRANI, M., ARTS, R. & LEEUWENBURGH, O. 2012. Seismic history matching of fluid fronts using the ensemble Kalman filter. *SPE Journal,* 18**,** 159-171.

TRANI, M., WOJNAR, K., MONCORGÉ, A. & PHILIPPE, B. Ensemble-Based Assisted History Matching Using 4D Seismic Fluid Front Parameterization. SPE Middle East Oil & Gas Show and Conference, 2017. Society of Petroleum Engineers.

TURA, A. & LUMLEY, D. E. Estimating pressure and saturation changes from time-lapse AVO data. Offshore Technology Conference, 2000. Offshore Technology Conference.

VAILLANT, M. & GLAUNÈS, J. Surface Matching via Currents. 2005 Berlin, Heidelberg. Springer Berlin Heidelberg, 381-392.

VAN DE HOEK, P., SOMMERAUER, G., NNABUIHE, L. & MUNRO, D. Large-scale produced water re-injection under fracturing conditions in Oman. Abu Dhabi International Petroleum Exhibition and Conference, 2000. Society of Petroleum Engineers.

VAN DEN HOEK, P., HUSTEDT, B., SOBERA, M., MAHANI, H., MASFRY, R., SNIPPE, J. & ZWARTS, D. Dynamic induced fractures in waterfloods and EOR. Paper SPE 115204 presented at the 2008 SPE Russian Oil and Gas Technical Conference and Exhibition. Moscow, Russia, 2008. 29-30.

WAGGONER, J. R. & HUANG, X. Integrating Time-Lapse Seismic and Reservoir Simulation for Improved Asset Management. Offshore Technology Conference.

WANG, Z. 2000. Seismic and acoustic velocities in reservoir rocks *Geophysics Reprint Series Number 19.* . Society of Exploration Geophysicists (December 1, 2000).

WEN, X.-H., DURLOFSKY, L. J. & CHEN, Y. 2006. Efficient 3D implementation of local-global upscaling for reservoir simulation. *Spe Journal,* 11**,** 443-453.

WEN, X.-H. & GÓMEZ-HERNÁNDEZ, J. J. 1996. Upscaling hydraulic conductivities in heterogeneous media: An overview. *Journal of Hydrology,* 183**,** ix-xxxii.

WHITE, C. D., WILLIS, B. J., NARAYANAN, K. & DUTTON, S. P. 2001. Identifying and estimating significant geologic parameters with experimental design. *SPE Journal,* 6**,** 311-324.

WIDESS, M. 1973. How thin is a thin bed? *Geophysics,* 38**,** 1176-1180.

WU, Z. & DATTA-GUPTA, A. Rapid history matching using a generalized travel time inversion method. SPE Reservoir Simulation Symposium, 2001. Society of Petroleum Engineers.

XU, W., TRAN, T., SRIVASTAVA, R. & JOURNEL, A. G. Integrating seismic data in reservoir modeling: the collocated cokriging alternative. SPE annual technical conference and exhibition, 1992. Society of Petroleum Engineers.

YILDIZ, H., VALAT, M. & MORROW, N. 1999. Effect of brine composition on wettability and oil recovery of a Prudhoe Bay crude oil. *Journal of Canadian Petroleum Technology,* 38.

YIN, Z., MACBETH, C. & CHASSAGNE, R. Joint interpretation of interwell connectivity by integrating 4D seismic with injection and production fluctuations. EUROPEC 2015, 2015. Society of Petroleum Engineers.

YOUSEF, A., GENTIL, P., JENSEN, J. & LAKE, L. 2005a. A Capacitance Model to Infer Interwell Connectivity From Production and Injection Rate Fluctuations. Paper SPE 95322, presented at the SPE Annual Technical Conference and Exhibition, Dallas, TX, 9-12 October.

YOUSEF, A. A., GENTIL, P. H., JENSEN, J. L. & LAKE, L. W. A capacitance model to infer interwell connectivity from production and injection rate fluctuations. SPE Annual Technical Conference and Exhibition, 2005b. Society of Petroleum Engineers.

YOUSEF, A. A., JENSEN, J. L. & LAKE, L. W. 2009. Integrated interpretation of interwell connectivity using injection and production fluctuations. *Mathematical Geosciences,* 41**,** 81-102.

ZABALZA-MEZGHANI, I., MANCEAU, E. & ROGGERO, F. A new approach for quantifying the impact of geostatistical uncertainty on production forecasts: The joint modeling method. paper to be presented at the, 2001. 6-12.